Interacting and hopping spin qubits in germanium

Wang, C.A.

DOI
10.4233/uuid:38216eaa-4b36-4633-94d0-113ade4849e5

Publication date
2025

Document Version
Final published version

Citation (APA)
Wang, C. A. (2025). *Interacting and hopping spin qubits in germanium*. [Dissertation (TU Delft), Delft University of Technology]. https://doi.org/10.4233/uuid:38216eaa-4b36-4633-94d0-113ade4849e5

Interacting and Hopping Spin Qubits in Germanium

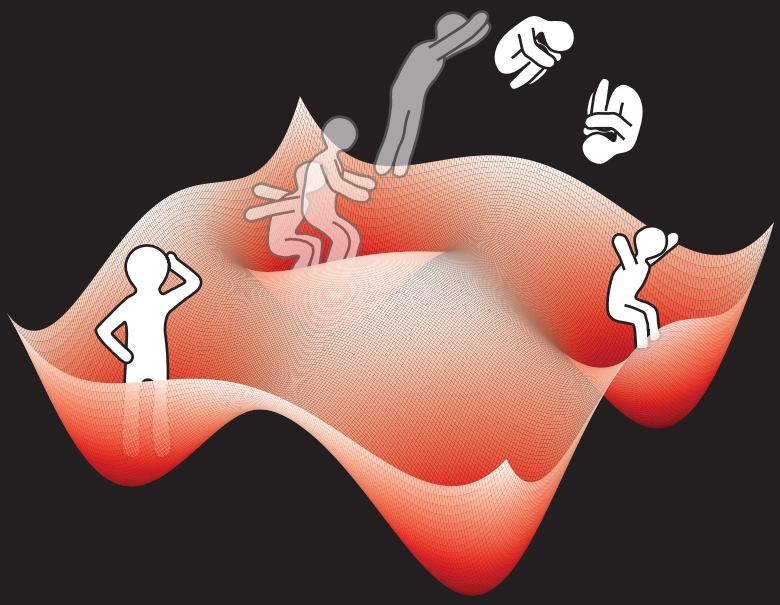

Chien-An Wang

INTERACTING AND HOPPING SPIN QUBITS IN GERMANIUM

Dissertation

for the purpose of obtaining the degree of doctor
at Delft University of Technology
by the authority of the Rector Magnificus, prof. dr. ir. T.H.J.J. van der Hagen,
chair of the Board for Doctorates
to be defended publicly on
Wednesday, 5 February 2025 at 12:30 o'clock

by

Chien-An WANG

Master of Science in Applied Physics,
Delft University of Technology, Netherlands,
born in Chiayi, Taiwan

This dissertation has been approved by the promotors.

Composition of the doctoral committee:

Rector Magnificus,	chairperson
Dr. ir. M. Veldhorst,	Delft University of Technology, promotor
Dr. G. Scappucci,	Delft University of Technology, copromotor

Independent members:

Prof. dr. ir. L.P. Kouwenhoven	Delft University of Technology
Prof. dr. L. DiCarlo	Delft University of Technology
Dr. S. Bosco	Delft University of Technology
Prof. dr. F. Kuemmeth	University of Copenhagen
Dr. Y.-M. Niquet	University of Grenoble Alpes

Printed by: Gildeprint - www.gildeprint.nl

Front & Back: Illustration of hole spin qubits in the potential of a quantum dot array.

ISBN 978-94-6384-722-3

An electronic version of this dissertation is available at
http://repository.tudelft.nl/.

CONTENTS

1

INTRODUCTION

1

Quantum mechanics has been playing a central role for physics innovations since the last century. It was applied to a wide variety of situations and changed our understanding about the nature. One of the examples is the Standard Model, a confluence of quantum mechanics and special relativity that unites fundamental forces and particles. Another example is the physical properties of phases of matters, which cannot be understood without involving quantum mechanics. Lastly, quantum mechanics allows nonlocal correlations on the particles that are far from each other, which violates any theories based on local hidden variables [1, 2].

The development of quantum mechanics not only shaped our understanding about the physical world but also led to important applications in modern technology, such as lasers, magnetic resonance imaging, and integrated circuits. One of the emerging applications is quantum computation, which exploits quantum mechanics for information processing. This is a highly active research field, as it promises to resolve challenges that are beyond the reach of classical computers.

1.1. QUANTUM COMPUTATION

Conventional computers operate according to classical physics, such that the basic unit for computation, the bit, is always in a state of 0 or 1. Quantum computers operate according to quantum mechanics. The basic unit for information processing is the quantum bit, or qubit. Unlike a classical bit in a classical computer which can only be either 0-state or 1-state, a qubit adheres to the superposition principle of quantum mechanics, allowing it to be in a state of superposition of 0 and 1. The difference between conventional computers and quantum computers become even more apparent when concerning multiple qubits. When dealing with multiple qubits, they can be regarded as a single entity that also follows the superposition principle. A system comprising N qubits can be in a state of superposition of 2^N states, leading to non-trivial multi-qubit states known as entangled states. By leveraging multi-qubit entanglement, quantum algorithms can process encoded information and extract useful quantity at the end, achieving speed-up for certain computational tasks.

The physical form of a qubit is a quantum mechanical two-level system that can be in a state of coherent superposition. Quantum mechanical two-level systems have been demonstrated in various physical systems. Examples include atomic levels of ions or atoms [3–8], superconducting circuits [9–12], photons [13], spins of nuclei [14, 15], and spins of electrons or quasi-particles in solid-state systems [16–18]. For making a practical quantum computer, however, there are additional requirements to be considered. Important aspects are defined by the DiVincenzo criteria [19], stating that on (1) a scalable physical system with well characterized qubits, we should have (2) the ability to reliably initialize qubits into a known state. These qubits should have (3) long coherence time. Furthermore, we should be able to perform (4) a universal set of quantum gates and have (5) measurement capability.

Advancing the state of the art in the qubit quantity and quality is essential for executing quantum algorithms for relevant problems [20–22]. The first DiVincenzo criteria, a scalable physical system, should be regarded as an umbrella term encompassing the integration of many qubits, efforts and yields [23], interconnections and wiring [24], control electronics [25], power dissipation [26], and the degree of automation [27]. In a

scaled-up system, it is also essential to improve qubit operation fidelities. The error rate of the quantum gates needs to be reduced, such that all the qubits can interact effectively and maintain a low accumulated error in quantum circuits. Quantum error correction codes have been developed to extend quantum coherence and reduce gate error by combining multiple defective physical qubits into a logical qubit with an improved error rate [28]. The fidelity of the physical qubits need to exceed certain thresholds, which depend on the details of error correction protocol. As an example, in a qubit platform with 2D connectivity, the surface code typically requires gate fidelity above 99% [29]. This necessitates scalable and high-fidelity qubit control protocols.

1.2. SPIN QUBITS IN PLANAR GERMANIUM QUANTUM DOTS

Spins in gate-defined semiconductor quantum dots are considered as a promising approach for quantum computation, as their production method is compatible with the classical computer based on semiconductor technology [30–33]. Among all the semiconductor materials, hole spins in germanium quantum dots have several advantages, including strong spin-orbit interaction (SOI), absence of valley degeneracy and large heavy hole - light hole splitting [34], small in-plane effective mass [35], and the formation of ohmic contacts with metals [35–37]. Based on these developments, in this thesis we further explore the physics and control protocols enabled by hopping spins in the quantum dot arrays. Our results provide insights into challenges in spin-qubit systems, such as qubit addressability in large qubit arrays, charge-noise limited dephasing, interconnects that extend beyond nearest neigbours, efficient single-qubit gates, and high fidelity two-qubit gates.

1.3. THESIS OUTLINE

In this thesis, we study germanium spin qubits in experiments and numerical simulations. The rest of the thesis is organized in the following chapters.

- In **chapter 2** we provide the background information relevant to the work in this thesis, including the theoretical description of spins in germanium quantum dots, as well as the measurement setup used in the experiments.
- In **chapter 3** we study the control protocols for spin-spin exchange interactions, and quantify the individual coupling strength in a configuration of 2×2 array when all the nearest neighboring coupling are turned on. We can tune to a regime of equal coupling strength, in which the four-spin entangled states emerge as the resonating valence bond states.
- In **chapter 4** we model the qubit frequency susceptibility to charge noise and predict the optimal magnetic field orientation for extended qubit coherence time.
- In **chapter 5** we show multi-photon transitions in a two-spin system, and discuss opportunities to use this method for qubit addressability in large qubit array based on shared control architecture.
- In **chapter 6** we demonstrate coherent spin qubit shuttling through quantum dots. We quantify the loss of the quantum information during the process.

- In **chapter 7** we demonstrate high-fidelity baseband control of single qubit and two qubit gates, with extended coherence times by operating at low magnetic field. The single qubit gate is realized based on shuttling between the quantum dots, resembling the original spin qubit proposal by Loss and Divincenzo. The two-qubit CPhase gate achieves average fidelity 99.3% in the randomized benchmarking experiments.
- In **chapter 8** we conclude and provide an outlook on the near future for germanium spin-qubits operations.

BIBLIOGRAPHY

[1] J. S. Bell. “On the Einstein Podolsky Rosen paradox”. In: Physics Physique Fizika 1.3 (1964), pp. 195–200.

[2] A. Aspect, J. Dalibard, and G. Roger. “Experimental test of Bell’s inequalities using time-varying analyzers”. In: Phys. Rev. Lett. 49 (1982), p. 1804.

[3] C. Monroe et al. “Demonstration of a Fundamental Quantum Logic Gate”. In: Phys. Rev. Lett. 75 (1995), p. 4714.

[4] D. J. Wineland et al. “Experimental Issues in Coherent Quantum-State Manipulation of Trapped Atomic Ions”. In: NIST J. Res 103 (1998), pp. 259–328.

[5] D. Jaksch et al. “Fast Quantum Gates for Neutral Atoms”. In: Phys. Rev. Lett. 85 (Sept. 2000), pp. 2208–2211.

[6] I. H. Deutsch, G. K. Brennen, and P. S. Jessen. “Quantum computing with neutral atoms in an optical lattice”. In: Fortschritte der Physik: Progress of Physics 48.9-11 (2000), pp. 925–943.

[7] M. Anderlini et al. “Controlled exchange interaction between pairs of neutral atoms in an optical lattice”. In: Nature 448 (2007), pp. 452–456. ISSN: 1476-4687.

[8] D. Bluvstein et al. “A quantum processor based on coherent transport of entangled atom arrays”. In: Nature 604 (2022), pp. 451–456. ISSN: 1476-4687.

[9] Y. Nakamura, Yu. A. Pashkin, and J. S. Tsai. “Coherent control of macroscopic quantum states in a single-Cooper-pair box”. In: Nature 398 (1999), pp. 786–788. ISSN: 1476-4687.

[10] J. E. Mooij et al. “Josephson Persistent-Current Qubit”. In: Science 285.5430 (1999), pp. 1036–1039.

[11] J. M. Martinis et al. “Rabi Oscillations in a Large Josephson-Junction Qubit”. In: Phys. Rev. Lett. 89 (2002), p. 117901.

[12] J. Koch et al. “Charge-insensitive qubit design derived from the Cooper pair box”. In: Phys. Rev. A 76 (4 2007), p. 042319.

[13] E. Knill, R. Laflamme, and G. J. Milburn. “A scheme for efficient quantum computation with linear optics”. In: Nature 409 (2001), pp. 46–52. ISSN: 1476-4687.

[14] L. M. K. Vandersypen et al. “Experimental realization of Shor’s quantum factoring algorithm using nuclear magnetic resonance”. In: Nature 414 (2001), pp. 883–887. ISSN: 1476-4687.

[15] F. Jelezko et al. “Observation of Coherent Oscillations in a Single Electron Spin”. In: Phys. Rev. Lett. 92 (2004), p. 076401.

[16] X. Li et al. “An All-Optical Quantum Gate in a Semiconductor Quantum Dot”. In: Science 301.5634 (2003), pp. 809–811.

[17] J. M. Elzerman et al. “Single-shot read-out of an individual electron spin in a quantum dot”. In: Nature 430 (2004), pp. 431–435. ISSN: 1476-4687.

[18] M. Hays et al. “Coherent manipulation of an Andreev spin qubit”. In: Science 373.6553 (2021), pp. 430–433.

[19] David P. DiVincenzo. “The Physical Implementation of Quantum Computation”. In: Fortschritte der Physik 48.9-11 (2000), pp. 771–783.

[20] M. E. Beverland et al. “Assessing requirements to scale to practical quantum advantage”. In: arXiv (2022). eprint: 2211.07629.

[21] Y. Quek et al. “Exponentially tighter bounds on limitations of quantum error mitigation”. In: arXiv (2024). eprint: 2210.11505.

[22] D. Stilck França and R. García-Patrón. “Limitations of optimization algorithms on noisy quantum devices”. In: Nature Physics 17 (2021), pp. 1221–1227.

[23] S. Neyens et al. “Probing single electrons across 300-mm spin qubit wafers”. In: Nature 629 (2024), pp. 80–85. ISSN: 1476-4687.

[24] Ruoyu Li et al. “A crossbar network for silicon quantum dot qubits”. In: Science Advances 4.7 (2018), eaar3960.

[25] Xiao Xue et al. “CMOS-based cryogenic control of silicon quantum circuits”. In: Nature 593.7858 (May 2021), pp. 205–210. ISSN: 1476-4687.

[26] L. M. K. Vandersypen et al. “Interfacing spin qubits in quantum dots and donors—hot, dense, and coherent”. In: npj Quantum Inf. 3 (2017), p. 34.

[27] Hannes Watzinger et al. “Machine learning enables completely automatic tuning of a quantum device faster than human experts”. In: Nature Communications 11.1 (Aug. 2020), p. 4161. ISSN: 2041-1723.

[28] P. W. Shor. “Scheme for reducing decoherence in quantum computer memory”. In: Phys. Rev. A 52 (Oct. 1995), R2493–R2496.

[29] Austin G. Fowler et al. “Surface codes: Towards practical large-scale quantum computation”. In: Phys. Rev. A 86.3 (Sept. 2012), p. 032324. ISSN: 1050-2947.

[30] R. Maurand et al. “A CMOS silicon spin qubit”. In: Nature Communications 7.1 (Nov. 2016), p. 13575. ISSN: 2041-1723.

[31] A. M. J. Zwerver et al. “Qubits made by advanced semiconductor manufacturing”. In: Nat. Electron. 5.3 (2022), pp. 184–190. ISSN: 2520-1131.

[32] L. M. K. Vandersypen et al. “Interfacing Spin Qubits in Quantum Dots and Donors—Hot, Dense, and Coherent”. In: npj Quantum Information 3.1 (2017), pp. 1–10. ISSN: 2056-6387.

[33] Giordano Scappucci et al. “The Germanium Quantum Information Route”. In: Nature Reviews Materials (2020), pp. 1–18. ISSN: 2058-8437.

[34] L. A. Terrazos et al. “Theory of Hole-Spin Qubits in Strained Germanium Quantum Dots”. In: Physical Review B 103.12 (2021), p. 125201.

[35] N. W. Hendrickx et al. “Gate-Controlled Quantum Dots and Superconductivity in Planar Germanium”. In: Nature Communications 9.1 (2018), p. 2835. ISSN: 2041-1723.

[36] Hannes Watzinger et al. “A Germanium Hole Spin Qubit”. In: Nature Communications 9.1 (2018), p. 3902. ISSN: 2041-1723.

[37] M. Lodari et al. “Light Effective Hole Mass in Undoped Ge/SiGe Quantum Wells”. In: Physical Review B 100.4 (2019), p. 041304.

2

THEORY AND BACKGROUND INFORMATION

2.1. MATERIALS AND DEVICES FOR SPIN QUBITS IN GERMANIUM

A quantum dot device is a physical structure in the solid state system that can confine particles, typically electrons or holes, in a small region with a size of about 100 nm. Here, we will consider the quantum dot implementation of gate-defined semiconductor quantum dots. In this method, carriers are confined in the z-direction by band misalignment of the semiconductor heterostructure, and confinement in the xy-direction is established by shaping the electrical potential landscape via voltage-biased metallic electrodes. The spin degree of freedom of the trapped carriers can be controlled and used as spin qubits. Spin qubits in gate-defined quantum dots have been pioneered in III-V materials (e.g. GaAs). More recently group IV materials such as silicon have become the workhorse, as the spin coherence time is extended by order of magnitude due to the natural abundance of isotopes with zero nuclear spin. Silicon spin qubits steadily advance in qubit numbers [1, 2] as well as control fidelity [3–6].

In this thesis we work on spin qubits in another group-IV material - germanium. The planar Ge/SiGe heterostructure plays an important role in forming quantum dots and spin qubits. The schematic of the material stack is shown in Fig. 2.1a. The energy profile in Fig. 2.1b provides the confinement in the out-of-plane direction. It also reveals an important property: the lowest heavy hole bands are separated from the light hole and split-off bands by more than tens of meV, thanks to the spin-orbit coupling and the engineered compressive strain in the quantum well.

The confinement potential in the in-plane direction is created by applying voltages

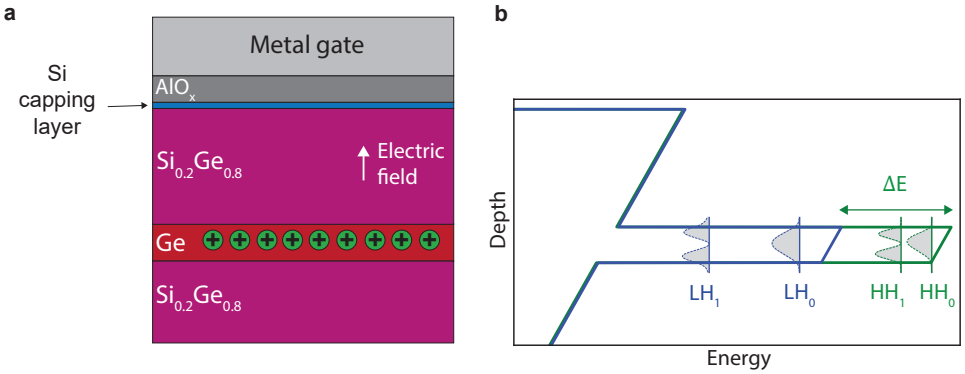

Figure 2.1: **Ge/SiGe heterostructure and valence band energy. a**, Schematic illustration of the material stack, including Ge/SiGe heterostructure, metal electrodes and the dielectric in between. The thickness of the quantum well is typically around 16 nm. The insulating gate dielectrics AlO_x electrically isolates metal gate from the heterostructure. The gate creates electric field and accumulates two-dimensional hole gas (2DHG) in the quantum well. **b**, Simplified illustration of valence band of the heavy hole band (blue) and light hole (green). We plot the lowest two heavy hole sub-bands $HH_{0,1}$ and light hole sub-bands $LH_{0,1}$. They are the results of out-of-plane valence band confinement potential. The compressive strain in the quantum well results in valence band energy difference ΔE. Here we assume the strain in the SiGe layers are homogeneous and relaxed to zero, resulting in a zero heavy hole - light hole splitting (which is an oversimplification). In this plot we assume a linear potential is created by the out-of-plane electric field. This is another simplification which neglect the screening effect of the accumulated holes as well as the finite dimension effect of the metal gate, in which both should create curvature in the potential profile. The figure is modified from Fig. 4.2A.

on the metallic gate electrodes on top of the heterostructure. The gate electrodes are electrically isolated from other gates and heterostructures by the dielectrics (e.g. AlO_x). As depicted in Fig. 2.2, the electrodes are patterned in specific shapes, circular plungers and elongated barriers, to create the desired electrical potential at the depth of the quantum well plane to trap holes. The distance between barriers is typically on the scale of 100 nm, to have strong in-plane confinement and a sizable quantized orbital energy level spacing which isolates the orbital excited states from the orbital ground state. Designing the plungers and barriers to arrange several quantum dot potential wells together realizes a basic unit cell of spin qubits. In reality, the concept mentioned above is not possible without high-quality heterostructures. The quantum well with low-disorder and high electrical uniformity allows the potential experienced by holes to be shaped as designed, without interruption or extra dots forming at unintended locations.

To detect a single low energy excitation in the solid-state device, we have to amplify the signal generated from the device and meanwhile suppress energy excitations as well as noise from the environment. The first-stage amplification is realized by the charge sensor, a single-hole transistor (SHT), as part of the drawing in Fig. 2.2. The current through the sensor can be very sensitive to the electrostatic potential experienced by the sensor quantum dot, amplifying the signal of charge movement nearby [7, 8]. This property is used to measure the change of hole occupations of the neighbouring quantum dots, which reveals the spin states of the holes after spin-to-charge conversion (Section 2.5.1). Without averaging for multiple experimental runs, this scheme can resolve the charge occupation of a single experimental run (single-shot readout) with high con-

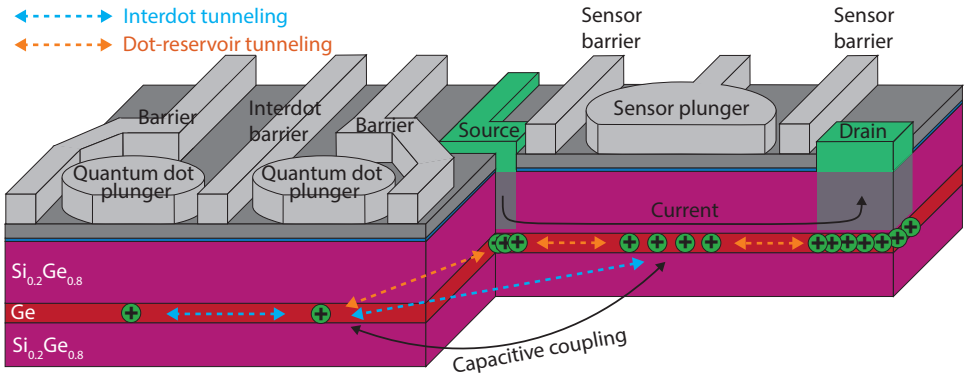

Figure 2.2: **Schematics of a quantum dot device.** Cross-sectional illustration of a device containing three gate-defined quantum dots. In the ideal scenario, by applying appropriate voltages on the individual plunger (circular metal gate in grey) and the surrounding barriers (finger-shape metal gate in grey), the confinement in three directions is formed underneath the plunger and in the plane of the Ge-quantum well, which can trap the positively charged holes. The quantum dots on the left typically accumulate in a few-hole regime. The sensor dot on the right typically accumulates more holes, and tunnel-coupled to the reservoirs which have high carrier density. The reservoirs are contacted to the source and drain (in green) by diffusing the metal, typically Al or Pt, into the heterostructure. The interdot (dot-reservoir) tunnelling processes are marked in dashed-cyan (-orange) arrows. The tunnelling current through the sensor is sensitive to the hole occupations of the quantum dots via the capacitive coupling. In this plot the fanouts of the quantum dot plunger gates are not plotted. Several parts of the AlO_x are omitted.

fidence.

Several procedures are taken to suppress noise. As explained in Section 2.7, the device is placed in a radiation shield and cooled to a nominal temperature of 20 mK in the dilution refrigerator. The wires connected to it are attenuated or filtered. These experimental practices are meant to cool down electrons, phonons and photons that can interact with charges and spins in the quantum dots. There are still some degrees of freedom in the environment that remain unfrozen at such low temperature. The charge noise from the two-level fluctuators can interfere the charge sensor signals and also dephase spin qubits. To establish low noise, it is key to have a high quality heterostructure, dielectric, and metal gate stack [9, 10]. The nuclear spins in the semiconductor quantum well can dephase the spin qubits via hyperfine interaction. In the case of germanium, thanks to the anisotropic hyperfine interaction, the effective noise strength can be made smaller by applying an in-plane magnetic field [11]. Further nuclear spin noise reduction may be established by isotopically enriching the germanium to nuclear spin-free isotopes.

2.2. CONFINED HOLES IN PLANAR GERMANIUM

In the valence band of germanium the low energy states near the Γ-point are holes that have total angular momentum $\frac{3}{2}\hbar$ or $\frac{1}{2}\hbar$ as a result of the underlying electron spin ($\frac{1}{2}\hbar$) and the p-like orbital ($1\hbar$). The angular momentum eigenstates are$|j, m_j\rangle = |\frac{3}{2}, \pm\frac{3}{2}\rangle$ for heavy holes, $|\frac{3}{2}, \pm\frac{1}{2}\rangle$ for light holes, and $|\frac{1}{2}, \pm\frac{1}{2}\rangle$ for the split-off bands [12]. The planar heterostructure used in this thesis has growth direction [001] corresponding to the z-axis at out-of-plane direction. This defines the rotational symmetry and the quantum number m_j is related to the projection of angular momentum along z-direction ($m_j\hbar$). At low energy regime that the wave-functions are localized close to the Γ-point and neglecting the split-off band which is 0.29 eV above heavy hole and light hole bands, we can study the energy levels of the germanium using 4×4 Luttinger-Kohn Hamiltonian with effective mass approximation [13, 14]. The full Hamiltonian of a hole confined in a quantum dot, in the basis $|j, m_j\rangle = \{|\frac{3}{2}, \frac{3}{2}\rangle, |\frac{3}{2}, -\frac{3}{2}\rangle, |\frac{3}{2}, \frac{1}{2}\rangle, |\frac{3}{2}, -\frac{1}{2}\rangle\}$, is written as

$$H = H_{\mathrm{LK}} + H_{\mathrm{BP}} + V_{\mathrm{confine}}(x, y, z) + H_{\mathrm{Zeeman}}, \tag{2.1}$$

where $V_{\mathrm{confine}}(x, y, z)$ is the confinement potential, H_{LK} is the Luttinger-Kohn Hamiltonian describing kinetic energy [13]

$$H_{\mathrm{LK}} = \begin{pmatrix} P+Q & 0 & S & R \\ 0 & P+Q & R^\dagger & -S^\dagger \\ S^\dagger & R & P-Q & 0 \\ R^\dagger & -S & 0 & P-Q \end{pmatrix}, \tag{2.2}$$

$\{P, Q, S, R, S^\dagger, R^\dagger\}$ are in the form $\sum_{\alpha\beta} c_{\alpha\beta} \frac{p_\alpha p_\beta}{m}$ with the generalized momentum $p_\alpha = -i\hbar\partial_\alpha + eA_\alpha$ including vector potential A_α at the direction $\alpha \in \{x, y, z\}$ (see **chapter 4** for explicit formulas; see [14, 15] for extensive discussion). H_{BP} is Bir-Pikus term describing the effect of strain field. The Zeeman energy is [14]

$$H_{\mathrm{Zeeman}} = 2\mu_B \kappa \vec{J} \cdot \vec{B} + 2\mu_B q (J_x^3 B_x + J_y^3 B_y + J_z^3 B_z). \tag{2.3}$$

Here μ_B is Bohr's magneton, $\kappa = 3.41$, $q = 0.066$, $\vec{B} = (B_x, B_y, B_z)$ is the magnetic field, and $\vec{J} = (J_x, J_y, J_z)$ are spin-3/2 matrices [14]

$$J_x = \begin{pmatrix} 0 & 0 & \sqrt{3}/2 & 0 \\ 0 & 0 & 0 & \sqrt{3}/2 \\ \sqrt{3}/2 & 0 & 0 & 1 \\ 0 & \sqrt{3}/2 & 1 & 0 \end{pmatrix}, \tag{2.4}$$

$$J_y = \begin{pmatrix} 0 & 0 & -i\sqrt{3}/2 & 0 \\ 0 & 0 & 0 & i\sqrt{3}/2 \\ i\sqrt{3}/2 & 0 & 0 & -i \\ 0 & -i\sqrt{3}/2 & i & 0 \end{pmatrix}, \tag{2.5}$$

$$J_z = \begin{pmatrix} 3/2 & 0 & 0 & 0 \\ 0 & -3/2 & 0 & 0 \\ 0 & 0 & 1/2 & 0 \\ 0 & 0 & 0 & -1/2 \end{pmatrix}, \tag{2.6}$$

which show the intrinsic spin-3/2 structure of heavy holes $m_j = \pm\frac{3}{2}$ and light holes $m_j = \pm\frac{1}{2}$.

Despite the complicated Hamiltonian Eq. (2.1), we can take H_{Zeeman} as the starting point when describing the hole spin qubit in the planar germanium heterostructure used in this thesis. The reason is that the heavy hole ($|\frac{3}{2}, \pm\frac{3}{2}\rangle$) - light hole ($|\frac{3}{2}, \pm\frac{1}{2}\rangle$) energy separation, created in germanium quantum well by the compressive strain and the confinement in growth direction, is the dominant energy scale in Eq. (2.1). Therefore, we can first look at the block of heavy holes in Eq. (2.1), find out the main components of the lowest two energy eigenstates (with the spin wave functions determined by Eq. (2.3)), and later consider the perturbation from the terms which couple heavy hole and light hole sectors. These coupling terms include $\{J_x, J_y, J_x^3, J_y^3\}$ in H_{Zeeman} and the off-diagonals $\{S, R, S^\dagger, R^\dagger\}$ in H_{LK} and H_{BP}.

In this picture, heavy holes (for both $m_j = \pm\frac{3}{2}$) have the effective mass $m_\perp = m_0/(\gamma_1 - 2\gamma_2) \approx 0.20 m_0$ at out-of-plane and $m_\parallel = m_0/(\gamma_1 + \gamma_2) \approx 0.057 m_0$ at in-plane direction, with Luttinger parameters $\gamma_1 = 13.38$ and $\gamma_2 = 4.24$ for Ge [16]. The ground state spatial wave-function $\Psi_0^H(x, y, z)$ of the heavy holes subjected to the confinement potential $V_{\text{confine}}(x, y, z)$ can be obtained accordingly. By plugging the explicit form of spin-3/2 matrices (Eq. (2.4)- (2.6)) in Eq. (2.3), the Zeeman interaction in the heavy hole block is

$$H_{\text{Zeeman}}^H = \frac{1}{2}\mu_B \left(3q\sigma_x B_x - 3q\sigma_y B_y + (6\kappa + 13.5q)\sigma_z B_z\right). \tag{2.7}$$

Combining the orbital and the spin degree of freedom, we can write the lowest two energy eigenstates $\{|g\rangle, |e\rangle\}$ as $|g\rangle = (c_g^- |\frac{3}{2}, -\frac{3}{2}\rangle + c_g^+ |\frac{3}{2}, +\frac{3}{2}\rangle) \otimes \Psi_0^H(x, y, z)$ and $|e\rangle = (c_e^- |\frac{3}{2}, -\frac{3}{2}\rangle + c_e^+ |\frac{3}{2}, +\frac{3}{2}\rangle) \otimes \Psi_0^H(x, y, z)$, where the coefficients $c_{g,e}^\pm$ depend on the magnetic field orientation (B_x, B_y, B_z).

When including the heavy hole-light hole interaction, the above expressions of $\{|g\rangle, |e\rangle\}$ become the approximation of the energy eigenstates. The true eigenstates will be the superposition of the heavy hole (major part) and the light hole (minor part). The resulting energy structure is discussed in the next section.

2.2.1. EFFECTIVE SPIN-1/2 SYSTEM AND g-MATRIX

For spin-qubit applications we can simplify the system and only look at the lowest two energy eigenstates $\{|g\rangle,|e\rangle\}$ of Eq. (2.1). At zero magnetic field, these two states are degenerate. At finite magnetic field, the energy difference between the two eigenstates depends on the magnetic field strength and orientation, forming an effective spin-1/2 system. The g-matrix is defined by the effective spin-1/2 Hamiltonian [17]

$$H = \frac{1}{2}\mu_B \vec{\sigma}\cdot\hat{g}\cdot\vec{B}, \tag{2.8}$$

where the Pauli matrices $\vec{\sigma}$ acting on the states spanned by $\{|\downarrow\equiv|g\rangle,|\uparrow\rangle\equiv|e\rangle\}$. The g-matrix can have singular value decomposition $\hat{g}=\hat{U}\hat{g_d}\hat{V}$, where the matrix $\hat{g_d}$ is diagonal, the matrix $\hat{V}$ defines the magnetic axes, and the matrix $\hat{U}$ defines the qubit basis. Thus, the g-matrix depends on the choice of the qubit basis and cannot be uniquely defined. Notice that it is possible to be made symmetric with certain sets of qubit basis and magnetic axes, while in general it can be non-symmetric in other basis.

We note that the g-matrix mentioned in this chapter is equivalent to the term 'g-tensor' in some literature, but may differ in others. For example, 'g-tensor' is sometimes used to refer to a 3×3 real symmetric matrix that represents the measurable eigenvalues in $\hat{g_d}$ and magnetic axes $\hat{V}$. In a planar, uniform heterostructure, $\hat{g_d}$ and $\hat{V}$ of a spin are independent of the position of its wave function along the plane. A hole spin will rotate when it is moving along the plane and in the presence of spin-orbit coupling (e.g. linear Rashba $H_R \propto p_y\sigma_x - p_x\sigma_y$). One way of modelling this is to include both the spin and the orbital degrees of freedom in the Hamiltonian. The other way of modelling is to absorb the spin-orbit coupling in the g-matrix. In this framework, the g-matrix depends on the position in the presence of a spin-orbit interaction. After the hole is displaced along the plane to a new position, the Hamiltonian Eq (2.8) is different than the Hamiltonian before the displacement. This effect can be captured by the position-dependent matrix $\hat{U}$.

When the heavy hole-light hole interactions are neglected, $\hat{g}$ is entirely given by Eq. (2.7), which has magnetic axes aligned with the symmetry axes of the heterostructure (x-, y-, z-axis), and is highly anisotropic as (g_{xx}, g_{yy}, g_{zz})= ($3q$, $-3q$, $6\kappa+13.5q$)= (0.2, -0.2, 21.4). The g-matrix is modified when taking into account the heavy hole-light hole interactions. The interaction mixes the heavy hole states $\{|\downarrow\rangle,|\uparrow\rangle\}$ with virtual states of light holes. The changes of energies can be seen in the second order perturbation. As an example, we can look at the spin in the out-of-plane magnetic field $\vec{B}=B\hat{z}$. Before adding the heavy hole-light hole interactions, the qubit ground state is $|\downarrow\rangle=|\frac{3}{2},-\frac{3}{2}\rangle\otimes\Psi_0^H(x,y,z)$ and excited state is $|\uparrow\rangle=|\frac{3}{2},\frac{3}{2}\rangle\otimes\Psi_0^H(x,y,z)$, with the orbital energy E_h and the Zeeman splitting $E_\uparrow - E_\downarrow = g_{zz}\mu_B B$. H_{Zeeman} and heavy hole-light hole interactions H_{HL} (off-diagonals $\{S, R, S^\dagger, R^\dagger\}$ in H_{LK} and H_{BP}) introduce energy corrections via the light hole states labelled by the index l:

$$\Delta E_\uparrow = \sum_l \frac{1}{E_h - E_l}\langle\uparrow|H_{HL}+H_{\text{Zeeman}}|l\rangle\langle l|H_{HL}+H_{\text{Zeeman}}|\uparrow\rangle \tag{2.9}$$

$$\Delta E_\downarrow = \sum_l \frac{1}{E_h - E_l}\langle\downarrow|H_{HL}+H_{\text{Zeeman}}|l\rangle\langle l|H_{HL}+H_{\text{Zeeman}}|\downarrow\rangle \tag{2.10}$$

From these we obtain the correction of one of the components $\Delta g_{zz} = \frac{\Delta E_{\uparrow} - \Delta E_{\downarrow}}{\mu_B B}$. The corrections of the other components (e.g. Δg_{xx}, Δg_{yy}) can be obtained similarly. These formula also indicates that, by changing the spatial wave functions of $\{|\uparrow\rangle, |\downarrow\rangle, |l\rangle\}$ and the orbital energies $E_{h,l}$ via $V_{\text{confine}}(x, y, z)$, the energy corrections $\Delta E_{\uparrow,\downarrow}$ as well as the g-matrix components change accordingly.

In theory, the g-matrix still remains highly anisotropic, $g_{zz} \gg g_{xx}, g_{yy}$, if the quantization energy of the z-direction confinement is still dominant. The anisotropy is predicted to change when the wave function is squeezed such that the confinement potential in x or y direction becomes comparable to z-direction [18]. The strain profile in H_{BP} can also change the g-matrix, as shown in the theory [19]. In particular, the off-diagonal elements become non-zero when shear strain is present. In this case, the magnetic axes of $\hat{g}$ are not along the original coordinate axes but can be tilted. The tilting angle can vary from dot to dot, as reported in the experimental work [11].

2.2.2. ZEEMAN ENERGY

The Zeeman energy $\Delta E_Z = \mu_B |\hat{g} \cdot \vec{B}|$ of a spin is the energy difference between the eigenenergies of Eq. (2.8). It is linearly proportional to magnetic field strength and depends on the alignment between the magnetic field and the magnetic axes of the g-matrix. The constant-Zeeman energy surface is an ellipsoid in the three-dimensional space of magnetic field, $\Delta E_Z^2 = \vec{B} \cdot (\hat{g}^T \hat{g}) \cdot \vec{B}$. Three symmetry axes of the ellipsoid, or the eigenvectors of the matrix $\hat{g}^T \hat{g}$, is the magnetic axes of the g-matrix. Thus, the magnetic axes can be determined through the measurement of the Zeeman energy as a function of field orientation.

The g-factor (omitting the sign) is a scalar defined by the measurable quantities ΔE_Z and $\vec{B}$ as $g = \frac{\Delta E_Z}{\mu_B B}$, or $g = \frac{|\hat{g} \cdot \vec{B}|}{|\vec{B}|}$, where the magnetic field strength $B = |\vec{B}|$.

2.2.3. DRIVING MECHANISM - ELECTRIC DIPOLE SPIN RESONANCE

The typical methods of driving a single spin qubit (flipping from $|\downarrow\rangle$ to $|\uparrow\rangle$) are either applying oscillating magnetic field as electron spin resonance [3, 20] (ESR) or applying oscillating electric field as electric dipole spin resonance (EDSR), which couples the motion to the spin via micromagnets [4, 21] or spin-orbit interaction [22–25].

Germanium has strong spin-orbit interaction allowing EDSR. When applying an oscillating electric field, there are two effects happening at the microscopic levels: g-matrix magnetic resonance (g-TMR) and iso-Zeeman EDSR [26]. g-TMR is the result of the change of magnetic axes of the g-matrix due to the deformation of the wave function, moving in non-harmonic potential, or moving in a spatially varying strain field [27, 28]. This effect can be correlated to the measurement of the gate-voltage-dependent g-matrix (e.g. measuring magnetic axes and the corresponding g-factors at various gate voltage settings). Iso-Zeeman EDSR is the result of the effective magnetic field seen in the moving frame of the hole due to spin-orbit interaction. This effect occurs as if the hole were moving in a perfectly uniform quantum well without its spatial wave function changing during the motion. In this ideal case, the magnetic axes and the g-factor components do not depend on the position of the hole (translational invariance in the lab frame). The effective spin-orbit interaction for holes in the two-dimensional plane has been stud-

ied theoretically [16, 22, 29, 30]. The effective cubic Rashba spin-orbit coupling mediates EDSR when the wave function is in the moving potential that is circular in the xy-plane [16, 31]. The effective linear Rashba spin-orbit coupling can appear and allow much faster EDSR when the potential is elliptic in the xy-plane [18, 32].

One of the descriptions for EDSR mechanism is the g-matrix formalism [17] that includes both effects mentioned above. The g-matrix is modulated by the oscillating gate voltage nearby the confined hole. The wave function of the hole can be displaced and deformed at the same time, changing the g-matrix through heavy hole-light hole interaction. In this model it is assumed the linear modulation $\hat{g}(V_g) = \hat{g}_0 + \hat{g}' V_g$, with the gate voltage $V_g(t) = V_{ac}\cos(\omega_d t)$ oscillating in the angular frequency ω_d that is in the resonant condition with the spin, $\hbar\omega_d = \Delta E_Z = g\mu_B B$. When the system is fully coherent, the spin can evolve between the states $|\downarrow\rangle$ and $|\uparrow\rangle$ at the Rabi frequency given by [17]

$$f_{\text{Rabi}} = \frac{\mu_B B V_{ac}}{2hg} |(\hat{g}_0 \cdot \vec{b}) \times (\hat{g}' \cdot \vec{b})|, \tag{2.11}$$

where the unit vector $\vec{b} = \frac{\vec{B}}{B}$, the magnetic field strength $B = |\vec{B}|$ and the effective g-factor g.

2.3. TUNNEL COUPLINGS BETWEEN QUANTUM DOTS

Spin-qubits in gate-defined quantum dot heavily rely on tunnel coupling between two dots for their operations. Due to the g-factor anisotropy and spin-orbit effect, the tunnelling process between two dots can simultaneously cause the spin to flip. A general spin non-conserving tunnelling Hamiltonian of an electron (or a hole) between orbital ground state levels of the two quantum dots L, R can be written as [33]

$$H_t = \sum_{\alpha,\beta=\uparrow,\downarrow} t_{\alpha\beta} c^\dagger_{L\alpha} c_{R\beta} + \text{h.c.}, \tag{2.12}$$

where α, β are spin indices, $c^\dagger_{L\alpha}$ ($c_{R\beta}$) is creation (annihilation) operator in dot L (R), h.c. is hermitian conjugate and $t_{\alpha\beta}$ are tunnel couplings in a matrix form. If we consider the coupling has time reversal symmetry, we can parametrize the tunnel coupling matrix with four real numbers $(t_c, \vec{t_{so}}) = (t_c, t_x, t_y, t_z)$. The corresponding terms are expressed as $t_{\alpha\beta} = (t_c I + i\vec{t_{so}}\cdot\vec{\sigma})_{\alpha\beta}$, where $\vec{\sigma}$ denotes Pauli matrices. In the basis $\{|L\uparrow\rangle, |L\downarrow\rangle, |R\uparrow\rangle, |R\downarrow\rangle\}$, we explicitly write down the tunnelling Hamiltonian in the matrix form

$$H_t = \begin{pmatrix} 0 & t_c I + i\vec{t_{so}}\cdot\vec{\sigma} \\ t_c I - i\vec{t_{so}}\cdot\vec{\sigma} & 0 \end{pmatrix} = \begin{pmatrix} 0 & 0 & t_c + it_z & t_y + it_x \\ 0 & 0 & -t_y + it_x & t_c - it_z \\ t_c - it_z & -t_y - it_x & 0 & 0 \\ t_y - it_x & t_c + it_z & 0 & 0 \end{pmatrix}. \tag{2.13}$$

This 4 by 4 matrix is also a minimal model for describing tunnel coupling of a single spin in a double quantum dot. Here the double quantum dot needs to be **isolated**, meaning negligible particle-exchanging interactions to the environment such as reservoirs or the third quantum dot. If this assumption does not hold, we will need more basis states to describe the full system.

In the case of an isolated two-spin system in a double quantum dot, we have a minimal model with five basis states $\{ S(2,0),\ S(1,1),\ T^0(1,1),\ T^+(1,1),\ T^-(1,1) \}$. The basis states are defined by acting creation operators on the vacuum $|0\rangle$ with the order $(L\uparrow, L\downarrow, R\uparrow, R\downarrow)$. The explicit forms of the states are: $|S(2,0)\rangle = c^\dagger_{L\downarrow} c^\dagger_{L\uparrow}|0\rangle$, $|S(1,1)\rangle = \frac{|\uparrow,\downarrow\rangle - |\downarrow,\uparrow\rangle}{\sqrt{2}} = \frac{c^\dagger_{R\downarrow} c^\dagger_{L\uparrow} - c^\dagger_{R\uparrow} c^\dagger_{L\downarrow}}{\sqrt{2}}|0\rangle$, $|T^0(1,1)\rangle = \frac{|\uparrow,\downarrow\rangle + |\downarrow,\uparrow\rangle}{\sqrt{2}} = \frac{c^\dagger_{R\downarrow} c^\dagger_{L\uparrow} + c^\dagger_{R\uparrow} c^\dagger_{L\downarrow}}{\sqrt{2}}|0\rangle$, $|T^+(1,1)\rangle = |\uparrow,\uparrow\rangle = c^\dagger_{R\uparrow} c^\dagger_{L\uparrow}|0\rangle$, $|T^-(1,1)\rangle = |\downarrow,\downarrow\rangle = c^\dagger_{R\downarrow} c^\dagger_{L\downarrow}|0\rangle$. Computing the matrix elements of Eq. (2.12) accordingly, we can derive the following Hamiltonian [33, 34]

$$
\begin{aligned}
H_{t,2Q} &= \sqrt{2}t_c\,|S_{11}\rangle\langle S_{20}| + i\sqrt{2}t_z\,|T^0\rangle\langle S_{20}| - \sum_{\pm}(t_y \pm i t_x)\,|T^\pm\rangle\langle S_{20}| + \text{h.c.} \\
&= \begin{pmatrix} 0 & \sqrt{2}t_c & -i\sqrt{2}t_z & -t_y + i t_x & -t_y - i t_x \\ \sqrt{2}t_c & 0 & 0 & 0 & 0 \\ i\sqrt{2}t_z & 0 & 0 & 0 & 0 \\ -t_y - i t_x & 0 & 0 & 0 & 0 \\ -t_y + i t_x & 0 & 0 & 0 & 0 \end{pmatrix}.
\end{aligned} \tag{2.14}
$$

2.4. SINGLE SPIN IN A DOUBLE QUANTUM DOT

The minimal Hamiltonian for the charge and spin dynamics of a single spin in an **isolated** double quantum dot can be obtained by adding the Zeeman energies and charging energies of the single spin to the tunnel coupling Hamiltonian Eq. (2.13), similar to the model in [35]. Fig. 2.3a is an illustration. In the basis $\{|L\uparrow\rangle, |L\downarrow\rangle, |R\uparrow\rangle, |R\downarrow\rangle\}$ we have the Hamiltonian

$$
H_{1Q} = \begin{pmatrix} \epsilon I & t_c I + i\vec{t_{so}}\cdot\vec{\sigma} \\ t_c I - i\vec{t_{so}}\cdot\vec{\sigma} & -\epsilon I \end{pmatrix} + \frac{1}{2}\mu_B \begin{pmatrix} \vec{\sigma}\cdot(\hat{g_L}\cdot\vec{B}) & 0 \\ 0 & \vec{\sigma}\cdot(\hat{g_R}\cdot\vec{B}) \end{pmatrix}. \tag{2.15}
$$

In this formula, ϵ is the detuning energy of the double quantum dot and has an operational meaning that the energy difference between (1,0) and (0,1) configurations equals to 2ϵ when ϵ is the dominant energy scale. t_c is the spin-conserving tunneling, $\vec{t_{so}}$ are

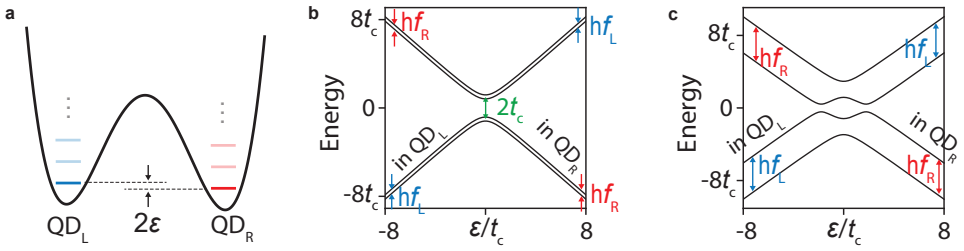

Figure 2.3: **Single spin in a double quantum dot. a,** An illustration of the double quantum dot potential and spin-degenerate orbital levels on the left and right quantum dots ($QD_{L,R}$). The fainted lines are excited orbital levels that are not taken into account in the effective model. **b,c,** Four energy levels of the single spin in double quantum dot given by Eq. (2.15). Parameters used here: $\theta_R = 50°$, Zeeman energies $hf_L = hf_R = 0.4t_c$ in (b) and $hf_L = hf_R = 4t_c$ in (c). In this thesis we focus more on the situation similar to (b) where $2t_c \gg hf_{L,R}$.

spin-dependent tunnelings, $g\hat{}_{\mathrm{L,R}}$ are g-matrices of the left and right dots, and $\vec{B}$ is the magnetic field. Here $\vec{B}$ is expressed in the coordinate system of the lab frame. Here the g-matrices can be defined slightly different than Eq (2.8). Because the orbital degree of freedom and the spin-orbit effect ($\vec{t_{so}}$) are explicitly included in the Hamiltonian, the g-matrices ($\hat{g} = \hat{U}\hat{g}_d\hat{V}$ in Eq (2.8)) can be chosen as real symmetric matrices that can be uniquely determined by measuring the eigenvalues $\hat{g}_d$ and the magnetic axes $\hat{V}$ when the orbital wave function is static and localized in dot L and R.

Due to the different microscopic details in dot L and dot R, such as inhomogeneous strain, confinement potential and the interface, the g-matrices $g\hat{}_{\mathrm{L,R}}$ can be unequal and the vectors $g\hat{}_{\mathrm{L,R}} \cdot \vec{B} \equiv \frac{h}{\mu_{\mathrm{B}}} \vec{f}_{\mathrm{L,R}}$ do not point to the same direction. In other words, the effective magnetic fields in dot L and dot R which define the spin quantization axes are not aligned.

We can reduce the number of parameters in the model by going into the local spin basis [36]. We apply a rotation matrix $R = R_{\mathrm{L}} \otimes R_{\mathrm{R}}$ to transform the Hamiltonian $H'_{1Q} = R^{\dagger} H_{1Q} R$ such that the diagonal blocks of the Zeeman interaction become $\propto f_{\mathrm{L}}\sigma_z \otimes \vec{f}_{\mathrm{R}} \cdot \vec{\sigma}$ and the transformed spin-orbit tunnel couplings $\vec{t'_{so}}$ become all zero,

$$H_{1\mathrm{Q,local}} = \begin{pmatrix} \epsilon I & t'_c I \\ t'_c I & -\epsilon I \end{pmatrix} + \frac{1}{2} h \begin{pmatrix} f_{\mathrm{L}}\sigma_z & 0 \\ 0 & f_{\mathrm{R}}(\sigma_z \cos\theta_{\mathrm{R}} + \sigma_x \sin\theta_{\mathrm{R}}) \end{pmatrix}. \tag{2.16}$$

Here $t'_c = \sqrt{t_c^2 + |\vec{t_{so}}|^2}$ is the transformed spin-conserving tunnel coupling (in the following we use t_c to stand for t'_c), θ_{R} is the polar angle of $\vec{f}_{\mathrm{R}}$. Since there are only two quantum dots in the system, not a chain of dots forming a loop, the azimuthal angle of $\vec{f}_{\mathrm{R}}$ can be arbitrary and we set it to zero. We note that this model is similar to that of a flopping-mode qubit [35]. The local spin basis used in this model is valid for a specific magnetic field direction. When the field direction changes, the local spin basis changes and the parameters in Eq. (2.16) also change.

2.4.1. SINGLE-SPIN SHUTTLING

In this thesis we use the model Eq. (2.16) to describe spin shuttling between two dots. Here the discussion is limited to the case of small Zeeman energy ($2t_{\mathrm{c}} \gg h f_{\mathrm{L,R}}$) such that the spin-doublets of the double-dot orbital ground state are always energetically lower than the double-dot orbital excited state, as indicated in Fig. 2.3b. We assume the requirement for coherent spin shuttling is adiabatic in the charge dynamics (we notice that theoretically this requirement may not be necessary if the charge relaxation is much faster than the qubit energy splitting). The degree of adiabaticity is quantified by the Landau Zener transition probability $P_{\mathrm{LZ}}^{\mathrm{charge}} = \exp(-2\pi^2 t_{\mathrm{c}}^2 / (h\frac{d\epsilon}{dt}))$. This formula implies that, to maintain the same charge adiabaticity, we should double t_{c} if we want to increasing the ramp speed $\frac{d\epsilon}{dt}$ by four times.

Once the process satisfies the adiabatic charge transfer, we can simplify the system and only look at the spin of the orbital ground state by projecting the Eq. (2.16) onto the orbital ground state and obtain

$$H_{2\times 2} = \frac{h f_{\mathrm{L}}}{4}\left(1 - \frac{\epsilon}{\sqrt{t_{\mathrm{c}}^2 + \epsilon^2}}\right)\sigma_z + \frac{h f_{\mathrm{R}}}{4}\left(1 + \frac{\epsilon}{\sqrt{t_{\mathrm{c}}^2 + \epsilon^2}}\right)(\sigma_z \cos\theta_{\mathrm{R}} + \sigma_x \sin\theta_{\mathrm{R}}). \tag{2.17}$$

The above Hamiltonian describes the spin precession frequency and precession direction that can be tuned between two generally fixed values (between f_L and f_R, between $\hat{z}$ and $\vec{f}_R$) by ϵ. This gives us a qualitative understanding about spin adiabaticity in the shuttling process. Putting into the framework of Landau Zener transition, the level velocity of the spin is on the order of $\propto f_{L,R}\frac{d}{dt}(\frac{\epsilon}{t_c})$, and the size of avoided-crossing is $\propto f_{L,R}$. This implies that to maintain the same degree of adiabaticity, we have to keep the quantity $f_{L,R}/\frac{d}{dt}(\frac{\epsilon}{t_c})$ to be the same. In another word, the experimental parameters, including the Larmor frequencies $f_{L,R}$, the ramp speed $\frac{d\epsilon}{dt}$, and the tunnel coupling t_c, should be varied in the following ways:

(1) When doubling the external magnetic field (which doubles the Larmor frequencies $f_{L,R}$), the ramp speed $\frac{d\epsilon}{dt}$ needs to be doubled.

(2) When doubling the tunnel coupling t_c, the ramp speed $\frac{d\epsilon}{dt}$ needs to be doubled.

(3) When doubling the external magnetic field while keeping the same ramp speed, the tunnel coupling needs to be halved.

2.4.2. SPIN SHUTTLING AS A SINGLE QUBIT GATE

It is worth to notice that, in addition to coherent evolution, the spin interacts more to the environment and decoheres much faster at the charge anti-crossing $\epsilon = 0$, compared to the point far from charge anti-crossing $|\epsilon| \gg t_c$. The decoherence can be due to the low-frequency fluctuations of the position of the charge anti-crossing, or due to the spin-flip accompanied by absorption (relaxation) the energies from (to) the environment [35]. Both effects are more pronounced at the charge anti-crossing because the charge states become delocalized and the spin couples more to the charge noise. This can be seen in Eq. (2.17), in the experiments Fig. 6.16 and Fig. 7.11.

Because of the above consideration regarding spin coherence, it can be beneficial to do single-spin rotation by moving the spin quickly from $\epsilon \ll -t_c$ to $\epsilon \gg t_c$, letting the spin precesses for a certain period (as short as possible to minimize dephasing), and finally moving the spin quickly from $\epsilon \gg t_c$ back to $\epsilon \ll -t_c$ (see experiments in **chapter 7**). This operation method can be seen as an extreme version of flopping-mode qubits. The key difference is the reduced exposure to the decoherence near the charge anti-crossing. With this method, the spin spends most of the time in the region with longer coherence time. The trade-off is the requirement of larger detuning amplitude, which increases the power dissipation compared to flopping-mode qubits. As shown in the latter chapter, this operation method can have short gate time, on the order of the spin precession period, if the quantization axis angle θ_R is sufficiently large (e.g. $\geq 22.5°$). The short gate time reduces the dephasing of the target qubit as well as the spectator qubits and achieves high average gate fidelity.

This operation can also be seen as extreme version g-matrix modulation, where the double quantum dot is considered as a single quantum dot which has highly-tunable orbital energy levels and highly tunable spin quantization axis. In the situation of $\theta_R > 45°$, a spin flip requires only four shuttles. The entire process can be viewed as a strong driving system, where the resonance condition of the driving field $\epsilon(t)$ becomes more than just a monochromatic driving field at the qubit frequency.

2.5. TWO SPINS IN A DOUBLE QUANTUM DOT

The two spins in a double quantum dot form a basic unit for spin-qubit operations in this thesis. It allows initialization and readout of the two-spin states. The charge stability diagram of a double quantum dot is shown in Fig. 2.4a. In this diagram there are three regions having two spins in total: (2,0), (1,1), and (0,2). To describe the charge and spin dynamics over these three regions, we assume the two-spin system is well **isolated** such that there is negligible tunnel coupling to other quantum dots or reservoirs and therefore we only consider six basis states $\{S(2,0), S(0,2), S(1,1), T^0(1,1), T^+(1,1), T^-(1,1)\}$. Here we neglect higher orbital states such as the triplets $T^{+,-,0}(2,0)$ and $T^{+,-,0}(0,2)$, which are typically few hundreds of μeV above the singlet ground states in the single-hole regime of germanium devices presented in this thesis [37]. We also neglect zero-field splittings that can appear in heavy hole system with cubic spin-orbit coupling [36, 38, 39].

Adding the Zeeman energies and charging energies of the two spins to the tunnel coupling Hamiltonian Eq. (2.14), the complete Hamiltonian is

$$H_{\text{2Q,local}} = \begin{pmatrix} U_c+\epsilon & 0 & \sqrt{2}t_c & -i\sqrt{2}t_z & -t_y+it_x & -t_y-it_x \\ 0 & U_c-\epsilon & \sqrt{2}t_c & -i\sqrt{2}t_z & -t_y+it_x & -t_y-it_x \\ \sqrt{2}t_c & \sqrt{2}t_c & 0 & E_{Z-} & 0 & 0 \\ i\sqrt{2}t_z & i\sqrt{2}t_z & E_{Z-} & 0 & 0 & 0 \\ -t_y-it_x & -t_y-it_x & 0 & 0 & E_{Z+} & 0 \\ -t_y+it_x & -t_y+it_x & 0 & 0 & 0 & -E_{Z+} \end{pmatrix}, \tag{2.18}$$

where U_c is the charging energy, ϵ is the detuning energy (difference of the chemical potentials of the two dots), $E_{Z\pm} = \frac{1}{2}(g_1 \pm g_2)\mu_B B$ are the Zeeman energies. Similar to the treatment in Eq. (2.17) (2.16), here we use the local spin basis and move the effect of misalignment between two spins to spin-non-conserving tunnelings $t_{c,x,y,z}$. The Hamiltonian written in the global spin basis, where the quantization axes of the two dots are described in the lab frame, can be found in [34].

2.5.1. INITIALIZATION AND READOUT

In this system the charging energy and detuning energy are typically the largest energy scales, which results in the energy levels as function of detuning energy ϵ in Fig. 2.4b, where the Zeeman splittings between $S(1,1)$ and $T^{+,-,0}(1,1)$ are invisible. The large energy scale created by the detuning energy is used to initialize the spin state in (0,2) and then adiabatically converted to one of the eigenstates in (1,1) charge configuration. The first part is performed by pulsing ϵ to (0,2) (or (2,0)) and waiting for typically tens or hundreds of μs. This makes the spins relax mostly to the ground state S(0,2) because the excited state energy can be as high as hundreds of μeV and much larger than the phonon or electron temperature if operating at base temperature of 20 mK ($1K \approx 86\mu eV$).

The second part of the initialization is performed by pulsing ϵ from (0,2) to (1,1) with certain speed. The corresponding adiabatic state evolutions are marked by the orange double-arrow in Fig. 2.4c-e. Depending on the adiabaticity when passing through the spin-orbit gap Δ_{ST_-}, the final spin state (at the center of charge configuration of (1,1)) can be $|\uparrow\downarrow\rangle$ or $T^- \equiv |\downarrow\downarrow\rangle$. Fig. 2.4c is the case when spin-non-conserving tunnelings are zero, which makes $\Delta_{ST_-} = 0$ and the spin state after initialization is $|\uparrow\downarrow\rangle$. Fig. 2.4de are the

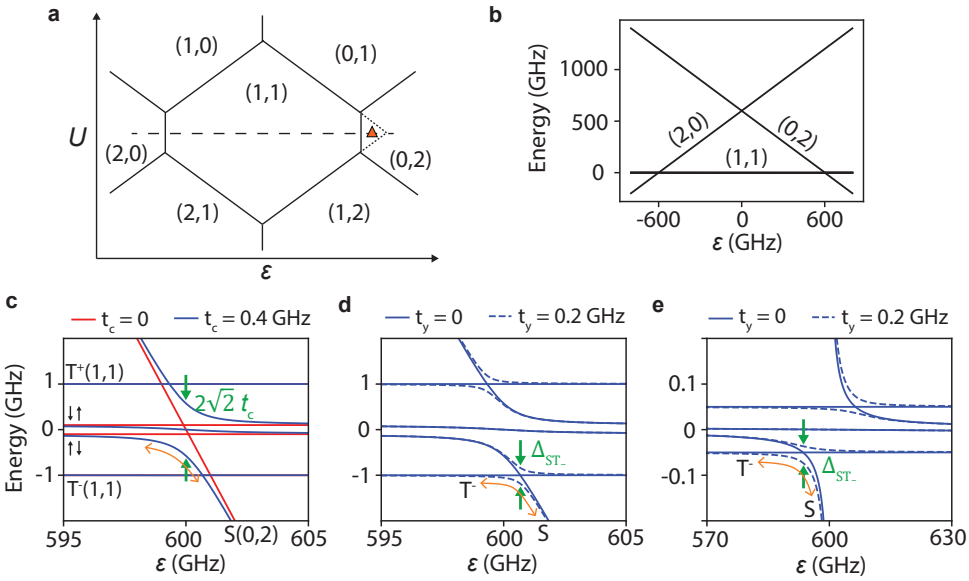

Figure 2.4: **Energy levels of a two-spin system.** **a**, Charge stability diagram. The triangular marker is the point for PSB. The dashed lines mark the PSB triangle. **b**, Energy levels. $S(1,1)$ and $T^{+,-,0}(1,1)$ are overlapped. **c**, The zoom-in of the energy levels near the charge anti-crossing. The red (blue) lines are the energy levels when $t_c = 0(0.4)$ GHz. The spin-non-conserving tunnelings $t_{x,y,z}$ are set to zero. Zeeman energies are $E_{Z+} = 1$ GHz and $E_{Z-} = 0.1$ GHz. **d**, The blue solid (dashed) lines are the energy levels when $t_y = 0(0.2)$ GHz. Non-zero spin-non-conserving tunnelings open the spin-orbit gap Δ_{ST-}. **e**, The energy levels when Zeeman energies are $E_{Z+} = 0.05$ GHz and $E_{Z-} = 0.005$ GHz. In c-e, the orange double-arrows mark the state evolution of adiabatic initialization and readout.

cases when non-zero spin-non-conserving tunnelings open the gap Δ_{ST-}, and the spin states after initialization are T^-.

The readout method, termed Pauli spin blockade (PSB), is the reverse of the initialization. The PSB implementation in this thesis is also done adiabatically, where we pulse ϵ from (1,1) to a point in the PSB triangle in (0,2) (Fig. 2.4a). The pulse moves the states along the energy levels in Fig. 2.4c-e, bringing $T^-(1,1)$ (or $|\uparrow\downarrow\rangle$ in the case of zero spin-non-conserving tunnelings) to $S(0,2)$ while other spin states remain in the charge configurations of (1,1). The charge states, (0,2) and (1,1), are measured by the nearby charge sensor. From the signal of the charge states, we acquire one bit of information of the spin states. Typically, one of the spins is used as ancilla qubit, where we do not apply any manipulation pulses to it and we assume the spin state is not rotated by the manipulation pulses applied to the other spin. Knowing the state of the ancilla qubit, we can infer the state of the other qubit using one bit of information acquired via PSB. It needs more involved operation protocols to acquire the complete two-spin state.

The spin-state relaxation time at the readout point of PSB is usually much shorter than the relaxation time at the center of (1,1) charge configuration, due to the spin-orbit interaction. At high magnetic field the relaxation time can be only few μs or lower, which is not sufficient for the charge sensor to distinguish (0,2) and (1,1) charge states. In this

situation, we use latch-PSB to convert (1,1) charge state to the (0,1) charge state which has longer relaxation time enabled by the low transition rate between (0,1)-(0,2) [40, 41].

To conclude this subsection, we remark that the double quantum dot system allows qubit manipulation even the energy splittings of the spin states are much smaller than the thermal energy of the environment. This can be realized without any feedback or post-selection protocol. Here, the adiabatic initialization from (0,2) and (1,1) makes the effective temperature of the two-spin system, at (1,1) charge configuration, much lower than the environmental temperature. After initialization, we typically set the voltage deep in (1,1) charge configuration, where the hole wave functions are highly localized and coupling of the spin states to the environment is weak. In this circumstance, the absorption and relaxation time are typically above 1 ms, which is slow enough and allows multiple quantum gates operations.

2.5.2. ADIABATIC TWO-QUBIT GATE

The two spins in the double quantum dot are coupled via the intermediate virtual states which has charge configuration of (0,2) or (2,0). Based on Eq.(2.18), when $U_c \pm \epsilon \gg t_c, E_{Z\pm}$, we can use second-order perturbation to compute the interactions between the four spin states in the (1,1) charge configuration. In the simplified case when $t_{x,y,z} = 0$, the result is the Heisenberg Hamiltonian [42]

$$H_{\text{exchange}} = \begin{pmatrix} -E_{Z+} & 0 & 0 & 0 \\ 0 & -E_{Z-} - J/2 & J/2 & 0 \\ 0 & J/2 & E_{Z-} - J/2 & 0 \\ 0 & 0 & 0 & E_{Z+} \end{pmatrix}, \tag{2.19}$$

where $J = \frac{4U_c t_c^2}{U_c^2 - \epsilon^2}$ is the exchange coupling and the basis states are rearranged to the computational basis $\{|\downarrow\downarrow\rangle, |\downarrow\uparrow\rangle, |\uparrow\downarrow\rangle, |\uparrow\uparrow\rangle\}$. Considering $J(t)$ is turned on and off adiabatically, the state evolution from $t = 0$ to $t = t_g$ follows the unitary

$$U_{\text{adiabatic}} = \begin{pmatrix} 1 & 0 & 0 & 0 \\ 0 & e^{-i\phi_{\downarrow\downarrow\to\downarrow\uparrow}} & 0 & 0 \\ 0 & 0 & e^{-i\phi_{\downarrow\downarrow\to\uparrow\downarrow}} & 0 \\ 0 & 0 & 0 & e^{-i\phi_{\downarrow\downarrow\to\uparrow\uparrow}} \end{pmatrix}, \tag{2.20}$$

where $\phi_{\downarrow\downarrow\to i} = 2\pi \int_0^{t_g} f_{\downarrow\downarrow\to i}(t)dt$ is the phase accumulation of the instantaneous eigenstate i and $f_{\downarrow\downarrow\to i}(t)$ is the transition frequency from $|\downarrow\downarrow\rangle$ to instantaneous eigenstate i that depends on the exchange $J(t)$.

We can decompose the unitary into the single-qubit phase gates and the rest:

$$U_{\text{adiabatic}} = \begin{pmatrix} 1 & 0 \\ 0 & e^{-i\phi_{\downarrow\downarrow\to\downarrow\uparrow}} \end{pmatrix} \otimes \begin{pmatrix} 1 & 0 \\ 0 & e^{-i\phi_{\downarrow\downarrow\to\uparrow\downarrow}} \end{pmatrix} \begin{pmatrix} 1 & 0 & 0 & 0 \\ 0 & 1 & 0 & 0 \\ 0 & 0 & 1 & 0 \\ 0 & 0 & 0 & e^{-i(\phi_{\downarrow\downarrow\to\uparrow\uparrow} - \phi_{\downarrow\downarrow\to\downarrow\uparrow} - \phi_{\downarrow\downarrow\to\uparrow\downarrow})} \end{pmatrix}. \tag{2.21}$$

In the situation $\phi_{\downarrow\downarrow\to\uparrow\uparrow} - \phi_{\downarrow\downarrow\to\downarrow\uparrow} - \phi_{\downarrow\downarrow\to\uparrow\downarrow} \neq 0$, the two-spin system acquires a non-trivial two-qubit phase. This two-qubit phase can be expressed as the integral of $f_{\downarrow\uparrow\to\uparrow\uparrow} -$

$f_{\downarrow\downarrow\to\uparrow\downarrow}$, which is interpreted as the frequency shift of the first qubit that depends on the state of the second qubit. This frequency shift can be measured straightforwardly by preparing the second qubit in $|\uparrow\rangle$ and $|\downarrow\rangle$, and measuring the corresponding frequencies of the first qubit.

In the simplified example of Eq. (2.19) when $t_{x,y,z} = 0$ and $J(t)$ is adiabatic and approximated as a square pulse to simplify the calculation (takes value of $J_{\text{on}} \ll E_{Z-}$ in the time interval $0 < t < t_g$), the frequency shift is $f_{\downarrow\uparrow\to\uparrow\uparrow} - f_{\downarrow\downarrow\to\uparrow\downarrow} = J_{\text{on}}$ and the two-qubit phase is $2\pi J_{\text{on}} t_g$. To realize a two-qubit Controlled-Phase gate of π, the gate time needs to be $t_g = \frac{1}{2J_{\text{on}}}$.

In a more complicated case when $t_{x,y,z} \neq 0$, all the matrix elements between the computational states are non-zero, unlike the simplified case in Eq. (2.19) [36, 43]. Despite the non-zero matrix elements, as long as the state evolution is adiabatic when turning on and turning off the exchange, the unitary of the state evolution will still be in the form as Eq. (2.20). The formula relating the two-qubit phase and the exchange pulse $\phi_{\downarrow\downarrow\to\uparrow\uparrow} - \phi_{\downarrow\downarrow\to\downarrow\uparrow} - \phi_{\downarrow\downarrow\to\uparrow\downarrow} = 2\pi \int_0^{t_g} f_{\downarrow\uparrow\to\uparrow\uparrow}(t) - f_{\downarrow\downarrow\to\uparrow\downarrow}(t)\mathrm{d}t$ will still hold. The relation of required gate time t_g and the amount of exchange $f_{\downarrow\uparrow\to\uparrow\uparrow}(t) - f_{\downarrow\downarrow\to\uparrow\downarrow}(t)$ can be determined accordingly.

2.6. ROTATING FRAME AND LAB FRAME

In this section we show the conventional way of qubit operation, the rotating frame, as well as the lab frame operations implemented in **chapter 7**. Firstly we outline the conventional single-spin EDSR control (the microscopic mechanism is discussed in 2.2.3). To describe the evolution of qubit state under the driven signal, we start from the basis of lab frame, defined by the ground state of an undriven spin $|\downarrow\rangle$ and the excited state $|\uparrow\rangle$. In this basis, the Hamiltonian of the driven system can be written as [44]

$$H = \frac{1}{2}\hbar\omega_{\text{q}}\sigma_{\text{z}} + \hbar\Omega(t)\sigma_{\text{x}}\cos\left(\omega_{\text{d}}t + \phi(t)\right), \tag{2.22}$$

where ω_{q} is the qubit angular frequency, ω_{d} is the angular frequency of the drive (typically at the microwave frequency), $\hbar\Omega(t)$ ($\phi(t)$) is the envelop (phase) of the drive which is time-dependent and is usually slower than ω_{d}. As shown in the next section, for a constant drive pulse such that $\Omega(t) = \Omega$ and $\phi(t) = 0$ for $0 < t < t_g$, the spin state evolves around x-axis with the Rabi frequency $f_{\text{Rabi}} = \Omega/2\pi$.

SINGLE-QUBIT GATE IN THE ROTATING FRAME

Driven by the sinusoidal signals, the state of a qubit can be conveniently described in the rotating frame. Going into the frame that rotates around z-axis with angular frequency ω_{r}, the basis states become time-dependent: $|\tilde{\uparrow}(t)\rangle = e^{-i\omega_{\text{r}}t/2}|\uparrow\rangle$ and $|\tilde{\downarrow}(t)\rangle = e^{i\omega_{\text{r}}t/2}|\downarrow\rangle$. The evolution of qubit states in the lab frame and rotating frame are depicted in Fig. 2.5. When choosing the rotating frame frequency to be the same as drive frequency ($\omega_{\text{r}} = \omega_{\text{d}}$), under the rotating wave approximation the fast time-dependent term in Eq. (2.22), $\sigma_{\text{x}}\cos(\omega_{\text{d}}t + \phi(t))$, is down-converted. The resulting Hamiltonian in this rotating frame is

$$H = \frac{1}{2}\hbar(\omega_{\text{q}} - \omega_{\text{d}})\sigma_{\text{z}} + \frac{1}{2}\hbar\Omega(t)\left(\sigma_{\text{x}}\cos\phi(t) + \sigma_{\text{y}}\sin\phi(t)\right). \tag{2.23}$$

The first term vanishes if the drive frequency matches resonant condition $\omega_q = \omega_d$. In this situation, the Hamiltonian has a simple form

$$H = \frac{1}{2}\hbar\Omega(t)\left(\sigma_x \cos\phi(t) + \sigma_y \sin\phi(t)\right). \tag{2.24}$$

This allows single-qubit gates that rotate the spin along x- or y-axis by applying a non-zero drive envelop $\Omega(t)$ and the phase $\phi(t) = 0$ or $\pi/2$ (Fig. 2.6). If we do not apply any drive signal, $\Omega(t) = 0$, the spin undergoes free evolution which does not evolve in the rotating frame, while it evolves as a free precession in the lab frame. To perform a

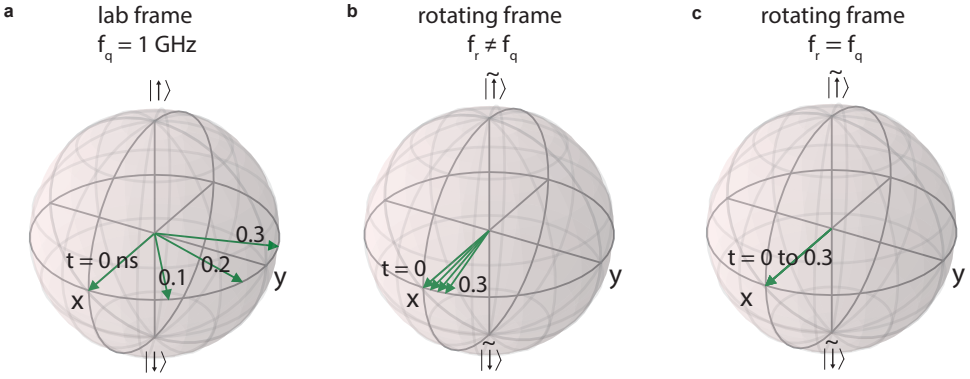

Figure 2.5: **Illustration of the qubit free precession in lab frame and rotating frame.** The qubit undergoes free precession ($\Omega(t) = 0$ in Eq. (2.23)) with frequency $f_q \equiv \omega_q/2\pi = 1$ GHz. **a,** In the lab frame, the free evolution of the qubit state at time $t = 0$, 0.1, 0.2, 0.3 ns. **b,** The free evolution of the state in a rotating frame that $f_r \equiv \omega_r/2\pi = 0.9$ GHz. **c,** The state remains as the initial state in a rotating frame that $f_r = f_q = 1$ GHz. Here we use the convention that $|\downarrow\rangle$ represents the qubit ground state and $|\uparrow\rangle$ represents the excited state.

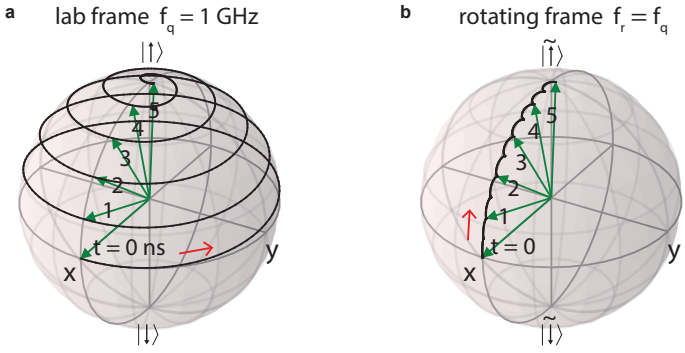

Figure 2.6: **Illustration of the driven qubit in lab frame and rotating frame.** The qubit frequency is $f_q \equiv \omega_q/2\pi = 1$ GHz. The drive signal with frequency matching qubit resonance ($f_d \equiv \omega_d/2\pi = 1$ GHz) is turned on at $t = 0$. The driving envelop is $\Omega(t)/2\pi = 0.05$ GHz with a phase $\phi = -\pi/2$ (Eq. (2.23)). The state evolves under the drive as plotted in green arrows at time $t = 0$, 1, 2, 3, 4, 5 ns. The continuous state evolutions are plotted in black curves, observed in (a) the lab frame and (b) the rotating frame which rotates at frequency $f_r = 1$GHz. In (b) the state rotates around -y-axis. The small wiggles are the result of the counter rotating term that is neglected in rotating wave approximation (Eq. (2.23)).

rotation along z-axis, we update the phases in the subsequent drive signals of x- and y-rotations [45]. This 'virtual Z-gate' has advantages compared to the 'real Z-gate' described in the coming paragraphs.

TWO-QUBIT OPERATIONS IN THE LAB FRAME

There are scenarios when the qubit dynamics can be better understood in the lab frame. One scenario concerns the single-qubit state evolution in a series of shuttling events and precession around unparallel quantization axes of the quantum dots that the spin is shuttled to. The second scenario is when the drive is not a sinusoidal signal but with other shapes without periodic structure, such as a simple square pulse (i.e. baseband signal).

The shuttling-based single-qubit gates implemented in **chapter 7** contain both ingredients. There we make use of unparallel quantization axes to create a $X_{\pi/2}$ gate in the lab frame. Because the drive field is not sinusoidal, we cannot simply update the phases of the subsequent drive signals as the implementation of 'virtual-Z gate' [45]. Instead, we implement the 'real-Z gate' by idling the qubit for a period τ, which allows the spin to precess around z-axis for an angle $\phi = 2\pi f_q \tau$. With $X_{\pi/2}$ and Z_ϕ, we can implement arbitrary single-qubit rotations, such as $Y_{\pi/2} = Z_{\pi/2} X_{\pi/2} Z_{3\pi/2}$ and $Y_\phi = X_{3\pi/2} Z_\phi X_{\pi/2}$. Therefore, we have an universal single-qubit gate set $\{X_{\pi/2}, Z_\phi\}$.

The lab frame operation can be extended to two-qubit circuits by taking care of the 'real Z-gate' we make when idling the individual qubit, such that the 'real Z-gate' are identity operations and do not change the quantum circuits we want to execute. This problem is not present if the single-qubit gate does not interfere with each other. In this ideal case, we can execute the circuit directly, applying multiple $X_{\pi/2,A}$ on qubit A and multiple $X_{\pi/2,B}$ on qubit B as we want. With the concern of the interference, however, we apply single-qubit gates $X_{\pi/2,A}$ and $X_{\pi/2,B}$ sequentially without overlapping the drive signals, as implemented in **chapter 7**. To avoid the overlap, we have to idle one of the qubits, which creates a 'real Z-gate'. What we have to do is to make the 'real Z-gate' become an identity operation. As an example, if we want to execute the circuit $X_{\pi/2,A} X_{\pi/2,B} X_{\pi/2,A}$, we make the time separation Δt between two $X_{\pi/2,A}$ to accommodate the drive signal of $X_{\pi/2,B}$. The timing of the second $X_{\pi/2,A}$ is then scheduled such that qubit A precesses integer number of rounds for the time duration Δt and make an identity operation. In the experiments we typically observed a phase crosstalk, where $X_{\pi/2,A}$ results in a phase accumulation on qubit B that is different than the phase acquired during free precession for the same amount of time. This effect appears to be linear and can be compensated by adjusting the time separation Δt.

We remark that, instead of idling the spectator qubit, an alternative scheme is to drive the spectator qubit to make an identity gate with the gate time identical to the gate time of the driven qubit [46]. This can eliminate the required additional idle time to make identity gate on the spectator qubit.

In the large-scale qubit system, the sequential operations mentioned above appear to be not scalable. It is desired to execute quantum gates in a parallel fashion. One possibility is to have a working empirical model to estimate the amount of interference and apply a compensation signal. The other possibility is to operate in a sparse qubit array where qubits are placed further apart. This is expected to reduce the amount of

interference and allow simultaneous single-qubit operations.

2.7. MEASUREMENT SETUP

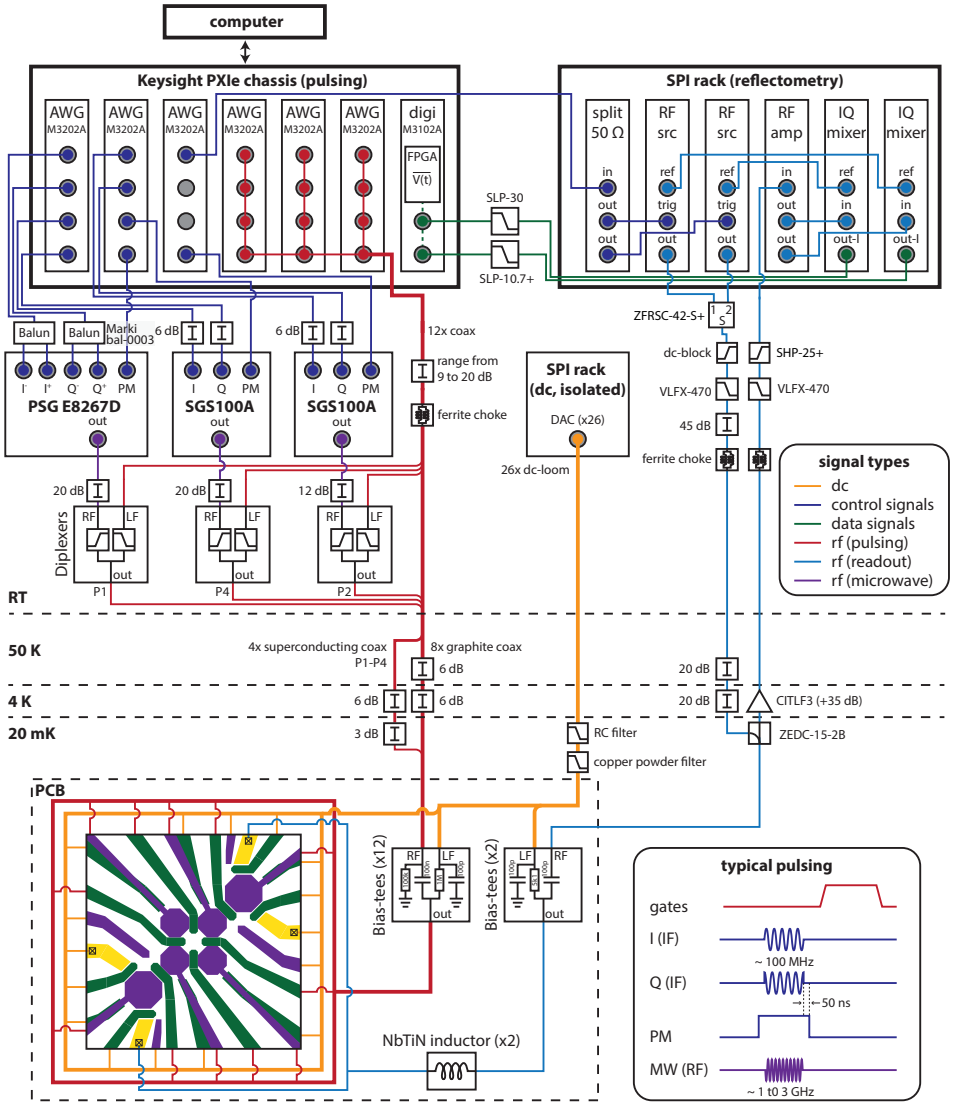

Figure 2.7: **Schematics of the measurement setup (adapted from [47]).**

The main experimental results presented in each chapter are acquired using the device and measurement setup shown in Fig. 2.7. For experiments in **chapter 3 and 7** that only involve baseband qubit control, the microwave sources (PSG E8267D, SGS100A) are

not used but remain connected. The setup is identical to the previous work [47] with minor modifications (e.g. attenuation and connection of coax lines at room temperature).

The 2×2 quantum dot device is wire-bonded on a printed circuit board (PCB). The PCB is mounted on the cold finger and surrounded by a radiation shield; both are thermally anchored on the mixing chamber plate of the dilution refrigerator. On the PCB are bias tees combining high-frequency (>kHz) and dc signals, as well as the NbTiN inductors for RF reflectometry measurement of the charge sensors (described below).

The dc voltages of the gates and ohmics on the device are provided by digital-to-analog converters (DACs) of a SPI rack at room temperature which is powered by batteries and gyrators, through the dc lines (orange) which are filtered by RC-filters and copper powder filters mounted at mixing chamber plate.

For baseband control of the qubits, we use Keysight M3202A arbitrary waveform generators (AWG) to generate voltage pulses with 1 ns time resolution and in the frequency range of dc-400 MHz. The baseband signals travel through ferrite common mode chokes as well as attenuators at room temperature and cryogenic temperature, and combine with dc voltages via the bias tees on the PCB.

For the EDSR experiments at high magnetic field and high qubit frequencies (**chapter 5 and 6**), we superimpose oscillating signals (at microwave frequency of 1-3 GHz) onto the baseband voltage pulses that are delivered to the gates {P1, P4, P2}. In our implementation, microwave signals (purple lines) from the vector sources are combined with three of the high-frequency lines from AWGs via the room temperature diplexers with pass bands dc-400 MHz and 1.5-10 GHz.

The vector sources output microwave pulses with controllable amplitude, frequency, phase and duration via IQ modulation. The I- and Q-components of the microwave are modulated by the signals at the input ports I and Q, which are generated by AWGs (dark blue). Additionally, we use pulse modulation to improve the microwave suppression to a total of -120 dB. When the absolute phase of EDSR pulse is relevant (the synchronization experiment in **chapter 6**), we synchronize the microwave and the AWGs by connecting the 10 MHz reference clock signal of the vector source of P2 to Keysight PXIe chassis, and setting the vector source frequency to integer multiple of 10 MHz.

We use RF reflectometry to detect the resistance change of the charge sensors that are embedded in the LC circuits (NbTiN inductors). The relevant modules in the SPI rack (reflectometry) are built in-house. Two RF signals around the resonant frequencies of the LC circuits (≈140 MHz) are emitted by the RF sources (RF src), which can be turned on and off by the splitted AWG signals at the trig ports. They are combined (splitter ZFRSC-42-S+), attenuated and superimposed onto the dc voltage with the bias tees on the PCB. The RF signal is reflected by the LC circuits, guided by the directional coupler to the cryogenic amplifier CITLF3 at 4 K stage. The signal is further amplified at room temperature (RF amp), downconverted (IQ mixer) by the frequencies of the RF sources, measured and averaged by the Keysight M3102A digitizer. Both I- and Q-components of the two signals are measured. We typically fine-tune the RF frequencies to have most of the signals in one of the components (shown as OUT-I in Fig. 2.7).

BIBLIOGRAPHY

[1] T. F. Watson et al. “A cold-atom Fermi–Hubbard antiferromagnet”. In: Nature (2018), pp. 633–637.

[2] Stephan G. J. Philips et al. “Universal control of a six-qubit quantum processor in silicon”. In: Nature 609.7929 (Sept. 2022), pp. 919–924. ISSN: 1476-4687.

[3] M. Veldhorst et al. “An addressable quantum dot qubit with fault-tolerant control-fidelity”. In: Nature Nanotechnology 9 (2014), pp. 941–985.

[4] Jun Yoneda et al. “A quantum-dot spin qubit with coherence limited by charge noise and fidelity higher than 99.9%”. In: Nature Nanotechnology 13.2 (Feb. 2018), pp. 102–106. ISSN: 1748-3395.

[5] Xiao Xue et al. “Quantum logic with spin qubits crossing the surface code threshold”. In: Nature 601.7893 (Jan. 2022), pp. 343–347. ISSN: 1476-4687.

[6] A. Noiri et al. “A shuttling-based two-qubit logic gate for linking distant silicon quantum processors”. In: Nature Communications 13 (2022), p. 5740.

[7] P. Lafarge et al. “Direct observation of macroscopic charge quantization”. In: Zeitschrift für Physik B Condensed Matter 85 (1991), pp. 327–332.

[8] Michel H. Devoret and Robert J. Schoelkopf. “Amplifying quantum signals with the single-electron transistor”. In: Nature 406 (2000), pp. 1039–1046.

[9] Mario Lodari et al. “Low Percolation Density and Charge Noise with Holes in Germanium”. In: Materials for Quantum Technology 1.1 (2021), p. 011002. ISSN: 2633-4356.

[10] Lucas E. A. Stehouwer et al. “Germanium wafers for strained quantum wells with low disorder”. In: Applied Physics Letters 123.9 (2023), p. 092101.

[11] N. W. Hendrickx et al. “Sweet-spot operation of a germanium hole spin qubit with highly anisotropic noise sensitivity”. In: Nature Materials (May 2024). ISSN: 1476-4660.

[12] Manuel Cardona and Fred H. Pollak. “Energy-Band Structure of Germanium and Silicon: The k·p Method”. In: Phys. Rev. 142 (1966), pp. 530–543.

[13] J. M. Luttinger and W. Kohn. “Motion of Electrons and Holes in Perturbed Periodic Fields”. In: Phys. Rev. 97 (1955), pp. 869–883.

[14] R. G. Winkler. “Spin-orbit Coupling Effects in Two-Dimensional Electron and Hole Systems”. In: Springer (2003).

[15] K. Suzuki and J. C. Hensel. “Quantum resonances in the valence bands of germanium. I. Theoretical considerations”. In: Phys. Rev. B 9 (1974), pp. 4184–4218.

[16] L. A. Terrazos et al. “Theory of Hole-Spin Qubits in Strained Germanium Quantum Dots”. In: Physical Review B 103.12 (2021), p. 125201.

[17] Benjamin Venitucci et al. “Electrical manipulation of semiconductor spin qubits within the g-matrix formalism”. In: Phys. Rev. B 98 (15 Oct. 2018), p. 155319.

[18] S. Bosco et al. “Squeezed hole spin qubits in Ge quantum dots with ultrafast gates at low power”. In: Phys. Rev. B 104 (11 2021), p. 115425.

[19] José Carlos Abadillo-Uriel et al. “Hole Spin Driving by Strain-Induced Spin-Orbit Interactions”. In: Phys. Rev. Lett. 131 (9 Sept. 2023), p. 097002.

[20] F. H. L. Koppens et al. “Driven coherent oscillations of a single electron spin in a quantum dot”. In: Nature 442.7104 (Aug. 2006), pp. 766–771. ISSN: 1476-4687.

[21] M. Pioro-Ladrière et al. “Micromagnets for coherent control of spin-charge qubit in lateral quantum dots”. In: Applied Physics Letters 90.2 (2007), p. 024105.

[22] Denis V. Bulaev and Daniel Loss. “Electric Dipole Spin Resonance for Heavy Holes in Quantum Dots”. In: Phys. Rev. Lett. 98 (9 Feb. 2007), p. 097202.

[23] S. Nadj-Perge et al. “Spin–orbit qubit in a semiconductor nanowire”. In: Nature 468.7327 (Dec. 2010), pp. 1084–1087. ISSN: 1476-4687.

[24] Ke Wang et al. “Ultrafast coherent control of a hole spin qubit in a germanium quantum dot”. In: Nature Communications 13.1 (Jan. 2022), p. 206. ISSN: 2041-1723.

[25] N. W. Hendrickx et al. “Fast two-qubit logic with holes in germanium”. In: Nature 577.7791 (Jan. 2020), pp. 487–491. ISSN: 0028-0836.

[26] Alessandro Crippa et al. “Electrical spin driving by g-matrix modulation in spin-orbit qubits”. In: Physical Review Letters 120.13 (2018), p. 137702.

[27] José Carlos Abadillo-Uriel et al. “Hole-Spin Driving by Strain-Induced Spin-Orbit Interactions”. In: Phys. Rev. Lett. 131 (9 Sept. 2023), p. 097002.

[28] Biel Martinez et al. “Hole spin manipulation in inhomogeneous and nonseparable electric fields”. In: Phys. Rev. B 106 (23 Dec. 2022), p. 235426.

[29] M. V. Durnev, M. M. Glazov, and E. L. Ivchenko. “Spin-orbit splitting of valence subbands in semiconductor nanostructures”. In: Phys. Rev. B 89 (7 Feb. 2014), p. 075430.

[30] E. Marcellina et al. “Spin-orbit interactions in inversion-asymmetric two-dimensional hole systems: A variational analysis”. In: Phys. Rev. B 95 (7 Feb. 2017), p. 075305.

[31] Zhanning Wang et al. “Optimal Operation Points for Ultrafast, Highly Coherent Ge Hole Spin-Orbit Qubits”. In: npj Quantum Information 7.1 (2021), pp. 1–8. ISSN: 2056-6387.

[32] Christoph Adelsberger et al. “Hole-spin qubits in Ge nanowire quantum dots: Interplay of orbital magnetic field, strain, and growth direction”. In: Phys. Rev. B 105 (7 Feb. 2022), p. 075308.

[33] J. Danon and Yu. V. Nazarov. “Pauli spin blockade in the presence of strong spin-orbit coupling”. In: Phys. Rev. B 80 (4 2009), p. 041301.

[34] P. M. Mutter and G. Burkard. “All-electrical control of hole singlet-triplet spin qubits at low-leakage points”. In: Phys. Rev. B 104 (19 2021), p. 195421.

[35] M. Benito et al. “Electric-field control and noise protection of the flopping-mode spin qubit”. In: Phys. Rev. B 100 (2019), p. 125430.

[36] Simon Geyer et al. “Two-Qubit Logic with Anisotropic Exchange in a Fin Field-Effect Transistor”. In: Nature Physics (2022).

[37] N. W. Hendrickx et al. “A single-hole spin qubit”. In: Nat. Commun. 11 (2020), p. 3478.

[38] G. Katsaros et al. “Zero Field Splitting of Heavy-Hole States in Quantum Dots”. In: Nano Letters 20.7 (June 2020), pp. 5201–5206. ISSN: 1530-6984.

[39] Bence Hetényi, Stefano Bosco, and Daniel Loss. “Anomalous Zero-Field Splitting for Hole Spin Qubits in Si and Ge Quantum Dots”. In: Phys. Rev. Lett. 129 (11 Sept. 2022), p. 116805.

[40] Patrick Harvey-Collard et al. “High-Fidelity Single-Shot Readout for a Spin Qubit via an Enhanced Latching Mechanism”. In: Phys. Rev. X 8 (2 May 2018), p. 021046.

[41] N. W. Hendrickx et al. “A four-qubit germanium quantum processor”. In: Nature 591 (2021), pp. 580–585.

[42] T. Meunier, V. E. Calado, and L. M. K. Vandersypen. “Efficient controlled-phase gate for single-spin qubits in quantum dots”. In: Phys. Rev. B 83 (2011), p. 121403.

[43] Bence Hetényi, Christoph Kloeffel, and Daniel Loss. “Exchange interaction of hole-spin qubits in double quantum dots in highly anisotropic semiconductors”. In: Phys. Rev. Res. 2 (3 July 2020), p. 033036.

[44] I. I. Rabi. “Space Quantization in a Gyrating Magnetic Field”. In: Phys. Rev. 51 (8 Apr. 1937), pp. 652–654.

[45] David C. McKay et al. “Efficient Z gates for quantum computing”. In: Phys. Rev. A 96 (2017), p. 022330.

[46] D.K. Weiss et al. “Fast High-Fidelity Gates for Galvanically-Coupled Fluxonium Qubits Using Strong Flux Modulation”. In: PRX Quantum 3 (4 Dec. 2022), p. 040336.

[47] N. W. Hendrickx et al. “A four-qubit germanium quantum processor”. In: Nature 591 (2021), pp. 580–585.

3

PROBING RESONATING VALENCE BONDS ON A PROGRAMMABLE GERMANIUM QUANTUM SIMULATOR

Simulations using highly tunable quantum systems may enable investigations of condensed matter systems beyond the capabilities of classical computers. Quantum dots and donors in semiconductor technology define a natural approach to implement quantum simulation. Several material platforms have been used to study interacting charge states, while gallium arsenide has also been used to investigate spin evolution. However, decoherence remains a key challenge in simulating coherent quantum dynamics. Here, we introduce quantum simulation using hole spins in germanium quantum dots. We demonstrate extensive and coherent control enabling the tuning of multi-spin states in isolated, paired, and fully coupled quantum dots. We then focus on the simulation of resonating valence bonds and measure the evolution between singlet product states which remains coherent over many periods. Finally, we realize four-spin states with s-wave and d-wave symmetry. These results provide means to perform non-trivial and coherent simulations of correlated electron systems.

Parts of this chapter have been published in C.-A. Wang, C. Déprez, H. Tidjani, W.I.L. Lawrie, N.W. Hendrickx, A. Sammak, G. Scappucci, and M. Veldhorst, Probing resonating valence bonds on a programmable germanium quantum simulator, *npj Quantum Information* **9**, 58 (2023).

3.1. INTRODUCTION

Quantum computers have the potential of simulating physics beyond the capacity of classical computers [1–4]. Gate-defined quantum dots are extensively studied for quantum computation [5, 6], but are also a natural platform for implementing quantum simulations [7–11]. The control over the electrical charge degree of freedom has facilitated the exploration of novel configurations such as effective attractive electron-electron interactions [12], collective Coulomb blockade [13], and topological states [14]. Coherent systems may be simulated when using the spin states of electrons in quantum dots, though experiments thus far have relied on gallium arsenide heterostructures [15–17], where the hyperfine interaction limits the spin coherence and therefore the complexity of simulations that can be performed. This bottleneck can be tackled by using group IV materials with nuclear spin-free isotopes. A natural candidate would be silicon, but this material comes with additional challenges due to the presence of valley states and a large effective electron mass [18].

Hole quantum dots in planar Ge/SiGe heterostructures exhibit many favorable properties found in different quantum dot platforms [19]. Natural germanium has a high abundance of nuclear spin-free isotopes and can be isotopically purified [20]. Holes in germanium benefit from a low effective mass [21, 22], absence of valley degeneracies, ohmic contacts to metals [23], and strong spin-orbit coupling for all-electrical control [24, 25]. Recent advances in heterostructure growth have resulted in stable, low-noise germanium devices [26]. This has sparked rapid progress, with demonstrations of hole quantum dots [23], single hole qubits [25], singlet-triplet (ST) qubits [27], two-qubit logic [28], and a four qubit quantum processor [29].

Here, we explore the prospects of hole quantum dots in Ge/SiGe for quantum simulation. We focus on the simulation of resonating valence bond (RVB) states, which are of fundamental relevance in chemistry [30] and solid state physics [31–34] and have been used in other platforms as a feasibility test for quantum simulation [35–38]. In our simulation, we probe RVB states in a square 2×2 configuration. First, we realize ST qubits for all nearest-neighbour configurations. We then study the coherent evolution of four-spin states and demonstrate exchange control spanning an order of magnitude. Furthermore, we tune the system to probe valence bond resonances whose observed characteristics comply with predictions derived from the Heisenberg model. We finally demonstrate the preparation of s-wave and d-wave RVB states from spin-singlet states via adiabatic initialization and tailored pulse sequences.

The experiments are based on a quantum dot array defined in a high-quality Ge/SiGe quantum well, as shown in Fig. 3.1a [29, 39]. The array comprises four quantum dots and we obtain good control over the system, enabling to confine zero, one, or two holes in each quantum dot as required for the quantum simulation. The dynamics of resonating valence bonds is governed by Heisenberg interactions. The spin states in germanium quantum dots, however, also experience Zeeman, spin-orbit and hyperfine interactions (see Section 3.7). We therefore operate in small magnetic fields and acquire a detailed understanding of the system dynamics to apply tailored pulses. In the regime where Heisenberg interactions are dominating, the total spin is conserved. We can therefore study the subspaces of different total spin separately. The relevant subspace for the RVB physics is the zero total spin space spanned by the basis formed by the four-spin states

$|S_x\rangle = |S_{12}S_{34}\rangle$ and $\frac{1}{\sqrt{3}}(|T^+_{12}T^-_{34}\rangle + |T^-_{12}T^+_{34}\rangle - |T^0_{12}T^0_{34}\rangle)$, where $|S_{ij}\rangle = \frac{1}{\sqrt{2}}(|\uparrow_i\downarrow_j\rangle - |\downarrow_i\uparrow_j\rangle)$ and $|T^0_{ij}\rangle = \frac{1}{\sqrt{2}}(|\uparrow_i\downarrow_j\rangle + |\downarrow_i\uparrow_j\rangle)$, $|T^+_{ij}\rangle = |\uparrow_i\uparrow_j\rangle$, $|T^-_{ij}\rangle = |\downarrow_i\downarrow_j\rangle$ denote the singlet and triplet states formed by the spins in the quantum dots i and j. In this basis, the Heisenberg Hamiltonian H_J reads:

$$H_J(S_{\text{tot}}=0) \equiv H_S = \begin{pmatrix} -J_x - \frac{J_y}{4} & \frac{\sqrt{3}}{4}J_y \\ \frac{\sqrt{3}}{4}J_y & -\frac{3}{4}J_y \end{pmatrix}, \tag{3.1}$$

where $J_x = J_{12} + J_{34}$ and $J_y = J_{14} + J_{23}$. Figures 3.1.b-c show the eigen energies and eigenstates of H_S for different regimes of exchange interaction. When the exchange interaction is turned on in only one direction, $J_x \gg J_y$ or $J_x \ll J_y$, the system is equivalent to two uncoupled double quantum dots. The ground state is then a product of singlet states $|S_x\rangle$ or $|S_y\rangle = |S_{14}S_{23}\rangle$. However, when all exchanges are on and in particular when they are equal, $J_x = J_y$, the eigenstates are coherent superpositions of $|S_x\rangle$ and $|S_y\rangle$, which simulate the RVB state. In this regime, the ground state is the s-wave superposition state $|s\rangle = \frac{1}{\sqrt{3}}(|S_x\rangle - |S_y\rangle)$ and the excited state is the d-wave superposition state $|d\rangle = |S_x\rangle + |S_y\rangle$.

Fig. 3.1.b shows that RVB states can be generated from uncoupled spin singlets by adiabatically equalizing the exchange couplings. Alternatively, if the exchange couplings are pulsed diabatically to equal values, valence bond resonances between $|S_x\rangle$ or $|S_y\rangle$ states occur.

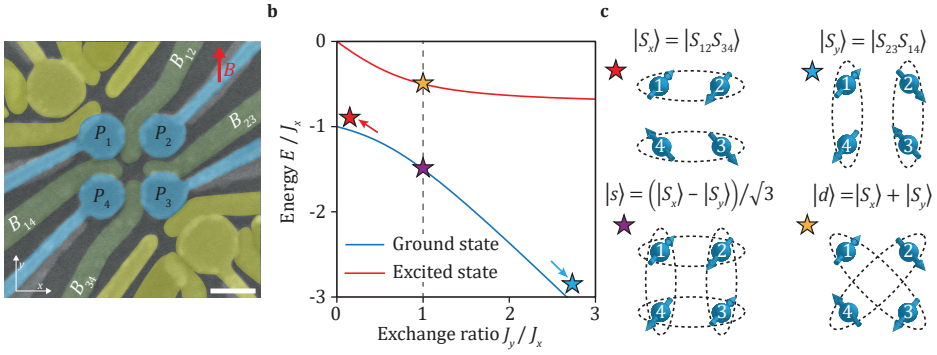

Figure 3.1: **RVB states in a 2×2 quantum dot array. a**, False-coloured scanning electron micrograph of the Ge quantum dot array. Plunger and barrier gates are coloured in blue and green respectively, and the corresponding gate voltages applied on them are labelled. To achieve independent control of the quantum dot potentials and tunnel couplings, virtual plunger and barrier gate voltages are defined (see Supplementary Note 1 [40]). Single hole transistors used as charge sensors are coloured in yellow. The scale bar corresponds to 100 nm. **b**, Energy diagram corresponding to the Hamiltonian H_S. The stars denote the corresponding eigenstates depicted in **c**. When the exchange interaction is dominated by horizontal (vertical) pairs, the ground state is $|S_x\rangle$ ($|S_y\rangle$), and in our experiments we use this configuration for initialization. Resonating valence bond states appear when $J_y = J_x$, the eigenstates are the ground state with s-wave symmetry and excited state with d-wave symmetry.

3.2. RESULTS

3.2.1. SINGLET-TRIPLET OSCILLATIONS IN THE FOUR DOUBLE QUANTUM DOTS

Probing the RVB physics relies on measuring the singlet probabilities in the (1,1) charge state [17, 36]. We thus investigate singlet-triplet (ST) oscillations within all nearest-neighbour pairs.

To generate ST oscillations, we operate in a virtual gate landscape and apply pulses on the virtual plunger gates vP_i of each quantum dot pair according to the pulse sequence depicted in Fig. 3.2.a [27, 41–44]. The double quantum dot system is initialized in a singlet (0,2) state. Then, the detuning between the quantum dots is varied by changing the virtual plunger gate voltages. The system is diabatically brought to a manipulation point in the (1,1) sector creating a coherent superposition of $|S\rangle$, $|T^-\rangle$ and $|T^0\rangle$ [27, 41–44]. After a dwell time t_D, the system is diabatically pulsed back to the (0,2) sector where the ST probabilities are determined via single-shot readout using (latched) Pauli-spin-blockade [45–47].

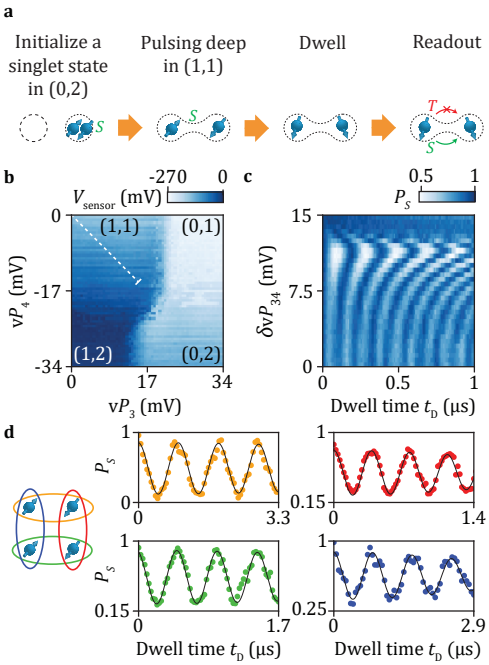

Figure 3.2: **Singlet-triplet qubits on all nearest-neighbour configurations.** **a**, Schematics of the pulse sequence used to generate singlet-triplet oscillations in double quantum dots. **b**, Charge stability diagram of a double quantum dot (Q_3Q_4) in the few-hole regime. **c**, S-T^- oscillations as a function of time and detuning $\delta vP_{34} = 0.5(vP_3 - vP_4)$ varied along the dashed line in **b**. At larger magnetic fields, here B = 3 mT, and limited tunnel couplings, we observe a minimum oscillation frequency due to the S-T^- anticrossing. We tune the system in a regime with smaller magnetic fields (B = 1 mT) and larger tunnel couplings, to operate away from this point. **d**, S-T^- oscillations observed in this regime for all possible permutations of nearest-neighbour quantum dot pairs. Black lines are fits of the data (see Section 3.4).

Results of such experiments performed at $B = 3$ mT with Q_3Q_4 pair are presented in Fig. 3.2.c. Clear oscillations between the $|S\rangle$ and $|T^-\rangle$ state are observed over a large range of gate voltage. Importantly, using this method we find the S-T^- anticrossing, which is the position where the frequency has a minimum. The observation of such oscillations, predominating over oscillations between $|S\rangle$ and $|T^0\rangle$ states, agrees with recent investigations suggesting that S-T^- oscillations dominate in germanium ST qubits placed in an in-plane B field [44].

Fig. 3.2.c also suggests that a (1,1)-singlet can be initialized from a (0,2)-singlet, by changing the energy detuning between the quantum dots while avoiding to pass the S-T^- anticrossing. We achieve this by shifting the anticrossing towards the center of the (1,1) charge sector by decreasing the magnetic field to $B = 1$ mT and increasing the tunnel couplings (Fig. 3.6). Fig. 3.2.d demonstrates clear S-T^- oscillations observed in this regime for all nearest-neighbour configurations (see also Fig. 3.7). Importantly, these oscillations also enable to determine the singlet/triplet states on two parallel quantum dot pairs by using sequential readout [48].

3.2.2. TUNING OF INDIVIDUAL EXCHANGES USING COHERENT OSCILLATIONS

The overlap of the H_S eigenstates with $|S_x\rangle$ and $|S_y\rangle$ depends on J_x and J_y (see Section 3.5). A quantitative comparison between experiments and theoretical expectations thus requires fine control over the exchange couplings.

In this purpose, we focus on the evolution of coherent four-spin ST oscillations. These oscillations are induced using the experimental sequence depicted in Fig. 3.3.a (see also Supplementary Figure 3 [40]). We turn off two parallel exchange couplings and initialize a $|S_x\rangle$ or a $|S_y\rangle$ state in parallel double quantum dots. We then rotate one of the singlet pairs to a triplet $|T^-\rangle$ state through coherent time evolution after pulsing to the S-T^- anticrossing, creating a four-spin singlet-triplet product state (e.g. $|T^-_{34}S_{12}\rangle$ or $|T^-_{23}S_{14}\rangle$). All barrier gate voltages are then diabatically pulsed to turn on all the exchange couplings leading to coherent evolution of the four-spin system. After a dwell time t_D, two pairs are isolated (not necessarily the initial ones) and their spin-states are readout sequentially, which allows to deduce spin-correlations of opposite pairs, as was realized in linear arrays in GaAs [17].

The observation of resonating valence bond requires equal couplings between all four quantum dots. In navigating to this point, we carefully develop a virtual landscape, keep control over all the individual exchange interactions. First, we separately equalize the horizontal ($J_{12} = J_{34}$) and vertical ($J_{14} = J_{23}$) exchange couplings. Then, we tune the vertical and horizontal exchanges to the same coupling strength. The Chevron patterns displayed in Fig. 3.3.c-d are consistent with a Heisenberg Hamiltonian (see see Fig. 3.8 to Fig. 3.10) and the minima in the oscillation frequency mark the location of equal exchange couplings for horizontal ($J_{12} \simeq J_{34} \simeq J_x/2$ for Fig. 3.3.c) or vertical pairs ($J_{14} \simeq J_{23} \simeq J_y/2$ for Fig. 3.3.d). Through an iterative process, we can find ranges of virtual gate voltages where $J_{12} \simeq J_{34}$ and $J_{23} \simeq J_{14}$.

We can now control the spin pairs simultaneously, while maintaining the exchange couplings in both the horizontal and vertical directions equal (see Section 3.6), with *a priori* $J_x \neq J_y$. Through the readout of both pairs, we can obtain the frequency of four-spin ST oscillations observed in this regime (Fig. 3.3.e), which is given by $f_{ST} = J_y/2h$ or

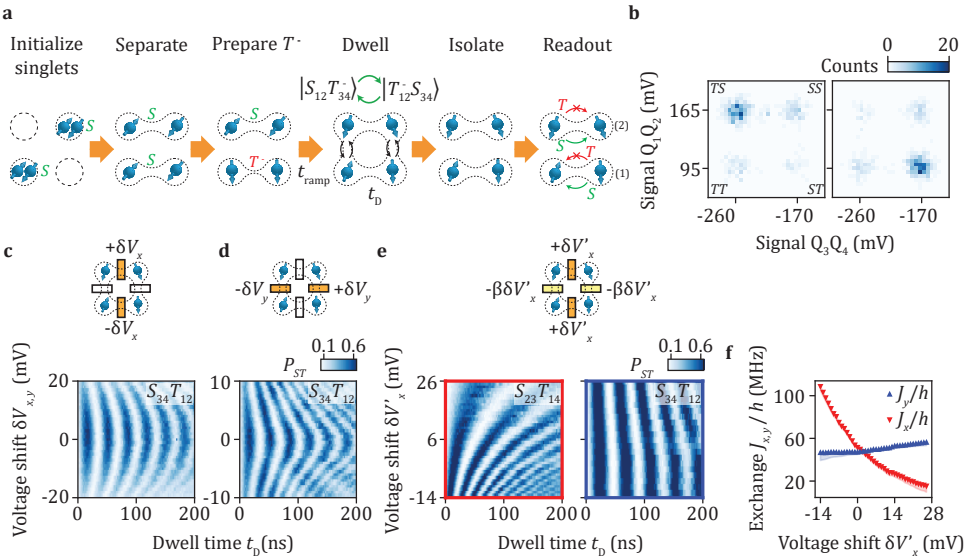

Figure 3.3: **Four-spin coherent singlet-triplet oscillations and exchange characterization.** **a**, Schematics of the pulse sequence used to measure four-spin ST oscillations from an initial $|T^-_{34}S_{12}\rangle$ state. **b**, The 2D histograms of the sensor signals formed by sequential 500 single-shot readouts of Q_3Q_4 and Q_1Q_2 ST states. The left panel shows the initial state $|T^-_{34}S_{12}\rangle$ at $t_D = 0$ ns. The right panel shows the state at $t_D = 19$ ns corresponding to half an oscillation period. (Data corresponds to **c** for $\delta V_x = 0$.) **c**, Oscillations in ST probability $P_{S_{34}T_{12}}$ as a function of gate voltage variation δV_x. The amplitude of exchange pulses applied on the virtual barrier gates during the free evolution step are varied between measurements around a predetermined set of barrier gate voltages where $J_x < J_y$. The amplitude of voltage pulses on v$B_{12,34}$ are varied anti-symmetrically while the amplitudes of the pulses on v$B_{23,14}$ are kept constant, as shown in the top illustration. The initial state is $|T^-_{34}S_{12}\rangle$. **d**, Similar experiment where oscillations in $P_{S_{34}T_{12}}$ are studied as a function of the gate voltage variation δV_y. δV_y is the shift in the amplitudes of the exchange pulses applied anti-symmetrically on v$B_{23,14}$ (see top illustration). The initial state is $|T^-_{34}S_{12}\rangle$. **e**, Oscillations in $P_{S_{23}T_{14}}$ (left) and $P_{S_{34}T_{12}}$ (right) as functions of t_D and $\delta V'_x$. The amplitude of exchange pulses are varied symmetrically around the operation point ($\delta V'_x = 0$ mV where $J_x \simeq J_y$) according to the top illustration ensuring that $J_{12} \simeq J_{34}$ and $J_{14} \simeq J_{23}$ along the full voltage range. The initial states are respectively a $|T^-_{23}S_{14}\rangle$ (left) and a $|T^-_{34}S_{12}\rangle$ state (right). **f**, Exchange couplings $J_{x,y}$ extracted by fitting the oscillations in **e** with $A\cos(2\pi f_{ST} t_D + \phi)\exp(-(t_D/T_\varphi)^2) + A_0$ as a function of gate voltage variation $\delta V'_x$. The oscillation frequencies of $P_{S_{23}T_{14}}$ ($P_{S_{34}T_{12}}$) corresponds to $J_x/2h$ ($J_y/2h$). The shaded areas correspond to the estimated uncertainty on the exchange couplings derived based on assumptions discussed in Section 3.6.

$J_x/2h$ depending on the initial state, and with that determine the exchange interaction. As highlighted in Fig. 3.3.f., the virtual control enables to tune J_x from 15 MHz to 109 MHz with J_y remaining between 46 and 56 MHz. Clearly, the exchange interaction can be controlled and measured over a significant range and tuned to a regime where all couplings are equal (we obtain a precision of ≈ 3 MHz, as discussed in Section 3.6, mostly determined by drifts between experiments).

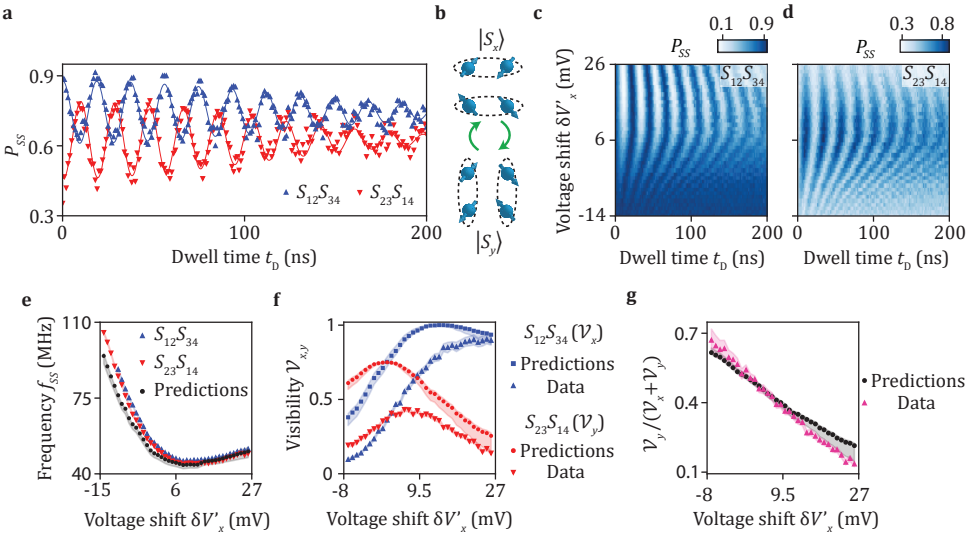

Figure 3.4: **Valence bond resonances.** **a**, Probabilities of having horizontal singlet pairs $P_{S_{12}S_{34}}$ and vertical singlet pairs $P_{S_{23}S_{14}}$ as a function of dwell time t_D. All the exchange couplings are tuned toward an identical value of $J_{ij}/h \simeq 25$ MHz. Lines are fits to the data with $P_{SS} = 1/2\,\mathcal{V}\cos(2\pi f_{SS} t_D + \phi)\exp(-(t_D/T_\varphi)^2) + A_0$ giving respectively $T_\varphi = 167$ ns and 143 ns for data corresponding to $P_{S_{12}S_{34}}$ and $P_{S_{23}S_{14}}$. The state is initialized as $|S_x\rangle$. **b**, Illustration showing valence bond resonances characterized by oscillations between the singlet product states $|S_x\rangle$ and $|S_y\rangle$. **c**, $P_{S_{12}S_{34}}$ and, **d**, $P_{S_{23}S_{14}}$ as a function of t_D and virtual barrier gate voltage variation $\delta V'_x$. The state is initialized as $|S_x\rangle$. **e**, The oscillation frequency as a function of $\delta V'_x$. The blue (red) points are extracted from **c** (**d**). The black points are the theoretical predictions $f_{SS} = \sqrt{J_x^2 + J_y^2 - J_x J_y}/h$ computed using the exchanges J_x and J_y measured in Fig. 3.3.e. **f**, Visibility $\mathcal{V}_{x,y}$ as a function of gate voltage variation $\delta V'_x$. The triangles in blue (red) are extracted from **c** (**d**). The expected values are derived from equations (3.4) and (3.6) of Section 3.5 using the measured exchanges. The shaded areas correspond to one standard deviation from the best fit for the experimental data, and for the theoretical data they correspond to the uncertainties on the amplitude and the frequency computed using the uncertainties on the exchange couplings values. **g**, Ratio of the visibilities $\mathcal{V}_y/(\mathcal{V}_x + \mathcal{V}_y)$ as a function of the gate voltage variation $\delta V'_x$.

3.2.3. VALENCE BOND RESONANCES

Valence band resonances can occur when all J_{ij} are equal. To experimentally assess this, we prepare $|S_x\rangle$ or $|S_y\rangle$, which are superposition states of H_S. We then pulse the exchanges such that $J_x \approx J_y$. Fig. 3.4.a shows the result of the time evolution in this regime of equal exchange couplings. Since we start from a superposition state of H_S, the time evolution leads to coherent oscillations between $|S_x\rangle$ or $|S_y\rangle$, which results in periodic swaps between the singlet states as depicted in Fig. 3.4.b. In addition, we readout both in the horizontal and vertical configuration, and observe an anti-correlated signal, consistent with signatures of valence bond resonances [32, 36]. The observation of more than ten oscillations shows the relatively high level of coherence achieved during these experiments further confirmed by the characteristic dephasing time $T_\varphi \approx 150$ ns.

Fig. 3.4.c-d show a more detailed measurement, which we can fit using $\frac{\mathcal{V}_{x,y}}{2}\cos(2\pi f_{SS} t_D +$

$\phi)\exp(-(t_D/T_\varphi)^2)+A_0$ to extract the evolution of the frequencies f_{SS} and of the visibilities $\mathcal{V}_{x,y}$, plotted on Fig. 3.4.e and Fig. 3.4.f. We find a quantitative agreement between the measured frequencies and the theoretical expectation $f_{SS}=\sqrt{J_x^2+J_y^2-J_xJ_y}/h$ despite deviations for the lowest values of $\delta V_x'$ that could result from the uncertainties in the exchange couplings. We also find a qualitative agreement for the visibilities though the measured $\mathcal{V}_{x,y}$ remain lower, in particular when the exchange is larger. Fermi-Hubbard simulations and further analysis (see Supplementary Notes 7 and 8 [40]) reveal that part of the visibility loss can be attributed to leakage and to the insufficient diabaticity of the voltages pulses. We speculate that the rest of the visibility loss is mainly due to the decoherence induced by the voltage pulses at the manipulation stage, or by pulse distortion arising from the non-ideal electrical response of the wiring. The underlying mechanism affects similarly the results of the measurements in the both readout directions over most of the voltage range spanned (see Supplementary Note 8 [40]). Consequently, a more quantitative agreement is reached when comparing the ratio $\mathcal{V}_y/(\mathcal{V}_x+\mathcal{V}_y)$ (Fig. 3.4.g) of the visibilities measured over the visibilities predicted, similarly as is done in ref. [36]. Overall, the good agreement observed confirms that the dynamics is governed by H_S.

3.2.4. PREPARATION OF RESONATING VALENCE BOND EIGENSTATES

Having observed valence bond resonances, we now focus on the preparation of eigenstates of H_S which are the $|s\rangle$ and $|d\rangle$ RVB states. $|s\rangle$ is the ground state of H_S when $J_x=J_y$, whereas $|S_x\rangle$ and $|S_y\rangle$ are the ground states when $J_x\gg J_y$ and $J_x\ll J_y$. Experimentally we therefore prepare $|s\rangle$ from $|S_x\rangle$ or $|S_y\rangle$ by adiabatically tuning the exchange interactions to equal values. Fig. 3.5.a shows experiments where we control the ramp time t_{ramp} to tune to this regime and we observe a progressive vanishing of phase oscillations. For large $t_{\text{ramp}}\gtrsim 140$ ns, the oscillations nearly disappear and the measured probability saturates to $P_{S_{12}S_{34}}\simeq 0.78$. Performing similar experiments starting from a $|S_y\rangle$ state or measuring $P_{S_{23}S_{14}}$ leads to identical features with singlet-singlet probabilities saturating between 0.66 and 0.72 (see Supplementary Figure 22 [40]). These values are close to the probabilities $|\langle S_{x,y}|s\rangle|^2=3/4$ expected when the s-wave state is prepared.

We can now also prepare the ground state H_S for arbitrary exchange values, by carefully tuning the ramp time ($t_{\text{ramp}}=160$ ns in our experiments). Fig. 3.5.b shows the evolution of $P_{S_{12}S_{34}}$ for different $\delta V_x'$. Since we prepare the ground state, coherent phase evolution results in a $P_{S_{12}S_{34}}$ that is virtually constant for any $\delta V_x'$ and only faint oscillations are observed. $P_{S_{12}S_{34}}$, however, is strongly dependent on $\delta V_x'$, as increasing J_x changes the ground state to $|S_x\rangle$.

The measured $P_{S_{12}S_{34}}$ values can be compared with predictions using $J_{x,y}$ values extracted from four-spin singlet-triplet oscillations (see Section 3.5). Fig. 3.5.c shows that a good agreement exists between the theory and the experiments. The raw experimental probabilities $P_{S_{12}S_{34}}$ remains smaller than the theoretical predictions due to systematic errors during the experiments, which are most likely state initialization and readout errors (see Supplementary Note 8 [40]). Measuring $P_{S_{23}S_{14}}$ leads to a similar agreement, although the imperfections have a larger impact in this experiment. Rescaling the data by constant factors, that compensate for systematic errors, allows to reach a quantitative agreement, as shown in Fig. 3.5.c. From this we conclude that the ground state of H_S is

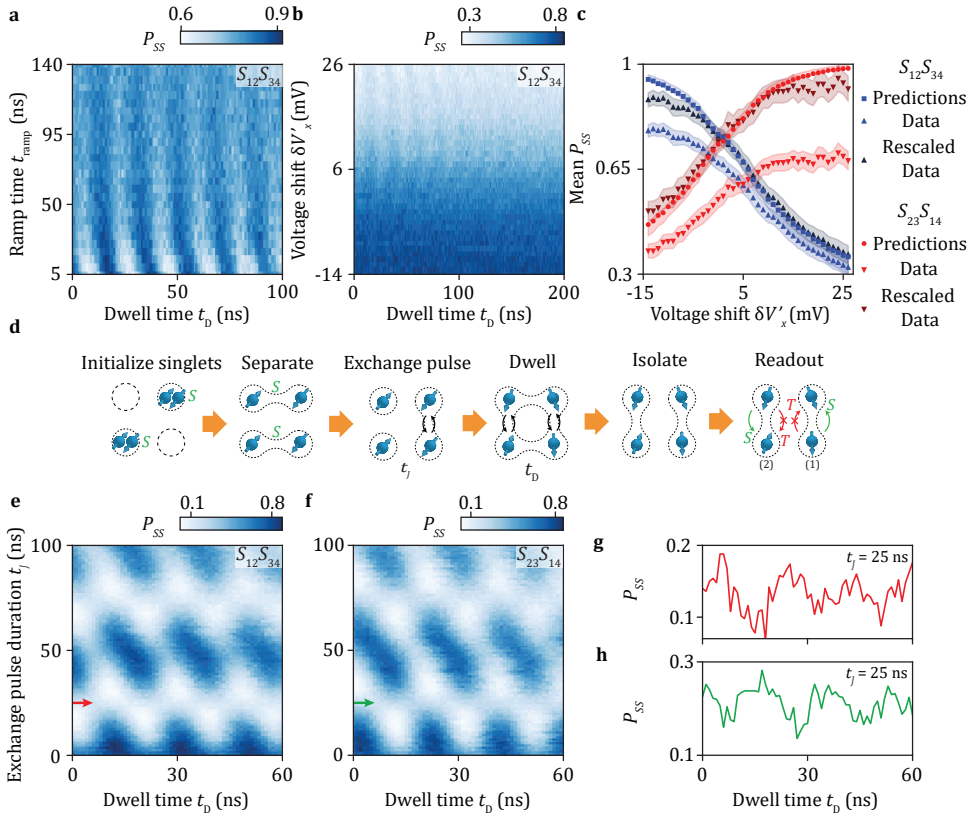

Figure 3.5: **Initialization of RVB eigenstates. a**, Evolution of RVB oscillations as a function of the time to set all exchanges equal ($J_{ij} \simeq 25$ MHz) (see Fig. 3.3.a). For $t_{\text{ramp}} \gtrsim 140$ ns, the ground state with s-wave symmetry is adiabatically prepared. **b**, Evolution of the singlet-singlet probability $P_{S_{12}S_{34}}$ with $\delta V'_x$ after adiabatic initialization of the ground state. **c**, Evolution of the mean singlet-singlet probability measured after adiabatic initialization of the ground state with $\delta V'_x$ for both readout directions. The experiments are compared to theoretical expectations using exchange coupling values extracted from four-spin singlet-triplet oscillations (Section 3.5 and 3.6). The shaded areas correspond to one standard deviation from the best fit for the experimental data, and for the theoretical data they correspond to the uncertainties on the amplitude and the frequency computed using the uncertainties on the exchange couplings values. Rescaled data (dark red and blue triangles) are obtained by multiplying each raw dataset (red and blue triangles) by a constant factor corresponding to the mean ratio of the predicted probabilities over the measured probabilities. **d**, Experimental sequence used to investigate the formation of the d-wave state. Before the free evolution step, one exchange pulse on vB_{23} is applied for a time t_J. **e, f**, Evolution of singlet-singlet oscillations measured for different exchange pulse durations t_J. The vanishing of oscillations at $t_J \simeq 25$ ns marks the formation of a d-wave state. **g, h**, Linecuts of **e** and **f** for $t_J = 25$ ns.

adiabatically initialized in these experiments.

We prepare the d-wave state by including an additional operation where we exchange two neighbouring spins [36]. This results in a transformation of neighbouring spin-spin correlations to diagonal correlations. We experimentally implement this step by adding, before the free evolution step, an exchange pulse of duration t_J during which only one

exchange coupling is turned on (see Fig. 3.5.d).

Fig. 3.5.e-f shows $P_{S_{12}S_{34}}$ and $P_{S_{23}S_{14}}$ measured as functions of t_D and t_J in experiments where the system is initialized in $|S_x\rangle$ and the exchange J_{23} is pulsed. As a function of the exchange pulse duration, we observe a periodic vanishing of RVB oscillations (linecuts provided in Fig. 3.5.g-h, imperfections in exchange control cause residual oscillations). Due to the exchange pulse, a periodic swapping of neighbouring spins occurs, and thus a periodic evolution between neighbouring spin-spin correlations and diagonal correlations. Thus the regime where the d-wave eigenstate is prepared is marked by the vanishing of RVB states. The mean of the probabilities, $P_{S_{23}S_{14}} \simeq 0.21$ and $P_{S_{12}S_{34}} \simeq 0.13$, measured for $t_J = 25$ ns are in the direction of theoretical expectations $|\langle S_{x,y}|d\rangle|^2 = 1/4$.

3.3. DISCUSSION

In this work we demonstrated a coherent quantum simulation using germanium quantum dots. Clear evolution of resonating valence bond states appeared after tuning to a regime where all nearest neigbours have equal exchange coupling. We furthermore established the preparation of the s-wave and d-wave eigenstates. In addition, we have shown that we can control the exchange interaction over a significant range in a multi-spin setting.

The low-disorder and quantum coherence make germanium a compelling candidate for more advanced quantum simulations. Improving the initialization and readout fidelities will enable to observe a stronger correspondence between ideal predictions and experimental results. Additionally, advanced voltage pulsing may facilitate to reduce errors occurring when controlling the spin states. Furthermore, a significant improvement in the quantum coherence may be obtained by exploring sweet spots [49] and by using purified germanium.

Controlling multi-spin states is also highly relevant in the context of quantum computation. The realization of exchange-coupled singlet-triplet qubits enables to implement fast two-qubit gates [50–53]. Leakage may then be reduced by exploiting the large out-of-plane g-factor for holes in germanium [27, 44]. Also, operation with four-spin manifolds provides means for decoherence-free subspaces [54].

Extensions of this work leveraging the full tunability of germanium quantum dots could provide new insights for extensive studies of strongly-correlated magnetic phases and associated quantum phase transitions. In particular, the implementation of similar simulations in triangular lattices offer new possibilities to investigate the emergence of non-trivial phases arising from frustration [33, 34]. Likewise, the preparation of RVB states and the investigation of their dynamics in larger devices may help to probe their properties experimentally and explore how they relate to superconductivity in doped cuprates [31].

3.4. EXTENDED DATA OF TWO-SPIN S-T^- OSCILLATIONS

In a double dot, the (1,1) singlet energy reads as $E_S \simeq \frac{\varepsilon}{2} - \sqrt{\frac{\varepsilon^2}{4} + 2t_c^2}$, with t_c the tunnel coupling between the quantum dots and ε the detuning between the quantum dots (taken as zero at the (2,0)-(1,1) charge transition) [27]. The energy of the triplet states are $E_{T^0} \simeq 0$ and $E_{T^\pm} \simeq \pm\frac{\Sigma g}{2}\mu_B B$ with Σg the g-factor sum. The corresponding energy diagram is sketched in Fig. 3.6.

In the (1,1) charge sector, the ground state is the singlet $|S\rangle$. Above a given value of detuning ε_{SO}, the $|T^-\rangle$ state becomes the ground state. Consequently there is an anticrossing between the $|S\rangle$ and $|T^-\rangle$ due to the spin-orbit interaction. In order to maintain the singlet ground state in the (1,1) charge sector, one can decrease the magnetic field B or increase the tunnel coupling t_c.

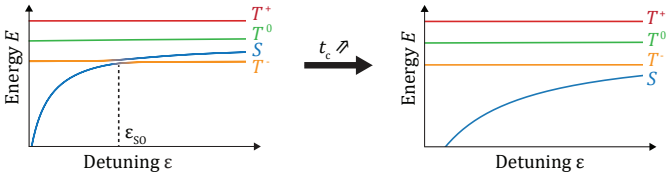

Figure 3.6: **Energy diagrams of a double quantum dot system at low fields.** At low tunnel couplings t_c, the singlet S and the triplet T^- energy states anti-cross due to the spin-orbit interaction. Increasing t_c, the energy of singlet state is lowered. At sufficiently large t_c, the singlet state remains the ground state in the (1,1) charge state for any value of the detuning ε.

At $B = 1$ mT, the ground state is the singlet state for Q_1Q_2 and Q_1Q_4 pairs in the whole (1,1) charge sector. It gives more freedom for the singlet-(1,1) initialization with these two quantum dot pairs. For the Q_2Q_3 and Q_3Q_4, there is still a S-T^- anticrossing that appears at finite detuning but sufficiently far from the charge transition line. It reduces charge noise effects detrimental for four-spin experiments.

To observe high visibility ST oscillations, pulses on the virtual barrier voltages are applied to reduce t_c while going from the initialization to the manipulation point. This configuration offers more flexibility to initialize $|S_x\rangle$ or $|S_y\rangle$ states.

Fig. 3.7 presents the ST oscillations of Fig. 3.2.d over larger ranges of dwell time t_D. By fitting the data, we extract the characteristic dephasing times T_φ and the frequency of the oscillations f for each pair (3.1). We note that there are large variations of both T_φ and f. The variation of f can be explained by differences in the strengths of the tunnel couplings t_c, the differences in the g-factor and in the amplitudes of the barrier voltage pulses. They lead to variations of the energy splitting between the $|T^-\rangle$ and $|S\rangle$ states. The variations of T_φ can result from different effects like residual exchange interactions with the other quantum dots or leakage to the $|T^0\rangle$ states. The lower coherence of Q_2Q_3 and Q_1Q_4 pairs compared to that of Q_1Q_2 and Q_3Q_4 could also result from the field orientation. Additionally, the spin life time is reduced when the spin-orbit field is oriented perpendicular to the external magnetic field [29, 55].

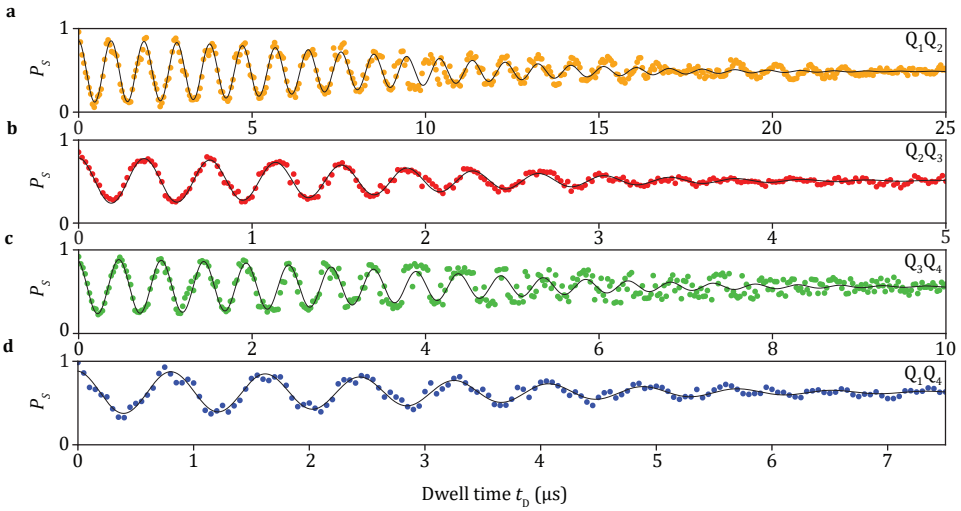

Figure 3.7: **Singlet-Triplet oscillations observed with each double quantum dot.** Same measurements than ones showed in Fig. 3.2.d. Data (points) are fitted with $A\cos(2\pi f t_D + \phi)\exp(-(t/T_\varphi)^2) + A_0$ to extract T_φ and f.

Dot Pair	Frequency (MHz)	T_φ (μs)
Q_1Q_2	1.056 ± 0.001	11.2 ± 0.4
Q_2Q_3	2.636 ± 0.005	2.5 ± 0.1
Q_3Q_4	2.043 ± 0.004	5.1 ± 0.3
Q_1Q_4	1.223 ± 0.004	4.2 ± 0.2

Table 3.1: **Characteristics of singlet-triplet oscillations of individual dot pairs.** The uncertainties correspond to one standard deviation from the best fits.

3.5. FOUR-SPIN COHERENT OSCILLATIONS IN THE GLOBAL SINGLET SUBSPACE

THEORETICAL MODEL

The Heisenberg Hamiltonian H_S in the global singlet subspace can be written, up to an overall energy shift, as:

$$H_S = (-\frac{1}{2}J_x + \frac{1}{4}J_y)\sigma_z + \frac{\sqrt{3}}{4}J_y\sigma_x = h_0\cos\theta\sigma_z + h_0\sin\theta\sigma_x, \tag{3.2}$$

where $\cos\theta = \frac{-2J_x+J_y}{2\sqrt{J_x^2-J_xJ_y+J_y^2}}$, $\sin\theta = \frac{\sqrt{3}J_y}{2\sqrt{J_x^2-J_xJ_y+J_y^2}}$, $h_0 = \frac{1}{2}\sqrt{J_x^2-J_xJ_y+J_y^2}$, and $\sigma_{x,z}$ are the Pauli matrices. Here we denote the basis states $\{|0\rangle, |1\rangle\} \equiv \{|S_{12}S_{34}\rangle, \frac{1}{\sqrt{3}}(|T_{12}^+T_{34}^-\rangle + |T_{12}^-T_{34}^+\rangle - |T_{12}^0T_{34}^0\rangle)\} \equiv \{\begin{pmatrix}1\\0\end{pmatrix}, \begin{pmatrix}0\\1\end{pmatrix}\}$.

The eigen energies are $E_g = -h_0$ and $E_e = h_0$. The eigenstates are:

$$\begin{cases} |g\rangle = \begin{pmatrix} -\sin\frac{\theta}{2} \\ \cos\frac{\theta}{2} \end{pmatrix} \\ |e\rangle = \begin{pmatrix} \cos\frac{\theta}{2} \\ \sin\frac{\theta}{2} \end{pmatrix} \end{cases}. \tag{3.3}$$

In the singlet-singlet oscillation experiments, the state is initialized in a singlet-singlet state $|S_{12}S_{34}\rangle = \begin{pmatrix}1\\0\end{pmatrix}$ which can be written as $-\sin\frac{\theta}{2}|g\rangle + \cos\frac{\theta}{2}|e\rangle$. After the free evolution this state becomes, up to a phase factor:

$$|\psi(t)\rangle = -\sin\tfrac{\theta}{2}|g\rangle + \cos\tfrac{\theta}{2}e^{-i\omega_{eg}t}|e\rangle = \begin{pmatrix} \sin^2(\frac{\theta}{2}) + \cos^2(\frac{\theta}{2})e^{-i\omega_{eg}t} \\ \sin(\frac{\theta}{2})\cos(\frac{\theta}{2})(-1+e^{-i\omega_{eg}t}) \end{pmatrix} = e^{-i\omega_{eg}t/2}\begin{pmatrix} \cos(\frac{\omega_{eg}t}{2}) - i\cos\theta\sin(\frac{\omega_{eg}t}{2}) \\ -i\sin\theta\sin(\frac{\omega_{eg}t}{2}) \end{pmatrix},$$

where $\omega_{eg} \equiv \omega_e - \omega_g = \frac{1}{\hbar}\sqrt{J_x^2 - J_xJ_y + J_y^2}$ is the frequency of the singlet oscillations.

The probability of being in the state $|0\rangle$ is $P_{S_{34}S_{12}}(t) = |\langle S_{12}S_{34}|\psi(t)\rangle|^2 = \frac{1}{2}\left(1+\cos^2\theta+\sin^2\theta\cos(\omega_{eg}t)\right)$. The visibility of the oscillations is then:

$$\mathcal{V}_x = P^{\max}_{S_{34}S_{12}} - P^{\min}_{S_{34}S_{12}} = \sin^2\theta = \frac{3J_y^2}{4(J_x^2 - J_xJ_y + J_y^2)}. \tag{3.4}$$

To describe the readout in the y direction, we use the basis $\{|0_y\rangle, |1_y\rangle\} = \{|S_{14}S_{23}\rangle, \frac{1}{\sqrt{3}}(|T_{14}^+T_{23}^-\rangle + |T_{14}^-T_{23}^+\rangle - |T_{14}^0T_{23}^0\rangle)\}$. The original basis can be re-written in terms of the new basis as:

$$\begin{cases} |0\rangle = -\frac{1}{2}|0_y\rangle - \frac{\sqrt{3}}{2}|1_y\rangle \\ |1\rangle = \frac{\sqrt{3}}{2}|0_y\rangle - \frac{1}{2}|1_y\rangle \end{cases}. \tag{3.5}$$

Therefore, $P_{S_{23}S_{14}}(t) = |\langle 0_y|\psi(t)\rangle|^2 = \frac{1}{4}(1+(\sin^2\theta - \sqrt{3}\sin\theta\cos\theta)\left(1-\cos(\omega_{eg}t)\right)$. The visibility is then:

$$\mathcal{V}_y = \frac{1}{2}(\sin^2\theta - \sqrt{3}\sin\theta\cos\theta) = \frac{3J_xJ_y}{4(J_x^2 - J_xJ_y + J_y^2)}. \tag{3.6}$$

We note that $\sin^2\theta - \sqrt{3}\sin\theta\cos\theta = \frac{6J_yJ_x}{4(J_x^2-J_xJ_y+J_y^2)} > 0$ and thus $P_{S_{34}S_{12}}(t)$ and $P_{S_{23}S_{14}}(t)$ oscillate in phase opposition. There are periodic swaps between $|S_x\rangle$ and $|S_y\rangle$ which are the resonating valence bond oscillations as shown in Fig. 3.4.

3

SINGLET PROBABILITIES OF S-WAVE AND D-WAVE STATES

To prepare the s-wave and d-wave states, the exchanges are set to be equal. It corresponds to the Hamiltonian of equation (3.2) with $\theta = 120°$. The s-wave state is the ground state and reads $|s\rangle = |g\rangle = (-\frac{\sqrt{3}}{2}, \frac{1}{2})$. The singlet-singlet probability in both x and y directions for this state are $P_{S_{34}S_{12}} = P_{S_{23}S_{14}} = \frac{3}{4}$. The d-wave state is the excited state and reads $|d\rangle = |e\rangle = (\frac{1}{2}, \frac{\sqrt{3}}{2})$. The singlet-singlet probabilities for this state are $P_{S_{34}S_{12}} = P_{S_{23}S_{14}} = \frac{1}{4}$.

When the exchanges are different, the equation (3.3) gives the ground state singlet-singlet readout probability $P_{S_{34}S_{12}} = \sin^2\frac{\theta}{2} = \frac{1-\cos\theta}{2} = \frac{1}{2} - \frac{-2J_x+J_y}{4\sqrt{J_x^2-J_xJ_y+J_y^2}}$ and $P_{S_{23}S_{14}} = (\frac{1}{2}\sin\frac{\theta}{2} + \frac{\sqrt{3}}{2}\cos\frac{\theta}{2})^2 = \frac{1}{2} + \frac{1}{4}\cos\theta + \frac{\sqrt{3}}{4}\sin\theta = \frac{1}{2} + \frac{-J_x+2J_y}{4\sqrt{J_x^2-J_xJ_y+J_y^2}}$. These formula are used in Fig. 3.5.c.

3.6. FOUR-SPIN COHERENT OSCILLATIONS IN THE GLOBAL TRIPLET SUBSPACE

THEORETICAL MODEL

Here we derive the theoretical results used to infer the exchange coupling $J_{x,y}$ from the four-spin singlet-triplet oscillations. In our experiments, we operated in the $m_S = -1$ global triplet subspace spanned by a natural basis $\{|S_{12}T_{34}^-\rangle, |T_{12}^-S_{34}\rangle, \frac{1}{\sqrt{2}}(|T_{12}^0T_{34}^-\rangle - |T_{12}^-T_{34}^0\rangle)\}$. Considering only Heisenberg exchange interactions, the Hamiltonian can be written as:

$$H_T = \begin{pmatrix} -J_{12} - \frac{J_{23}+J_{14}}{4} & -\frac{J_{23}+J_{14}}{4} & -\frac{J_{23}-J_{14}}{2\sqrt{2}} \\ -\frac{J_{23}+J_{14}}{4} & -J_{34} - \frac{J_{23}+J_{14}}{4} & -\frac{J_{23}-J_{14}}{2\sqrt{2}} \\ -\frac{J_{23}-J_{14}}{2\sqrt{2}} & -\frac{J_{23}-J_{14}}{2\sqrt{2}} & -\frac{J_{23}+J_{14}}{2} \end{pmatrix} = \begin{pmatrix} -\frac{J_x+\delta_x}{2} - \frac{J_y}{4} & -\frac{J_y}{4} & -\frac{\delta_y}{2\sqrt{2}} \\ -\frac{J_y}{4} & -\frac{J_x-\delta_x}{2} - \frac{J_y}{4} & -\frac{\delta_y}{2\sqrt{2}} \\ -\frac{\delta_y}{2\sqrt{2}} & -\frac{\delta_y}{2\sqrt{2}} & -\frac{J_y}{2} \end{pmatrix}. \tag{3.7}$$

We focus on the situation where $\delta_{x,y} \ll J_{x,y}$. First, we notice that in this limit $\frac{1}{\sqrt{2}}(|T_{12}^0T_{34}^-\rangle - |T_{12}^-T_{34}^0\rangle)$ is decoupled from the other states. Thus, when the system is diabatically initialized to $|S_{12}T_{34}^-\rangle$, it evolves to $|T_{12}^-S_{34}\rangle$ and back to $|S_{12}T_{34}^-\rangle$ at a frequency f_{ST}. To calculate f_{ST}, we perform a basis change to $\{|0\rangle, |1\rangle, |2\rangle\} \equiv \{\frac{1}{\sqrt{2}}(|S_{12}T_{34}^-\rangle - |T_{12}^-S_{34}\rangle), \frac{1}{\sqrt{2}}(|S_{12}T_{34}^-\rangle + |T_{12}^-S_{34}\rangle), \frac{1}{\sqrt{2}}(|T_{12}^0T_{34}^-\rangle - |T_{12}^-T_{34}^0\rangle)\}$ and separate the Hamiltonian into two terms:

$$H'_T = \begin{pmatrix} -\frac{J_x}{2} & -\frac{\delta_x}{2} & 0 \\ -\frac{\delta_x}{2} & -\frac{J_x+J_y}{2} & -\frac{\delta_y}{2} \\ 0 & -\frac{\delta_y}{2} & -\frac{J_y}{2} \end{pmatrix} = \begin{pmatrix} -\frac{J_x}{2} & 0 & 0 \\ 0 & -\frac{J_x+J_y}{2} & 0 \\ 0 & 0 & -\frac{J_y}{2} \end{pmatrix} + \begin{pmatrix} 0 & -\frac{\delta_x}{2} & 0 \\ -\frac{\delta_x}{2} & 0 & -\frac{\delta_y}{2} \\ 0 & -\frac{\delta_y}{2} & 0 \end{pmatrix} = H_0 + V, \tag{3.8}$$

where H_0 only contains diagonal elements $J_{x,y}$ and V only contains off-diagonal elements $\delta_{x,y}$. In the non-degenerate case $\delta_{x,y} \lesssim |J_x - J_y|$, we apply the second order perturbation theory to the term V. The eigen energies become:

$$E_0 = E_0^{(0)} + E_0^{(1)} + E_0^{(2)} = \langle 0|H_0|0\rangle + \langle 0|V|0\rangle + \sum_{i=\{1,2\}} \frac{|\langle i|V|0\rangle|^2}{E_0^{(0)} - E_i} = -\frac{J_x}{2} + \frac{\delta_x^2}{2J_y}, \tag{3.9}$$

$$E_1 = E_1^{(0)} + E_1^{(1)} + E_1^{(2)} = \langle 1|H_0|1\rangle + \langle 1|V|1\rangle + \sum_{i=\{0,2\}} \frac{|\langle i|V|1\rangle|^2}{E_1^{(0)} - E_i} = -\frac{J_x+J_y}{2} - \frac{\delta_x^2}{2J_y} - \frac{\delta_y^2}{2J_x}, \tag{3.10}$$

$$E_2 = E_2^{(0)} + E_2^{(1)} + E_2^{(2)} = \langle 2|H_0|2\rangle + \langle 2|V|2\rangle + \sum_{i=\{0,1\}} \frac{|\langle i|V|2\rangle|^2}{E_2^{(0)} - E_i} = -\frac{J_y}{2} + \frac{\delta_y^2}{2J_x}. \tag{3.11}$$

$|S_{12}T_{34}^-\rangle = \frac{1}{\sqrt{2}}(|0\rangle + |1\rangle)$ and $|T_{12}^-S_{34}\rangle = \frac{1}{\sqrt{2}}(|1\rangle - |0\rangle)$. Thus, we infer that f_{ST} corresponds to the energy difference:

$$f_{ST} = \frac{E_0 - E_1}{h} = \frac{J_y}{2h} + \frac{\delta_x^2}{J_y h} + \frac{\delta_y^2}{2J_x h}. \tag{3.12}$$

Equation (3.12) shows that the S-T^- oscillation frequency minimum allows to extract the exchange value J_y.

According to these calculations, when the barrier gate voltages are varied by δV_x and δV_y at fixed evolution time t, the constant ST probability lines should draw ellipses centered at the voltages where $J_{12} = J_{34}$ and $J_{14} = J_{23}$. One can use this property to equalize the exchange couplings.

The Hamiltonian H'_T can also be diagonalized in the degenerate case $J_x = J_y = J$. The eigen energies read as:

$$\begin{cases} E_g = \frac{-3J - \sqrt{J^2 + 4\delta_x^2 + 4\delta_y^2}}{4} \approx -J - \frac{\delta_x^2 + \delta_y^2}{2J} \\ E_{e_1} = -\frac{J}{2} \\ E_{e_2} = \frac{-3J + \sqrt{J^2 + 4\delta_x^2 + 4\delta_y^2}}{4} \approx -\frac{J}{2} + \frac{\delta_x^2 + \delta_y^2}{2J} \end{cases} \tag{3.13}$$

$$\begin{cases} |g\rangle = \frac{2\delta_x|0\rangle+(J+\sqrt{J^2+4\delta_x^2+4\delta_y^2})|1\rangle+2\delta_y|2\rangle}{N_g} \approx |1\rangle \\ |e_1\rangle = \frac{-\delta_y|0\rangle+\delta_x|2\rangle}{N_{e_1}} \approx \frac{\delta_y}{\sqrt{\delta_x^2+\delta_y^2}}|0\rangle + \frac{\delta_x}{\sqrt{\delta_x^2+\delta_y^2}}|2\rangle \\ |e_2\rangle = \frac{2\delta_x|0\rangle+(J-\sqrt{J^2+4\delta_x^2+4\delta_y^2})|1\rangle+2\delta_y|2\rangle}{N_{e_2}} \approx -\frac{\delta_x}{\sqrt{\delta_x^2+\delta_y^2}}|0\rangle + \frac{\delta_y}{\sqrt{\delta_x^2+\delta_y^2}}|2\rangle \end{cases} \tag{3.14}$$

The initialized $|S_{12}T_{34}^-\rangle$ state can be decomposed as:

$$|S_{12}T_{34}^-\rangle = \frac{1}{\sqrt{2}}|g\rangle + \frac{1}{\sqrt{2}}\left(\frac{\delta_y}{\sqrt{\delta_x^2+\delta_y^2}}|e_1\rangle - \frac{\delta_x}{\sqrt{\delta_x^2+\delta_y^2}}|e_2\rangle\right). \tag{3.15}$$

As the system evolves, the measured singlet-triplet probability is:

$$\begin{aligned} P_{ST}(t) &= |\langle S_{12}T_{34}^-|e^{-iH_T' t/\hbar}|S_{12}T_{34}^-\rangle|^2 = |\frac{1}{2}e^{-i\omega_g t} + \frac{1}{2}\frac{\delta_y^2}{\delta_x^2+\delta_y^2}e^{-i\omega_{e_1} t} + \frac{1}{2}\frac{\delta_x^2}{\delta_x^2+\delta_y^2}e^{-i\omega_{e_2} t}|^2 \\ &= \frac{\delta_x^4+\delta_x^2\delta_y^2+\delta_y^4}{2(\delta_x^2+\delta_y^2)^2} + \frac{\delta_x^2}{2(\delta_x^2+\delta_y^2)}\cos\left((\omega_{e_2}-\omega_g)t\right) + \frac{\delta_y^2}{2(\delta_x^2+\delta_y^2)}\cos\left((\omega_{e_1}-\omega_g)t\right) + \frac{\delta_x^2\delta_y^2}{2(\delta_x^2+\delta_y^2)^2}\cos\left((\omega_{e_2}-\omega_{e_1})t\right) \\ &= \frac{\delta_x^4+\delta_x^2\delta_y^2+\delta_y^4}{2(\delta_x^2+\delta_y^2)^2} + \frac{1}{2}\cos\left(\frac{\omega_{e_1}+\omega_{e_2}-2\omega_g}{2}t\right)\cos\left(\frac{\omega_{e_1}-\omega_{e_2}}{2}t\right) + \frac{\delta_x^2-\delta_y^2}{2(\delta_x^2+\delta_y^2)}\sin\left(\frac{\omega_{e_1}+\omega_{e_2}-2\omega_g}{2}t\right)\sin\left(\frac{\omega_{e_1}-\omega_{e_2}}{2}t\right) \\ &\quad + \frac{\delta_x^2\delta_y^2}{2(\delta_x^2+\delta_y^2)^2}\cos\left((\omega_{e_2}-\omega_{e_1})t\right). \end{aligned} \tag{3.16}$$

According to equation (3.16), in two special cases (1) when $\delta_x = 0$, f_{ST} equals to $\frac{J}{2\hbar} + \frac{\delta_y^2}{2J\hbar}$ and (2) when $\delta_y = 0$, f_{ST} equals to $\frac{J}{2\hbar} + \frac{\delta_x^2}{J\hbar}$. In the general case $\delta_{x,y} \neq 0$, P_{ST} oscillates with three frequencies where two of them are close to each other resulting in a beating. More specifically, P_{ST} oscillates with a fast frequency $\frac{\omega_{e_1}+\omega_{e_2}-2\omega_g}{2} = \frac{J}{2\hbar} + \frac{3}{4}\frac{\delta_x^2}{J\hbar}$ while the amplitude is modulated at a lower frequency $\frac{\omega_{e_1}-\omega_{e_2}}{2} = \frac{\delta_x^2+\delta_y^2}{4J\hbar}$. Therefore, as long as $\delta_{x,y}$ remains sufficiently small, such that $\frac{\delta_x^2+\delta_y^2}{2J\hbar}t \lesssim \pi$, a frequency minimum still appears when $\delta_{x,y} = 0$ which allows us to extract $J_{x,y}$.

COMPARISON WITH EXPERIMENTS

We perform experiment where we study how four-spin singlet-triplet oscillations evolve when δV_x, δV_y and the dwell time t_D are varied. Fig. 3.8-3.10 show the results of these experiments for different operation points that we compare with numerical simulations of time evolution using the Hamiltonian H_T.

To perform the simulations, the exchange couplings away from $\delta V_{x,y} = 0$ are modelled using exponential models $J_{34/12} = \frac{J_x}{2}\exp(\pm\kappa\delta V_x)$ and $J_{14/23} = \frac{J_y}{2}\exp(\pm\kappa\delta V_y)$ [16]. The factor $\kappa = 0.059$ mV^{-1} is extracted from the frequency of isolated two-spin S-T^- oscillations whereas the $J_{x,y}$ values are taken from the frequency minimum in the corresponding sub-figures c-f. The exchange values here are within 10 % of deviation compared to the exchanges displayed in Fig. 3.3.f.

Fig. 3.8, 3.9, and 3.10 show three sets of data/simulations corresponding to experiments where the barrier gate voltages are varied by $\delta V_{x,y}$ around the points $\{vB^0_{12} + \delta V'_x, vB^0_{23} - \beta\delta V'_x, vB^0_{34} + \delta V'_x, vB^0_{14} - \beta\delta V'_x\}$ with $\delta V'_x$ =20, 0, -20 mV and $vB_0 = \{vB^0_{12}, vB^0_{34}, vB^0_{23}, vB^0_{14}\} = \{16, -10.5, 0, 9.5\}$ mV (vB_0 is the predetermined set of voltages where exchange couplings are approximately equals mentioned in the main text). These $\delta V'_x$ values correspond approximately to the center and the limits of the range spanned in Fig. 3.3.e. In the three cases, the data and the simulations show an overall remarkably good agreement.

Fig. 3.8.a-b, 3.9.a-b and 3.10.a-b show the results of these measurements consisting in varying δV_x, δV_y at fixed t_D and the corresponding simulations. We observe that constant probability lines form a network of stripes drawing ellipses centered around $\delta V_{x,y} \simeq 0$ mV in agreement with the above discussion.

Fig. 3.8.c-f, 3.9.c-f and 3.10.c-f display the time evolution of four-spin singlet-triplet probabilities measured while varying either δV_x or δV_y around the centers of these ellipses. It confirms that the frequency minimum is reached when $\delta V_{x,y} \simeq 0$ mV i.e. at the center of the ellipse.

In these three configurations, we clearly have $J_{12} \simeq J_{34}$ and $J_{14} \simeq J_{23}$ for $\delta V_{x,y} \simeq 0$ mV. Similarly for $\delta V'_x = 26$ mV, singlet-triplet probabilities also draw an ellipse centered on $\delta V_{x,y} \simeq 0$ mV (Fig. 3.11). Extrapolating these results, we assume that these equalities remain valid over the full range of voltage -20 mV $\leqslant \delta V'_x \leqslant 26$ mV spanned in Fig. 3.3.e and thus that the frequency of four-spin ST oscillations f_{ST} directly gives $J_{x,y}/2$.

We note that the ellipses are tilted and even distorted especially when J_x is large. It could indicate a cross-talk between vertical and horizontal virtual barrier gates but also a deviation from the equations derived above which are valid only for small variations of exchange couplings.

In Fig. 3.9.b (initialization/readout in y direction), we also remark that both the measurements and the simulation show a complex pattern when voltages are varied away from the origin. This pattern appears less clearly in the measurement data of Fig. 3.9.a (initialization/readout in x direction).

Likewise, we notice beating patterns in Fig. 3.8.e and 3.10.d. They result from the third level, $\frac{1}{\sqrt{2}}(|T^0_{12}T^-_{34}\rangle - |T^-_{12}T^0_{34}\rangle)$, that is not completely decoupled and has an overlap with the initial state.

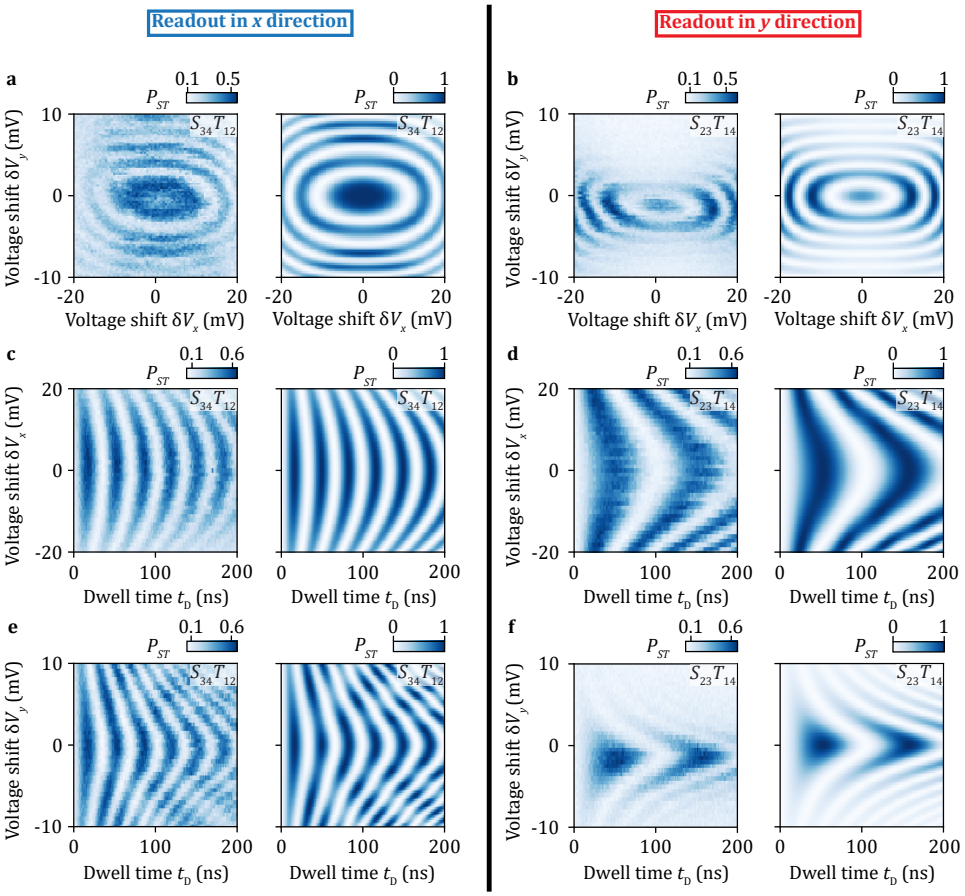

Figure 3.8: **Additional measurement data and numerical simulations of four-spin coherent singlet-triplet oscillations at low J_x. a**, **b**, Probabilities $P_{S_{34}T_{12}}$ and $P_{S_{23}T_{14}}$ as functions of barrier gate voltage variations $\delta V_{x,y}$ at fixed evolution time $t_D = 180$ ns. **c**, **d**, Oscillations in $P_{S_{34}T_{12}}$ and $P_{S_{23}T_{14}}$ as functions of gate voltage variation δV_x. **e**, **f**, Oscillations in $P_{S_{34}T_{12}}$ and $P_{S_{23}T_{14}}$ as functions of virtual gate voltage variation δV_y. The right panels are numerical simulations based on the Hamiltonian H_T. The virtual barrier voltages are varied around the operation point $\{36, -14.1, 20, 5.9\}$ mV which corresponds to the point $\delta V_x' = 20$ mV in Fig. 3.3.e.

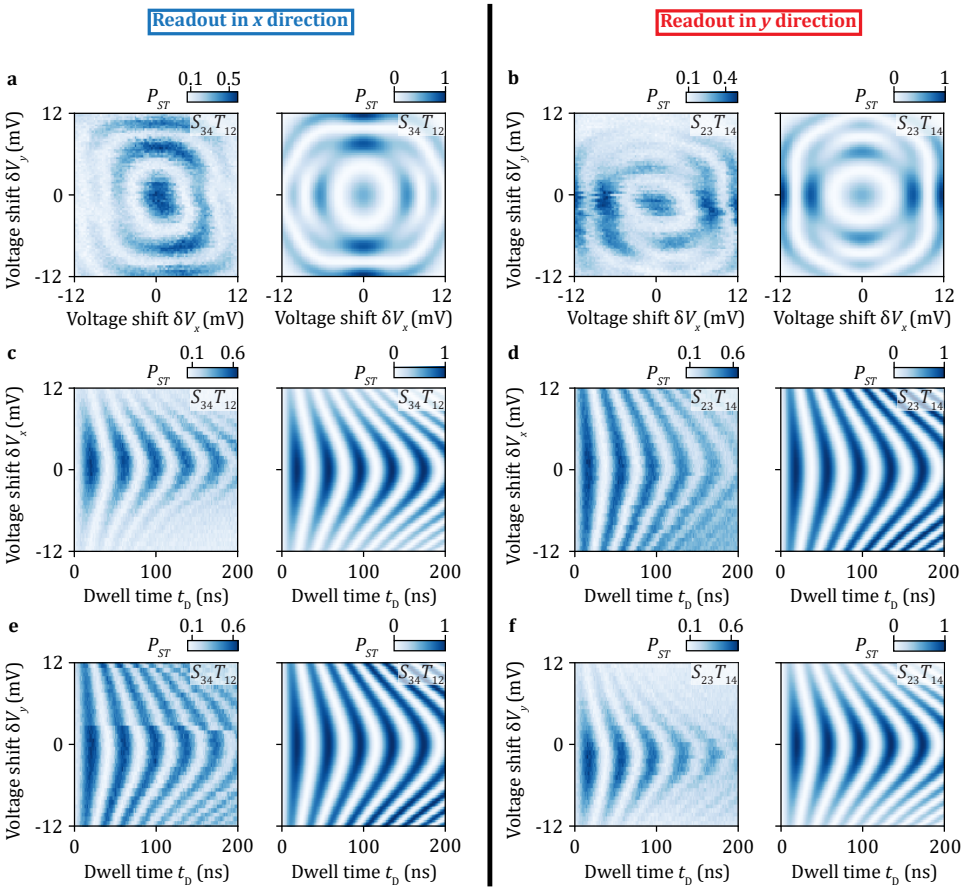

Figure 3.9: **Additional measurement data and numerical simulations of four-spin coherent singlet-triplet oscillations at medium J_x. a**, **b**, Probabilities $P_{S_{34}T_{12}}$ and $P_{S_{23}T_{14}}$ as functions of virtual barrier voltage variations $\delta V_{x,y}$ with a fixed evolution time $t_D = 105$ ns. **c**, **d**, Oscillations in $P_{S_{34}T_{12}}$ and $P_{S_{23}T_{14}}$ as functions of gate voltage variation δV_x. **e**, **f**, Oscillations in $P_{S_{34}T_{12}}$ and $P_{S_{23}T_{14}}$ as functions of gate voltage variations δV_y. The right panels are numerical simulations based on the Hamiltonian H_T. The virtual barrier voltages are varied around $vB_0 = \{16, -10.5, 0, 9.5\}$ mV which corresponds to the point $\delta V_x' = 0$ mV in Fig. 3.3.e.

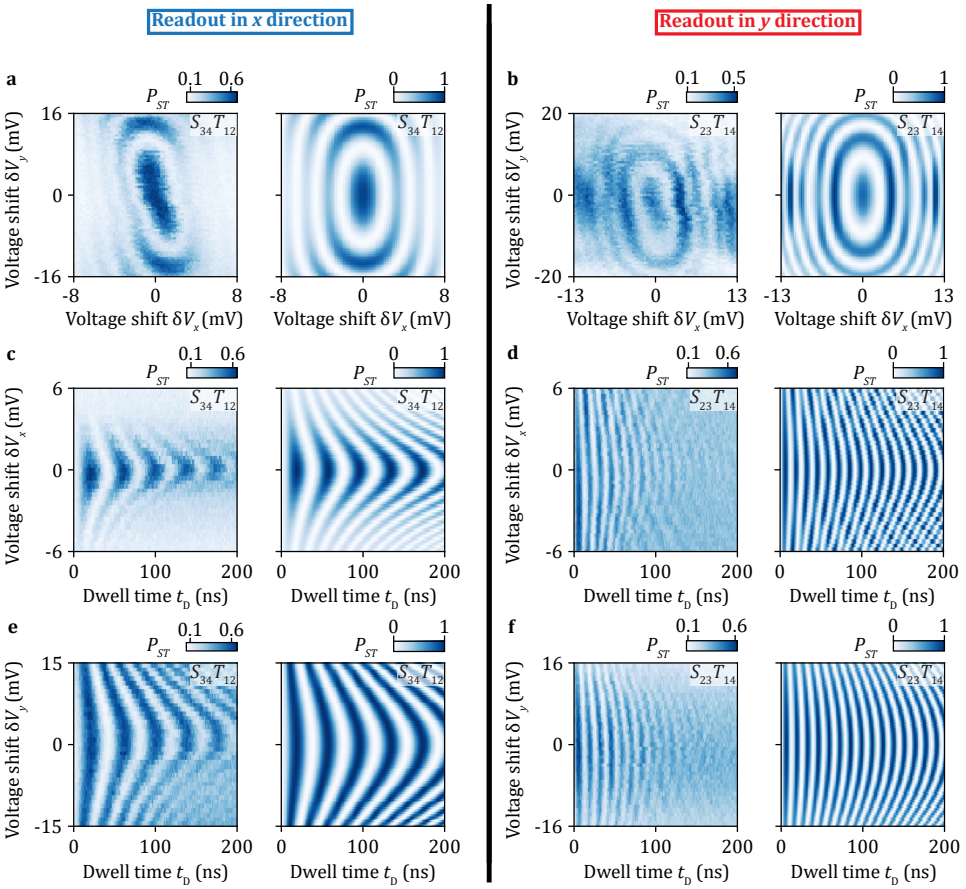

Figure 3.10: **Additional measurement data and numerical simulations of four-spin coherent singlet-triplet oscillations at large J_x. a**, **b**, Probabilities $P_{S_{34}T_{12}}$ and $P_{S_{23}T_{14}}$ as functions of virtual barrier voltage variations $\delta V_{x,y}$ with a fixed evolution time $t_D = 60$ ns. **c**, **d**, Oscillations in $P_{S_{34}T_{12}}$ and $P_{S_{23}T_{14}}$ probabilities as functions of gate voltage variation δV_x. **e, f**, Oscillations in $P_{S_{34}T_{12}}$ and $P_{S_{23}T_{14}}$ as functions of gate voltage variation δV_y. The panels on the right are numerical simulation based on the Hamiltonian H_T. The virtual barrier voltages are varied around $\{-4, -6.9, -20, 13.1\}$ mV, which corresponds to the point $\delta V_x' = -20$ mV (outside the range spanned in Fig. 3.3.e).

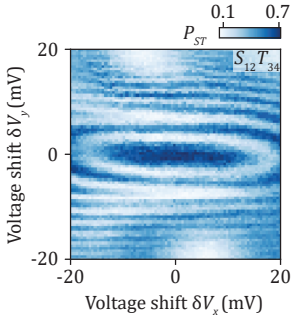

Figure 3.11: **Signature of equal exchange couplings.** Probability $P_{S_{12}T_{34}}$ as a function of the voltage variation $\delta V_{x,y}$ at fixed t_D = 113 ns. The barrier gate voltages are varied around $\{42,-15.18,26,4.82\}$ mV which corresponds to the extreme point δV_x^I = 26 mV in Fig. 3.3.e. The ellipse drawn by constant probability lines is centered around $\delta V_{x,y} \simeq 0$ indicating that at this point $J_{12} \simeq J_{34}$ and $J_{23} \simeq J_{14}$.

UNCERTAINTY ON THE EXCHANGE COUPLING VALUES

Our method to determine the barrier gate voltages required to have $J_{12} = J_{34}$ and $J_{23} = J_{14}$ leads to some uncertainties on the values of the exchange couplings. They originate from the uncertainty on the determination of the center of ellipse drawn by the oscillations when varying $\delta V_{x,y}$ at fixed t_D (see Fig. 3.8 to 3.11). We estimate that the center's position can be determined with a ±2 mV precision. Small drifts between experiments also typically lead to such uncertainties. Using the exponential models described above, we can then translate this uncertainty into an uncertainty on the exchange values at a given set of barrier gate voltages.

To express it, we assume that at $\delta V_{x,y} = 0$, the parallel exchange couplings are actually imbalance ($J_{12} \neq J_{34}$ and $J_{14} \neq J_{23}$). We note $\delta V_{x,y}^0$ the voltage shifts required to reach the balance $J_{12} = J_{34} = J_x^0/2$ and $J_{14} = J_{23} = J_y^0/2$. Then, as $\kappa|\delta V_{x,y} - \delta V_{x,y}^0| \lesssim 0.1$, we can write the differences of exchange couplings as:

$$\begin{cases} \delta_x = J_{12} - J_{34} = \frac{J_x^0}{2}\exp(-\kappa(\delta V_x - \delta V_x^0)) - \frac{J_x^0}{2}\exp(\kappa(\delta V_x - \delta V_x^0)) \simeq J_x^0\kappa(\delta V_x^0 - \delta V_x) \\ \delta_y = J_{23} - J_{14} = \frac{J_y^0}{2}\exp(-\kappa(\delta V_y - \delta V_y^0)) - \frac{J_y^0}{2}\exp(\kappa(\delta V_y - \delta V_y^0)) \simeq J_y^0\kappa(\delta V_y^0 - \delta V_y) \end{cases} . \tag{3.17}$$

Likewise, the sums of the exchange couplings are given by:

$$\begin{cases} J_x = J_{12} + J_{34} \simeq J_x^0(1 + \frac{\kappa^2(\delta V_x - \delta V_x^0)^2}{2}) \\ J_y = J_{14} + J_{24} \simeq J_y^0(1 + \frac{\kappa^2(\delta V_y - \delta V_y^0)^2}{2}) \end{cases} . \tag{3.18}$$

Using equation (3.12), the errors on the exchange couplings extracted are then given by:

$$\begin{cases} \sigma_{J_y} = 2f_{ST} - J_y/h = 2\frac{(J_x^0)^2}{J_y^0 h}\kappa^2(\delta V_x - \delta V_x^0)^2 + \frac{(J_y^0)^2}{J_x^0 h}\kappa^2(\delta V_y - \delta V_y^0)^2 \\ \sigma_{J_x} = 2\frac{(J_y^0)^2}{J_x^0 h}\kappa^2(\delta V_y - \delta V_y^0)^2 + \frac{(J_x^0)^2}{J_y^0 h}\kappa^2(\delta V_x - \delta V_x^0)^2 \end{cases} . \tag{3.19}$$

Notably, the uncertainty on the position of the center of the ellipse can only lead to an overestimation of the exchange values. The latter is about 3 MHz in average for the data displayed in Fig. 3.3.f. Additionally, fitting the four-spin singlet-triplet oscillations also leads to uncertainty on the value of f_{ST} from which the exchanges are inferred. We thus assume that the precision on the determination of the exchange couplings is set by the maximum of the two above uncertainties and we use it to draw the error bars in Fig. 3.3.f. Typically the former uncertainty is much larger than the uncertainty on the frequency fit.

The errors bars on the predicted singlet-singlet oscillation frequency f_{SS} (Fig. 3.4.e), visibilities $\mathcal{V}_{x,y}$ (Fig. 3.4.f) and on the singlet-singlet probabilities in the RVB ground state (Fig. 3.5.c) are then drawn by computing the minimum and maximum values of these quantities in the exchange coupling ranges fixed by the uncertainties on $J_{x,y}$.

3.7. LIMITS OF THE THEORETICAL DESCRIPTIONS

Up to now, we assumed that the system dynamics is only governed by the Heisenberg Hamiltonian. Yet, the effective Hamiltonian H_{tot} of the system contains other terms. When each quantum dot contains one hole, H_{tot} can be written as:

$$H_{\text{tot}} = H_J + H_Z + H_{SO} + H_{hp}, \tag{3.20}$$

where $H_J = \sum_{<i,j>} J_{ij}(\vec{S}_i \cdot \vec{S}_j - \frac{1}{4})$, $H_Z = \sum_i g_i \mu_B B$, H_{SO} and H_{hp} are respectively the Heisenberg, Zeeman, spin-orbit and hyperfine terms. The physics of RVB states is solely determined by the Heisenberg term H_J that conserves the total spin and the spin projection whereas the other terms couple states of different spin subspaces. To prevent these couplings, we operate the device with few milli-Teslas in-plane magnetic fields ensuring that the exchange couplings are the largest energy scales. In that case, one can assume that $H_{\text{tot}} \simeq H_J$ and derive analytical formulas describing the system dynamics. Here we justify further this approximation by quantifying the magnitude of the other terms.

HYPERFINE INTERACTION

We first focus on the effects of hyperfine interaction. It results in a Zeeman-like term that randomly varies in time and couple different total spin subspaces. In ref. [27], the authors evaluated the Zeeman energy noise in germanium ST qubits placed in a 1 mT perpendicular magnetic field, supposedly the most unfavorable direction regarding hyperfine interaction [56, 57]. They found $\delta E_Z < 2$ neV or $\delta E_Z/h < 0.48$ MHz [44]. This suggests that the hyperfine coupling can be safely discarded in the theoretical description.

ZEEMAN GRADIENTS

To express the Zeeman term H_Z, we need a full basis of the 16×16 Hilbert space. A convenient choice of basis for our theoretical description consists in using the basis $\psi_{1111} = \{0_S, 1_S, 0_{T^-}, 1_{T^-}, 2_{T^-}, 0_{T^0}, 1_{T^0}, 2_{T^0}, 0_{T^+}, 1_{T^+}, 2_{T^+}, Q^-, Q^0, Q^+, Q^{--}, Q^{++}\}$ that decomposes the Hilbert space into the different total spin S subspaces and that also decomposes these subspaces into smaller subspaces with different spin projections m_S [17]. The different states that compose the ψ_{1111} basis are expressed in Table 3.2. Note that the states

$\{0_S, 1_S\}$ and $\{0_{T^-}, 1_{T^-}, 2_{T^-}\}$ correspond to the basis-states of the global singlet and $m_S = -1$ triplet subspaces used above.

(S, m_S)	States
(0,0)	$\{0_S, 1_S\} = \{\|S_{12}S_{34}\rangle, \frac{1}{\sqrt{3}}(\|T^+_{12}T^-_{34}\rangle + \|T^-_{12}T^+_{34}\rangle - \|T^0_{12}T^0_{34}\rangle)\}$
(-1,1)	$\{0_{T^-}, 1_{T^-}, 2_{T^-}\} = \{\|S_{12}T^-_{34}\rangle, \|T^-_{12}S_{34}\rangle, \frac{1}{\sqrt{2}}(\|T^0_{12}T^-_{34}\rangle - \|T^-_{12}T^0_{34}\rangle)\}$
(0,1)	$\{0_{T^0}, 1_{T^0}, 2_{T^0}\} = \{\|S_{12}T^0_{34}\rangle, \|T^0_{12}S_{34}\rangle, \frac{1}{\sqrt{2}}(\|T^+_{12}T^-_{34}\rangle - \|T^-_{12}T^+_{34}\rangle)\}$
(1,1)	$\{0_{T^+}, 1_{T^+}, 2_{T^+}\} = \{\|S_{12}T^+_{34}\rangle, \|T^+_{12}S_{34}\rangle, \frac{1}{\sqrt{2}}(\|T^0_{12}T^+_{34}\rangle - \|T^+_{12}T^0_{34}\rangle)\}$
(-1,2)	$\{Q^-\} = \frac{1}{\sqrt{2}}(\|T^0_{12}T^-_{34}\rangle + \|T^-_{12}T^0_{34}\rangle)$
(0,2)	$\{Q^0\} = \frac{1}{\sqrt{6}}(\|T^+_{12}T^-_{34}\rangle + \|T^-_{12}T^+_{34}\rangle + 2\|T^0_{12}T^0_{34}\rangle)$
(1,2)	$\{Q^+\} = \frac{1}{\sqrt{2}}(\|T^0_{12}T^+_{34}\rangle + \|T^+_{12}T^0_{34}\rangle)$
(-2,2)	$\{Q^{--}\} = \|T^-_{12}T^-_{34}\rangle$
(2,2)	$\{Q^{++}\} = \|T^+_{12}T^+_{34}\rangle$

Table 3.2: **16 basis-states used to describe the effect of Zeeman gradients.** Each line corresponds to a subspace with given total spin S and a given spin projection m_S. The states that form the basis of each subspace are expressed in terms of two-spin singlet and triplet states. The Heisenberg Hamiltonian does not couple the different subspaces.

In this basis, the Zeeman Hamiltonian can be expressed as:

$$H_{\text{Zeeman}} = \mu_B B \begin{pmatrix}
0 & 0 & 0 & 0 & 0 & \frac{g^-_{34}}{2} & \frac{g^-_{12}}{2} & 0 & 0 & 0 & 0 & 0 & 0 & 0 & 0 & 0 \\
0 & 0 & 0 & 0 & 0 & \frac{-g^-_{12}}{2\sqrt{3}} & \frac{-g^-_{34}}{2\sqrt{3}} & \frac{g^-}{\sqrt{6}} & 0 & 0 & 0 & 0 & 0 & 0 & 0 & 0 \\
\hline
0 & 0 & \frac{-g^+_{34}}{2} & 0 & \frac{g^-_{12}}{2\sqrt{2}} & 0 & 0 & 0 & 0 & 0 & 0 & \frac{g^-_{12}}{2\sqrt{2}} & 0 & 0 & 0 & 0 \\
0 & 0 & 0 & \frac{-g^+_{12}}{2} & \frac{-g^-_{34}}{2\sqrt{2}} & 0 & 0 & 0 & 0 & 0 & 0 & \frac{g^-_{34}}{2\sqrt{2}} & 0 & 0 & 0 & 0 \\
0 & 0 & \frac{g^-_{12}}{2\sqrt{2}} & \frac{-g^-_{34}}{2\sqrt{2}} & \frac{-g^+}{4} & 0 & 0 & 0 & 0 & 0 & 0 & \frac{g^-}{4} & 0 & 0 & 0 & 0 \\
\hline
\frac{g^-_{34}}{2} & \frac{-g^-_{12}}{2\sqrt{3}} & 0 & 0 & 0 & 0 & 0 & 0 & 0 & 0 & 0 & 0 & \frac{g^-_{12}}{\sqrt{6}} & 0 & 0 & 0 \\
\frac{g^-_{12}}{2} & \frac{-g^-_{34}}{2\sqrt{3}} & 0 & 0 & 0 & 0 & 0 & 0 & 0 & 0 & 0 & 0 & \frac{g^-_{34}}{\sqrt{6}} & 0 & 0 & 0 \\
0 & \frac{g^-}{\sqrt{6}} & 0 & 0 & 0 & 0 & 0 & 0 & 0 & 0 & 0 & 0 & \frac{g^-}{2\sqrt{3}} & 0 & 0 & 0 \\
\hline
0 & 0 & 0 & 0 & 0 & 0 & 0 & 0 & \frac{g^+_{34}}{2} & 0 & \frac{g^-_{12}}{2\sqrt{2}} & 0 & 0 & \frac{g^-_{12}}{2\sqrt{2}} & 0 & 0 \\
0 & 0 & 0 & 0 & 0 & 0 & 0 & 0 & 0 & \frac{g^+_{12}}{2} & \frac{-g^-_{34}}{2\sqrt{2}} & 0 & 0 & \frac{g^-_{34}}{2\sqrt{2}} & 0 & 0 \\
0 & 0 & 0 & 0 & 0 & 0 & 0 & 0 & \frac{g^-_{12}}{2\sqrt{2}} & \frac{-g^-_{34}}{2\sqrt{2}} & \frac{g^+}{4} & 0 & 0 & \frac{-g^-}{4} & 0 & 0 \\
\hline
0 & 0 & \frac{g^-_{12}}{2\sqrt{2}} & \frac{g^-_{34}}{2\sqrt{2}} & \frac{g^-}{4} & 0 & 0 & 0 & 0 & 0 & 0 & \frac{-g^+}{4} & 0 & 0 & 0 & 0 \\
0 & 0 & 0 & 0 & 0 & \frac{g^-_{12}}{\sqrt{6}} & \frac{g^-_{34}}{\sqrt{6}} & \frac{g^-}{2\sqrt{3}} & 0 & 0 & 0 & 0 & 0 & 0 & 0 & 0 \\
0 & 0 & 0 & 0 & 0 & 0 & 0 & 0 & \frac{g^-_{12}}{2\sqrt{2}} & \frac{g^-_{34}}{2\sqrt{2}} & \frac{-g^-}{4} & 0 & 0 & \frac{g^+}{4} & 0 & 0 \\
0 & 0 & 0 & 0 & 0 & 0 & 0 & 0 & 0 & 0 & 0 & 0 & 0 & 0 & \frac{-g^+}{2} & 0 \\
0 & 0 & 0 & 0 & 0 & 0 & 0 & 0 & 0 & 0 & 0 & 0 & 0 & 0 & 0 & \frac{g^+}{2}
\end{pmatrix}, \tag{3.21}$$

where $g^-_{ij} = g_i - g_j$, $g^\pm = g_1 + g_2 \pm g_3 \pm g_4$. We observe that the Zeeman terms lead to leakage outside from the global singlet subspace $\{0_S, 1_S\}$ and from $m_S = -1$ triplet subspace $\{0_{T^-}, 1_{T^-}, 2_{T^-}\}$ which are relevant for our experiments. It can lead to discrepancies between experimental results and theoretical expectations derived only from the Heisenberg Hamiltonian. In our system, we have $0.15 < g_i < 0.3$. Therefore the magnitudes of the couplings induced by the Zeeman fields remain typically of the order of a

few MHz at 1 mT and thus are small compared to the exchange couplings J_{ij}. That is why we can neglect them in our theoretical description.

As a side note, we mention that this expression assumes that the spin quantization axis of all the quantum dots are the same. In practise, for an in-plane magnetic field, the spin quantization axis in the laboratory frame can be different for the different quantum dots due to the variations in the local electrostatic potentials. Yet, we can always redefine with a local spin basis ensuring that all quantization axis are aligned providing a renormalization of the spin-conserving and spin-non-conserving tunnel couplings.

SPIN-ORBIT TERMS

In absence of spin-orbit interaction, a double quantum dot system can be described by the following Hamiltonian [58]:

$$H_{\mathrm{DQD}} = \epsilon\,|S_{20}\rangle\langle S_{20}| + \sqrt{2}t_{\mathrm{c}}\,(|S_{20}\rangle\langle S_{11}| + |S_{11}\rangle\langle S_{20}|) + H_{\mathrm{Z}}. \tag{3.22}$$

In this expression, H_{Z} is the Zeeman term, ϵ the energy detuning (taken as zero at (0,2) - (1,1) charge transition), t_{c} the spin-conserving tunnel coupling whereas $|S_{20}\rangle$ and $|S_{11}\rangle$ are respectively the singlet (2,0) and (1,1) states.

To take into account the spin-orbit effects, one can allow for spin-non-conserving tunneling processes to occur [58]. This can be model by adding another term H_{SO} to the previous Hamiltonian. It writes as :

$$H_{\mathrm{SO}} = \mathrm{i}\sqrt{2}t_z\,|T^0\rangle\langle S_{20}| - \sum_{\pm}(t_y \pm \mathrm{i}t_x)\,|T^{\pm}\rangle\langle S_{20}| + \mathrm{h.c.}, \tag{3.23}$$

where $t_{\mathrm{SO}} = (t_x, t_y, t_z)$ is the spin-non-conserving tunneling term due to spin-orbit coupling and $|T^0\rangle$,$|T^-\rangle$ and $|T^+\rangle$ are the different triplet (1,1) states. The main effect of the spin-orbit interaction is thus to couple the singlet states to the triplet states. Similarly to the Zeeman gradients, the spin-orbit coupling leads to leakage outside the total singlet and $m_S = -1$ triplet subspaces.

In our experiments we operate in the regime $t_{\mathrm{c}} < 10$ GHz and $\epsilon \sim 300$ GHz, which allows us to treat the effect of the higher excited charge state $|S_{20}\rangle$ using the second order quasi-degenerate perturbation theory [59]. The resulting energy change of the state $|S_{11}\rangle$ due to the spin-conserving coupling to the $|S_{20}\rangle$ is $-\frac{2t_{\mathrm{c}}^2}{\epsilon}$. This change of energy corresponds to the exchange coupling J. Alternatively, the effective couplings between the $|S_{11}\rangle$ state and triplet states mediated by the virtual state $|S_{20}\rangle$ are $-\frac{2\mathrm{i}t_{\mathrm{c}}t_z}{\epsilon}$ for the coupling between the $|T^0\rangle$ and $|S_{11}\rangle$ states, and $-\frac{\sqrt{2}t_{\mathrm{c}}(t_y \pm \mathrm{i}t_x)}{\epsilon}$ for the coupling between the $|T^{\pm}\rangle$ and$|S_{11}\rangle$ states. Therefore, the relative amplitude of the spin-orbit couplings over the exchange couplings is given by $t_{\mathrm{SO}}/t_{\mathrm{c}}$. In ref. [44], a ratio $t_{\mathrm{SO}}/t_{\mathrm{c}}$ of 0.034 was found in germanium double quantum dots. Although the exact values of t_{SO} and t_{c} depend on the details of the electrostatics, we still expect the ratio $t_{\mathrm{SO}}/t_{\mathrm{c}}$ to remain small in our system and thus we also expect that the spin-orbit terms have a limited impact on the dynamics of the system. This is in agreement with the measured leakage features and Fermi-Hubbard model simulations presented in Supplementary Note 7 [40]. We observe that the probability of leakage fluctuates slower than the four-spin singlet-singlet oscillations or singlet-triplet oscillations, and the magnitude is in general below 0.2 if it is away

from the point $J_x \approx J_y$ (Supplementary Figure 9, Supplementary Figure 10 and Supplementary Figure 12 to Supplementary Figure 15 [40]).

DIAGONAL EXCHANGE COUPLINGS

We have also neglected the impact of diagonal exchange couplings J_{13} and J_{24} in our system. This assumption is based on different arguments. First, from the square geometry of our device, we expect that the spin-conserving tunnel couplings t_c between Q_1 and Q_3 and between Q_2 and Q_4 are much smaller than the couplings between adjacent quantum dots due the larger distance between quantum dots. Considering that for, a double quantum dot, the exchange coupling is given by $J = \sqrt{\epsilon^2/4 + 2t_c^2} - \epsilon/2 \simeq \frac{2t_c^2}{\epsilon}$ (limit $\frac{t_c}{\epsilon} \ll 1$), one can expect a significant reduction of the exchange couplings along the diagonals. Further, for four-spin experiments, the operation point O is chosen far from the center of the (1,1,1,1) charge region, as shown in Supplementary Figure 3 [40]. It ensures that the double well potentials of Q_1Q_2, Q_2Q_3, Q_3Q_4 and Q_4Q_1 pairs are all asymmetric and it allows to induce a finite exchange couplings between spins in adjacent quantum dots. At this point, the quantum dots' energy levels corresponding to different charge configurations are positioned with respect to each other as depicted in Fig. 3.12. In this configuration, it is likely that $\epsilon_{13}, \epsilon_{24} > \epsilon_{12}, \epsilon_{23}, \epsilon_{34}, \epsilon_{41}$ suggesting again that the diagonal exchange couplings are reduced compared to the vertical and horizontal ones.

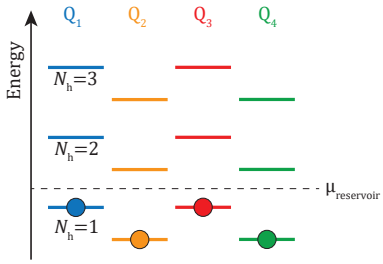

Figure 3.12: **Sketch of the quantum dot energy levels at the operation point O.** The chemical potentials of the quantum dots are tuned by controlling the plunger gate voltages to ensure charge occupations N_h of one hole per quantum dot while keeping a sufficiently large asymmetry of the double well potentials for adjacent quantum dots. The asymmetries of the potentials for Q_2Q_4 and Q_1Q_3 are comparatively smaller.

To get more understanding of the effects of diagonal exchange couplings on the measurements, we can compare theoretical predictions with and without diagonal exchange couplings.

Adding the diagonal exchange couplings, the Heisenberg Hamiltonian becomes:

$$H_J^* = \sum_{<i,j>} J_{ij}(\vec{S}_i \cdot \vec{S}_j - \frac{1}{4}) + J_{13}(\vec{S}_1 \cdot \vec{S}_3 - \frac{1}{4}) + J_{24}(\vec{S}_2 \cdot \vec{S}_4 - \frac{1}{4}), \tag{3.24}$$

and in the singlet subspace, with the $\{|0\rangle, |1\rangle\} = \{|S_{12}S_{34}\rangle, \frac{1}{\sqrt{3}}(|T_{12}^+ T_{34}^-\rangle + |T_{12}^- T_{34}^+\rangle - |T_{12}^0 T_{34}^0\rangle)\}$ basis, it can be written as:

$$H_S^* = \begin{pmatrix} -J_x - \frac{J_y+J_D}{4} & \frac{\sqrt{3}}{4}(J_y - J_D) \\ \frac{\sqrt{3}}{4}(J_y - J_D) & -\frac{3}{4}(J_y + J_D) \end{pmatrix}, \tag{3.25}$$

where $J_D = J_{13} + J_{24}$.

When $J_x = J_y = J$, the Hamiltonian becomes:

$$H_S^* = \begin{pmatrix} -\frac{5}{4}J - \frac{1}{4}J_D & \frac{\sqrt{3}}{4}(J - J_D) \\ \frac{\sqrt{3}}{4}(J - J_D) & -\frac{3}{4}(J + J_D) \end{pmatrix}. \tag{3.26}$$

This Hamiltonian can be diagonalized easily and the eigen energies are $E_1 = -\frac{3}{2}J$ and $E_2 = -\frac{1}{2}J - J_D$ (see also ref. [60, 61], note that there is a difference in the conventions for the overall energy offset). The associated eigenvectors are actually still the s-wave RVB state $|s\rangle = \frac{1}{\sqrt{3}}(|S_x\rangle - |S_y\rangle)$ and the d-wave RVB state $|d\rangle = |S_x\rangle + |S_y\rangle$ independently of the values of J and J_D (providing $J_D \neq J$). $|s\rangle$ is the ground state for $J > J_D$ which corresponds the regime investigated in our experiments according to the data displayed in Fig. 3.5.a-c. On the other hand, $|d\rangle$ is the ground state for $J < J_D$. In both cases, we expect to see resonating valence bond oscillations having a frequency given by $f_{SS}^* = \frac{1}{h}|E_1 - E_2| = \frac{1}{h}|J - J_D|$. More generally, f_{SS}^* is given by:

$$f_{SS}^* = \sqrt{J_x^2 + J_y^2 - J_x J_y + J_D^2 - J_D(J_x + J_y)} = \sqrt{(J_x - J_D)^2 + (J_y - J_D)^2 - (J_x - J_D)(J_y - J_D)}. \tag{3.27}$$

Therefore, in the limit where $J_{x,y} > J_D$, the presence of diagonal exchange leads to an effective reduction of the exchange couplings that drives the oscillations between singlet product states.

In the $m_S = -1$ global triplet subspace spanned by $\{|S_{12}T_{34}^-\rangle, |T_{12}^- S_{34}\rangle, \frac{1}{\sqrt{2}}(|T_{12}^0 T_{34}^-\rangle - |T_{12}^- T_{34}^0\rangle)\}$, the Hamiltonian can be written as:

$$\begin{aligned} H_T &= \begin{pmatrix} -J_{12} - \frac{J_{23}+J_{14}+J_{13}+J_{24}}{4} & \frac{-J_{23}-J_{14}+J_{13}+J_{24}}{4} & \frac{J_{23}-J_{14}-J_{13}+J_{24}}{2\sqrt{2}} \\ \frac{-J_{34}-J_{14}+J_{13}+J_{24}}{4} & -J_{34} - \frac{J_{23}+J_{14}+J_{13}+J_{24}}{4} & \frac{J_{23}-J_{14}-J_{13}+J_{24}}{2\sqrt{2}} \\ \frac{J_{23}-J_{14}-J_{13}+J_{24}}{2\sqrt{2}} & \frac{J_{23}-J_{14}-J_{13}+J_{24}}{2\sqrt{2}} & -\frac{J_{23}+J_{14}+J_{13}+J_{24}}{2} \end{pmatrix} \\ &= \begin{pmatrix} -\frac{J_x+\delta_x}{2} - \frac{J_y+J_D}{4} & -\frac{J_y-J_D}{4} & \frac{\delta_y+\delta_D}{2\sqrt{2}} \\ -\frac{J_y-J_D}{4} & -\frac{J_x-\delta_x}{2} - \frac{J_y+J_D}{4} & \frac{\delta_y+\delta_D}{2\sqrt{2}} \\ \frac{\delta_y+\delta_D}{2\sqrt{2}} & \frac{\delta_y+\delta_D}{2\sqrt{2}} & -\frac{J_y+J_D}{2} \end{pmatrix}, \end{aligned} \tag{3.28}$$

where $\delta_D = -J_{13} + J_{24}$.

Repeating the calculation of four-spin singlet-triplet oscillations in Section 3.6, we derive that for the initial state $|S_{12}T_{34}^-\rangle$, the minimum singlet-triplet oscillation frequency occurs when $\delta_x = \delta_y + \delta_D = 0$. Similarly, for the initial state $|S_{14}T_{23}^-\rangle$, the minimum frequency occurs when $\delta_x + \delta_D = \delta_y = 0$. The corresponding minimum oscillation frequencies are $f_{ST,\min}^{x(y)} = \frac{1}{2}(J_{y(x)} - J_D)$. Thus diagonal exchange may be one of the contributions to the small shift of frequency minimum $\delta V_{x,\min} - \delta V_{y,\min}$ observed in the experiments

shown in Fig. 3.8 to 3.10. We notice that the voltage shift between x and y direction readout $|\delta V_{x,\min} - \delta V_{y,\min}| < 2$ mV are small. Therefore we can assume that the measured frequency of four-spin singlet-triplet oscillations at every voltage shift $\delta V_x'$ in Fig. 3.3.e-f is approximately equal to the corresponding frequency minimum, $f_{ST}^{x(y)} \simeq f_{ST,\min}^{x(y)} = \frac{1}{2h}(J_{y(x)} - J_D)$, with an estimated frequency uncertainty described in Section 3.6. The singlet-singlet oscillation frequency derived from the Hamiltonian (3.25) can then be expressed as $f_{SS}^* = 2\sqrt{(f_{ST,\min}^y)^2 + (f_{ST,\min}^x)^2 - f_{ST,\min}^y f_{ST,\min}^x}$. Therefore, the method used to equalize parallel exchange couplings and tune them does not allow us to determine the magnitude of the diagonal exchange couplings.

To summarize, we expect that diagonal exchange couplings to have a very limited effects in the four-spin oscillation experiments but our measurements do not allow to estimated their values.

BIBLIOGRAPHY

[1] R. P. Feynman. “Simulating physics with computers”. In: Int. J. Theor. Phys. 21 (1982), pp. 467–488.

[2] Seth Lloyd. “Universal Quantum Simulators”. In: Science 273 (1996), pp. 1073–1078.

[3] D. S. Abrams and S. Lloyd. “Simulation of Many-Body Fermi Systems on a Universal Quantum Computer”. In: Phys. Rev. Lett. 79 (13 1997), pp. 2586–2589.

[4] Alán Aspuru-Guzik et al. “Simulated Quantum Computation of Molecular Energies”. In: Science 309.5741 (2005), pp. 1704–1707.

[5] Daniel Loss and David P. DiVincenzo. “Quantum computation with quantum dots”. In: Phys. Rev. A 57 (1 1998), pp. 120–126.

[6] L. M. K. Vandersypen et al. “Interfacing spin qubits in quantum dots and donors—hot, dense, and coherent”. In: npj Quantum Inf. 3 (2017), p. 34.

[7] E. Manousakis. “A Quantum-Dot Array as Model for Copper-Oxide Superconductors: A Dedicated Quantum Simulator for the Many-Fermion Problem”. In: J. Low Temp. Phys. 126 (2002), pp. 1501–1513.

[8] A. Y. Smirnov et al. “Modelling chemical reactions using semiconductor quantum dots”. In: EPL 80 (2007), p. 67008.

[9] T. Byrnes et al. “Quantum simulation of Fermi-Hubbard models in semiconductor quantum-dot arrays”. In: Phys. Rev. B 78 (7 2008), p. 075320.

[10] P. Barthelemy and L. M. K. Vandersypen. “Quantum Dot Systems: a versatile platform for quantum simulations”. In: Annalen der Physik 525 (2013), pp. 808–826.

[11] J. Gray et al. “Unravelling quantum dot array simulators via singlet-triplet measurements”. In: Phys. Rev. B 94 (19 2016), p. 195136.

[12] A. Hamo et al. “Electron attraction mediated by Coulomb repulsion”. In: Nature 535 (2016), pp. 395–400.

[13] T. Hensgens et al. “Quantum simulation of a Fermi-Hubbard model using a semiconductor quantum dot array”. In: Nature 548 (2017), pp. 70–73.

[14] M. Kiczynski et al. “Engineering topological states in atom-based semiconductor quantum dots”. In: Nature 606 (2022), pp. 694–699.

[15] J. P. Dehollain et al. “Nagaoka ferromagnetism observed in a quantum dot plaquette”. In: Nature 579 (2020), pp. 528–533.

[16] H. Qiao et al. “Coherent Multispin Exchange Coupling in a Quantum-Dot Spin Chain”. In: Phys. Rev. X 10 (3 2020), p. 031006.

[17] C. J. van Diepen et al. “Quantum Simulation of Antiferromagnetic Heisenberg Chain with Gate-Defined Quantum Dots”. In: Phys. Rev. X 11 (4 2021), p. 041025.

[18] F. A. Zwanenburg et al. “Silicon quantum electronics”. In: Rev. Mod. Phys. 85 (3 2013), pp. 961–1019.

[19] G. Scappucci et al. “The germanium quantum information route”. In: Nature Reviews Materials 6 (2021), pp. 926–943.

[20] A. J. Sigillito et al. “Electron Spin Coherence of Shallow Donors in Natural and Isotopically Enriched Germanium”. In: Phys. Rev. Lett. 115 (24 2015), p. 247601.

[21] A. Sammak et al. “Shallow and Undoped Germanium Quantum Wells: A Playground for Spin and Hybrid Quantum Technology”. In: Adv. Funct. Mater. 29.14 (2019), p. 1807613.

[22] M. Lodari et al. “Light effective hole mass in undoped Ge/SiGe quantum wells”. In: Phys. Rev. B 100 (2019), p. 041304.

[23] N. W. Hendrickx et al. “Gate-controlled quantum dots and superconductivity in planar germanium”. In: Nat. Commun. 9 (2018), p. 2835.

[24] H. Watzinger et al. “A germanium hole spin qubit”. In: Nat. Commun. 9 (2018), p. 3902.

[25] N. W. Hendrickx et al. “A single-hole spin qubit”. In: Nat. Commun. 11 (2020), p. 3478.

[26] M. Lodari et al. “Low percolation density and charge noise with holes in germanium”. In: Mater. Quantum. Technol. 1 (2021), p. 011002.

[27] D. Jirovec et al. “A singlet-triplet hole spin qubit in planar Ge”. In: Nature Materials 20 (2021), pp. 1106–1112.

[28] N. W. Hendrickx et al. “Fast two-qubit logic with holes in germanium”. In: Nature 577 (2020), pp. 487–491.

[29] N. W. Hendrickx et al. “A four-qubit germanium quantum processor”. In: Nature 591 (2021), pp. 580–585.

[30] L. Pauling. “The nature of chemical bonds. Application of results obtained from quantum mechanics and from a theory of paramagnetic susceptibility to the structures of molecules”. In: J. Am. Chem. Soc. 53 (4 1931), pp. 1367–1400.

[31] P. W. Anderson. “The Resonating Valence Bond State in La_2CuO_4 and Superconductivity”. In: Science 235 (1987), pp. 1196–1198.

[32] S. A. Kivelson, D. S. Rokhsar, and J. P. Sethna. “Topology of the resonating valence-bond state: Solitons and high-T_c superconductivity”. In: Phys. Rev. B 35 (16 1987), pp. 8865–8868.

[33] H. T. Diep. “Frustrated Spin Systems, 2nd Edition”. In: World Scientific Publishing (2013).

[34] Y. Zhou, K. Kanoda, and T.-K. Ng. “Quantum spin liquid states”. In: Rev. Mod. Phys. 89 (2 2017), p. 025003.

[35] S. Trebst et al. "d-Wave Resonating Valence Bond States of Fermionic Atoms in Optical Lattices". In: Phys. Rev. Lett. 96 (25 2006), p. 250402.

[36] S. Nascimbène et al. "Experimental Realization of Plaquette Resonating Valence-Bond States with Ultracold Atoms in Optical Superlattices". In: Phys. Rev. Lett. 108 (20 2012), p. 205301.

[37] X.-S. Ma et al. "Quantum simulation of the wavefunction to probe frustrated Heisenberg spin systems". In: Nature Physics 7 (2011), pp. 399–405.

[38] K. Yang et al. "Probing resonating valence bond states in artificial quantum magnets". In: Nat. Commun. 12 (2021), p. 993.

[39] F. van Riggelen et al. "A two-dimensional array of single-hole quantum dots". In: Appl. Phys. Lett. 118.4 (2021), p. 044002.

[40] "See Supplementary Information of npj Quantum Information 9, 58 (2023)." In: ().

[41] J. R. Petta et al. "Coherent Manipulation of Coupled Electron Spins in Semiconductor Quantum Dots". In: Science 309 (2005), pp. 2180–2184.

[42] J. R. Petta, H. Lu, and A. C. Gossard. "A Coherent Beam Splitter for Electronic Spin States". In: Science 327 (2010), pp. 669–672.

[43] X. Wu et al. "Two-axis control of a singlet-triplet qubit with an integrated micromagnet". In: PNAS 111.33 (2014), pp. 11938–11942.

[44] D. Jirovec et al. "Dynamics of hole Singlet-Triplet qubits with large g-factor differences". In: Phys. Rev. Lett. 128 (2022), p. 126803.

[45] K. Ono et al. "Current Rectification by Pauli Exclusion in a Weakly Coupled Double Quantum Dot System". In: Science 297 (2002), pp. 1313–1317.

[46] S. A. Studenikin et al. "Enhanced charge detection of spin qubit readout via an intermediate state". In: Appl. Phys. Lett. 101.23 (2012), p. 233101.

[47] P. Harvey-Collard et al. "High-Fidelity Single-Shot Readout for a Spin Qubit via an Enhanced Latching Mechanism". In: Phys. Rev. X 8 (2 2018), p. 021046.

[48] M. D. Shulman et al. "Demonstration of Entanglement of Electrostatically Coupled Singlet-Triplet Qubits". In: Science 336 (2012), pp. 202–205.

[49] N. Piot et al. "A single hole spin with enhanced coherence in natural silicon". In: Nat. Nanotechnol. 17 (2022), pp. 1072–1077.

[50] J. Levy. "Universal Quantum Computation with Spin-1/2 Pairs and Heisenberg Exchange". In: Phys. Rev. Lett. 89 (2002), p. 147902.

[51] R. Li, X. Hu, and J. Q. You. "Controllable exchange coupling between two singlet-triplet qubits". In: Phys. Rev. B 86 (2012), p. 205306.

[52] J. Klinovaja et al. "Exchange-based CNOT gates for singlet-triplet qubits with spin-orbit interaction". In: Phys. Rev. B 86 (2012), p. 085423.

[53] M. P. Wardrop and A. C. Doherty. "Exchange-based two-qubit gate for singlet-triplet qubits". In: Phys. Rev. B 90 (2014), p. 045418.

[54] D. A. Lidar, I. L. Chuang, and K. B. Whaley. "Decoherence-Free Subspaces for Quantum Computation". In: Phys. Rev. Lett. 81 (1998), pp. 2594–2597.

[55] J. Danon and Yu. V. Nazarov. “Pauli spin blockade in the presence of strong spin-orbit coupling”. In: Phys. Rev. B 80 (4 2009), p. 041301.

[56] J. Fischer et al. “Spin decoherence of a heavy hole coupled to nuclear spins in a quantum dot”. In: Phys. Rev. B 78 (2008), p. 155329.

[57] C. Testelin et al. “Hole–spin dephasing time associated with hyperfine interaction in quantum dots”. In: Phys. Rev. B 79 (2009), p. 195440.

[58] P. M. Mutter and G. Burkard. “All-electrical control of hole singlet-triplet spin qubits at low-leakage points”. In: Phys. Rev. B 104 (19 2021), p. 195421.

[59] R. G. Winkler. “Spin-orbit Coupling Effects in Two-Dimensional Electron and Hole Systems”. In: Springer (2003).

[60] Rajiv R. P. Singh et al. “Dimer order with striped correlations in the $J_1 - J_2$ Heisenberg model”. In: Phys. Rev. B 60 (1999), pp. 7278–7283.

[61] R. L. Doretto. “Plaquette valence-bond solid in the square-lattice J_1-J_2 antiferromagnet Heisenberg model: A bond operator approach”. In: Phys. Rev. B 89 (10 2014), p. 104415.

4

MODELLING OF PLANAR GERMANIUM HOLE QUBITS IN ELECTRIC AND MAGNETIC FIELDS

Hole-based spin qubits in strained planar germanium quantum wells have received considerable attention due to their favourable properties and remarkable experimental progress. The sizeable spin-orbit interaction in this structure allows for efficient qubit operations with electric fields. However, it also couples the qubit to electrical noise. In this work, we perform simulations of a heterostructure hosting these hole spin qubits. We solve the effective mass equations for a realistic heterostructure, provide a set of analytical basis wave functions, and compute the effective g-factor of the heavy-hole ground-state. Our investigations reveal a strong impact of highly excited light-hole states located outside the quantum well on the g-factor. We find that sweet spots, points of operations that are least susceptible to charge noise, for out-of-plane magnetic fields are shifted to impractically large electric fields. However, for magnetic fields close to in-plane alignment, partial sweet spots at low electric fields are recovered. Furthermore, sweet spots with respect to multiple fluctuating charge traps can be found under certain circumstances for different magnetic field alignments. This work will be helpful in understanding and improving coherence of germanium hole spin qubits.

Parts of this chapter have been published in C.-A. Wang, H. Ekmel Ercan, Mark F. Gyure, G. Scappucci, M. Veldhorst, and M. Rimbach-Russ, Modelling of planar germanium hole qubits in electric and magnetic fields, *npj Quantum Information* **10**, 102 (2024).

Hole spins in germanium quantum dots constitute a compelling platform for quantum computation [1, 2]. Holes in germanium benefit from the strong spin-orbit interaction (SOI), absence of valley degeneracy and large heavy-hole and light-hole splitting [3], small in-plane effective mass [4], and the formation of ohmic contacts with metals [4–6]. These properties allowed a rapid development of planar germanium spin qubits from quantum dots [4], single and two qubit manipulation [7], singlet-triplet qubits [8], to a 2x2 qubit array [9] as well as high-fidelity operations [10], and rudimentary error correction circuits [11].

The challenge for hole spin qubits is to overcome decoherence due to charge noise coupling through the spin-orbit interaction [12–14]. Current dephasing times are $T_2^\star = 100\,\text{ns}$ - $10\,\mu\text{s}$, which could be extended to $T_2 = 1000\,\mu\text{s}$ using dynamical decoupling [10, 15]. The possibility of extended coherence times in germanium hole qubits is studied in several theoretical works for nanowire [16–19] and planar systems [20–23]. The coherence time can be greatly extended by operating at optimal operation points, so-called sweet spots, where the qubit resonance frequency has a vanishing derivative with respect to electric fields. Interestingly, it is predicted that at such sweet spots the electric dipole spin resonance (EDSR) driving is also be the most efficient [24]. In this work, we investigate the existence of sweet spots in detail. We model the system based on recent experiments, considering a realistic potential profile resulting from a SiGe/Ge/SiGe heterostructure [25]. We show that many basis wave-functions are required for predicting the susceptibility of the g-factor to electric fields [26–28], shifting predictions for sweet spots in out-of-plane magnetic fields to experimentally inaccessible electric field values. However, we also show that sweet spots with respect to electric fields in arbitrary directions can exist, when the magnetic field is applied with angle $\theta \lesssim \arctan(g_\parallel / g_\perp)/3 = 0.2°$, where $g_\parallel$ ($g_\perp$) is the bare in-plane (out of plane) g-factor of the heavy-hole state.

4.1. MODEL

In this work we describe a single hole confined vertically in a strained SiO_2/ $Si_{0.2}Ge_{0.8}$/ Ge/ $Si_{0.2}Ge_{0.8}$ planar heterostructure using an electrostatic potential through metallic gates. Fig. 4.1 shows a sketch of the modelled device. The full Hamiltonian describing the hole reads

$$H = H_{\text{kin}} + V_\perp(z) + V_\parallel(x, y) + H_{\text{Zeeman}}, \tag{4.1}$$

where H_{kin} is the kinetic energy operator, $V_\perp(z)$ and $V_\parallel(x, y)$ describes the vertical and planar confinement, and H_{Zeeman} describes the interaction of the spin and the magnetic field.

EFFECTIVE MASS THEORY FOR STRAINED GERMANIUM

Since our quantum dot structures are large compared to the inter-atom distances and operated at low densities $\rho \sim 10^{10}\,\text{cm}^{-2}$ (single hole regime), the wave-functions are localized close to the Γ point at $\boldsymbol{k} = 0$. In this regime and within the effective mass approximation, the kinetic energy is well-described by the 6×6 Luttinger-Kohn Hamiltonian. Additionally, in germanium the split-off band is far separated in energy by $\Delta_{\text{SO}} = 0.29\,\text{eV}$ and thus negligible for the low-energy dynamics. This allows us to reduce our investiga-

tion to the standard 4×4 Luttinger-Kohn Hamiltonian. In the basis of total angular momentum eigenstates $|j, m_j\rangle = \{|\frac{3}{2}, \frac{3}{2}\rangle, |\frac{3}{2}, -\frac{3}{2}\rangle, |\frac{3}{2}, \frac{1}{2}\rangle, |\frac{3}{2}, -\frac{1}{2}\rangle\}$ the Luttinger-Kohn Hamiltonian reads

$$H_{\text{kin}} = H_{\text{LK}} = \begin{pmatrix} P+Q & 0 & S & R \\ 0 & P+Q & R^\dagger & -S^\dagger \\ S^\dagger & R & P-Q & 0 \\ R^\dagger & -S & 0 & P-Q \end{pmatrix}. \tag{4.2}$$

The upper-left block $P+Q$ describe the kinetic energy of the spin-$\frac{3}{2}$ heavy-hole state, the lower-right block $P-Q$ describes the kinetic energy of the spin-$\frac{1}{2}$ light-hole state, S describes the heavy-light-hole coupling with same spin, and R describes the heavy-light-hole coupling with opposite spin direction. The operators are described by

$$P = \frac{\hbar^2}{2m_0}\gamma_1(k_x^2 + k_y^2 + k_z^2), \tag{4.3}$$

$$Q = \frac{\hbar^2}{2m_0}\gamma_2(k_x^2 + k_y^2 - 2k_z^2), \tag{4.4}$$

$$R = \sqrt{3}\frac{\hbar^2}{2m_0}\left[-\gamma_2(k_x^2 - k_y^2) + i\gamma_3 k_x k_y + i\gamma_3 k_y k_x\right], \tag{4.5}$$

$$S = -\sqrt{3}\frac{\hbar^2}{2m_0}\gamma_3\left[(k_x - ik_y)k_z + k_z(k_x - ik_y)\right], \tag{4.6}$$

where $\hbar k_\xi = -i\hbar\partial_\xi$ is the momentum operator in $\xi = x, y, z$ direction, $\hbar$ the reduced Planck constant, m_0 the bare electron mass, and $\gamma_1 = 13.38$, $\gamma_2 = 4.24$, and $\gamma_3 = 5.69$ the Luttinger parameters for Ge [3]. Hamiltonian (4.2) also defines the vertical effective mass $m_\perp^{H(L)} = m_0/(\gamma_1 \mp 2\gamma_2)$ and in-plane effective mass $m_\parallel^{H(L)} = m_0/(\gamma_1 \pm \gamma_2)$. The spin quantization is given by the growth direction [001] corresponding to out-of-plane z-direction. The effect of an external magentic field is included by substituting the momentum with the generalized momentum $\boldsymbol{p} \to \boldsymbol{p} + e\boldsymbol{A}$, where $\boldsymbol{A} = (2zB_y - yB_z, -2zB_x + xB_z, 0)^T/2$ is the electromagnetic vector potential in the Landau gauge [29] and e is the electron charge.

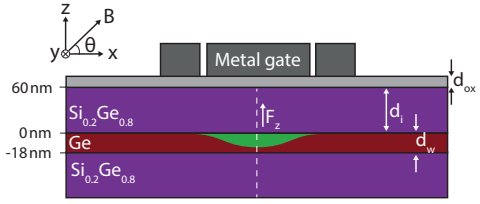

Figure 4.1: Schematics of a gate-defined quantum dot in a planar germanium heterostructure. The quantum dot is confined in the z-direction by the SiGe-Ge-SiGe layers and the Ge quantum well has width $d_w = 18\,\text{nm}$. The insulating oxide layer has width $d_{ox} = 5\,\text{nm}$. The in-plane confinement is created by the electrostatic gates which are located at the top of the heterostructure. Our model assumes a uniform electric field in the z-direction and a parabolic potential in the xy-plane. The potential profile along the dashed line is plotted in Fig. 4.2A. The illustration of the accumulated hole wave function is colored in green.

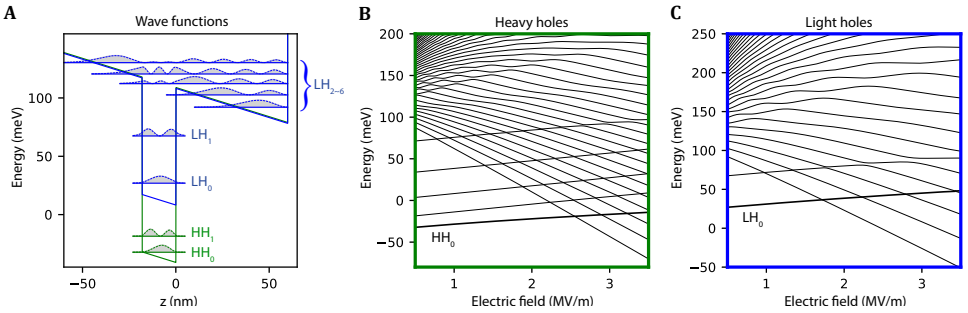

Figure 4.2: **A**, The potential of the heterostructure along the growth direction and the n$^{\text{th}}$ sub-band of the heavy (light) hole levels HH_n (LH_n). For this plot, the electric field strength is $F_z = 0.5\,\text{MV/m}$. **B, C**, The energy levels of the n$^{\text{th}}$ heavy-hole sub-bands and the light-hole sub-bands. The levels with negative slope are located in the quantum well, while levels with a positive slope spread outside the quantum well.

4

The effect of strain in the Ge well in between the SiGe layers is described by the Bir-Pikus Hamiltonian (see Methods). We assume uniaxial strain ($\epsilon_{xy} = \epsilon_{xz} = \epsilon_{yz} = 0$), such that the strain operators become a constant in the different materials. This allows us to describe the effect of strain and an applied electric field in the z-direction using the following potential

$$V_\perp(z) = -eF_z z - \begin{cases} 0, & 0 < z < d_i \\ U_l, & -d_w < z < 0 \\ 0, & z < -d_w \end{cases}. \tag{4.7}$$

Here, $d_w = 18\,\text{nm}$ is the thickness of the strained-Ge quantum well, $d_i = 60\,\text{nm}$ is the thickness of the $Si_{0.2}Ge_{0.8}$ top layer, F_z is the out-of-plane electric field necessary for hole accumulation, and U_l is the band-offset of the heavy-hole ($l = \text{HH}$) and light-hole ($l = \text{LH}$) for the strained Ge layer (see Methods). The SiGe/Ge/SiGe heterostructure is capped by a SiO_2 top interface, modelled as an infinite potential with appropriate boundary conditions $\Psi(z = a_w) = 0$. An illustration is shown in Fig. 4.2A. The in-plane confinement is modelled as a displaced harmonic potential $V_\parallel(x,y) = \frac{1}{2} m_\parallel^{H(L)} \omega_{0,H(L)}^2 (x^2 + y^2) + eF_x + eF_y$ with in-plane masses $m_\parallel^{H(L)}$ and strength of the harmonic potential $m_\parallel^{H(L)} \omega_{0,H(L)}^2 \equiv \frac{\gamma_1 + \gamma_2}{m_0} \frac{\hbar^2}{a_0^4}$ with $a_0 = 50\,\text{nm}$. In-plane electric fields, F_x and F_y, are centred and have average $\langle F_x \rangle = \langle F_y \rangle = 0$. The magnetic field has a magnitude of $B = 0.1\,\text{T}$ for the simulations presented in this work if not mentioned explicitly, and is applied in the x-z-plane with an angle θ between the field direction and x-axis.

The last term in Eq. (4.1) $H_\text{Zeeman} = 2\mu_B \kappa \boldsymbol{J}\cdot\boldsymbol{B} + 2\mu_B q (J_x^3 B_x + J_y^3 B_y + J_z^3 B_z)$ describes the interaction between the hole spin and the magnetic field, where $\mu_B = e\hbar/(2m_0)$ is Bohr's magneton, $\boldsymbol{B} = (B_x, B_y, B_z)^T$ the magnetic field, $\boldsymbol{J} = (J_x, J_y, J_z)^T$ the vector consisting of the spin-$\frac{3}{2}$ matrices, and $\kappa = 3.41$ and $q = 0.067$ the isotropic and an-isotropic Zeeman coefficients for Ge [30].

SIMULATION OF G-FACTOR OF THE GROUND STATE

The total Hamiltonian Eq. (4.2) is projected on a set of basis states and then diagonalized numerically. The basis vectors in our simulations consist of product states $\Psi_{j,k}^{H(L)}(x,y,z) = \phi_j^{H(L)}(x,y)\psi_k^{H(L)}(z)$, which are given by independently solving the in-plane and out-of-plane effective mass Schrödinger equation for the heavy-hole and light-hole bands. The in-plane orbital wave functions are Fock-Darwin states, labelled as $|n,l\rangle$. The z-direction sub-bands of heavy (light) holes HH_n (LH_n) have the form of piece-wise Airy functions [31, 32] with Ben-Daniel–Duke boundary conditions (see Methods) $\psi_p(z=a) = \psi_q(z=a)$ and $\partial_z\psi_p(z=a) = \partial_z\psi_q(z=a)$ with $(p,q) = (Si_{0.2}Ge_{0.8}, Ge), (Ge, Si_{0.2}Ge_{0.8})$ and $a = 0, -d_w$. Calculations involving higher orbital states in the realistic heterostructures are computationally expensive. As the first attempt to simulate sweet spots in the realistic systems, we only considered the effective potentials created in the region of $Si_{0.2}Ge_{0.8}$ and Ge, while neglecting the difference of other material parameters such as the Luttinger parameters and Zeeman coefficients. Fig. 4.2 shows the lowest sub-band states in the heterostructure. The wave-functions of the sub-bands can be separated into states which are localized inside the quantum well, localized at the triangular potential at the surface, or delocalized between well and top-interface. For electric fields $F_z < 3.5\,\mathrm{MV/m}$, there are five heavy-hole states and two light-hole states completely localized inside the quantum well as indicated by the spectrum in Fig. 4.2B and 4.2C. We note that with increasing electric fields, first the light-hole states and then the heavy states "leak" out of the quantum well. The heavy-hole ground state is confined in the quantum well for the electric field lower than $F_z \approx 2.5\,\mathrm{MV/m}$, which marks the upper limit of electric field in this work. We consider three heavy-hole sub-bands and 1 to 57 light-hole sub-bands to simulate the Zeeman splittings of the heavy-hole ground state, which we justify as a sufficient set due to convergence with increasing states. The effective g-factor $g(F_z)$ is then the ratio between Zeeman splitting and the magnetic field strength.

SIMULATION OF THE DEPHASING TIME

In order to estimate the performance of the planar hole qubits we also compute the effective dephasing times in the presence of charge noise. We first model charge noise as random fluctuations of the electric field. For the electric field fluctuations, we assume that the noise follows a $S(f) = A_\xi^2/f$ spectral density [9, 33] with $\xi = x, y, z$. To efficiently model the dynamics due to charge noise, we make the following additional assumptions. Firstly, the noise is coupled to the qubit linearly [34, 35], secondly, there are no spatial noise correlations, and thirdly, we assume noise in x and y direction to be identical. However, note that these assumptions may break in the presence of alloy disorder, stray strain from metallic gates [36], or extremely close fluctuating charge traps [21]. Using these assumptions, the pure dephasing time is then given by

$$T_2^\star(F_\xi) = \frac{\hbar}{\mu_B\sqrt{\log(r)}A_\xi\left|\frac{\partial g(F_\xi)}{\partial F_\xi}B\right|}. \tag{4.8}$$

Here, $g(F_\xi)$ is the effective g-factor of the ground state and the bandwidth $r = 1.68\times10^9$ is the ratio of the lower and higher frequency cutoff. First-order sweet spots are defined by a vanishing linear noise coupling $\frac{\partial g(F_\xi)}{\partial F_\xi} = 0$, thus give rise to exceptionally long de-

phasing times. Because of the finite numbers of basis states included in our simulations and the finite step size in electric field, the g-factor is not completely a smooth function, which gives rise to local variations that overshadow the general trend of $\frac{\partial g(F_z)}{\partial F_z}$. Since these local variations are mostly an artifact of our simulations and our interest lies in the general trend, the interpolated g-factor $g(F_z)$ is fitted to a fourth order polynomial.

The fluctuation strength of the linear out-of-plane electric field noise is estimated to be $A_z = 3.5\,\mathrm{kV/m}$ inside the quantum well, based on the charge noise estimation [37] from plunger gate fluctuations and Schrödinger-Poisson simulation that includes metal / dielectrics gate layers and the germanium heterostructure [38], but on the larger side of estimations based on microscopic 3D charge noise simulations [39] in silicon. Since the g-factor is independent under translation in the xy-plane, fluctuating linear in-plane electric fields do not cause any dephasing. However, the hole spin can still be strongly affected by higher-order coupling terms [23].

To provide a realistic comparison, we follow reference [39] and investigate the impact of randomly distributed fluctuating charge traps located at the interface between SiGe and the oxide [40]. Assuming a continuous metal above the oxide, the potential of a fluctuating charge trap can be well-described by

$$\delta V_j = \Big(\frac{F_c}{|\boldsymbol{r}_j + \delta\boldsymbol{r}_j|} - \frac{F_c}{|\boldsymbol{r}_j|} - \frac{F_c}{|\boldsymbol{r}_j + \delta\boldsymbol{r}_j + \boldsymbol{r}_\mathrm{m}|} + \frac{F_c}{|\boldsymbol{r}_j + \boldsymbol{r}_\mathrm{m}|}\Big). \tag{4.9}$$

Here, $\boldsymbol{r}_i = (x_j, y_j, d_i)$ is the location of the charge trap, $\delta\boldsymbol{r}_j$ with $|\delta\boldsymbol{r}_j| = 0.1\,\mathrm{nm}$ is the displacement vector between the two metastable charge states of the fluctuating trap, $\boldsymbol{r}_\mathrm{m} = (0,0,2d_\mathrm{ox})^T$ is the vector pointing to its mirror charge, and $F_c = e/(4\pi\epsilon_0\epsilon_m)$ is the coupling strength from the Coulomb interaction with ϵ_0 and $\epsilon_m = 14.67$ being the vacuum and material permittivity of SiGe. To match a surface charge density of $1.2\times10^{-10}\,\mathrm{cm}^2$ [39], we generate 11 randomly positioned fluctuating charge traps in an $300\,\mathrm{nm}\times300\,\mathrm{nm}$ area with a random orientation of the displacement vector. In linear order of coupling strength (see Methods), the total dephasing time is then given in the quasistatic noise limit by [21, 39, 41]

$$T^\star_{2,\mathrm{tlf}} = \frac{\sqrt{2}\hbar}{\langle\sigma_{\delta E}\rangle} \tag{4.10}$$

where $\sigma_{\delta V}$ is the standard deviation of the energy shifts of the individual fluctuators for a given configuration and $\langle\cdot\rangle$ denotes the average over different of these configurations. Since the dephasing time as well as the qubit resonance frequency is strongly dependent on the magnitude of the applied magnetic field due to the strong g-factor anisotropy, a comparison of $T_2^\star$ with fixed magnetic field significantly favours small g-factors. To provide a fair comparison of $T_2^\star$ between different magnetic field angles (see Fig. 4.5), we rescale the magnetic field in $T_2^\star$ such that for different magnetic field angles the qubit resonance frequency are equal.

SIMULATION OF THE RABI FREQUENCY

Single-qubit gates can be implemented by periodic modulation of gate voltages in proximity of the quantum dot, giving rise to time-dependent electric fields $F_\xi \rightarrow F_\xi + F_{\xi,\mathrm{ac}} \sin(2\pi f_{\mathrm{res}} t)$ using the cubic Rashba interaction [3, 42]. The speed of the operation, the Rabi frequency, can be estimated by (see method 4.4)

$$\Omega_{\xi,\mathrm{Rabi}} = \frac{1}{h} \left| eF_{\xi,\mathrm{ac}} \langle 0 | \hat{\xi} | 1 \rangle \right|, \tag{4.11}$$

where $\hat{\xi} = \hat{x}, \hat{y}, \hat{z}$ is the position operator and $|0\rangle$ and $|1\rangle$) are the eigenvectors of the qubit states. To provide a fair comparison, we also rescale $\Omega_{\xi,\mathrm{Rabi}}$ such that for different magnetic field angles the qubit resonance frequency are equal.

4.2. RESULTS

OUT-OF-PLANE G-FACTOR AND CONVERGENCE BEHAVIOR

The out-of-plane g-factor strongly depends on the electric field, as shown in Fig. 4.3A. The g-factor and its derivative changes significantly with the choice of the light-hole states. If we only consider the states in the quantum well, the g-factor is monotonically increasing with respect to the electric field. By incorporating the highly excited light-hole states (up to the 56$^{\mathrm{th}}$ excited state in this work), the g-factor changes and is monotonically decreasing with respect to electric field. The zero-derivative point, i.e. the sweet spot, is not observed in the range of electric fields considered here. Applying larger electric fields would result in a ground state that is not located in the quantum well and therefore not considered. Our simulated g-factors match qualitatively with experiments using Hall-Bar measurements at low density [6, 43].

We investigate the dependence of the choice of the energy sorted light-hole levels in Fig. 4.3B. The g-factor converges slowly, indicating that the high energy light-hole states are not negligible for the estimation of the g-factor. Large steps in convergence originate from a light-hole state that is localized inside the quantum well, states localized at the top interfaces have minimal impact, and the small steps at larger number originate from delocalized states. We remark that the full 6-band model including the split-off-band (or even more bands) may have to be considered to achieve a higher accuracy of the g-factor.

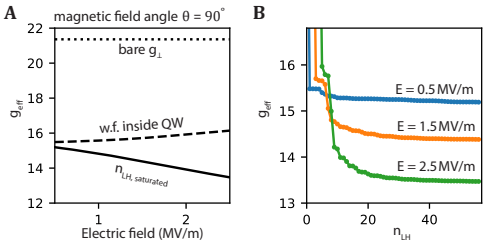

Figure 4.3: **A**, The out-of-plane g-factor of the ground-state as a function of electric field. The solid curve is the g-factor obtained by including $n_{\mathrm{LH,saturated}} = 57$ light-hole states in the simulation. The dashed curve is the g-factor obtained by simulating the light-hole states located in the germanium quantum well. **B**, The g-factor as a function of light-hole level numbers n_{LH}. Curves in different colors are the results taken at different electric field.

IN-PLANE G-FACTOR

The in-plane g-factor is plotted in Fig. 4.4A. Compared to the out-of-plane g-factor, the in-plane g-factor is much smaller and it has weaker dependence on the electric field. The g-factor is monotonically increasing with respect to the electric field in both choice of light-hole states, as shown in the dashed and solid curves in Fig. 4.4A. The g-factor dependence of the light-hole levels is plotted in Fig. 4.4B. Our simulation results match the measured g-factors $g = 0.2 \pm 0.1$ in devices using the same heterostructure [9], where the large spread can be attributed to non-circular confinement [8]. The slow convergence is qualitatively similar to the g-factor dependence for out-of-plane magnetic fields. In general, operating planar hole qubits in in-plane magnetic field direction will result in a longer coherence time than operation in out-of-plane magnetic fields.

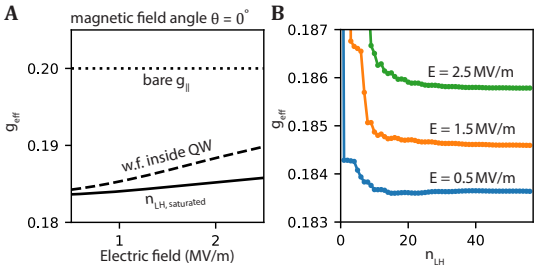

Figure 4.4: **A**, The in-plane g-factor of the ground-state as a function of electric field. The solid curve is the g-factor obtained by including $n_{LH,saturated} = 57$ light-hole states in the simulation. The dashed curve is the g-factor obtained by simulating the light-hole states located in the germanium quantum well. **B**, The g-factor as a function of light-hole level numbers n_{LH}. Curves in different colours are the results taken at different electric field.

OPTIMAL MAGNETIC FIELD ANGLE FOR OUT-OF-PLANE ELECTRIC FIELD NOISE

The opposite dependence of the g-factor on electric field for in-plane and out-of-plane magnetic fields, shown in Figs. 4.3A and 4.4A, suggests that an optimal field angle exists where the g-factor is first-order insensitive to changes in the out-of-plane electric field. In earlier works, an optimal angle for silicon nanowires was predicted close to $\theta = \arctan(g_\parallel / g_\perp)$ [18]. Here, we expect the optimal magnetic field angle close to $\theta = \arctan(g_\parallel / g_\perp)/3$ (see Methods). We therefore investigate the angle dependence, shown in Fig. 4.5A. The g-factor as a function of electric field becomes very flat for angles $\theta = 0.2° - 0.25°$. For certain magnetic field angles, the Zeeman splitting becomes insensitive to electric field fluctuations over a wide range of electric field values, which leads to enhancement of the spin coherence times. Fig. 4.5B shows the estimated dephasing $T^\star_{2,\perp}$ time as a function of electric field, considering fluctuations in F_z at various magnetic field angles. From the plot, we find sweet spots at an optimal magnetic field angle of $\theta = 0.22°$ if we operate the hole spin qubit at electric fields around $F_z = 1\,\mathrm{MV/m}$. The optimal field angle is decreased if we operate the qubit at lower electric field. We note, that current vector magnets already satisfy the required subdegree precision. In a large-scale germanium quantum processor, each qubit may be brought to its own sweet spot by tuning the electric field to compensate local variations.

OPTIMAL MAGNETIC FIELD ANGLE FOR FLUCTUATING CHARGE TRAPS

In Fig. 4.5C we show the dephasing time $T^{\star}_{2,\mathrm{tlf}}$ originating from randomly positioned two-level fluctuators (TLFs) averaged over 200 configurations and normalized with respect to the Lamor frequency. Our results show $T^{\star}_{2,\mathrm{tlf}}$ in the range $200-500\,\mathrm{ns}$ for $|\theta|<0.25^{\circ}$, and $T^{\star}_{2,\mathrm{tlf}}>1\,\mu\mathrm{s}$ for out-of-plane magnetic fields. While a few individual configurations show the emergence of sweet spots in the operation window $0.5\,\mathrm{MV/m}\leq F_z\leq 2.5\,\mathrm{MV/m}$ that greatly enhance the noise protection (see Fig. 4.6 in Methods), the averaged results do not show such a feature. In contrast to out-of-plane electric fluctuations, for suppressing fluctuating charge traps out-of-plane magnetic field directions are beneficial. We also see an approximately linear relationship between out-of-plane electric field and $T^{\star}_{2,\mathrm{tlf}}$ for all investigated magnetic fields, indicating a strong impact of higher-order multipole moments. This is in agreement with recent findings that non-separable confinement with respect to in- and out-of-plane can strongly enhance spin-orbit coupling, thus, the susceptibility to charge noise [44].

TOTAL OPTIMAL MAGNETIC FIELD ANGLE

The optimal point of operation is then given by the relative strengths of the different sources of fluctuations and their corresponding dephasing times. For uncorrelated noise the total dephasing time due to charge noise is given by

$$\left(\frac{1}{T^{\star}_{2,\mathrm{tot}}}\right)^2=\left(\frac{1}{T^{\star}_{2,\perp}}\right)^2+\left(\frac{1}{T^{\star}_{2,\mathrm{tlf}}}\right)^2. \tag{4.12}$$

Since both contributions are of similar order, $T^{\star}_{2,\perp}\simeq T^{\star}_{2,\mathrm{tlf}}$, the global optimum depends on the exact configuration of the fluctuating charges, thus be device dependent [45]. We note, since sweet spots for single charge fluctuators [21, 24] or gate electrodes [45] can be found, a partial sweet spot might be recovered through careful gate calibrations and re-

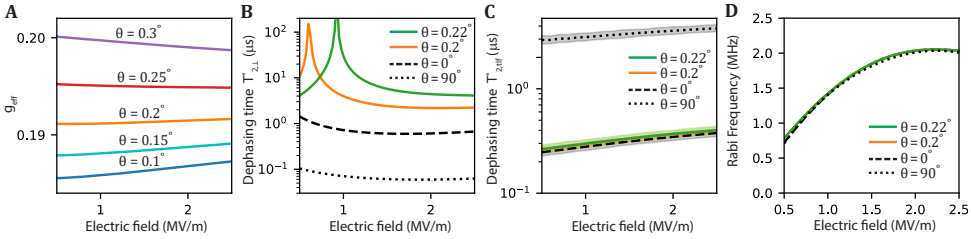

Figure 4.5: **A**, The g-factor of the ground-state as a function of out-of-plane electric field with different magnetic field angle when considering $\mathrm{n_{LH}}=57$ light-hole levels. **B**, Dephasing time $T^{\star}_{2,\perp}$ due to out-of-plane electric field noise with amplitude $A_z=3.5\,\mathrm{kV/m}$, plotted as a function of electric field at different magnetic field angle and strength. **C**, Dephasing time $T^{\star}_{2,\mathrm{tlf}}$ originating from 11 randomly positioned two-level fluctuators (TLFs) in the quantum dot vicinity, averaged over 200 configurations, and as a function of electric field at different magnetic field angle. The shaded regions represent standard deviations over the simulated configurations estimated through bootstrapping. **D**, Rabi frequency as a function of electric field at different magnetic field angle and strength. The EDSR driving is at in-plane direction with the magnitude $F_x=10\,\mathrm{kV/m}$. All four curves are almost overlapping. In plots B-D, the magnetic field strength is chosen such that for each angle the Zeeman splittings are equal (2.5 GHz).

quires further investigations. Furthermore, for hole qubits in natural Ge quantum wells, dephasing caused by fluctuations of the nuclear spin bath severely limits coherence [15, 46]

A qubit's quality factor is determined by the number of coherent oscillations within it's decoherence time. Therefore, it is also important to consider how the frequency of coherent oscillations respond to magnetic field angles that yield sweet spots. Fig. 4.5D shows the Rabi frequency for in-plane driving caused by the cubic Rashba spin-orbit interaction [3, 23]. We note that faster Rabi frequencies are accessible using a non-circular in-plane confinement [23], a non-separable confinement [44], and local strain variations [47]. Since we do not see a significant drop in Rabi frequency at small angles, the sweet spot allows for fast qubit operations combined with long coherence times. The ability to calibrate each qubit into its own sweet spot with local electric fields can allow compensating local variations through disorder, opening the possibility to a scalable architecture.

4.3. DISCUSSION

In conclusion, we simulated the effective g-factor of hole spins in planar germanium heterostructures and studied its dependence on the electric field, the magnetic field orientation, and the light-hole level numbers. We observed that the excited light-hole levels which are not confined by the quantum well have non-negligible contribution to the g-factor and its derivative with respect to the electric field. When including those light-hole levels, we find a tunable sweet spot of the g-factor with respect to out-of-plane electric field if the magnetic field is oriented close to in-plane direction. We note that recent experimental work reporting a sweet spot for holes in silicon FDSOI supports the opportunity for sweet spots for holes in planar germanium [45]. Decoherence is currently a bottleneck for scaling planar germanium hole qubits [9] thus operating at (scalable) sweet spots may therefore enable the next step in advancing to larger quantum circuits.

We presented proof-of-principle simulation results by including higher levels and a realistic heterostructure potential. Our model can be extended to study the response of hole qubits to decoherence from time-dependent charge noise, g-factor variability from realistic electrostatic and mechanical potentials.

4.4. METHODS

DERIVATION OF THE VERTICAL CONFINEMENT POTENTIAL FROM STRAIN TENSOR, BAND OFFSET, AND ELECTRIC FIELD

The vertical confinement $V_\perp(z)$ of the quantum dot consists of two contributions; alignment of the Fermi-energy of the heterostructure giving rise to a band offset and strain in the quantum well. The band offset is a constant for the different materials and can be experimentally measured or theoretically computed [48]. Strain is in general a 3×3 strain tensor ϵ for each band and its effect on the hole states is described by the Bir-Pikusr Hamiltonian. For simplifications, we only consider in this paper the effect of hydrostatic strain and uniaxial strain and ignore all shear-strain components ($\epsilon_{xy} = \epsilon_{xz} = \epsilon_{yz} = 0$). Consequently, the Bir-Pikus Hamiltonian becomes diagonal in the heavy-hole and light-

hole basis $|j,m_j\rangle = \{|\frac{3}{2},\frac{3}{2}\rangle,|\frac{3}{2},-\frac{3}{2}\rangle,|\frac{3}{2},\frac{1}{2}\rangle,|\frac{3}{2},-\frac{1}{2}\rangle\}$

$$H_{\mathrm{PB}} = \mathrm{diag}(P_\epsilon + Q_\epsilon, P_\epsilon + Q_\epsilon, P_\epsilon - Q_\epsilon, P_\epsilon - Q_\epsilon) \tag{4.13}$$

with the coefficients

$$P_\epsilon = -a_V(\epsilon_{xx}+\epsilon_{yy}+\epsilon_{zz}), \tag{4.14}$$

$$Q_\epsilon = -\frac{b_V}{2}(\epsilon_{xx}+\epsilon_{yy}-2\epsilon_{zz}), \tag{4.15}$$

where a_V and b_V are the deformation potentials, which strongly depend on the silicon concentration x in the Si_xGe_{1-x} layer of the heterostructure. For $x = 20\%$ we use $a_V = 2.0\,\mathrm{eV}$ and $b_V = -2.16\,\mathrm{eV}$ [3].

Since strain is only present in the quantum well and only depends on the band $j = \frac{1}{2},\frac{3}{2}$ and not the sign of the spin, we can rewrite the effect of the band offset and strain as an effective potential of the form

$$V_\perp(z) = -\begin{cases} 0, & 0 < z < d_i \\ U_l, & -d_w < z < 0 \\ 0, & z < -d_w \end{cases}, \tag{4.16}$$

where $l = \mathrm{HH},\mathrm{LH}$ denotes the band. Note, that solely due to the uniaxial strain components, the heavy and light-hole degeneracy is lifted inside the quantum well. For our simulations we use the following parameters $U_{\mathrm{HH}} = 150\,\mathrm{meV}$ and $U_{\mathrm{LH}} = 100\,\mathrm{meV}$ extracted from [48] and coincides with the values from [3]. By adding a global electric potential $-eF_z z$ originating from the metallic plunger gate on top we end up with expression (4.7) in the main text.

DERIVATION OF THE ANALYTICAL WAVEFUNCTIONS AND NUMERICAL SIMULATION

The total Hamiltonian Eq. (4.1) is projected on a set of basis states and then diagonalized numerically. The basis states for the heavy-hole (light-hole) are product states of in-plane Fock-Darwin wave functions $\phi_j^{H(L)}(x,y)$ and the derived wave-functions in z-direction consisting of piece-wise Airy functions

$$\Psi_{j,k}^{H(L)}(x,y,z) = \phi_j^{H(L)}(x,y)\psi_k^{H(L)}(z), \tag{4.17}$$

with

$$\psi_k^{H(L)}(z) = \begin{cases} c_{k,1}^{H(L)} Ai\left(u_{H(L)} - \epsilon_k^{H(L)} - z/\zeta_0^{H(L)}\right) + c_{k,2}^{H(L)} Bi\left(u_{H(L)} - \epsilon_k^{H(L)} - z/\zeta_0^{H(L)}\right), & 0 < z < d_i \\ c_{k,3}^{H(L)} Ai\left(-\epsilon_k^{H(L)} - z/\zeta_0^{H(L)}\right) + c_{k,4}^{H(L)} Bi\left(-\epsilon_k^{H(L)} - z/\zeta_0^{H(L)}\right), & -d_w < z < 0 \\ c_{k,5}^{H(L)} Ai\left(u_{H(L)} - \epsilon_k^{H(L)} - z/\zeta_0^{H(L)}\right), & z < -d_w \end{cases}. \tag{4.18}$$

Here, Ai and Bi are the conventional Airy functions, $\zeta_0^{H(L)} = (\hbar^2/(2m_{L(H)}eF_z))^{\frac{1}{3}}$ and $E_{\mathrm{tri}}^{H(L)} = \hbar^2/(2m_{H(L)}\zeta_0^{H(L)})$ are the effective confinement length and energy of the triangular potential, $u_{H(L)} = U_{H(L)}/E_{\mathrm{tri}}^{H(L)}$ is the effective potential barrier, and $\epsilon_k^{H(L)} = E_k^{H(L)}/E_{\mathrm{tri}}^{H(L)}$

is the effective eigenenergy of the heavy-hole (light-hole) sub-band k. The weighting factors $c_{k,n}^{H(L)}$ are defined via the Ben-Daniel-Duke boundary conditions [31, 32] $\psi_p(z=a) = \psi_q(z=a)$ and $\frac{1}{m_{\perp,p}^{H(L)}}\partial_z\psi_p(z=a) = \frac{1}{m_{\perp,q}^{H(L)}}\partial_z\psi_q(z=a)$ with $(p,q) = (\mathrm{Si_{0.2}Ge_{0.8}}, \mathrm{Ge}), (\mathrm{Ge}, \mathrm{Si_{0.2}Ge_{0.8}})$ and $a = 0, -d_w$. Assuming that the effective masses of the heavy-hole (light-hole) in SiGe are identical to the Ge effective masses, i.e. $m_{\perp,\mathrm{Ge}}^{H(L)} = m_{\perp,\mathrm{SiGe}}^{H(L)}$ and $m_{\parallel,\mathrm{Ge}}^{H(L)} = m_{\parallel,\mathrm{SiGe}}^{H(L)}$, the boundary conditions become independent of the effective mass, and we arrive at the expressions in the main text. We notice that this assumption causes an error of 5 % in $m_\perp^H$, 15 % in $m_\perp^L$ and $m_\parallel^H$, and 11 % in $m_\parallel^L$ outside the quantum well. We find the eigenenergies $E_k^{H(L)}$ of the heavy-hole (light-hole) band via the boundary conditions in Eq. (4.7) following Ref. [32] but translate it to a computational task of finding roots of a fifth-order polynomial of the Airy functions. The roots are solved numerically using the *Reduce* function in Mathematica. Afterwards, we check and add missing roots using a bisection algorithm.

The in-plane orbital wave-fucntions are the solution of a 2D harmonic confinement in the presence of a magnetic field. The general solutions are the Fock-Darwin states

$$\begin{aligned}\phi_{j=(n,l)}^{H(L)}(x,y) = &\sqrt{\frac{1}{\pi l^2}\frac{n!}{(n+|l|)!}}\exp\left(\frac{x^2+y^2}{2a_{B,H(L)}^2}\right)\\ &\times\left(\frac{x^2+y^2}{a_{B,H(L)}^2}\right)^{\frac{|l|}{2}}\mathscr{L}_n^{|l|}\left(\frac{x^2+y^2}{a_{B,H(L)}^2}\right)\\ &\times\exp(-i\,l\arctan(y/x)),\end{aligned} \tag{4.19}$$

where $\mathscr{L}_n^{|l|}(\xi)$ are the generalized Laguerre polynomials, $a_{B,H} = 50\,\mathrm{nm}$ and $a_{B,L} = 42.6\,\mathrm{nm}$ are the Bohr radii, and j labels the eigenenergies in ascending order.

For both heavy-hole and light-hole, we use a fixed number of 78 in-plane orbital wave functions. The expression and the integrals between the in-plane orbits are computed analytically. In z-direction, we consider n_{HH} heavy-hole sub-bands and n_{LH} light-hole sub-bands. We observe that the g-factors changes with n_{LH} and saturates as n_{LH} increases. The largest n_{LH} we consider is 57. Contrarily, the number of heavy-hole sub-bands has a significant smaller impact on the g-factor. The largest n_{HH} we consider is 4. The numbers of basis states are $78\times n_{\mathrm{HH}}$ and $78\times n_{\mathrm{LH}}$ for heavy-hole and light-hole. The total dimension of the projected Hamiltonian is then given by $n_{\mathrm{tot}} = 156\times(n_{\mathrm{HH}} + n_{\mathrm{LH}})$.

We consequently compute the effective g-factor, the ratio of Zeeman splitting to the magnetic field strength, of the heavy-hole ground state by diagonalizing the projected Hamiltonian

$$g = (E_1 - E_0)/(\mu_B B), \tag{4.20}$$

where E_i are the energy-sorted eigenvalues.

To find the electric field dependence of the g-factor, the above procedure is repeated for values of electric field in the interval $F_z = 0.5 - 3.5\,\mathrm{MV/m}$ with a step size of $\Delta F_z = 5\times10^{-3}\,\mathrm{MV/m}$. For each electric field value we compute the z-direction sub-bands of the heavy-hole and light-hole, construct the basis states, compute the projected total

Hamiltonian Eq. (4.1), diagonalize the matrix, obtain the eigenvalues and eigenstates, and finally compute the effective g-factor from the eigenvalues.

To keep the simulation tractable, we truncate the Hilbert space and limit the number of basis wavefunctions $\psi^{H(L)}$. However, due to the dense energy structure of the heavy and light-hole bands with multiple anti-crossings at higher energies (Fig. 4.2), our choice of truncations might miss the respective partner eigenstate at an energy anti-crossing. Together with a finite step size and numerical precision, this leads to small and local fluctuations in the resulting g-factor. While these simulations are not visible in the plots of the g-factors, these fluctuations can affect the derivative $dg(F_z)/dF_z$ and consequently the dephasing time. To avoid these artifacts in our results, we fit the resulting g-factor $g(F_z)$ to a Polynomial in F_z up to fourth order before taking the derivative. We note, that the results are well-approximated by the fitting.

SIMULATION OF RABI FREQUENCY

Single qubit operations for hole qubits can be implemented by applying an oscillating electric field, $F_\xi \rightarrow F_\xi + F_{\xi,\mathrm{ac}}\sin(2\pi f_{\mathrm{res}} t)$ with $\xi = x, y, z$, matching the resonance frequency of the qubit $f_{\mathrm{res}} = 2\mu_B g(F_x, F_y, F_z)B/(2\pi\hbar)$. The dynamics of the driven system can be best estimated in the adiabatic frame of Hamiltonian (4.1) [49]

$$H_{\mathrm{adiabatic}} = U^\dagger H U - i\hbar U^\dagger \frac{dU}{dt} \tag{4.21}$$

$$= H_{\mathrm{diag}} - 2\pi i\hbar f_{\mathrm{res}} e F_{\xi,\mathrm{ac}} \sin(2\pi f_{\mathrm{res}} t) U^\dagger \frac{dU}{dF_\xi}, \tag{4.22}$$

where $U^\dagger H U \equiv H_{\mathrm{diag}}$ contains only diagonal entries. From the first to the second line, we used $\frac{dU}{dt} = \frac{dF_\xi}{dt}\frac{dU}{dF_\xi}$ with $\frac{dF_\xi}{dt} = 2\pi f_{\mathrm{res}} F_{\xi,\mathrm{ac}} \sin(2\pi f_{\mathrm{res}} t)$ assuming a linear response and ignoring higher-order terms. The resonant transition amplitude between the qubit states $|0\rangle$ and $|1\rangle$ is then given in the rotating frame by

$$\langle 0| H_{\mathrm{adiabatic}} |1\rangle = \pi f_{\mathrm{res}} e F_{\xi,\mathrm{ac}} (1 + e^{4\pi i f_{\mathrm{res}} t}) \langle 0| U^\dagger \frac{\partial U}{\partial F_\xi} |1\rangle . \tag{4.23}$$

By ignoring the counter-rotating term, the so-called rotating wave-approximation, we end up with expression (4.11) of the main text. Conveniently, this method requires only knowledge about the instantaneous eigenvectors of the qubit space. The Rabi frequency is then given by

$$\Omega_{\xi,\mathrm{Rabi}} = \frac{2}{h} |\langle 0| H_{\mathrm{adiabatic}} |1\rangle|. \tag{4.24}$$

If we further use the linearity of the driving , i.e., $H_{\mathrm{tot}} = H + eF_{\xi,\mathrm{ac}}\sin(2\pi f_{\mathrm{res}} t)x$, the upper expression can be recast into the more familar expression

$$\Omega_{\xi,\mathrm{Rabi}} = \frac{1}{h} |eF_{\xi,\mathrm{ac}} \langle 0| \hat{\xi} |1\rangle|, \tag{4.25}$$

where $\hat{\xi} = \hat{x}, \hat{y}, \hat{z}$ is the corresponding position operator.

OPTIMAL MAGNETIC FIELD ANGLE FOR OUT-OF-PLANE FLUCTUATIONS

The emergence of an optimal magnetic field angle can be derived from Hamiltonian (4.1) of the main text. While this derivation can be easily generalized to arbitrary magnetic fields, we pursue a magnetic field in the xz-plane $\boldsymbol{B} = (B\cos(\theta), 0, B\sin(\theta))^T$. To diagonalize the heavy-hole state sector we apply the unitary rotation $U = e^{-i\phi\sigma_y/2}$ with σ_z being the Pauli matrix acting only on the heavy-hole space and

$$\phi = \arctan\left(\frac{4\kappa + 9q}{2q}\tan(\theta)\right) = \arctan\left(\frac{g_\perp}{g_\parallel}\tan(\theta)\right). \tag{4.26}$$

Here, κ and q are the isotropic and an-isotropic Zeeman coefficients and $g_\perp = 6\kappa + 27q/2$ and $g_\parallel = 3q$ are the out-of-plane and in-plane pure heavy-hole g-factors. While the angle θ describes the rotation of the magnetic field, the angle ϕ describes the rotation of the heavy-hole quantization axis. Minimal variation of the g-factor is then expected to be close to $\phi = 45°$ where the orbital contributions from in-plane and out-of-plane magnetic fields compensate each other [18]. From our simulations, we can see that the ratio of the slopes $\frac{\partial g(F_z)}{\partial F_z}$ normalized to equal qubit frequencies for $\theta = 90°$ and $\theta = 0°$ are not equal, therefore we end up with $\theta_{\text{opt}} \approx \arctan(g_\parallel/g_\perp)/3$.

OPTIMAL MAGNETIC FIELD ANGLE FOR FLUCTUATING CHARGE TRAPS

The potential caused by a single charge trap, approximated as point-charge, is given by the Coulomb potential. The potential difference of a two-level fluctuator (TLF) subject to screening from the metal gates (here assumed to be continuous) is given by

$$\begin{aligned}\delta V_j = \Big(&\frac{F_c}{|\boldsymbol{r}_j + \delta\boldsymbol{r}_j|} - \frac{F_c}{|\boldsymbol{r}_j|} \\ &- \frac{F_c}{|\boldsymbol{r}_j + \delta\boldsymbol{r}_j + \boldsymbol{r}_{\text{m}}|} + \frac{F_c}{|\boldsymbol{r}_j + \boldsymbol{r}_{\text{m}}|}\Big).\end{aligned} \tag{4.27}$$

The first two terms are the potentials caused by the two meta-stable states of the two-level fluctuator with the remaining terms being their image charges. Here, $\boldsymbol{r}_i = (x_j, y_j, d_i)$ is the location of the charge trap, $\delta\boldsymbol{r}_j$ with $|\delta\boldsymbol{r}_j| = 0.1\,\text{nm}$ is the displacement vector between the two metastable charge states of the fluctuating trap, $\boldsymbol{r}_{\text{m}} = (0, 0, 2d_{\text{ox}})^T$ is the vector pointing to its mirror charge, and $F_c = e/(4\pi\epsilon_0\epsilon_m)$ is the coupling strength from the Coulomb interaction with ϵ and $\epsilon_m = 14.67$ being the vacuum and material permittivity of SiGe.

We consider 11 randomly positioned charge traps that serve as two-level fluctuators (TLFs) in a $300\,\text{nm} \times 300\,\text{nm}$ area drawn from a uniform distribution. We furthermore draw the vector connecting the two meta-stable states of the fluctuator $\delta\boldsymbol{r}_j$ from a uniform 3D vector with fixed length $|\delta\boldsymbol{r}_j| = 0.1\,\text{nm}$. The corresponding potential for a given configuration reads

$$V_{\boldsymbol{b}} = \sum_{j=1}^{11} \delta V_j\Big|_{\delta\boldsymbol{r}_j \to b_j\delta\boldsymbol{r}_j}. \tag{4.28}$$

Here $\boldsymbol{b}$ is a binary vector indicating the current state of each TLF, i.e. 0 for not displaced and 1 for displaced. For example, $(0, \cdots, 0)^T$ represents all charge traps in their original

position. To get the average fluctuations, we compute for each state of the TLFs the corresponding qubit energy shift

$$\delta E_{\boldsymbol{b}_k} = \langle 0 | V_{\boldsymbol{b}_k} | 0 \rangle - \langle 1 | V_{\boldsymbol{b}_k} | 1 \rangle , \tag{4.29}$$

where $|0\rangle$ and $|1\rangle$ are the qubit states. To speed up the computation, we use instead a series expansion of the upper expression up to 6^{th}-order in x and y and up to second order in z. In our simulations, we make use of our analytical expressions and compute the matrix elements from a general polynomial and substitute later the actual values.

The total fluctuations caused by the TLFs are consequently given by the root-mean-square with respect to the TLF states

$$\sigma^2_{\delta E} = \frac{1}{N^2} \sum_k \delta E^2_{\boldsymbol{b}_k}, \tag{4.30}$$

where N is the number of TLF states. In our simulations, we linearize the problem and neglect TLF states with more than one excitation. This is a good approximation [39, 41] and becomes exact if $\delta E_{(\cdots,1,\cdots,1\cdots)} = \delta E_{(\cdots,1,\cdots,0\cdots)} + \delta E_{(\cdots,0,\cdots,1\cdots)}$ and if there is no correlation between the TLFs.

As a final step, we repeat the upper steps for 200 configurations of the 11 TLFs and average over them.

OPTIMAL MAGNETIC FIELD ANGLE FOR SELECTED INDIVIDUAL FLUCTUATING CHARGE TRAPS

Fig. 4.6 shows the dephasing time caused by a few selected TLF configurations as a function of out-of-plane electric field for different magnetic field configurations. Depending on the configuration, sweet spots can appear for small θ angles (Fig. 4.6A), just out-side the window of investigation (Fig. 4.6B), and also for $\theta = 90^\circ$ (Fig. 4.6C).

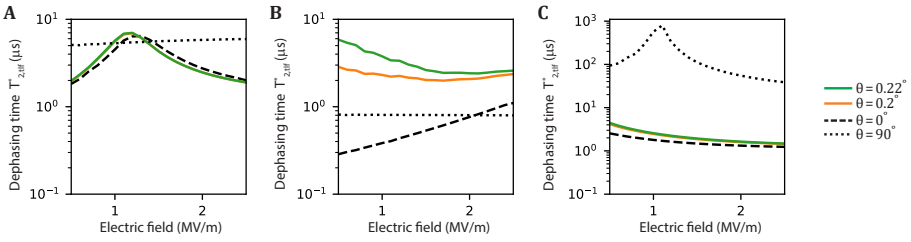

Figure 4.6: Dephasing time $T^{\star}_{2,\text{tlf}}$, caused by three different TLF configurations, as a function of out-of-plane electric field with different magnetic field angles. **A**. Emergence of a sweet spot for magnetic fields with small θ. The sweet spot is robust against small changes in magnetic field orientation. **B**. Emergence of incomplete sweet spot features that are highly sensitive to magnetic field orientations. **C**. Emergence for a sweet spot for out-of-plane magnetic field similar to the one reported in Ref. [21].

BIBLIOGRAPHY

[1] L. M. K. Vandersypen et al. “Interfacing Spin Qubits in Quantum Dots and Donors—Hot, Dense, and Coherent”. In: npj Quantum Information 3.1 (2017), pp. 1–10. ISSN: 2056-6387.

[2] Giordano Scappucci et al. “The Germanium Quantum Information Route”. In: Nature Reviews Materials (2020), pp. 1–18. ISSN: 2058-8437.

[3] L. A. Terrazos et al. “Theory of Hole-Spin Qubits in Strained Germanium Quantum Dots”. In: Physical Review B 103.12 (2021), p. 125201.

[4] N. W. Hendrickx et al. “Gate-Controlled Quantum Dots and Superconductivity in Planar Germanium”. In: Nature Communications 9.1 (2018), p. 2835. ISSN: 2041-1723.

[5] Hannes Watzinger et al. “A Germanium Hole Spin Qubit”. In: Nature Communications 9.1 (2018), p. 3902. ISSN: 2041-1723.

[6] M. Lodari et al. “Light Effective Hole Mass in Undoped Ge/SiGe Quantum Wells”. In: Physical Review B 100.4 (2019), p. 041304.

[7] N. W. Hendrickx et al. “Fast Two-Qubit Logic with Holes in Germanium”. In: Nature 577.7791 (2020), pp. 487–491. ISSN: 1476-4687.

[8] Daniel Jirovec et al. “Dynamics of Hole Singlet-Triplet Qubits with Large g-Factor Differences”. In: Physical Review Letters 128.12 (2022), p. 126803.

[9] N. W. Hendrickx et al. “A four-qubit germanium quantum processor”. In: Nature 591 (2021), pp. 580–585.

[10] W. I. L. Lawrie et al. “Simultaneous single-qubit driving of semiconductor spin qubits at the fault-tolerant threshold”. In: Nature Communications 14.3617 (2023).

[11] F. van Riggelen et al. “Phase Flip Code with Semiconductor Spin Qubits”. In: npj Quantum Information 8 (2022), p. 124. ISSN: 2056-6387.

[12] Peter Stano and Daniel Loss. “Review of Performance Metrics of Spin Qubits in Gated Semiconducting Nanostructures”. In: Nature Reviews Physics 4.10 (2022), pp. 672–688. ISSN: 2522-5820.

[13] F. N. M. Froning et al. “Strong Spin-Orbit Interaction and g-Factor Renormalization of Hole Spins in Ge/Si Nanowire Quantum Dots”. In: Physical Review Research 3.1 (2021), p. 013081.

[14] Ke Wang et al. “Ultrafast Coherent Control of a Hole Spin Qubit in a Germanium Quantum Dot”. In: Nature Communications 13.1 (2022), p. 206. ISSN: 2041-1723.

[15] N. W. Hendrickx et al. “Sweet-spot operation of a germanium hole spin qubit with highly anisotropic noise sensitivity”. In: Nature Materials (May 2024). ISSN: 1476-4660.

[16] Peter Stano et al. "g-Factor of Electrons in Gate-Defined Quantum Dots in a Strong in-Plane Magnetic Field". In: Physical Review B 98.19 (2018), p. 195314.

[17] Stefano Bosco, Bence Hetényi, and Daniel Loss. "Hole Spin Qubits in Si FinFETs With Fully Tunable Spin-Orbit Coupling and Sweet Spots for Charge Noise". In: PRX Quantum 2.1 (2021), p. 010348.

[18] Vincent P. Michal, Benjamin Venitucci, and Yann-Michel Niquet. "Longitudinal and Transverse Electric Field Manipulation of Hole Spin-Orbit Qubits in One-Dimensional Channels". In: Physical Review B 103.4 (2021), p. 045305.

[19] Stefano Bosco and Daniel Loss. "Hole Spin Qubits in Thin Curved Quantum Wells". In: Physical Review Applied 18.4 (2022), p. 044038.

[20] Benjamin Venitucci and Yann-Michel Niquet. "Simple Model for Electrical Hole Spin Manipulation in Semiconductor Quantum Dots: Impact of Dot Material and Orientation". In: Physical Review B 99.11 (2019), p. 115317.

[21] Zhanning Wang et al. "Optimal Operation Points for Ultrafast, Highly Coherent Ge Hole Spin-Orbit Qubits". In: npj Quantum Information 7.1 (2021), pp. 1–8. ISSN: 2056-6387.

[22] Christoph Adelsberger et al. "Hole-spin qubits in Ge nanowire quantum dots: Interplay of orbital magnetic field, strain, and growth direction". In: Phys. Rev. B 105 (7 Feb. 2022), p. 075308.

[23] Stefano Bosco et al. "Squeezed Hole Spin Qubits in Ge Quantum Dots with Ultrafast Gates at Low Power". In: Physical Review B 104.11 (2021), p. 115425.

[24] Lorenzo Mauro et al. "Geometry of the dephasing sweet spots of spin-orbit qubits". In: Phys. Rev. B 109 (15 Apr. 2024), p. 155406.

[25] Mario Lodari et al. "Low Percolation Density and Charge Noise with Holes in Germanium". In: Materials for Quantum Technology 1.1 (2021), p. 011002. ISSN: 2633-4356.

[26] Th. Wimbauer et al. "Zeeman splitting of the excitonic recombination in $In_xGa_{1-x}As/GaAs$ single quantum wells". In: Physical Review B 50.12 (1994), pp. 8889–8892.

[27] P. Del Vecchio et al. "Vanishing Zeeman Energy in a Two-Dimensional Hole Gas". In: Physical Review B 102.11 (2020), p. 115304.

[28] M. A. Semina, A. A. Golovatenko, and A. V. Rodina. "Influence of the Spin-Orbit Split-off Valence Band on the Hole g Factor in Semiconductor Nanocrystals". In: Physical Review B 104.20 (2021), p. 205423.

[29] Peter Stano et al. "Orbital Effects of a Strong In-Plane Magnetic Field on a Gate-Defined Quantum Dot". In: Physical Review B 99.8 (2019), p. 085308.

[30] Roland Winkler. "Spin-Orbit Coupling Effects in Two-Dimensional Electron and Hole Systems (Springer Tracts in Modern Physics)". In: (2003).

[31] P. Harrison and Alex Valavanis. "Quantum Wells, Wires and Dots: Theoretical and Computational Physics of Semiconductor Nanostructures. Quantum Wells, Wires and Dots". In: John Wiley & Sons (2016).

[32] Amin Hosseinkhani and Guido Burkard. “Electromagnetic Control of Valley Splitting in Ideal and Disordered Si Quantum Dots”. In: Physical Review Research 2.4 (2020), p. 043180.

[33] E. Paladino et al. “1/f Noise: Implications for Solid-State Quantum Information”. In: Rev. Mod. Phys. 86.2 (2014), pp. 361–418.

[34] G. Ithier et al. “Decoherence in a Superconducting Quantum Bit Circuit”. In: Phys. Rev. B 72.13 (2005), p. 134519.

[35] Maximilian Russ and Guido Burkard. “Asymmetric Resonant Exchange Qubit under the Influence of Electrical Noise”. In: Phys. Rev. B 91.23 (2015), p. 235411.

[36] Cedric Corley-Wiciak et al. “Nanoscale Mapping of the 3D Strain Tensor in a Germanium Quantum Well Hosting a Functional Spin Qubit Device”. In: ACS Applied Materials & Interfaces (2023). ISSN: 1944-8244.

[37] Xiao Xue et al. “Quantum Logic with Spin Qubits Crossing the Surface Code Threshold”. In: Nature 601.7893 (2022), pp. 343–347. ISSN: 1476-4687.

[38] Alberto Tosato et al. “A High-Mobility Hole Bilayer in a Germanium Double Quantum Well”. In: Advanced Quantum Technologies 5.5 (2022), p. 2100167. ISSN: 2511-9044.

[39] Marcin Kepa et al. “Simulation of 1/f Charge Noise Affecting a Quantum Dot in a Si/SiGe Structure”. In: Applied Physics Letters 123.3 (July 2023), p. 034005.

[40] Brian Paquelet Wuetz et al. “Reducing Charge Noise in Quantum Dots by Using Thin Silicon Quantum Wells”. In: Nature Communications 14.1 (2023), p. 1385. ISSN: 2041-1723. (Visited on 03/30/2023).

[41] M. Mohamed El Kordy Shehata et al. “Modeling Semiconductor Spin Qubits and Their Charge Noise Environment for Quantum Gate Fidelity Estimation”. In: Physical Review B 108.4 (2023), p. 045305.

[42] Abhikbrata Sarkar et al. “Electrical operation of planar Ge hole spin qubits in an in-plane magnetic field”. In: Phys. Rev. B 108 (24 Dec. 2023), p. 245301.

[43] M. Lodari et al. “Lightly Strained Germanium Quantum Wells with Hole Mobility Exceeding One Million”. In: Applied Physics Letters 120.12 (2022), p. 122104. ISSN: 0003-6951.

[44] Biel Martinez et al. “Hole spin manipulation in inhomogeneous and nonseparable electric fields”. In: Phys. Rev. B 106 (23 Dec. 2022), p. 235426.

[45] N. Piot et al. “A Single Hole Spin with Enhanced Coherence in Natural Silicon”. In: Nature Nanotechnology (2022), pp. 1–6. ISSN: 1748-3395.

[46] Jaime Saez-Mollejo et al. “Microwave Driven Singlet-Triplet Qubits Enabled by Site-Dependent g-Tensors”. In: arXiv (Feb. 2022). eprint: 2202.04482.

[47] José Carlos Abadillo-Uriel et al. “Hole Spin Driving by Strain-Induced Spin-Orbit Interactions”. In: Phys. Rev. Lett. 131 (9 Sept. 2023), p. 097002.

[48] Friedrich Schäffler. “High-Mobility Si and Ge Structures”. In: Semiconductor Science and Technology 12.12 (1997), pp. 1515–1549. ISSN: 0268-1242.

[49] A. Messiah. “Quantum Mechanics”. In: North-Holland (1961).

5

BICHROMATIC RABI CONTROL OF SEMICONDUCTOR QUBITS

Electrically-driven spin resonance is a powerful technique for controlling semiconductor spin qubits. However, it faces challenges in qubit addressability and off-resonance driving in larger systems. We demonstrate coherent bichromatic Rabi control of quantum dot hole spin qubits, offering a spatially-selective approach for large qubit arrays. By applying simultaneous microwave bursts to different gate electrodes, we observe multichromatic resonance lines and resonance anticrossings that are caused by the ac Stark shift. Our theoretical framework aligns with experimental data, highlighting interdot motion as the dominant mechanism for bichromatic driving.

Parts of this chapter have been published in V. John, F. Borsoi, Z. György, C.-A. Wang, G. Széchenyi, F. van Riggelen, W.I.L Lawrie, N.W. Hendrickx, A. Sammak, G. Scappucci, A. Pályi, and M. Veldhorst, Bichromatic Rabi control of semiconductor qubits, *Physical Review Letters* **132**, 067001 (2024).

5.1. INTRODUCTION

Spin qubits based on semiconductor quantum dots represent a promising platform for quantum computing owing to their small qubit footprint, long coherence times, and compatibility with semiconductor manufacturing techniques [1, 2]. However, the present control of spin qubit devices relies on a brute force approach, where each qubit is individually connected to at least one control line. This approach poses a significant challenge for scaling to larger systems and is affecting current progress [3, 4]. Multiplexing strategies will most likely become essential and this has been the motivation for various proposals, such as crossbar arrays with shared control [5, 6]. Executing quantum algorithms requires selective quantum control, but its implementation in large qubit arrays poses significant challenges. Recently, the concept of bichromatic spin resonance has been proposed to offer addressable microwave control in qubit crossbar architectures [7]. In this approach, two microwave tones with frequencies f_w and f_b are utilized. These tones are applied to the word and the bit line of the crossbar array, respectively. By exploiting the nonlinearity of electric dipole spin resonance (EDSR) [8–16], rotations of a qubit with Larmor frequency of $|f_w \pm f_b|$ at the intersection of the two lines [Fig. 5.1(a)] can be targeted. This operation scheme presents new opportunities for both spatially selective qubit addressing and gate parallelization [7]. Analogous two-photon processes have been utilized in Rydberg-atom processors [17, 18] and superconducting qubits [19] to optimize qubit performance.

Here, we investigate experimentally and theoretically the bichromatic driving of semiconductor spin qubits in a 2-qubit system defined in a strained germanium quantum well. We find that both qubits can be coherently driven by mixed frequency signals, including the sum and difference of the corresponding frequencies. We investigate the occurrence of resonance anticrossings in EDSR spectroscopy maps, which originate from the Autler-Townes (also known as ac Stark) shift of a photon-dressed spin transition. Additionally, we introduce a model that reveals the importance of spin-conserving and spin-flip tunneling terms in bi- and monochromatic EDSR.

We investigate bichromatic driving of spin qubits in a two-qubit system within a four-qubit germanium quantum processor (Figs.5.1b, c) [20, 21]. By tuning the electrostatic potential using plunger and barrier gates, we confine a single-hole quantum dot underneath each of the four plungers P1-P4, and define virtual gate voltages vP1-vP4 based on P1-P4 to achieve independent control ([22], Supplementary Note 1). We focus on the spin qubits Q1 and Q2, while Q3 and Q4 remain in their ground state. We furthermore define the detuning voltage ϵ_{12} =vP1−vP2 [23].

5.2. RESULTS

5.2.1. BICHROMATIC EDSR SPECTROSCOPY

Fig.5.1d displays the charge stability diagram of the double quantum dot system, obtained through rf-reflectometry charge sensing [24]. The device is operated in an in-plane magnetic field of 0.675 T, resulting in qubit frequencies of f_{Q1} = 1.514 GHz and f_{Q2} = 2.649 GHz. To investigate the bichromatic driving approach, we follow the pulse protocol outlined in Fig.5.2a. We initialise the Q1, Q2 qubits in the $|\downarrow\downarrow\rangle$ state by adiabatically pulsing ϵ_{12} from the (0, 2) to the (1, 1) charge state via the spin-orbit induced

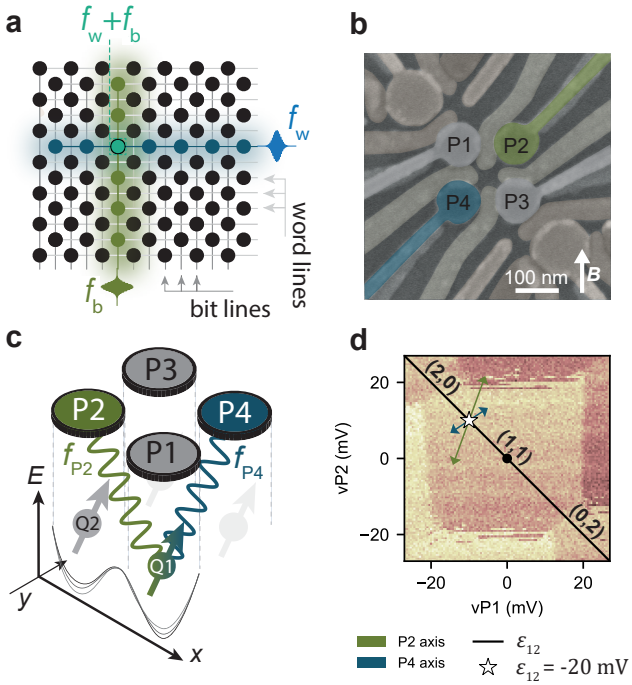

Figure 5.1: **Bichromatic control of a spin qubit. a,** Bichromatic driving in a crossbar architecture. **b,** False-color scanning electron microscopy of a 2x2 germanium quantum dot device, nominally identical to the one used here. **c,** Illustration of the four-qubit processor. We operate Q1 and Q2 with microwave bursts applied to P2 and P4. We model qubit rotations via AC detuning modulation (sketched potential). **d,** Charge stability diagram of the double quantum dot illustrating the (1, 1) charge sector and the detuning ϵ_{12} axis (black line). The white star indicates the gate voltages used for the qubit manipulation stage. The green and blue arrows indicate the displacement within the vP1, vP2 framework, when applying a microwave burst on P2 and P4, showcasing the different orientation of the driving fields. The displayed length of the arrows is proportional to the amplitude of the signal at the device, amplified by a factor of 5 for visibility.

anticrossing. Next, we manipulate the spins by two simultaneous microwave pulses on plunger gates P2 and P4, with a duration t_p and microwave frequencies f_{P2} and f_{P4}. We perform such two-tone qubit manipulation at the voltage point indicated in Fig.5.1c corresponding to $\epsilon_{12} = -20$ mV. Finally, we return to the (0, 2) charge sector and perform read-out using latched Pauli spin blockade [20].

The 2D EDSR spectroscopy in Fig.5.2b reveals resonance lines from monochromatic and bichromatic spin excitations. Monochromatic qubit transitions labelled as $Q1^{P2}$, $Q1^{P4}$, $Q2^{P2}$, $Q2^{P4}$ (with the superscript defining the driving plunger gate) are observed as vertical and horizontal lines at the corresponding Larmor frequencies. Bichromatic excitations appear as tilted resonance lines, with negative (positive) slopes indicating the frequency sum (difference) matching the qubit Lamor frequency. Three-photon bichromatic excitations can also be observed when a combination of two photons with the same frequency, and a third one with a different frequency match the qubit Larmor fre-

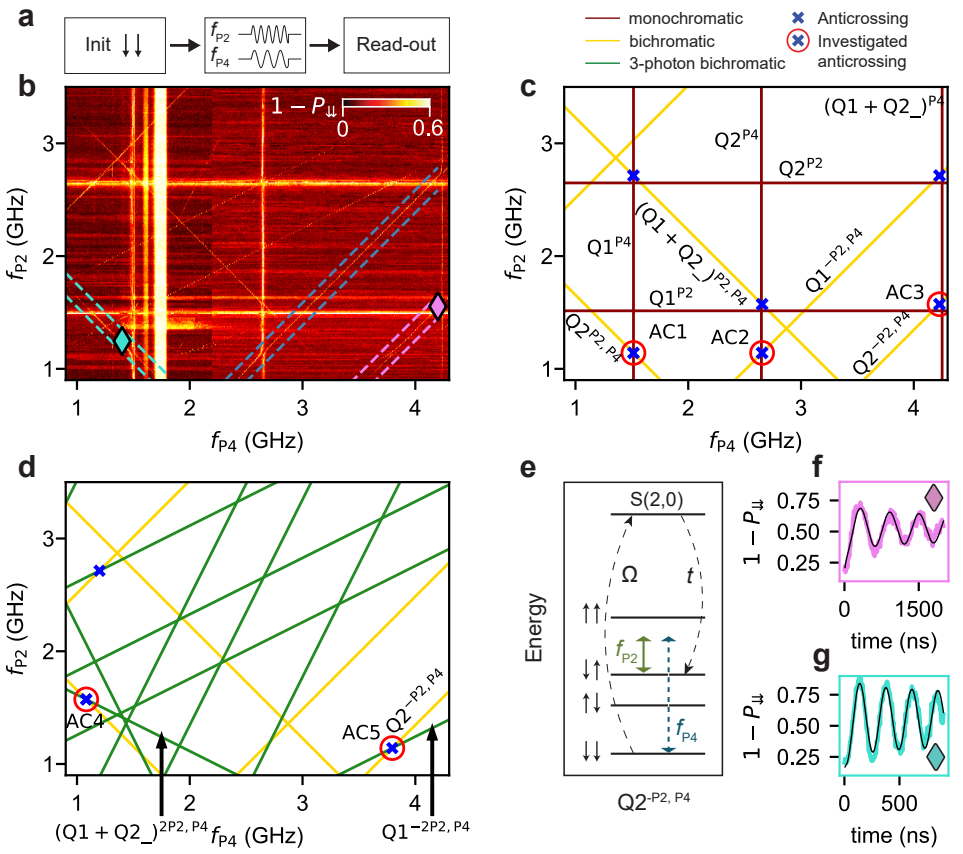

Figure 5.2: **Bichromatic EDSR spectroscopy.** **a,** Bichromatic control sequence. **b,** Single-shot probability versus f_{P4} and f_{P2}, at $\epsilon_{12} = -20$ mV. We include three turquoise, blue and purple dotted lines to enclose the bichromatic resonances of $Q2^{P2,P4}$, $Q1^{-P2,P4}$ and $Q2^{-P2,P4}$ respectively. The broad vertical excitation at $f_{P4} \sim 1.8$ GHz is associated to a transmission resonance in the lines, and not to a spin transition. **c, d** Monochromatic, bichromatic and three-photon bichromatic excitations in the 2D frequency plane, as predicted by theory. **e,** Energy diagram of a two-spin system with finite exchange and finite magnetic field. The green and blue arrows represent the applied microwave frequencies f_{P2} and f_{P4}, when driving the $Q2^{-P2,P4}$ transition. Driven spin-flipping processes originate from higher order processes via the S(2,0) state involving the spin-conserving tunneling term t and spin-flip tunneling term Ω. **f, g** Coherent Rabi oscillations of the $Q2^{-P2,P4}$ and $Q2^{P2,P4}$ bichromatic transition. The corresponding f_{P2} and f_{P4} frequencies are indicated with the purple and turquoise diamonds in **b**.

quency.

Figs. 5.2c, d depict the expected resonance lines considering the individual resonance frequencies of the two qubits. The qubits exchange interaction resulting from interdot tunnelling (55 MHz at $\epsilon_{12} = -20$ mV, see Section 5.4.3) is taken into account. To label the Larmor frequency of qubit i when qubit j is in the excited state, we use the notation $Qi\_$ (with $i, j \in \{1,2\}$ and $i \neq j$). The monochromatic transition from $|\downarrow\downarrow\rangle$ to $|\uparrow\uparrow\rangle$ driven by P4 is then denoted as $(Q1 + Q2\_)^{P4}$. A bichromatic transition can be visualised as a two-step process via a virtual state, as illustrated in Fig.5.2e. Following perturba-

tion theory, bichromatic spin transitions are activated thanks to spin-conserving (t) and spin-flipping (Ω) tunnelling terms, which hybridize the four possible spin states with the S(2,0) state, as discussed below and in Suppl. Note 8 [22].

We analyze three resonance lines (dashed lines in Fig.5.2b) resulting from bichromatic rotation of Q1 and Q2. The bichromatic Q1 spin resonance ($Q1^{-P2,P4}$) occurs when the frequency difference matches the Q1 Larmor frequency. Similarly, Q2 exhibits bichromatic resonance lines from both frequency difference ($Q2^{-P2,P4}$) and frequency sum ($Q2^{P2,P4}$). The bichromatic spin resonance $Q1^{P2,P4}$ is not investigated due to the presence of a high-pass filter (Section 5.4.5). The conditions for the three studied bichromatic qubit rotations are: $Q1^{-P2,P4}: f_{P4} - f_{P2} = f_{Q1}$, $Q2^{-P2,P4}: f_{P4} - f_{P2} = f_{Q2}$ and $Q2^{P2,P4}: f_{P4} + f_{P2} = f_{Q2}$. At these frequency combinations, we also achieve coherent bichromatic qubit rotations with a Rabi frequency exceeding 1 MHz, as we demonstrate in Figs. 5.2f, g and Fig. 5.8, Fig. 5.9, and Fig. 5.10.

5.2.2. ANTICROSSINGS IN THE BICHROMATIC SPECTROSCOPY AND AUTLER-TOWNES EFFECT

At the intersection of specific resonance lines (see Fig.5.2b), we also observe anticrossings (labelled as ACn with $n \in \{1,\ldots,5\}$ in Figs. 5.2c and d). In Fig.5.3, we analyse the evolution of the two bichromatic spin resonances, $Q2^{-P2,P4}$ and $Q2^{P2,P4}$, in the frequency plane. We vary the two microwave frequencies together to follow the two resonance

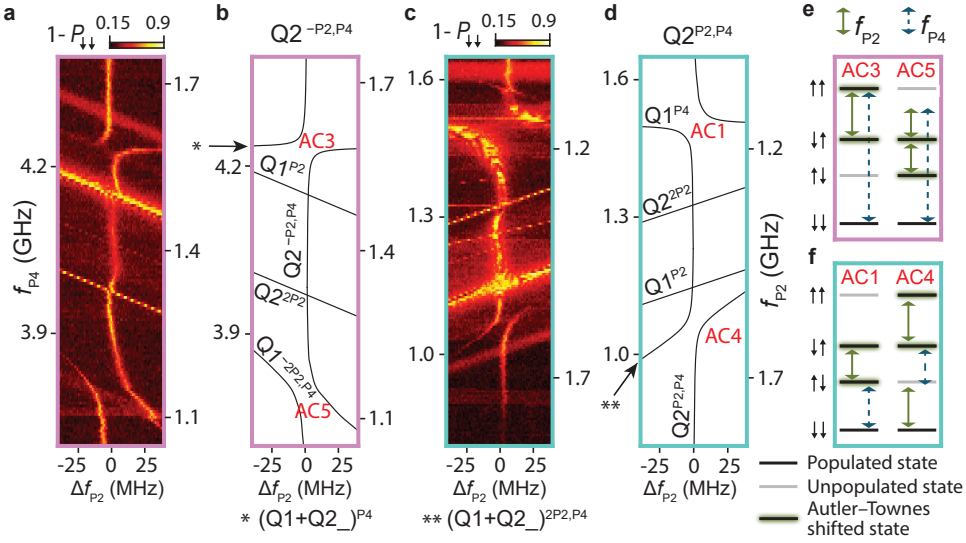

Figure 5.3: **Modelling the frequency anticrossings due to the Autler-Townes effect. a, c** Single-shot probabilities ($1 - P_{\downarrow\downarrow}$) in a frequency range around the bichromatic $Q2^{-P2,P4}$ and $Q2^{P2,P4}$ resonance conditions, respectively. These scans are higher-resolution measurements along the color-coded diagonals enclosed by two dashed lines in Fig.5.2b. Vertical lines of Fig.5.2b appear horizontal, and horizontal lines appear slightly tilted (as can be seen with $Q1^{P2}$ and $Q1^{P4}$ in **d**). The values on the f_{P2} axes are valid at $\Delta f_{P2} = 0$. **b, d** Calculated transitions nearby the $Q2^{-P2,P4}$ and $Q2^{P2,P4}$ resonances. **e, f** Illustration of the driven transitions at the four anticrossings. Strong driving via P2 induces a photon-dressed spin transition.

lines, using Δf_{P2} in the range of [-40, 40] MHz centered around the bichromatic resonance. This procedure allows to monitor in detail the Q2 bichromatic spin resonance within the boxed areas indicated in Fig.5.2b. The bichromatic resonance aligns with the expected value of $\Delta f_{P2} = 0$ for most of the frequency range. However, significant anticrossings occur when the resonance intersects with other qubit transitions. Examples of these anticrossings are observed at specific frequencies, and are labelled as AC5, AC3 (for $Q2^{-P2,P4}$), and AC4, AC1 (for $Q2^{P2,P4}$).

The appearance of anticrossings in the frequency plane, such as AC3 in Fig. 5.3a, result from resonant driving of monochromatic and bichromatic transitions from the $|\downarrow\downarrow\rangle$ state to higher (1,1) states. As shown in Figs. 5.3e-f, AC3 involves three resonant processes: the bichromatic transition $|\downarrow\downarrow\rangle \leftrightarrow |\downarrow\uparrow\rangle$, the monochromatic P4 drive $|\downarrow\downarrow\rangle \leftrightarrow |\uparrow\uparrow\rangle$, and the monochromatic P2 drive $|\downarrow\uparrow\rangle \leftrightarrow |\uparrow\uparrow\rangle$. Due to the greater driving efficiency of P2 compared to P4 (see projected amplitudes in Fig. 5.1c), the dominant transition is $|\downarrow\uparrow\rangle \leftrightarrow |\uparrow\uparrow\rangle$ (Suppl. Note 8 [22]).

Driving via P2 dresses up the spin states $|\downarrow\uparrow\rangle$ and $|\uparrow\uparrow\rangle$ with microwave photons. In the rotating frame where these states are degenerate in the absence of P2 driving, the eigenstates become dressed in the form $\frac{|\downarrow\uparrow\rangle \pm |\uparrow\uparrow\rangle}{\sqrt{2}}$, and the corresponding eigenvalues exhibit a splitting set by the Rabi frequency. In this context, dressing refers to the coherent interaction between the electromagnetic field and the spin system, resulting in entangled states of spins and photons becoming the eigenstates of the coupled system.

This effect, known as the Autler-Townes effect or ac Stark shift, has been observed in quantum optics and in strongly driven superconducting qubits [25, 26]. It is at the basis of control strategies for highly coherent solid-state qubits [27]. In particular, the continuous driving can decouple the spin from background magnetic field noise and thus extend their coherence [28, 29].

Due to the Autler-Townes effect, the resonance frequencies of the two weaker transitions ($|\downarrow\downarrow\rangle \leftrightarrow |\downarrow\uparrow\rangle$ and $|\downarrow\downarrow\rangle \leftrightarrow |\uparrow\uparrow\rangle$) are shifted by the Rabi frequency of the strongly driven $|\downarrow\uparrow\rangle \leftrightarrow |\uparrow\uparrow\rangle$ transition, resulting in the anticrossing between the resonance lines (AC3 in Figs. 5.3a, b).

We use a two-spin qubit Hamiltonian to model our system and gain a quantitative understanding. The model considers the lowest orbital in each dot, including four states in the (1,1) charge regime, as well as the (0,2) and (2,0) singlet states. Spin-conserving and spin-flip tunneling between the quantum dots are also included, with a coupling strength of t for spin-conserving transitions and Ω for spin-flip transitions (Suppl. Note 8A [22]). Despite neglecting additional electrical g-tensor modulations [2, 30], this minimal model successfully explains electrically driven spin transitions via ac modulation of the detuning voltage using both monochromatic and bichromatic resonance techniques. Here, spin dynamics occur through virtual transitions between the (1,1) spin states and the (0,2) and (2,0) singlet states, mediated by the spin-conserving and spin-flipping terms, as shown in Fig.5.2e.

Our model provides an explanation for the observed resonance crossings and anticrossings in Figs. 5.3a, c. Furthermore, by analyzing the five anticrossings AC1 to AC5 using Floquet theory as discussed in Suppl. Note 8C [22], we estimate the spin-conserving and spin-flip tunneling energies to be on average $t = (18.1 \pm 1.9)\mu eV$ and $\Omega = (14.3 \pm 2.4)\mu eV$ (Suppl. Note 8F [22]).

5.2.3. DEPENDENCE ON DETUNING ENERGY OF DOUBLE QUANTUM DOT

To verify our theoretical description, we investigate the dependence of the $Q1^{-P2,P4}$ resonance anticrossing on the detuning voltage. Experimental data and the expected detuning dependence from the model are shown in Figure 5.4. In the model, we use the average tunneling amplitudes and vary the detuning voltage. Moreover, we utilise an estimated detuning lever arm of $\alpha = 0.0917$ eV/V and quantum dot charging energy of $U = 2.56$ meV (Suppl. Note 8B [22]). Our theoretical model accurately captures the diminishing size of the anticrossing as the detuning approaches $\epsilon_{12} \sim 0$. Both the bichromatic and monochromatic resonance lines fade, indicating a reduced efficiency as detuning approaches zero. This is consistent with our model, since the transitions take place via the S(0,2) and S(2,0) states and in the high detuning limit the transition through S(0,2) dominates the driving. At zero detuning, the two contributions become equal,

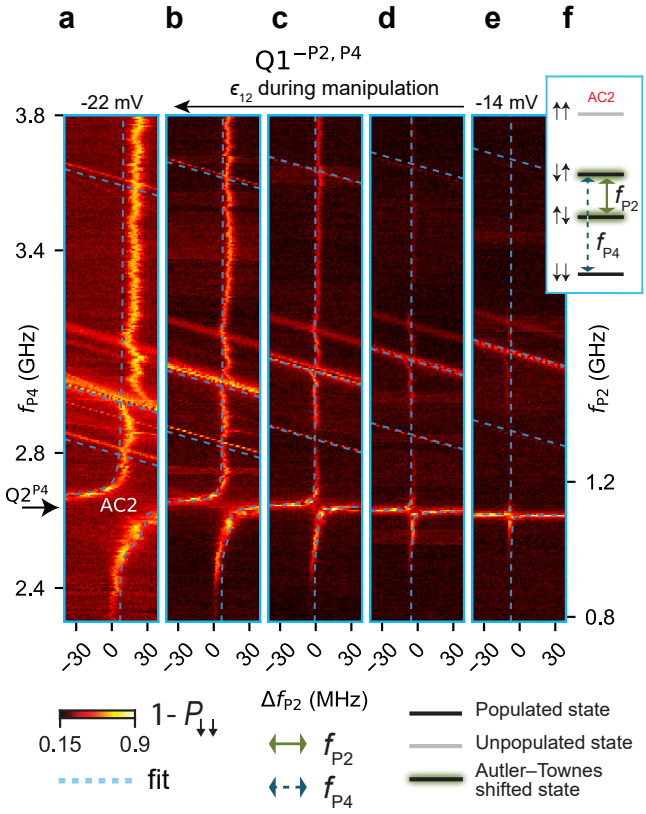

Figure 5.4: **Detuning dependence of the frequency anticrossings. a-e,** Bichromatic spectroscopy around the $f_{Q1} = f_{P4} - f_{P2}$ resonance versus detuning voltage. The anticrossing AC2 originates from strong driving of the $|\uparrow\downarrow\rangle \rightarrow |\downarrow\uparrow\rangle$ transition with P2 via the Autler-Townes shift. The AC2 frequency gap narrows down as a function of detuning voltage due to suppressed virtual transition from the (1, 1) to the (2, 0) charge state. We overlay the transition lines expected from theory. **f,** Driven transitions at AC2, displaying the four lowest states from Fig.5.2c.

while the Rabi frequency has a minimum.

The diminished efficiency of bichromatic operations near the charge-symmetry point supports the fundamental role of virtual interdot transitions as the underlying driving mechanism (Section 5.4.2). In Suppl. Note 8D [22], we discuss the limitations of our model and suggest that additional mechanisms, such as EDSR induced by g-tensor modulation, may be necessary to fully interpret all experimental observations [31–33].

5.3. CONCLUSIONS

Electric dipole spin resonance has enabled high-fidelity quantum gates on individual qubits, but a key challenge is the development of advanced operations for scalable control. Here, we have established bichromatic control of spin qubits, and turned challenges in EDSR [14] into an opportunity for addressable qubit control in larger arrays. Moreover, we showed the relevance of interdot motion in obtaining bichromatic and monochromatic driving. Furthermore, as the positions of the observed resonance anticrossings are predictible from the qubits parameters, we envision that, while on the one hand these can be exploited for the operation of dressed semiconductor qubits, on the other hand, these frequencies should be avoided when implementing bichromatic EDSR. Future experiments may focus on the optimization of bichromatic driving, for example by tuning parameters such as the interdot coupling, aiming to achieve high-fidelity control of large qubit arrays.

5.4. EXTENDED DATA

5.4.1. POWER DEPENDENCE OF ANTICROSSING AC2 ($Q1^{-P2,P4}$, $Q2^{P4}$)

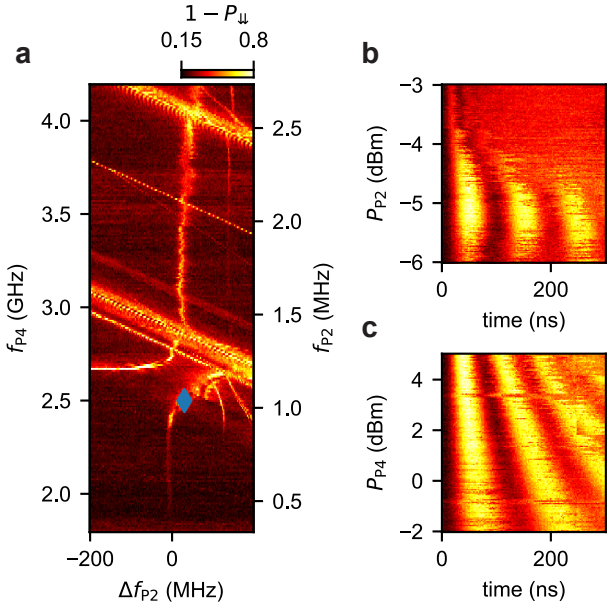

Figure 5.5: **Rabi oscillation of $Q1^{P4,-P2}$ as a function of microwave power applied to the two plunger gates at $\epsilon_{12} = -24$ mV. a,** EDSR spectroscopy map performed at ac driving power of $(P_{P2}, P_{P4}) = (-5, 3)$ dBm. **b, c** Rabi oscillations as a function of the power on the P2 and P4 driving gates. Here, the strong P2 driving field is resonant with the $\uparrow\downarrow \leftrightarrow \downarrow\uparrow$ transition. This results in a frequency shift of the Lamor frequency of the $\downarrow\downarrow \leftrightarrow \downarrow\uparrow$ transition when sweeping its power. In contrast, the weak P4 probe field does not alter the Lamor frequency, and sweeping its power leads, in fact, only to an increase in the Rabi frequency. This behaviour is consistent with the Autler-Townes splitting of the $\uparrow\downarrow$- and $\downarrow\uparrow$-state. Both plots are performed with $f_{P4} = 2.50$ GHz and $f_{P2} = 1.07$ GHz.

5.4.2. EDSR SPECTROSCOPY MAP AT ZERO DETUNING

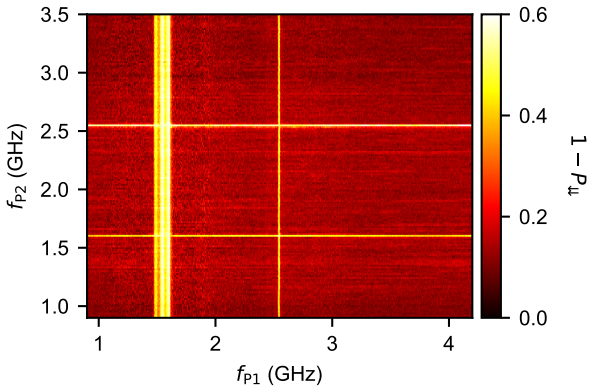

Figure 5.6: **Bichromatic EDSR spectroscopy at zero detuning voltage.** We prepare the double quantum dot system in the $\downarrow\downarrow$-state, apply the bichromatic control sequence, and measure the $1-P_{\downarrow\downarrow}$ probability. The major difference to Fig. 2 is the preparation of the system at zero detuning. In this configuration, only two vertical and two horizontal lines are observed, the monochromatic transitions Q1 at ~ 1.60 GHz and Q2 at ~ 2.55 GHz. Note that this plot has been taken with f_{P1} and f_{P2}, instead of f_{P2} and f_{P4}. However, we have also observed the absence of the bichromatic signal for f_{P2} and f_{P4} when decreasing the detuning.

5.4.3. EXCHANGE COUPLING AT OPERATION POINT

Here, we determine the exchange coupling at our operation point $\epsilon_{12} = -20$ mV by measuring the resonance frequencies f_{Q1}, $f_{Q1\_}$, f_{Q2}, and $f_{Q2\_}$, defined as:

$$\text{Q1}: \downarrow\downarrow \leftrightarrow \uparrow\downarrow \tag{5.1}$$

$$\text{Q1\_}: \downarrow\uparrow \leftrightarrow \uparrow\uparrow \tag{5.2}$$

$$\text{Q2}: \downarrow\downarrow \leftrightarrow \downarrow\uparrow \tag{5.3}$$

$$\text{Q2\_}: \uparrow\downarrow \leftrightarrow \uparrow\uparrow \tag{5.4}$$

We compare f_{Q1} with $f_{Q1\_}$, and f_{Q2}, $f_{Q2\_}$, obtaining similar values of 55 MHz for f_{Q1} and 57 MHz for f_{Q2}.

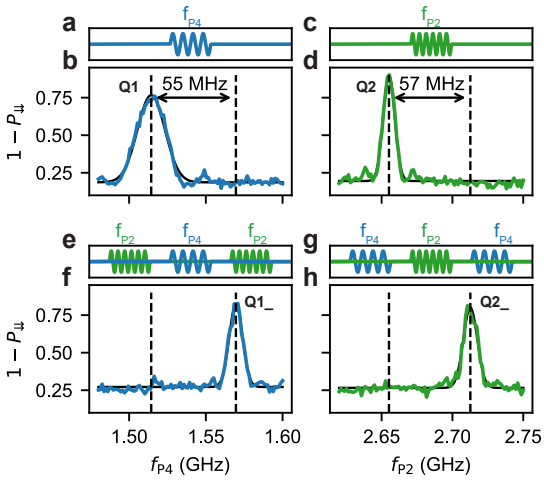

Figure 5.7: **Determination of exchange interaction via conditional EDSR spectroscopy. a, c, e, g,** Pulse sequences to prepare the control qubit in the two basis states and probe the target qubit. The blue (green) pulse is applied on P4 (P2) to control Q1 (Q2). **b, d, f, h** Measurement results from the corresponding pulse sequences to probe Q1, Q1_, Q2, and Q2_ respectively. The difference in resonance frequency concludes an exchange interaction of 56 MHz at a voltage of vP1 = -10 mV, and vP2 = 10 mV.

5

5.4.4. RESONANCE LINE IDENTIFICATION AND RABI ROTATIONS

To identify all the resonance lines of Figs. 3 and 4, we simulate the position of all the expected lines neglecting the Autler-Townes effect. We can write the considered bichromatic transitions as

$$m \cdot f_{\mathrm{P2}}^{\mathrm{offset}} + f_{\mathrm{P4}} = f_Q, m = \pm 1, \tag{5.5}$$

where f_Q represents the qubit frequencies f_{Q1} and f_{Q2}. Our expected resonance lines follow

$$f_{\mathrm{res}} = n_{\mathrm{P2}} \cdot f_{\mathrm{P2}} + n_{\mathrm{P4}} \cdot f_{\mathrm{P4}}, \tag{5.6}$$

where $f_{\mathrm{P2}} = f_{\mathrm{P2}}^{\mathrm{offset}} + \Delta f_{\mathrm{P2}}$. Here, f_{res} can be f_{Q1}, f_{Q2}, or $f_{\mathrm{Q1}} + f_{\mathrm{Q2\_}}$, and n_{P2} and n_{P4} are integers referring to the considered harmonic. By plugging in Eq. (5.5) into Eq. (5.6), we obtain

$$f_{\mathrm{P4}} = \frac{f_{\mathrm{res}}}{m \cdot n_{\mathrm{P2}} + n_{\mathrm{P4}}} + \frac{n_{\mathrm{P2}}}{m \cdot n_{\mathrm{P2}} + n_{\mathrm{P4}}} \cdot (m \cdot f_{Q1} - \Delta f_{\mathrm{P2}}) \tag{5.7}$$

We use these equations to calculate the expected resonance lines as visible in Fig. 5.8, Fig. 5.9, and Fig. 5.10.

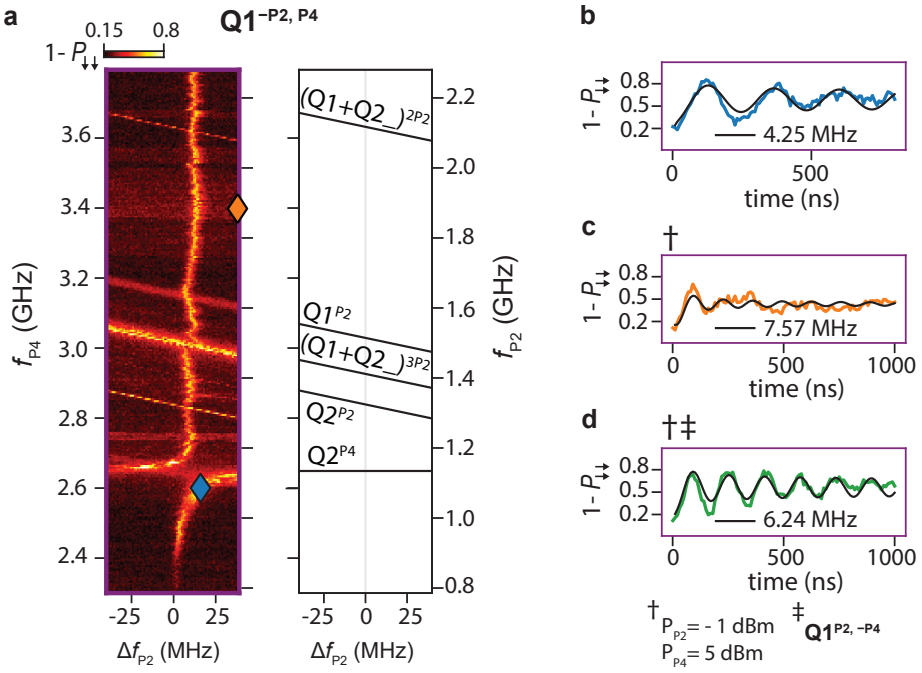

Figure 5.8: **Coherent Rabi control by bichromatic driving. a,** EDSR spectroscopy map of $Q1^{-P2,P4}$ with two indicated positions, where Rabi oscillations have been performed. **b, c,** Rabi oscillation corresponding to the blue and orange marker in (a). The marker of (c) are shifted 40 MHz away from the bichromatic line because the power on both plungers had to be increased from -5 to -1 dBm for P2 and from 3 to 5 dBm for P4 to see any oscillations. **d,** Rabi oscillations with similar power settings as in (c), but the values of f_{P2} and f_{P4} have been swapped, driving $Q1^{P2,-P4}$ instead of $Q1^{-P2,P4}$. This makes the corresponding marker falls outside the depicted regime shown in (a).

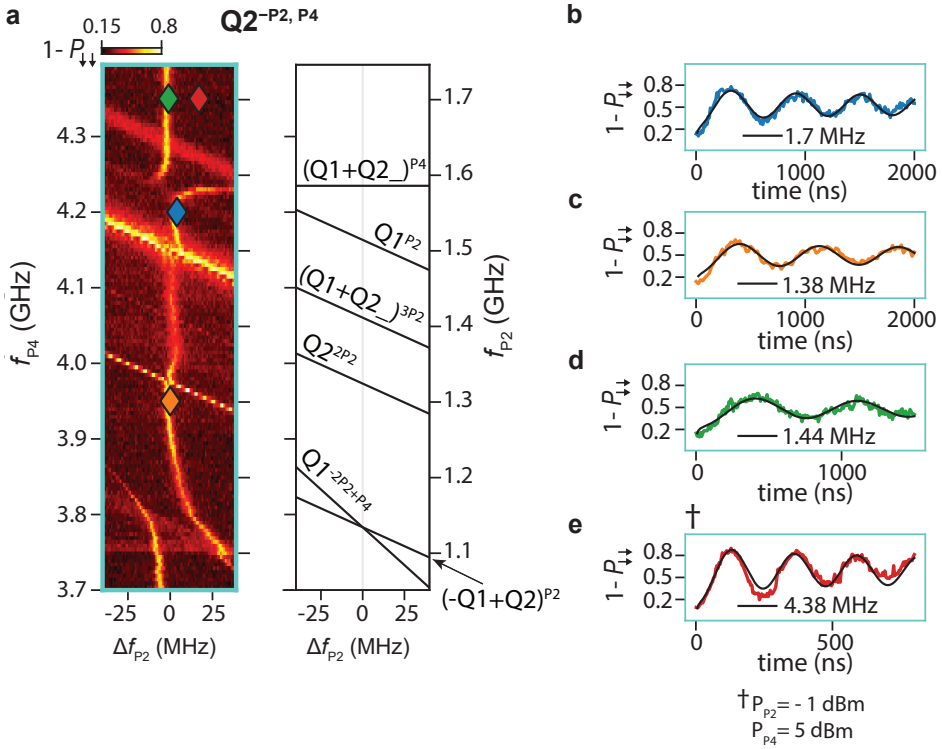

Figure 5.9: **Coherent Rabi control by bichromatic driving. a,** EDSR spectroscopy map of Q2$^{-P2,P4}$ with four indicated positions, where Rabi oscillations have been performed. **b, c, d, e** Rabi oscillation corresponding to the blue, orange, green, and red marker in (a). For the marker of (e) the power on both plungers increased from -5 to -1 dBm for P2 and from 3 to 5 dBm for P4.

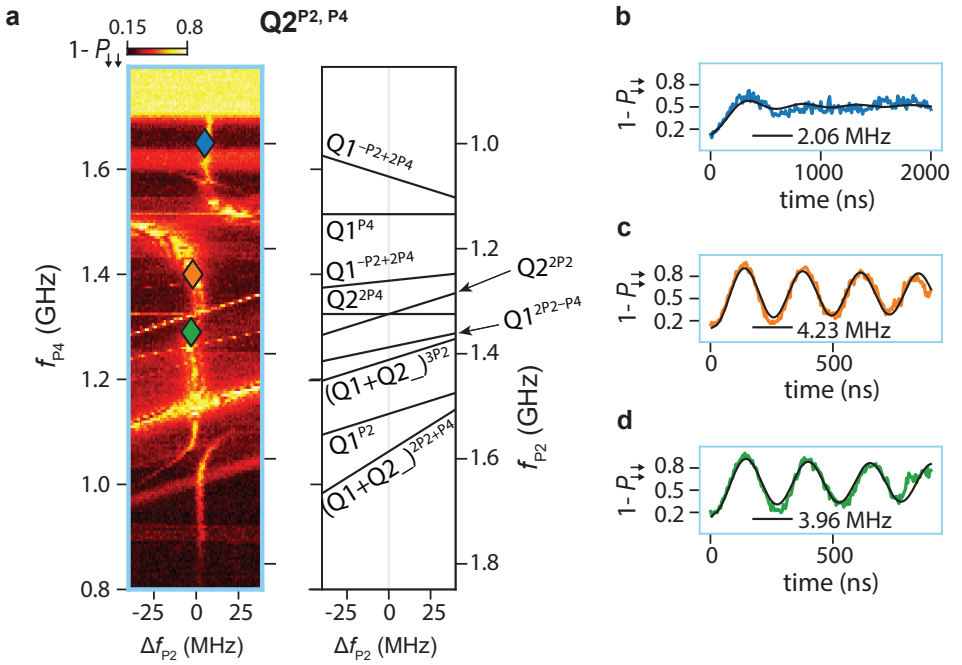

Figure 5.10: **Coherent Rabi control by bichromatic driving. a,** EDSR spectroscopy map of $Q2^{P2,P4}$ with three indicated positions, where Rabi oscillations have been performed. **b, c, d** Rabi oscillation corresponding to the blue, orange, and green marker in (a).

5.4.5. ATTENUATION

We approximate the amplitude arriving at the device by measuring the attenuation of the fridge lines of a comparable setup at cryogenic temperature, and the frequency response of an equivalent diplexer that is used to combine the microwave signal with the baseband pulses from the AWG. The measurement data with the Savitzky-Golay filter can be seen in Fig. 5.11. Since the measurement has only been performed on a similar setup, this constitutes only an approximation, but the general shape of the attenuation is expected to be the same.

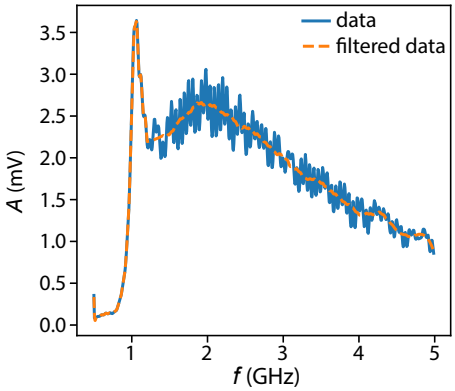

Figure 5.11: **Attenuation caused by diplexer and fridge cables.** Amplitude of the signal arriving at the device level considering $P_{P4} = 2.5\,\text{dBm}$. The signal of P2 with $P_{P2} = -6\,\text{dBm}$ is approximately the same since it has 8.5 dB less attenuation on the lines. A Savitzky-Golay filter is applied on the data, the result is shown with orange-dashed line.

5.4.6. MONOCHROMATIC RABI FREQUENCIES

Table 5.1 shows the measured monochromatic Rabi frequencies of the two considered qubits. Notably, $Q1\_^{P4}$ differs by a factor of two from $Q1^{P4}$. P_{mw} is the microwave power at the output of the signal generator, and corresponds to P_{P2} for Q1 and P_{P2} for Q2.

Table 5.1

Transition	$f_{\textbf{res}}$ **(GHz)**	$t_{\textbf{Rabi}}$ **(ns)**	$f_{\textbf{Rabi}}$ **(MHz)**	$P_{\textbf{mw}}$ **(dBm)**	A **(mV)**
$Q1^{P4}$	1.51	42.5	11.76	2.5	2.3
$Q1\_^{P4}$	1.57	88.6	5.65	2.5	2.4
$Q2^{P2}$	2.65	24.2	20.66	-6.0	2.3
$Q2\_^{P2}$	2.74	22.6	22.1	-5.8	2.2

BIBLIOGRAPHY

[1] Anasua Chatterjee et al. “Semiconductor qubits in practice”. In: Nature Reviews Physics 3.3 (Mar. 2021), pp. 157–177. ISSN: 2522-5820.

[2] Guido Burkard et al. “Semiconductor spin qubits”. In: Rev. Mod. Phys. 95 (2 June 2023), p. 025003.

[3] L. M. K. Vandersypen et al. “Interfacing spin qubits in quantum dots and donors—hot, dense, and coherent”. In: npj Quantum Information 3.1 (Sept. 2017), p. 34. ISSN: 2056-6387.

[4] D. P. Franke et al. “Rent’s rule and extensibility in quantum computing”. In: Microprocessors and Microsystems 67 (June 2019), pp. 1–7. ISSN: 0141-9331.

[5] Ruoyu Li et al. “A crossbar network for silicon quantum dot qubits”. In: Science Advances 4.7 (2018), eaar3960.

[6] Francesco Borsoi et al. “Shared control of a 16 semiconductor quantum dot crossbar array”. In: Nature Nanotechnology (Aug. 2023). ISSN: 1748-3395.

[7] Zoltán György, András Pályi, and Gábor Széchenyi. “Electrically driven spin resonance with bichromatic driving”. In: Phys. Rev. B 106 (15 Oct. 2022), p. 155412.

[8] W. A. Coish and Daniel Loss. “Exchange-controlled single-electron-spin rotations in quantum dots”. In: Phys. Rev. B 75 (16 Apr. 2007), p. 161302.

[9] E A Laird et al. “A new mechanism of electric dipole spin resonance: hyperfine coupling in quantum dots”. In: Semiconductor Science and Technology 24.6 (May 2009), p. 064004.

[10] Emmanuel I. Rashba. “Mechanism of half-frequency electric dipole spin resonance in double quantum dots: Effect of nonlinear charge dynamics inside the singlet manifold”. In: Phys. Rev. B 84 (24 Dec. 2011), p. 241305.

[11] P. Scarlino et al. “Second-Harmonic Coherent Driving of a Spin Qubit in a Si/SiGe Quantum Dot”. In: Phys. Rev. Lett. 115 (10 Sept. 2015), p. 106802.

[12] Judit Romhányi, Guido Burkard, and András Pályi. “Subharmonic transitions and Bloch-Siegert shift in electrically driven spin resonance”. In: Phys. Rev. B 92 (5 Aug. 2015), p. 054422.

[13] K. Takeda et al. “Optimized electrical control of a Si/SiGe spin qubit in the presence of an induced frequency shift”. In: npj Quantum Information 4.1 (Oct. 2018), p. 54. ISSN: 2056-6387.

[14] Brennan Undseth et al. “Nonlinear response and crosstalk of strongly driven silicon spin qubits”. In: Phys. Rev. Appl. 19 (4 Apr. 2023), p. 044078.

[15] Will Gilbert et al. “On-demand electrical control of spin qubits”. In: Nature Nanotechnology 18.2 (Feb. 2023), pp. 131–136. ISSN: 1748-3395.

[16] Stefano Bosco et al. “Phase driving hole spin qubits”. In: Phys. Rev. Lett. 131 (19 Nov. 2023), p. 197001.

[17] Harry Levine et al. “High-Fidelity Control and Entanglement of Rydberg-Atom Qubits”. In: Phys. Rev. Lett. 121 (12 Sept. 2018), p. 123603.

[18] Sepehr Ebadi et al. “Quantum phases of matter on a 256-atom programmable quantum simulator”. In: Nature 595.7866 (July 2021), pp. 227–232. ISSN: 1476-4687.

[19] Joseph A. Valery et al. “Dynamical Sweet Spot Engineering via Two-Tone Flux Modulation of Superconducting Qubits”. In: PRX Quantum 3 (2 May 2022), p. 020337.

[20] N. W. Hendrickx et al. “A four-qubit germanium quantum processor”. In: Nature 591 (2021), pp. 580–585.

[21] M. Lodari et al. “Low percolation density and charge noise with holes in germanium”. In: Mater. Quantum. Technol. 1 (2021), p. 011002.

[22] See Supplementary Material of PRL 132, 067001 (2024).

[23] T. Hensgens et al. “Quantum simulation of a Fermi-Hubbard model using a semiconductor quantum dot array”. In: Nature 548 (2017), pp. 70–73.

[24] W. I. L. Lawrie et al. “Spin Relaxation Benchmarks and Individual Qubit Addressability for Holes in Quantum Dots”. In: Nano Lett. 20.10 (2020). PMID: 32833455, pp. 7237–7242.

[25] M. Baur et al. “Measurement of Autler-Townes and Mollow Transitions in a Strongly Driven Superconducting Qubit”. In: Phys. Rev. Lett. 102 (24 June 2009), p. 243602.

[26] Mika A. Sillanpää et al. “Autler-Townes Effect in a Superconducting Three-Level System”. In: Phys. Rev. Lett. 103 (19 Nov. 2009), p. 193601.

[27] I. Hansen et al. “Implementation of an advanced dressing protocol for global qubit control in silicon”. In: Applied Physics Reviews 9.3 (Sept. 2022), p. 031409. ISSN: 1931-9401.

[28] Arne Laucht et al. “A dressed spin qubit in silicon”. In: Nature Nanotechnology 12.1 (Jan. 2017), pp. 61–66. ISSN: 1748-3395.

[29] Kevin C. Miao et al. “Universal coherence protection in a solid-state spin qubit”. In: Science 369.6510 (2020), pp. 1493–1497.

[30] Biel Martinez et al. “Hole spin manipulation in inhomogeneous and nonseparable electric fields”. In: Phys. Rev. B 106 (23 Dec. 2022), p. 235426.

[31] Maximilian Russ et al. “High-fidelity quantum gates in Si/SiGe double quantum dots”. In: Phys. Rev. B 97 (8 Feb. 2018), p. 085421.

[32] N. W. Hendrickx et al. “Sweet-spot operation of a germanium hole spin qubit with highly anisotropic noise sensitivity”. In: Nature Materials (May 2024). ISSN: 1476-4660.

[33] Abhikbrata Sarkar et al. “Electrical operation of planar Ge hole spin qubits in an in-plane magnetic field”. In: Phys. Rev. B 108 (24 Dec. 2023), p. 245301.

6

COHERENT SPIN QUBIT SHUTTLING THROUGH GERMANIUM QUANTUM DOTS

Quantum links can interconnect qubit registers and are therefore essential in networked quantum computing. Semiconductor quantum dot qubits have seen significant progress in the high-fidelity operation of small qubit registers but establishing a compelling quantum link remains a challenge. Here, we show that a spin qubit can be shuttled through multiple quantum dots while preserving its quantum information. Remarkably, we achieve these results using hole spin qubits in germanium, despite the presence of strong spin-orbit interaction. In a minimal quantum dot chain, we accomplish the shuttling of spin basis states over effective lengths beyond 300 µm and demonstrate the coherent shuttling of superposition states over effective lengths corresponding to 9 µm, which we can extend to 49 µm by incorporating dynamical decoupling. These findings indicate qubit shuttling as an effective approach to route qubits within registers and to establish quantum links between registers.

Parts of this chapter have been published in F. van Riggelen-Doelman, C.-A. Wang, S.L. de Snoo, W.I.L. Lawrie, N.W. Hendrickx, M. Rimbach-Russ, A. Sammak, G. Scappucci, C. Déprez, and M. Veldhorst, Coherent spin qubit shuttling through germanium quantum dots, *Nature Communication* **15**, 5716 (2024).

6.1. INTRODUCTION

The envisioned approach for semiconductor spin qubits towards fault-tolerant quantum computation centers on the concept of quantum networks, where qubit registers are interconnected via quantum links [1]. Significant progress has been made in controlling few-qubit registers [2, 3]. Recent efforts have led to demonstrations of high fidelity single- and two-qubit gates [4–7], quantum logic above one Kelvin [8–10] and operation of a 16 quantum dot array [11]. However, scaling up to larger qubit numbers requires changes in the device architecture [12, 13].

Inclusion of short-range and mid-range quantum links could be particularly effective to establish scalability, addressability, and qubit connectivity. The coherent shuttling of electron or hole spins is an appealing concept for the integration of such quantum links in spin qubit devices. Short-range coupling, implemented by shuttling a spin qubit through quantum dots in an array, can provide flexible qubit routing and local addressability [14, 15]. Moreover, it allows to increase connectivity beyond nearest-neighbour coupling and decrease the number of gates needed to execute algorithms. Mid-range links, implemented by shuttling spins through a multitude of quantum dots, may entangle distant qubit registers for networked computing and allow for qubit operations at dedicated locations [14, 16–18]. Furthermore, such quantum buses could provide space for the integration of on-chip control electronics [1], depending on their footprint.

The potential of shuttling-based quantum buses has stimulated research on shuttling electron charge [19–21] and spin [15, 22–29]. While nuclear spin noise prevents high-fidelity qubit operation in gallium arsenide, demonstrations of coherent transfer of individual electron spins through quantum dots are encouraging [22–26]. In silicon, qubits can be operated with high-fidelity and this has been employed to displace a spin qubit in a double quantum dot [15, 27]. Networked quantum computers, however, will require integration of qubit control and shuttling through chains of quantum dots, incorporating quantum dots that have at least two neighbours.

Meanwhile, quantum dots defined in strained germanium (Ge/SiGe) heterostructures have emerged as a promising platform for hole spin qubits [30, 31]. The high quality of the platform allowed for rapid development of single spin qubits [32, 33], singlet-triplet qubits [34–36], a four qubit processor [2], and a 4×4 quantum dot array with shared gate control [11]. While the strong spin orbit interaction allows for fast and all-electrical control, the resulting anisotropic g-tensor [31, 37] complicates the spin dynamics and may challenge the feasibility of a quantum bus.

Here, we demonstrate that spin qubits can be shuttled through quantum dots. These experiments are performed with two hole spin qubits in a 2×2 germanium quantum dot array. Importantly, we operate in a regime where we can implement single qubit logic and coherently transfer spin qubits through an intermediate quantum dot. Furthermore, by performing experiments with precise voltage pulses and sub-nanosecond time resolution, we can mitigate finite qubit rotations induced by spin-orbit interactions. In these optimized sequences we find that the shuttling performance is limited by dephasing and can be extended through dynamical decoupling.

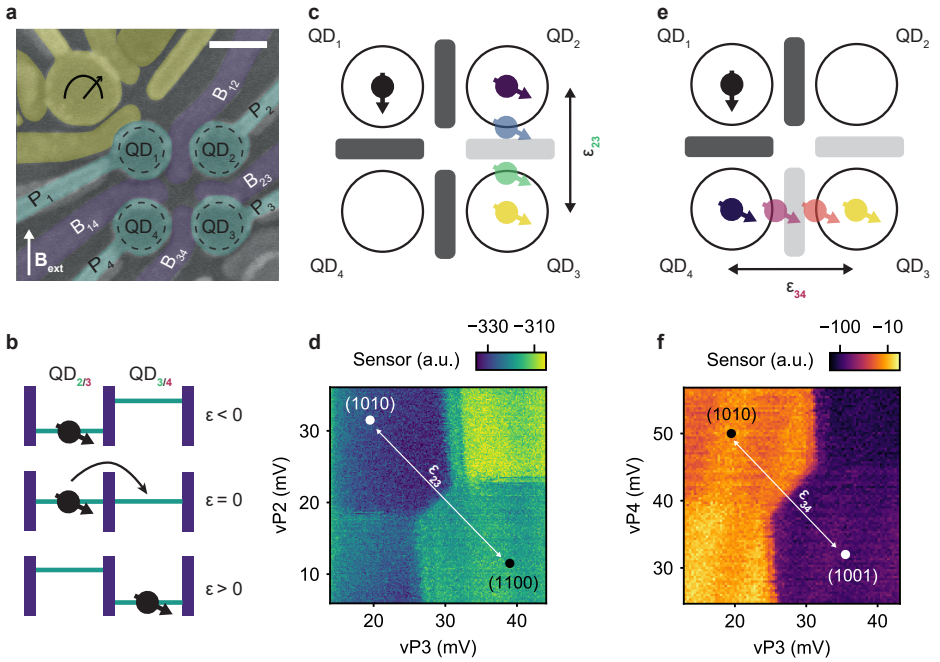

Figure 6.1: **Coherent shuttling of hole spin qubits in germanium double quantum dots - schematics and detuning axes. a**, False colored scanning electron microscope image of a representative quantum dot device. The quantum dots are formed under the plunger gates (light blue) and separated by barrier gates (dark blue) which control the tunnel couplings. A single hole transistor is defined by the yellow gates and is used as charge sensor. The scale bar corresponds to 100 nm. Unless specified otherwise, an external magnetic field of 0.25 T is applied in the direction indicated by the arrow. **b**, Schematic showing the principle of bucket-brigade-mode shuttling. The detuning energy $\epsilon_{23/34}$ between the two quantum dots is progressively changed such that it becomes energetically favorable for the hole to tunnel from one quantum dot to another. **c**, **e**, Schematic illustrating the shuttling of a spin qubit between QD_2 and QD_3 (e) and between QD_3 and QD_4 (i). **d**, **f**, Charge stability diagrams of QD_2-QD_3 (f) and QD_3-QD_4 (j). To shuttle the qubit from one site to another, the virtual plunger gate voltages are varied along the detuning axis (white arrow), which crosses the interdot charge transition line.

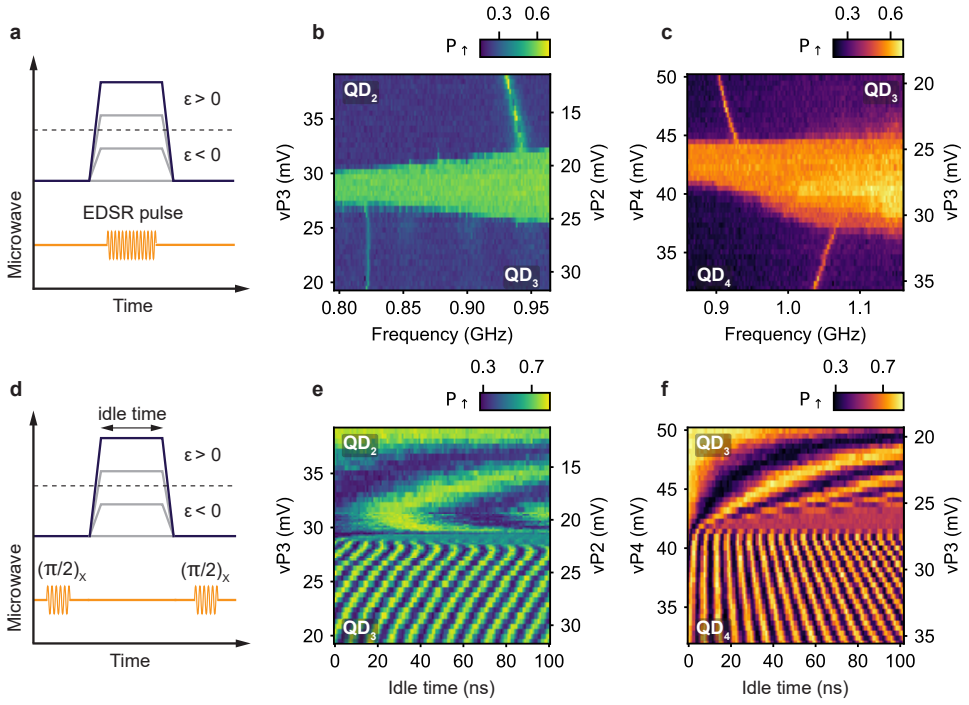

Figure 6.2: **Coherent shuttling of hole spin qubits in germanium double quantum dots - measurement results. a**, Schematic of the pulses used for the shuttling experiments shown in (b) and (c), where the resonance frequency of the qubit is probed after the application of a detuning pulse using a 4 μs EDSR pulse. **b, c** Probing of the resonance frequency along the detuning axis for the double quantum dot QD_2-QD_3 (b) and QD_3-QD_4 (c). The ramp time used to change the detuning is 40 ns for the measurement shown in (b) and 12 ns for the measurement shown in (c). Nearby the charge transition, the resonance frequency cannot be resolved due to a combination of effects discussed in Section 6.8.1. **d**, Schematic of the pulses used for coherent shuttling experiments of which the results are shown in (e) and (f). The qubit is prepared in a superposition state using a $\pi/2$ pulse and is transferred to the empty quantum dot with a detuning pulse of varying amplitude, and then brought back to its initial position after an idle time. After applying another $\pi/2$ pulse we readout the spin state. **e**, **f**, Coherent free evolution of a qubit during the shuttling between QD_2-QD_3 (e) and QD_3-QD_4 (f). Since the Larmor frequency varies along the detuning axes, the qubit initialized in a superposition state acquires a phase that varies with the idle time resulting in oscillations in the spin-up $P_\uparrow$ probabilities.

6.2. RESULTS

6.2.1. COHERENT SHUTTLING OF SINGLE HOLE SPIN QUBITS

Fig. 6.1.a shows a germanium 2×2 quantum dot array identical to the one used in the experiment [2]. The chemical potentials and the tunnel couplings of the quantum dots are controlled with virtual gates (vP_i, vB_{ij}), which consist of combinations of voltages on the plunger gates and the barrier gates. We operate the device with two spin qubits in quantum dots QD_1 and QD_2 and initialised the $|\downarrow\downarrow\rangle$ state (see Section 6.4). We use the qubit in QD_1 as an ancilla to readout the hole spin in QD_2, using latched Pauli spin blockade [2, 38, 39]. The other qubit starts in QD_2 and is shuttled to the other quantum dots by changing the detuning energies ($\epsilon_{23/34}$) between the quantum dots (Fig. 6.1.b, c and e). The detuning energies are varied by pulsing the plunger gate voltages as illustrated in Fig. 6.1.d and f. Additionally, we increase the tunnel couplings between QD_2-QD_3 and QD_3-QD_4 before shuttling to allow for adiabatic charge transfer. The hole carrying the spin remains in its orbital ground state and with increasing $|\epsilon|$, the charge becomes localized in the quantum dot with the lowest chemical potential as displayed in Fig. 6.1.b. In our experiments, we tune to have adiabatic evolution with respect to charge, and study adiabatic and diabatic shuttling with respect to spin.

The g-tensor of hole spin qubits in germanium is sensitive to the local electric field. Therefore, the Larmor frequency (f_L) is different in each quantum dot [32–34]. We exploit this effect to confirm the shuttling of a hole spin from one quantum dot to another. In Fig. 6.2.a. we show the experimental sequence used to measure the qubit resonance frequency, while changing the detuning to transfer the qubit. Fig 6.2.b (c) shows the experimental results for spin transfers from QD_2 to QD_3 (QD_3 to QD_4). Two regions can be clearly distinguished in between which f_L varies by 110 (130) MHz. This obvious change in f_L clearly shows that the hole is shuttled from QD_2 to QD_3 (QD_3 to QD_4) when applying a sufficiently large detuning pulse. To investigate whether such transfer is coherent, we probe the free evolution of qubits prepared in a superposition state after applying a detuning pulse (Fig. 6.2.d) [27]. The resulting coherent oscillations are shown in Fig. 6.2.e (f). They are visible over the full range of voltages spanned by the experiment and arise from a phase accumulation during the idle time. Their frequency f_{osc} is determined by the difference in resonance frequency between the starting and the end points in detuning as shown in Fig. 6.9. The abrupt change in f_{osc} marks the point where the voltage pulse is sufficiently large to transfer the qubit from QD_2 to QD_3 (QD_3 to QD_4). These results clearly demonstrate that single hole spin qubits can be coherently transferred.

6.2.2. THE EFFECT OF STRONG SPIN-ORBIT INTERACTION ON SPIN SHUTTLING

The strong spin-orbit interaction in our system has a significant impact on the spin dynamics during the shuttling. It appears when shuttling a qubit in a $|\downarrow\rangle$ state between QD_2 and QD_3 using fast detuning pulses with voltage ramps of 4 ns. Doing this generates coherent oscillations shown in Fig. 6.3.b that appear only when the qubit is in QD_3. They result from the strong spin-orbit interaction and the use of an almost in-plane magnetic field [40]. In this configuration, the direction of the spin quantization axis depends strongly on the local electric field [35, 37, 41–43] and can change significantly between

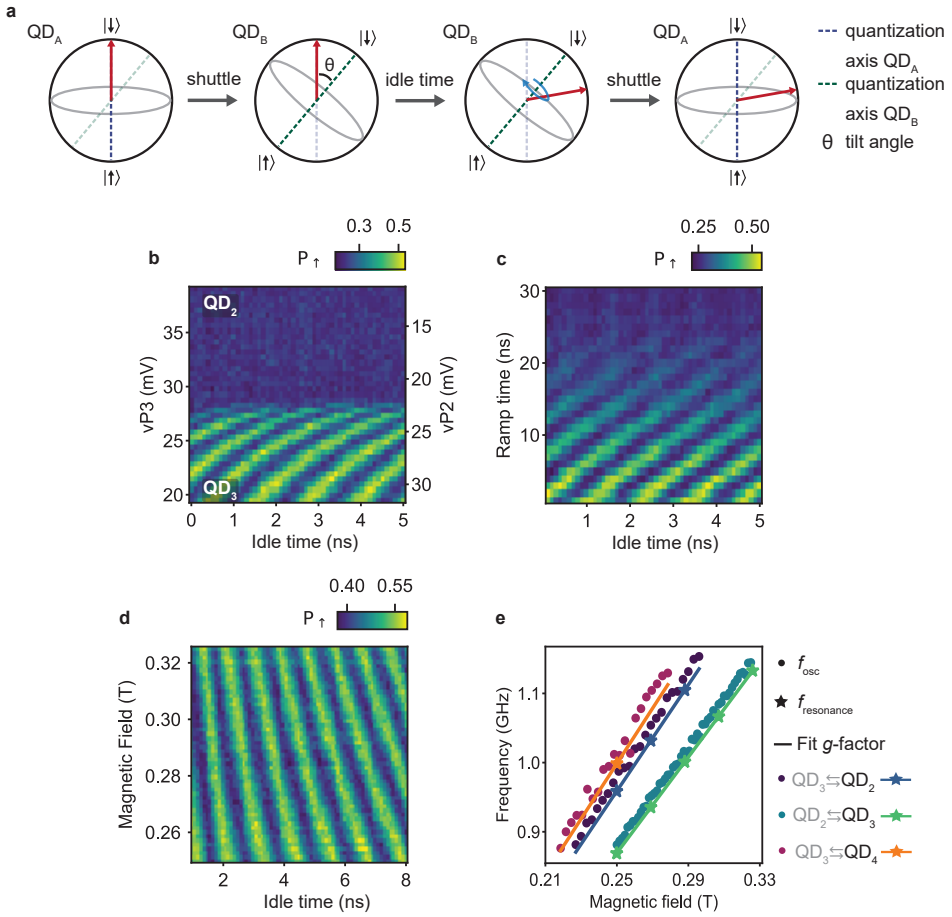

Figure 6.3: **Rotations induced while shuttling by the difference in quantization axes. a**, Schematic explaining the effect of the change in quantization axis direction that the qubit experiences during the shuttling process. The difference in quantization axis between quantum dots is caused by the strong spin-orbit interaction. **b**, Oscillations induced by the change in quantization axis while shuttling diabatically a qubit in a $|\downarrow\rangle$ state between QD_2 and QD_3. Ramp times of 4 ns are used for the detuning pulses. Note that the oscillations have a reduced visibility, meaning that the difference in quantization axes does not induce a full spin flip. The angle between the quantization axes of the two quantum dots can be estimated from the amplitude of the oscillations, see Section 6.8.2. **c**, Oscillations due to the change in quantization axis at a fixed point in detuning, as function of the voltage pulse ramp time used to shuttle the spin. When the ramp time is long enough, typically above 30 ns, the spin is shuttled adiabatically and the oscillations vanish. **d**, Magnetic-field dependence of the oscillations induced by the difference in quantization axis. **e**, Frequency of the oscillations f_{osc} induced by the change in quantization axis as a function of magnetic field for different shuttling processes. The oscillation frequency f_{osc} for QD_3 is extracted from measurements displayed in (d) (and similar experiments for the other quantum dot pairs) and is plotted with points. f_{osc} scales linearly with the magnetic field. Comparing f_{osc} with resonance frequencies measured using EDSR pulses (data points depicted with stars) reveals that f_{osc} is given by the Larmor frequency of the quantum dot towards which the qubit is shuttled (black label).

neighbouring quantum dots. Therefore, rapid shuttling of a hole results in a change of angle between the spin state and the local spin quantization axis. In particular, a qubit in a basis state in QD_2 becomes a qubit in a superposition state in QD_3 when it is shuttled diabatically with respect to the change in quantization axis. Consequently, the spin precesses around the quantization axis of QD_3 until it is shuttled back (Fig. 6.3.a). This leads to qubit rotations and the aforementioned oscillations.

While these oscillations are clearly visible for voltage pulses with ramp times t_{ramp} of few nanoseconds, they fade as the ramp times are increased, as shown in Fig. 6.3.c, and vanish for $t_{\text{ramp}} > 30$ ns. The qubit is then transferred adiabatically, can follow the change in quantization axis and therefore remains in the spin basis state in both quantum dots. From the visibility of the oscillations, we estimate that the quantization axis of QD_3 (QD_4) is tilted by at least 42° (33°) compared to the quantization axis of QD_2 (QD_3). These values are corroborated by independent estimations made by fitting the evolution of f_L along the detuning axes (see Section 6.8.2).

Fig. 6.3.d and Fig. 6.3.e display the magnetic field dependence of the oscillations generated by diabatic shuttling. Their frequencies f_{osc} increase linearly with the field and match the Larmor frequencies f_L measured for a spin in the target quantum dot. This is consistent with the explanation that the oscillations are due to the spin precessing around the quantization axis of the second quantum dot.

6.2.3. SHUTTLING PERFORMANCE

To quantify the performance of shuttling a spin qubit, we implement the experiments depicted in Fig. 6.4.a, c and d [15, 27] and study how the state of a qubit evolves depending on the number of subsequent shuttling events. For hole spins in germanium, it is important to account for rotations induced by the spin-orbit interaction. This can be done by aiming to avoid unintended rotations, or by developing methods to correct them. An example of the first approach is transferring the spin qubits adiabatically. This implies using voltage pulses with ramps of tens of nanoseconds, which are significant with respect to the dephasing time. However, this strongly limits the shuttling performance (see Fig. 6.14). Instead, we can mitigate rotations by carefully tuning the duration of the voltage pulses, such that the qubit performs an integer number of 2π rotations around the quantization axis of the respective quantum dot. This approach is demanding, as it involves careful optimization of the idle times in each quantum dot as well as the ramp times, as depicted in Fig. 6.4.b. However, it allows for fast shuttling, with ramp times of typically 4 ns and idle times of 1 ns, significantly reducing the dephasing experienced by the qubit during the shuttling. We employ this strategy in the rest of our experiments.

We first characterize the shuttling of a spin qubit initialized in a basis state. We do this by preparing a qubit in a $|\uparrow\rangle$ or $|\downarrow\rangle$ state and transferring it multiple times between the quantum dots. Fig. 6.5.a and b display the spin-up fraction $P_\uparrow$ measured as a function of the number of shuttling steps n. The probability of ending up in the initial state shows a clear exponential dependence on n. No oscillations of $P_\uparrow$ with n are visible, confirming that the pulses have been successfully optimized to account for unwanted spin rotations. We extract the characteristic decay constants n^* by fitting the data for the shuttling of qubits prepared in $|\uparrow\rangle$ and $|\downarrow\rangle$ states separately as they originate from distinct sets of

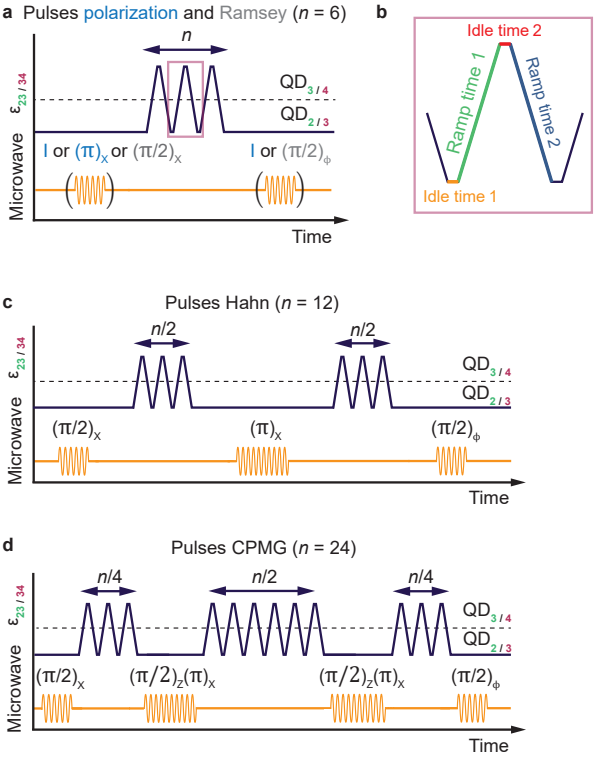

Figure 6.4: **Quantifying the performance for the shuttling of basis states in double quantum dots - pulse sequences. a**, Schematic of the pulse sequence used for quantifying the performance of shuttling basis states (blue) or a superposition state (grey). The spin qubit is prepared in the quantum dot where the shuttling experiment starts, by either applying an identity gate (shuttling a $|\downarrow\rangle$ state), a $(\pi)_X$ pulse (shuttling a $|\uparrow\rangle$ state) or $(\pi/2)_X$ pulse (shuttling a superposition state, also referred to as Ramsey shuttling experiments). Detuning pulses are applied to the plunger gates to shuttle the hole from one quantum dot to another, back and forth, and finally the appropriate pulses are applied to prepare for readout. Moving the qubit from one quantum dot to another is counted as one shuttling event $n = 1$. Since the hole always needs to be shuttled back for readout, n is always an even number. The schematic shows an example for $n = 6$. **b**, Zoom-in on the detuning pulses used for the shuttling. To make an integer number of 2π rotation(s) around the quantization axis of the second quantum dot, all ramp and idle times in the pulse need to be optimized. **c**, Pulse sequence used for implementing a Hahn echo shuttling experiment. In the middle of the shuttling experiment, an echo pulse $(\pi)_X$ is applied in the quantum dot where the spin qubit was initially prepared. Example for $n = 12$. **d**, Pulse sequence for a CPMG shuttling experiment. Two $(\pi/2)_Z(\pi)_X$ pulses are inserted between the shuttling pulses. Example for $n = 24$.

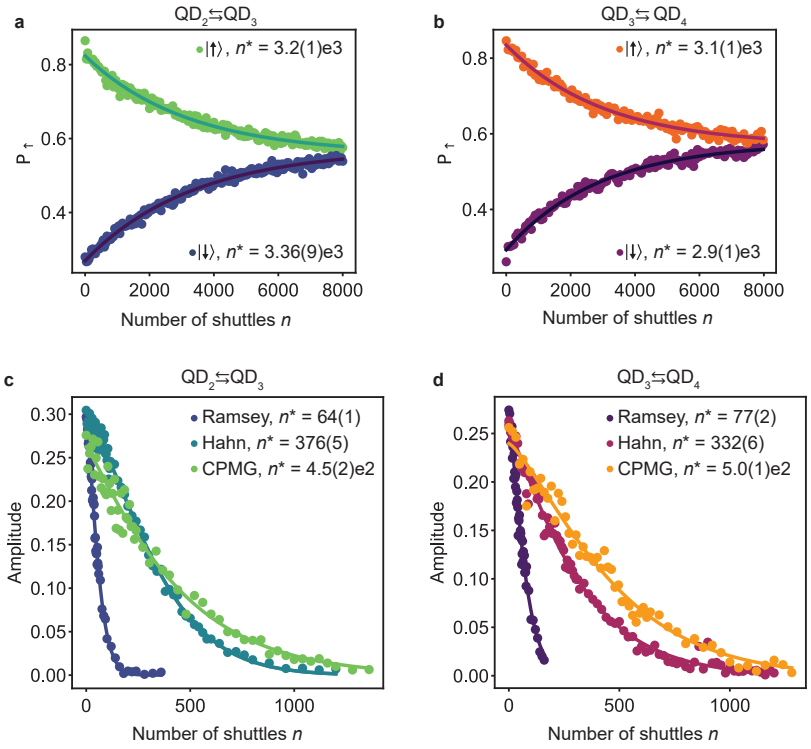

Figure 6.5: **Quantifying the performance for the shuttling coherent spin states in double quantum dots - results. a, b**, Spin-up probabilities $P_\uparrow$ measured after shuttling n times a qubit prepared in a spin basis state between QD_2 and QD_3 (c) and between QD_3 and QD_4 (d). The decay of $P_\uparrow$ as a function of n is fitted to an exponential function $P_\uparrow = P_0 \exp(-n/n^*) + P_{sat}$. **c, d**, Performance of the shuttling of superposition state between QD_2 and QD_3 (g) and QD_2 and QD_3 (h) for different shuttling sequences. The decay of the coherent amplitude A of the superposition state are fitted by $A_0 \exp(-(n/n^*)^\alpha)$ where α is a fitting parameter. The error bars indicate one standard deviation from the best fits.

experiments. In all cases, we find a characteristic decay $n^* \simeq 3000$ shuttles between quantum dots, corresponding to a polarization transfer fidelities of $F = \exp(-1/n^*) \simeq 99.97\,\%$ per shuttle within the sequence. This is similar to the fidelities reached in silicon devices [6, 27], despite the anisotropic g-tensors due to the strong spin-orbit interaction in our platform.

The exponential decay of the spin polarization to approximately 0.5 can emerge from different effects. At the charge anticrossing, the spin polarization life time is strongly reduced (see Fig. 6.16), due to high frequency charge noise and coupling to phonons [44]. Passing the charge anticrossing repeatedly thus leads to a randomization of the spin. Moreover, while the qubit starts in a basis state, it undergoes coherent rotations due to the diabatic spin shuttling and thus it is in a superposition state in the second quantum dot. The qubit, although initially in the spin basis state, then becomes sensitive to dephasing which can also lead to an exponential decay of $P_\uparrow$. The experimental decay observed probably results from a combination of these mechanisms.

We emphasize that the exact impact of dephasing on the performances of the shuttling of spin basis state depends on the difference in quantization axes of the quantum dots and on the pulse sequence used (see Section 6.6). In our experiment, the dephasing is probably mitigated by a decoupling effect induced by repeatedly waiting in the initial quantum dot (see explanation in Section 6.6). While extrapolating this result to a long chain of quantum dots is not straightforward, similar noise-averaging effects may occur in the presence of spatially correlated noise in the chain [45]. In the absence of decoupling effects and for the purpose of shuttling basis states, adiabatic shuttling still provides a good alternative as we find n^* to remain above 1000, corresponding to fidelities per shuttle within the sequence above 99.90 % (see Section 6.7.1).

We now focus on the performance of coherent shuttling. We prepare a superposition state via an EDSR $(\pi/2)_X$ pulse, shuttle the qubit, apply another $\pi/2$ pulse and measure the spin state. Importantly, one must account for $\hat{z}$-rotations experienced by the qubits during the experiments and the corresponding phase accumulation defined with respect to the qubit rotating frame in the initial quantum dots. The latter can be equivalently defined with respect to the lab frame. Therefore, we vary the phase of the EDSR pulse ϕ for the second $\pi/2$ pulse i.e. the final pulse is a $(\phi)_Z(\pi/2)_X = (\pi/2)_\phi$ pulse. For each n, we then extract the amplitude A of the $P_\uparrow$ oscillations that appear as function of ϕ [15, 27]. Fig. 6.5.c, d show the evolution of A as a function of n for shuttling between adjacent quantum dots. We fit the experimental results using $A_0 \exp(-(n/n^*)^\alpha)$ and find characteristic decay constants $n^*_{23} = 64 \pm 1$ and $n^*_{34} = 77 \pm 2$. Remarkably, these numbers compare favourably to $n^* \simeq 50$ measured in a SiMOS electron double quantum dot [27], where the spin-orbit coupling is weak.

The exponents, $\alpha_{23} = 1.36 \pm 0.05$ and $\alpha_{34} = 1.28 \pm 0.06$, characterize the spectrum of the noise experienced by the qubit while it is shuttled and suggest that the noise is neither purely quasi static nor white. The non-integer values of α contrast with observations in silicon [15, 27], and suggest that the shuttling of hole spins in germanium is limited by other mechanisms. Two types of errors can be distinguished. Errors may occur during the diabatic part of the spin dynamics. On the other hand, errors can also be induced by the dephasing experienced by the qubits during the finite time spent in each quantum dot, including the ramp times (see Section 6.6). To investigate the effect of de-

phasing, we modify the shuttling sequence and include a $(\pi)_X$ echoing pulse in the middle as displayed in Fig. 6.4.d. We note that the echoing pulses are defined with respect to the rotating frame of the qubit in the starting quantum dots. Fig. 6.5.c and d show the experimental results and it is clear that in germanium the coherent shuttling performance is improved significantly using an echo pulse: we can extend the shuttling by a factor of four to five, reaching a characteristic decay of more than 300 shuttles. Similarly, the use of CPMG sequences incorporating two decoupling $(\pi/2)_Z(\pi)_X$ pulses (Fig. 6.4.d) allows further, although modest, improvements. These enhancements in the shuttling performance confirm that dephasing is limiting the shuttling performance, contrary to observations in SiMOS [27]. We speculate that the origin of the difference is two-fold. Firstly, due to the stronger spin-orbit interaction, the spin is more sensitive to charge noise, resulting in shorter dephasing times. Secondly, the excellent control over the potential landscape in germanium allows minimizing the errors which are due to the shuttling itself.

While the results obtained for the diabatic shuttling in germanium double quantum dots are similar to those attained in silicon devices for adiabatic shuttling [15, 27], one should be careful in comparing and extrapolating them to predict the performance of shuttling through longer quantum dot chains. Quantum dot chains that would allow to couple spin qubits over appreciable length scales will put higher demands on tuning, on uniformity, and the ability to tune all couplings. Moreover, a qubit shuttled through a chain may probe different noise environments which can further affect the performance.

6.2.4. SHUTTLING THROUGH INTERMEDIATE QUANTUM DOTS

For distant qubit coupling, it is essential that a qubit can be coherently shuttled through chains of quantum dots. This is more challenging, as it requires control and optimization of a larger amount of parameters while more noise sources may couple to the system. Within a chain, a quantum dot will have at least two neighbours. To transport spin states from one site to another they have to pass through intermediates quantum dots. Therefore, an array of three quantum dots could be considered as the minimum size to explore the performance of shuttling in a chain.

We perform two types of experiments to probe the shuttling through chains of quantum dots, labelled corner shuttling and triangular shuttling. Fig. 6.6.b shows a schematic of the corner shuttling, which consists of transferring a qubit from QD_2 to QD_3 to QD_4 and back along the same route. The triangular shuttling, depicted in Fig. 6.6.c, consists of shuttling the qubit from QD_2 to QD_3 to QD_4, and then directly back to QD_2, without passing through QD_3 (for the charge stability diagram QD_4-QD_2 and a detailed description see Section 6.8.4).

To probe the feasibility of shuttling through a quantum dot, we first measure the free evolution of a superposition state while varying the detuning between the respective quantum dots. The results are shown in Fig 6.6.a. We find a remarkably clear coherent evolution for hole spin transfer from QD_2 to QD_3 to QD_4 and to QD_2. We observe one sharp change in the oscillation frequency for each transfer to the next quantum dot. We also note that after completing one round of the triangular shuttling, the phase evolution becomes constant, in agreement with a qubit returning to its original position. We thereby conclude that we can shuttle through quantum dots as desired.

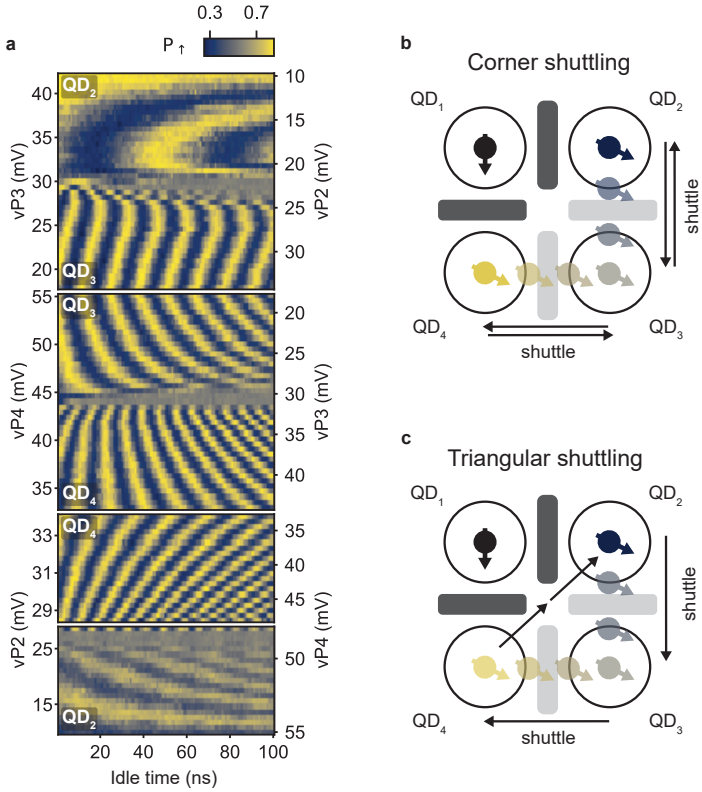

Figure 6.6: **Coherent shuttling through quantum dots - free evolution and schematics.** **a**, Results of free evolution experiments, similar to those displayed in Fig. 6.2.e and f for the corner and triangular shuttling processes. In these experiments, the amplitude of the detuning pulse is increased in steps, in order to shuttle a qubit from QD_2 to QD_3 and back (top panel), from QD_2 to QD_3 to QD_4 and back (second panel). The measurement in the third panel is identical to the measurement in the second panel, but the final point in the charge stability diagram is stepped towards the charge degeneracy point between QD_2 and QD_4. In the bottom panel the qubit is shuttled in a triangular fashion: from QD_2 to QD_3 to QD_4 to QD_2. The ramp times for this experiment are chosen in such a way that the shuttling is adiabatic with respect to the changes in quantization axis. **b**, **c**, Schematic illustrating the shuttling of a spin qubit around the corner: from QD_2 to QD_3 to QD_4 and back via QD_3 (b) and in a triangular fashion: from QD_2 to QD_3 to QD_4 and directly back to QD_2 (c). The double arrow from QD_4 to QD_2 indicates that this pulse is made in two steps, in order for the spin to shuttle via the charge degeneracy point of QD_4 - QD_2 and avoid crossing charge transition lines.

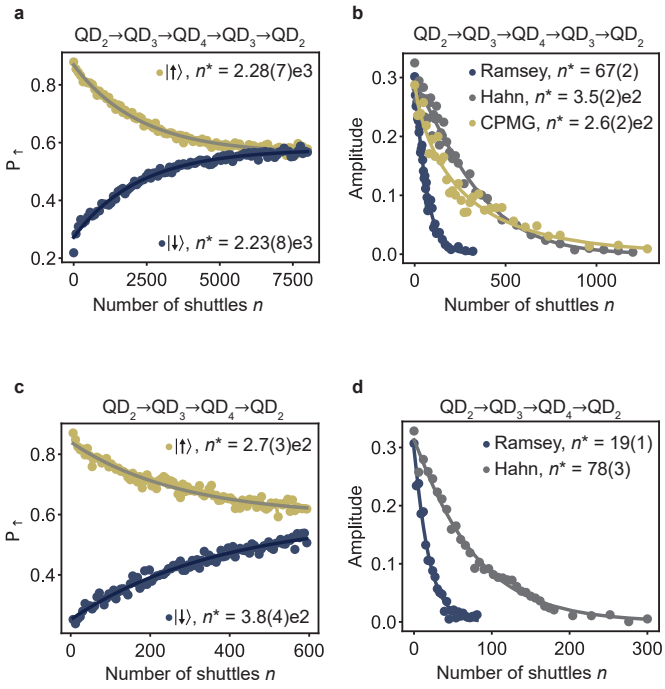

Figure 6.7: **Coherent shuttling through quantum dots. a**, **c**, Performance for the corner shuttling (a) and the triangular shuttling (c) of a qubit prepared in the basis states. **b**, **d**, Performance for shuttling a qubit prepared in a superposition state for the corner shuttling (b) and the triangular shuttling (d) and for different shuttling sequences. Shuttling performance for different processes are summarized in Table 6.1. The error bars indicate one standard deviation from the best fits.

We now focus on quantifying the performance of shuttling through quantum dots by repeated shuttling experiments. To allow comparisons with previous experiments, we define n as the number of shuttling steps between two quantum dots. Meaning that one cycle in the corner shuttling experiments results in $n = 4$, while a loop in triangular shuttling takes $n = 3$ steps. The results for shuttling basis states are shown in Fig. 6.7.a and Fig. 6.7.c. We note that the spin polarization decays faster compared to the shuttling in double quantum dots, in particular for the triangular shuttling. The corresponding fidelities per shuttle within the sequence are $F \simeq 99.96$ % for the corner shuttling and $F \geq 99.63$ % for the triangular shuttling.

For the corner shuttling, the faster decay of the basis states suggests a slight increase of the systematic error per shuttling. This may originate from the use of a more elaborated pulse sequence, which makes pulse optimization more challenging. Nonetheless, the characteristic decay constant n^* remains above 2000 and corresponds to effective distances beyond 300 μm (taking a 140 nm quantum dot spacing). The fast decay for the triangular shuttling is likely originating from the diagonal shuttling step. The tunnel coupling between QD_2 and QD_4 is low and more challenging to control, due to the absence of a dedicated barrier gate. The low tunnel coupling demands slower ramp times ($t_{ramp} \simeq 36$ ns) for the hole transfer. This increases the dephasing experienced by the qubit during each shuttle and also the time spent close to the (1,1,0,0)-(1,0,0,1) charge degeneracy point, where fast spin randomization will likely occur.

Remarkably, we find that the performance achieved for coherent corner shuttling (as shown in Fig. 6.7.b) are comparable to those of coherent shuttling between neighbouring quantum dots. This stems from the performance being limited by dephasing. However, the performance for the CPMG sequence appears inferior when compared to the single echo-pulse sequence. Since the shuttling sequence becomes more complex, we speculate that it is harder to exactly compensate for the change in quantization axes. Imperfect compensation may introduce errors, which are not fully decoupled using the CPMG sequence. Alternatively, simulations shown in Fig. 6.13 suggest that the decoupling achieved using a CPMG sequence depends on the idle time in the initial quantum dots. For an idle time corresponding to a $(2k+1)\pi$ (with k an integer) phase accumulation, the decoupling achieved using either an ideal echo or a CPMG sequence is very similar. In such a scenario, the effect of imperfect decoupling pulses would become more apparent in a CMPG sequence and would lead to decreased performance.

The performance of the coherent triangular shuttling, displayed in Fig. 6.7.d, fall short compared to the corner shuttling. Yet, the number of shuttles reached remains limited by dephasing as shown by the large improvement of n^* obtained using dynamical decoupling. The weaker performance are thus predominantly a consequence of the use of longer voltage ramps. A larger number of coherent shuttling steps may be achieved by increasing the diagonal tunnel coupling, which could be obtained by incorporating dedicated barrier gates.

6.3. CONCLUSION

We have demonstrated coherent spin qubit shuttling through quantum dots. While holes in germanium provide challenges due to an anisotropic g-tensor, we find that spin basis states can be shuttled $n^* = 2230$ times and coherent states up to $n^* = 67$ times and even

up to $n^* = 350$ times when using echo pulses. The small effective mass and high uniformity of strained germanium allow for a comparatively large quantum dot spacing of 140 nm. This results in effective length scales for shuttling basis states of $l_{\mathrm{spin}} = 312$ μm and for coherent shuttling of $l_{\mathrm{coh}} = 9$ μm. By including echo pulses we can extend the effective length scale to $l_{\mathrm{coh}} = 49$ μm. These results compare favourably to effective lengths obtained in silicon [15, 27–29]. However, we note that, in general, extrapolating the performance of shuttling experiments over few sites to predict the performance of practical shuttling links requires caution. Quantum dot chains that would allow to couple spin qubits over appreciable length scales will put higher demands on tuning, uniformity, and the ability to tune all the couplings, making the optimization of the shuttling more challenging. Moreover, the spin dynamics and thus the coherent shuttling performance will depend on the noise in the quantum dot chain. For example, if the noise is local, echo pulses may prove less effective. However, in that case, motional narrowing [22, 25, 29, 45–47] may facilitate the shuttling.

Furthermore, operating at even lower magnetic fields will boost the coherence times [4, 37, 40] and thereby increase the shuttling performance. Moreover, at lower magnetic fields the Larmor frequency is lower, which eases the requirements for the precision of the timing of the shuttling pulses. At very low fields, charge noise might not be the limiting noise source anymore and even further improvements may be achieved exploiting purified germanium [4, 37, 40]. Finally, shuttling could help mitigate problems in qubit addressability which may arise at low magnetic field.

While we have focused on bucket-brigade-mode shuttling, our results also open the path to conveyor-mode shuttling in germanium, where qubits would be coherently displaced in propagating potential wells using shared gate electrodes. This complementary approach holds promise for making scalable mid-range quantum links and has recently been successfully investigated in silicon [29], though on limited length scales. For holes in germanium, the small effective mass and absence of valley degeneracy will be beneficial in conveyor-mode shuttling. Rotations induced by the spin-orbit interaction while shuttling in conveyor-mode could be compensated by applying an appropriate EDSR pulse after the qubit transfer. Such methods could also be used in bucket-brigade-mode shuttling, as suggested by preliminary experiments shown in Section 6.7.2. It may allow for even faster qubit transfers and thus shuttling over longer distances.

Importantly, quantum links based on shuttling and spin qubits are realized using the same manufacturing techniques. Their integration in quantum circuits may provide a path toward networked quantum computing.

6.4. METHODS

MATERIALS AND DEVICE FABRICATION

The device is fabricated on a strained Ge/SiGe heterostructure grown by chemical vapour deposition [30, 48]. From bottom to top the heterostructure is composed of a 1.6 μm thick relaxed Ge layer, a 1 μm step graded $Si_{1-x}Ge_x$ (x going from 1 to 0.8) layer, a 500 nm relaxed $Si_{0.2}Ge_{0.8}$ layer, a strained 16 nm Ge quantum well, a 55 nm $Si_{0.2}Ge_{0.8}$ spacer layer and a < 1 nm thick Si cap. Contacts to the quantum well are made by depositing 30 nm of aluminium on the heterostructure after etching of the oxidized Si cap. The contacts

are isolated from the gate electrodes using a 7 nm aluminium oxide layer deposited by atomic layer deposition. The gates are defined by depositing Ti/Pd bilayers. They are separated from the each other and from the substrate by 7 nm of aluminium oxide.

EXPERIMENTAL PROCEDURE

To perform the experiments presented, we follow a systematic procedure composed of several steps. We start by preparing the system in a (1,1,1,1) charge state with the hole spins in QD_1 and QD_2 initialized in a $|\downarrow\rangle$ state, while the other spins are randomly initialized. Subsequently, QD_3 and QD_4 are depleted to bring the system in a (1,1,0,0) charge configuration. After that, the virtual barrier gate voltage vB_{12} is increased to isolate the ancilla qubit in QD_1. The tunnel couplings between QD_2 and QD_3 and, depending on the experiment, between QD_3 and QD_4 are then increased by lowering the corresponding barrier gate voltages on vB_{23} and vB_{34}. This concludes the system initialization.

Thereafter, the shuttling experiments are performed. Note that to probe the shuttling between QD_3 and QD_4, the qubit is first transferred adiabatically (with respect to the change in quantization axis) from QD_2 to QD_3. To determine the final spin state after the shuttlings, the qubit is transferred back adiabatically to QD_2. Next, the system is brought back in the (1,1,1,1) charge state, the charge regime in which the readout is optimized. This is done by first increasing vB_{23} and vB_{34}, then decreasing vB_{12} and finally reloading one hole in both QD_3 and QD_4. We finally readout the spin state via latched Pauli spin blockade by transferring the qubit in QD_1 to QD_2 and integrating the signal from the charge sensor for 7 µs. Spin-up probabilities are determined by repeating each experiment a few thousand times. Details about the experimental setup can be found in section 2.7 of this thesis.

SUB-NANOSECOND RESOLUTION ON VOLTAGE PULSES

For these experiments, we use voltage pulses applied to the electrostatic gates by the arbitrary wave form generators (AWGs). These pulses are compiled as a sequence of ramps, using control software. The ramps are defined by high precision floating points: time stamps and voltages. The maximum resolution in time is set by the maximum sample rate of the AWGs, which is 1 GSa/s and which translates to a resolution of 1 ns. Using this sample rate, the signal that is outputted by the AWGs has discrete steps, as depicted in Fig. 6.8.a. Simply moving this sampled pulse in time is only possible with a precision of 1 ns. However, it is possible to achieve sub-nanosecond resolution by slightly adjusting the voltages of the pulse instead. As illustrated in Fig. 6.8.a, in this way it is possible to delay a pulse with less than 1 ns. Quantitatively: to achieve a time delay of τ, the voltages forming the ramp are shifted by $-\tau \frac{\mathrm{d}V_{\mathrm{ramp}}(t)}{\mathrm{d}t}$. The output of the AWGs has a higher order low-pass filter with a cut-off frequency of approximately 400 MHz. This filter smoothens the output signal and effectively removes the effect of the time discretization, as is shown in Fig. 6.8.b. The time shift of the pulse is not affected by the filter, since it does not change the frequency spectrum of the pulse. To summarize, combining the high precision in the voltages of the pulse with the output filtering of the AWGs allows to output a smooth voltage ramp that is delayed by τ <1 ns, despite the limited sampling rate. Applying this technique to all voltage ramps results in sub-nanosecond resolution on the overall pulse sequence.

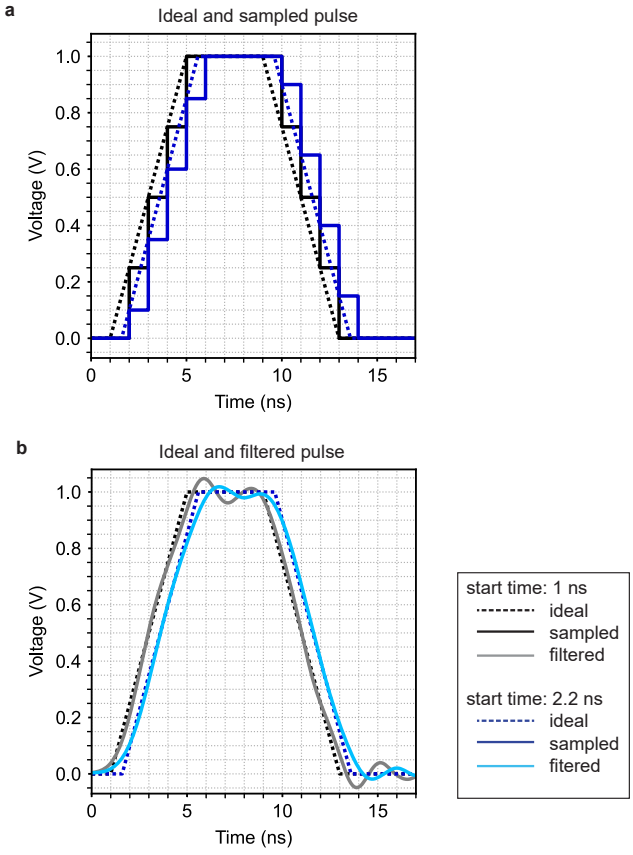

Figure 6.8: **AWG pulses with sub-nanosecond precision. a**, Ideal voltage pulse starting at 1 ns (dotted black) and ideal voltage pulse delayed by 0.6 ns with respect to the first one (dotted blue). For both pulses, the discretized sampling is plotted in solid lines. The delay between the two pulses combined with the sampling, leads to a shift of the voltage steps. **b**, Ideal pulses (starting at 1 ns and 1.6 ns) and pulses as outputted by the AWG after filtering without (light grey) and with the 0.6 ns delay (light blue). The filtering clearly smoothens the sampled pulses such that the outputted signals closely resemble the ideal pulses.

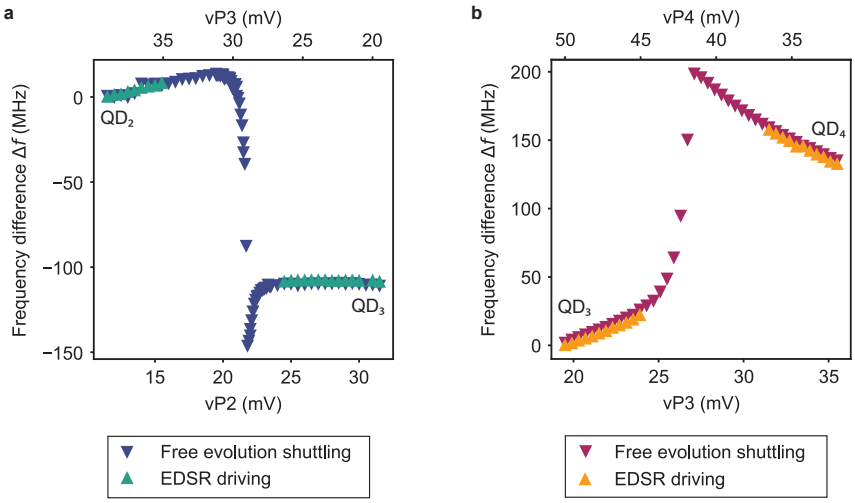

Figure 6.9: **Evolution of the Larmor frequency for shuttling in double quantum dots. a**, **b**, Larmor frequency differences $\Delta f = f_{\mathrm{L}}(\mathrm{vP2}, \mathrm{vP3}) - f_{\mathrm{L}}^{\mathrm{QD2}}$ (a) and $\Delta f = f_{\mathrm{L}}(\mathrm{vP3}, \mathrm{vP4}) - f_{\mathrm{L}}^{\mathrm{QD3}}$ (b) measured along the detuning axis of $\mathrm{QD_2}$-$\mathrm{QD_3}$ (a) and $\mathrm{QD_3}$-$\mathrm{QD_4}$ (b). The quantum dot where the shuttling experiment starts is taken as the reference point for the frequency. Δf is independently evaluated from measurements of the resonance frequency using an EDSR pulse (data displayed in Fig. 1.g and k) and from the frequency of the coherent oscillations that appear when a qubit is shuttled in a superposition state (data displayed in Fig. 1.h and l). Both sets of data points overlap in (a) and (b), confirming that the coherent oscillations arise due to a change in Larmor frequency along the detuning axis. For the free evolution experiments, the shuttling between $\mathrm{QD_2}$ and $\mathrm{QD_3}$ (shown in (a)) is completely adiabatic (ramp times of 40 ns) while the shuttling between $\mathrm{QD_3}$ and $\mathrm{QD_4}$ (shown in (b)) is only partially adiabatic (ramp times of 4 ns). In the latter case, the frequency difference measured is barely affected by the limited adiabaticity as the visibility M of the oscillations induced by the change in quantization axes ($M < 0.1$ from Fig.6.17) is sufficiently small compared to that of the oscillations arising from the phase evolution of the superposition state ($V \approx 0.5$ when the hole is in $\mathrm{QD_4}$). Moreover, the Larmor frequency of spins in both $\mathrm{QD_3}$ and $\mathrm{QD_4}$ are close to 1 GHz. The free evolution experiments were performed with a time resolution of 1 ns, meaning that the oscillations due to the diabaticity of the shuttling only show up as an aliasing pattern and do not disturb the oscillations due to free evolution.

	n^*, $\|\downarrow\rangle$ transfer	n^*, $\|\uparrow\rangle$ transfer	n^*, $\frac{\|\downarrow\rangle - i\|\uparrow\rangle}{\sqrt{2}}$ transfer	α, $\frac{\|\downarrow\rangle - i\|\uparrow\rangle}{\sqrt{2}}$ transfer
$QD_2 \rightleftarrows QD_3$	$(3.36\pm0.09)\times10^3$	$(3.2\pm0.1)\times10^3$	Ramsey: 64 ± 1	1.36 ± 0.05
			Hahn: 376 ± 5	1.44 ± 0.04
			CPMG: $(4.5\pm2)\times10^2$	1.14 ± 0.06
$QD_3 \rightleftarrows QD_4$	$(2.9\pm0.1)\times10^3$	$(3.1\pm0.1)\times10^3$	Ramsey: 77 ± 2	1.28 ± 0.06
			Hahn: 332 ± 6	1.17 ± 0.04
			CPMG: $(5.0\pm0.1)\times10^2$	1.3 ± 0.07
Corner	$(2.23\pm0.08)\times10^3$	$(2.28\pm0.07)\times10^3$	Ramsey: 67 ± 2	1.11 ± 0.06
			Hahn: $(3.5\pm0.2)\times10^2$	1.2 ± 0.1
			CPMG: $(2.6\pm0.2)\times10^2$	0.76 ± 0.07
Triangular	$(3.8\pm0.4)\times10^2$	$(2.7\pm0.3)\times10^2$	Ramsey: 19 ± 1	1.08 ± 0.07
			Hahn: 78 ± 3	1.07 ± 0.05

Table 6.1: **Summary of shuttling performance.** For the spin basis state shuttling experiments, the spin polarization decays are fitted by $P_0\exp(-(n/n^*))+P_{\text{sat}}$, with n the number of shuttles. For the coherent shuttling experiments, the coherence decays are fitted by $A_0\exp(-(n/n^*)^\alpha)$, where n^* represents the number of shuttles that can be achieved before the polarization or the coherence drops by $1/e$.

6.5. OPTIMIZATION OF THE SHUTTLING PULSES

MEASUREMENT DATA

In this section, we illustrate and discuss the importance of careful pulse optimization. Fig. 6.10 shows the results of experiments where we probe the performance of the coherent shuttling between QD_2 and QD_3 using the Ramsey sequence depicted in Fig. 6.4.a. The detuning pulses used for all these experiments are identical, except for the idle time t_{idle} in QD_3 (idle time 2 in Fig. 6.4.b). This idle time in QD_3 was optimized to 0.95 ns for the experiments displayed in the main text.

We observe that the evolution of amplitudes extracted at the end of the shuttling sequence is strongly dependent on the idle time in QD_3. For $t_{\text{idle}} = 0.9$ and $t_{\text{idle}} = 1$ ns, which are close to the optimum, the amplitude shows a smooth and progressive decay. When t_{idle} is increased, oscillations of the amplitude as function of the number of shuttling steps n appear and their periodicity varies with t_{idle}. These oscillations witness the rotations induced by the change of quantization axes, which are imperfectly compensated for $t_{\text{idle}} \geq 1.1$ ns. They lead to coherent errors after each shuttling event, which add up, and significantly modify the state of the qubit. For example, for $t_{\text{idle}} = 1.6$ ns, the superposition state is virtually transformed to a spin basis state after a few shuttling rounds. This emphasizes the necessity of optimizing the voltage pulses to compensate for the effect of rotations induced by the spin-orbit interaction.

The optimized idle times for each shuttling process can be found by performing measurements similar to those displayed in Fig. 6.10, and by looking for a regular decay of the amplitude as function of n. This optimization can also be done by studying the decay of the spin-up probabilities in spin basis state shuttling experiments.

SIMULATION OF THE STATE EVOLUTION

In Fig. 6.10, we see that for non-optimized idle times, like $t_{\text{idle}} = 1.5$ ns, the amplitude can saturate to a finite value at large n. This is in contrast to what we observe for optimized

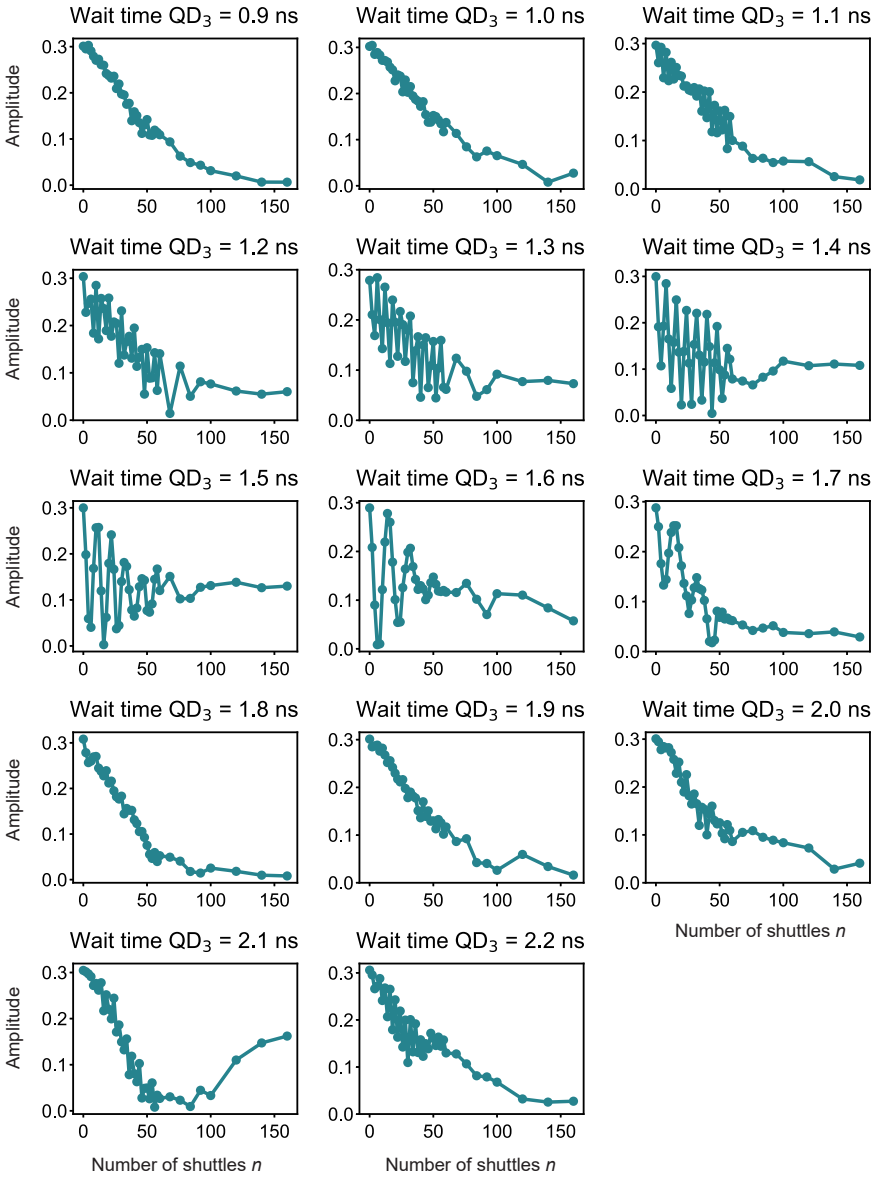

Figure 6.10: **Signatures of non-optimized idle times in Ramsey shuttling experiments.** Results of coherent shuttling experiments between QD_2 and QD_3 obtained using Ramsey sequences. The idle time spent in QD_3 is different for the results shown in the different subplots, as indicated by the titles. For non-optimized idle times, oscillations of the amplitude as function of the number of shuttles n appear and the amplitude can saturate to a non-zero value at large n.

idle times $t_{\text{idle}} = 0.9$ ns and $t_{\text{idle}} = 1$ ns, which decay to zero. To understand this feature, we carry out simulations of the dynamics of a qubit initialized in the $\frac{|\downarrow\rangle - i|\uparrow\rangle}{\sqrt{2}}$ superposition state which is shuttled between two neighboring quantum dots. Each shuttling step is modelled by a rotation. This rotation arises from the precession around the quantization axis of the quantum dot towards which the qubit is shuttled. We also calculate for every even n the expected measurement result, i.e. the amplitude of the $P_\uparrow$ oscillations that appear when the phase ϕ of the second $\pi/2$ pulse is varied. This is shown in Fig. 6.11.c, with two examples corresponding to a non-optimized idle time and an optimized idle time.

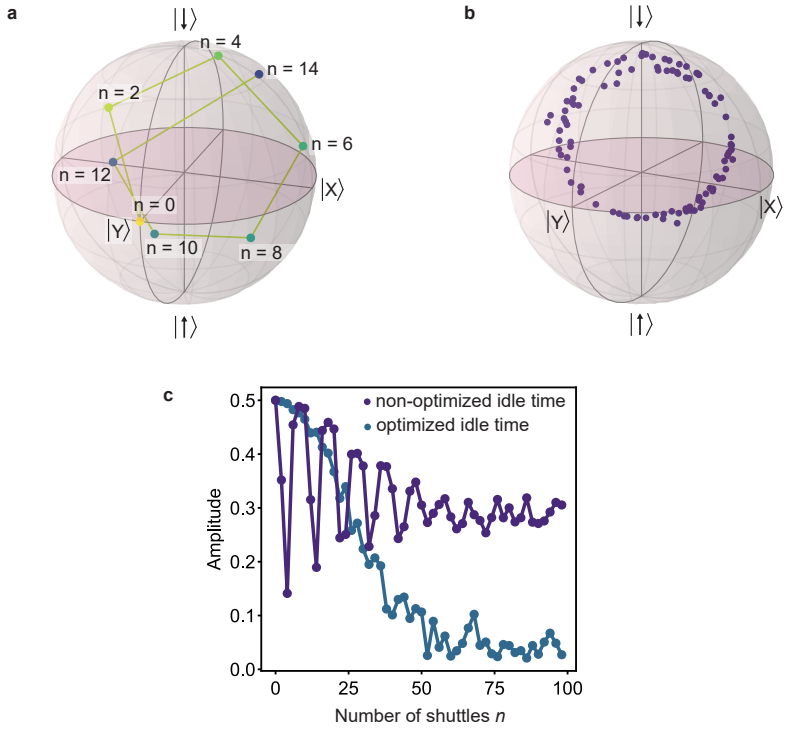

Figure 6.11: **Simulation of the effect of non-optimized idle times.** **a**, Distribution of the qubit states in the Bloch sphere after an even number of shuttles, for an non-optimized idle time. **b**, Spread of the qubit state after a large number of shuttles, when the qubit is dephased. **c**, Simulated measurement results, i.e. amplitude of the oscillations appearing while varying the phase of the second $\pi/2$ pulse, as a function of n, for a non-optimized idle time and an optimized idle time.

Fig. 6.11.a displays the trajectory in the Bloch sphere of the qubit for the first 14 shuttling steps, in the reference frame of the quantum dot where the shuttling experiment starts. The different states of the qubit map a circle which is tilted compared to the equator. The product of the two rotations generated by shuttling back-and-forth is equivalent to a single rotation around a fixed axis. Consequently, multiple shuttling cy-

cles can be seen as successive rotations around this fixed axis which elucidates the trajectory observed in the Bloch sphere. This also explains the oscillations of the amplitude as function of n seen in Fig. 6.10, as the distance between origin and the projection of the state on xy-plane can vary significantly depending on the number of shuttles for an non-optimized idle time. In contrast, when the idle times are well-optimized, the qubit states are on the equator of the Bloch sphere and no oscillations of the amplitude with n can be observed.

Next, we include the effects of dephasing in the simulations, by assuming that the qubit frequencies fluctuate between repetitions of a given experiment with a fixed n. We observe that the state of the qubit is spread along a circle with a distribution that becomes more uniform as n increases, meaning when the qubit experiences more dephasing. An example is shown in Fig. 6.11.b for $n = 98$, corresponding to the data shown in Fig. 6.11.c. The center of the circle, which is equivalent to the statistical average of the qubit state when the qubit is completely dephased, is not on the equator on Bloch sphere. This explains the finite amplitude observed in the measurements at large n. Except for the revival of the amplitude observed for $t_{\text{idle}} = 2.1$ ns, these simulations capture most of the features observed in Fig. 6.10.

6.6. MODELLING OF THE QUBIT DYNAMICS DURING SHUTTLING

MODEL USED AND UNDERLYING ASSUMPTIONS

In general, the quantum process of $2n$ shuttles, between QD_2 and QD_3 back-and-forth n times, is given by the sequential application of the individual processes:

$$\mathcal{U}_{2n\text{ shuttles}} = \langle \prod_{j=0}^{n} \mathcal{U}^{(j)}_{\text{QD2}} \mathcal{U}^{(j)}_{\text{r,QD2}} \mathcal{U}^{(j)}_{\text{QD3}} \mathcal{U}^{(j)}_{\text{r,QD3}} \rangle , \tag{6.1}$$

where $\mathcal{U}^{(j)}_{\text{QD2(QD3)}}$ is the j-th superoperator describing the dynamics in quantum dot QD_2(QD_3), $\mathcal{U}^{(j)}_{\text{r,QD2(r,QD3)}}$ is the j-th superoperator describing the dynamics of ramping to quantum dot QD_2 (QD_3), and $\langle\cdot\rangle$ denotes averaging over different noise initializations. The dynamics within the qubit subspace without decoherence is given by:

$$U_{\text{QD2}} = \exp\left(-i\frac{\phi_{\text{QD2}}}{2}\sigma_z\right) \tag{6.2}$$

$$U_{\text{r,QD2}} U_{\text{QD3}} U_{\text{r,QD3}} = \exp\left(-i\frac{\phi_{\text{QD3}}}{2}(\cos(\theta_{23})\sigma_z + \sin(\theta_{23})\sigma_x)\right), \tag{6.3}$$

where θ_{23} is the effective tilt angle between the quantization axes that also takes the ramping time into consideration, $\phi_{\text{QD2(QD3)}}$ are the effective phases accumulated around the corresponding quantization axis and $\sigma_{x,y,z}$ are the Pauli matrices in QD_2. In the superoperator representation, the unitary dynamics can be conveniently expressed by:

$$\mathcal{U}_{\text{QD2}} = U_{\text{QD2}} \otimes U^*_{\text{QD2}} \tag{6.4}$$

$$= e^{\mathcal{H}_{\text{QD2}}}. \tag{6.5}$$

Here, $\mathcal{H}_{\text{QD2}} = -i\phi_{\text{QD2}}(\sigma_z \otimes \mathbf{1}_2 - \mathbf{1}_2 \otimes \sigma_z)/2$ and $\otimes$ denotes the Kronecker product. To describe the effect of decoherence we consider for each process low-frequency charge

noise (modelled as quasistatic fluctuations of accumulated phases $\phi_{\mathrm{QD2(QD3)}} \rightarrow \phi_{\mathrm{QD2(QD3)}} + \delta\phi_{\mathrm{QD2(QD3)}}$), and high-frequency charge noise which causes dephasing and relaxation at the charge anticrossing. The latter noise sources are modelled within a standard Lindblad equation (allowing us to drop the index j) and described by the following Lindblad operators in superoperator representation using row-stacking convention [49]:

$$\mathscr{L}_{\mathrm{QD2}} = \begin{pmatrix} -\gamma^{\mathrm{r}}_{\mathrm{QD2}} & 0 & 0 & \gamma^{\mathrm{r}}_{\mathrm{QD2}} \\ 0 & -\gamma^{\mathrm{r}}_{\mathrm{QD2}} - \gamma^{\varphi}_{\mathrm{QD2}} & \gamma^{\mathrm{r}}_{\mathrm{QD2}} & 0 \\ 0 & \gamma^{\mathrm{r}}_{\mathrm{QD2}} & -\gamma^{\mathrm{r}}_{\mathrm{QD2}} - \gamma^{\varphi}_{\mathrm{QD2}} & 0 \\ \gamma^{\mathrm{r}}_{\mathrm{QD2}} & 0 & 0 & -\gamma^{\mathrm{r}}_{\mathrm{QD2}} \end{pmatrix}, \tag{6.6}$$

$$\mathscr{L}_{\mathrm{r,QD2}} = \begin{pmatrix} -\gamma^{\mathrm{r}}_{\mathrm{r,QD2}} & 0 & 0 & \gamma^{\mathrm{r}}_{\mathrm{r,QD2}} \\ 0 & -\gamma^{\mathrm{r}}_{\mathrm{r,QD2}} - \gamma^{\varphi}_{\mathrm{r,QD2}} & \gamma^{\mathrm{r}}_{\mathrm{r,QD2}} & 0 \\ 0 & \gamma^{\mathrm{r}}_{\mathrm{r,QD2}} & -\gamma^{\mathrm{r}}_{\mathrm{r,QD2}} - \gamma^{\varphi}_{\mathrm{r,QD2}} & 0 \\ \gamma^{\mathrm{r}}_{\mathrm{r,QD2}} & 0 & 0 & -\gamma^{\mathrm{r}}_{\mathrm{r,QD2}} \end{pmatrix}, \tag{6.7}$$

$$\mathscr{L}_{\mathrm{QD3}} = \left(R(\theta_{23}) \otimes R(-\theta_{23})^T\right) \begin{pmatrix} -\gamma^{\mathrm{r}}_{\mathrm{QD3}} & 0 & 0 & \gamma^{\mathrm{r}}_{\mathrm{QD3}} \\ 0 & -\gamma^{\mathrm{r}}_{\mathrm{QD3}} - \gamma^{\varphi}_{\mathrm{QD3}} & \gamma^{\mathrm{r}}_{\mathrm{QD3}} & 0 \\ 0 & \gamma^{\mathrm{r}}_{\mathrm{QD3}} & -\gamma^{\mathrm{r}}_{\mathrm{QD3}} - \gamma^{\varphi}_{\mathrm{QD3}} & 0 \\ \gamma^{\mathrm{r}}_{\mathrm{QD3}} & 0 & 0 & -\gamma^{\mathrm{r}}_{\mathrm{QD3}} \end{pmatrix} \left(R(-\theta_{23}) \otimes R(\theta_{23})^T\right), \tag{6.8}$$

$$\mathscr{L}_{\mathrm{r,QD3}} = \left(R(\theta_{23}) \otimes R(-\theta_{23})^T\right) \begin{pmatrix} -\gamma^{\mathrm{r}}_{\mathrm{r,QD3}} & 0 & 0 & \gamma^{\mathrm{r}}_{\mathrm{r,QD3}} \\ 0 & -\gamma^{\mathrm{r}}_{\mathrm{r,QD3}} - \gamma^{\varphi}_{\mathrm{r,QD3}} & \gamma^{\mathrm{r}}_{\mathrm{r,QD3}} & 0 \\ 0 & \gamma^{\mathrm{r}}_{\mathrm{r,QD3}} & -\gamma^{\mathrm{r}}_{\mathrm{r,QD3}} - \gamma^{\varphi}_{\mathrm{r,QD3}} & 0 \\ \gamma^{\mathrm{r}}_{\mathrm{r,QD3}} & 0 & 0 & -\gamma^{\mathrm{r}}_{\mathrm{r,QD3}} \end{pmatrix} \left(R(-\theta_{23}) \otimes R(\theta_{23})^T\right), \tag{6.9}$$

where $R(\theta) = e^{-i\theta\sigma_y/2}$ rotates the quantization axis by θ in the xz-plane. Here, $\gamma^{\varphi}_{\mathrm{QD2(QD3)}}$ is the dephasing rate and $\gamma^{\mathrm{r}}_{\mathrm{QD2(QD3)}}$ the relaxation/excitation rate for idling in $\mathrm{QD_2}$($\mathrm{QD_3}$) and $\gamma^{\varphi}_{\mathrm{r,QD2(QD3)}}$ is the dephasing rate and $\gamma^{r}_{\mathrm{r,\,QD2(QD3)}}$ the relaxation/excitation rate for shuttling from $\mathrm{QD_3}$ to $\mathrm{QD_2}$ ($\mathrm{QD_2}$ to $\mathrm{QD_3}$). To simplify the expressions, we further assumed that the qubit is coupled to a hot qubit bath at the anticrossing [44] giving rise to equal relaxation and excitation rates. This assumption is justified by the fast randomization of the spin state at the anticrossing observed in Fig. 6.16.

The basic repetition, a 2-shuttle process, can now be described as a Markov chain:

$$\mathscr{U}_{2\ \mathrm{shuttles}} = \langle e^{\mathscr{H}_{\mathrm{QD2}} + \mathscr{L}_{\mathrm{QD2}}} e^{\mathscr{L}_{\mathrm{r,QD2}}} e^{\mathscr{H}_{\mathrm{QD3}} + \mathscr{L}_{\mathrm{QD3}}} e^{\mathscr{L}_{\mathrm{r,QD3}}} \rangle . \tag{6.10}$$

Here, we make the following assumptions. Firstly, high-frequency noise, causing relaxation and dephasing processes and described by $\gamma^{\varphi}_{\mathrm{r,QD2(QD3)}}$ and $\gamma^{\mathrm{r}}_{\mathrm{r,QD2(QD3)}}$, is relevant only exactly at the anticrossing and is instantaneous. Secondly, we neglect high-frequency noise during the idling in QD_2 and QD_3 since idling dynamics is dominated by low-frequency noise. This allows us to add the coherent part of the dynamics during the ramp before (after) reaching the anticrossing to the dynamics described by $\mathscr{H}_{\mathrm{QD2}}$ ($\mathscr{H}_{\mathrm{QD3}}$). We note that this is a good approximation if $\langle\phi_{\mathrm{QD3}}\rangle$ is close to an integer multiple of 2π, i.e. the shuttling rounds are well calibrated. Using the Zassenhaus expansion formula, we can now further approximate the 2-shuttling process by a product of two matrices:

$$\mathscr{U}_{2\text{ shuttles}} = \langle e^{\mathscr{C}} e^{\mathscr{D}} \rangle . \tag{6.11}$$

Here, the $\mathscr{C}$-matrix only consists of the average phase accumulated $\langle\phi_{\mathrm{QD2}}\rangle$ and describes a unitary process while all decoherence is included in the D-matrix. For n being an even integer, a $2n$-shuttle process can then be written as:

$$\mathscr{U}_{2n\text{ shuttles}} = \left\langle \prod_{i=1}^{n/2} e^{\mathscr{D}} \begin{pmatrix} 1 & 0 & 0 & 0 \\ 0 & e^{-i\langle\phi_{\mathrm{QD2}}\rangle} & 0 & 0 \\ 0 & 0 & e^{i\langle\phi_{\mathrm{QD2}}\rangle} & 0 \\ 0 & 0 & 0 & 1 \end{pmatrix} e^{\mathscr{D}} \right\rangle , \tag{6.12}$$

with the decoherence matrix:

$$\mathscr{D} \approx \mathscr{L}_{\mathrm{r,QD2}} + \mathscr{L}_{\mathrm{r,QD3}} + \mathscr{H}_{\mathrm{QD2}} + \mathscr{H}_{\mathrm{QD3}} - \langle \mathscr{H}_{\mathrm{QD2}} \rangle . \tag{6.13}$$

SHUTTLING OF SPIN BASIS STATES

The return probability of the basis states, which are identical for both basis states as the excitation and relaxation rate are assumed to be equal close to the charge anticrossing, can be computed from the superoperator $\langle\widetilde{\uparrow}|\mathscr{U}_{2n\text{ shuttle}}|\widetilde{\uparrow}\rangle$, where $|\widetilde{\uparrow}\rangle$ is the vectorized density matrix of the $|\uparrow\rangle$ basis state. We now consider two extreme cases, $\langle\phi_{\mathrm{QD2}}\rangle = m$ with even or odd m multiple of π. If m is an even multiple of π, we can simplify the expression to $\mathscr{U}_{2n\text{ shuttles}} = \langle e^{n\mathscr{D}} \rangle$, while for m being an odd multiple of π, the sequence corresponds to a Hahn echo experiment with a phase-flip operation instead of a bit-flip operation. In Fig. 6.12, we have simulated the basis state decay for varying m considering (a) uncorrelated and (b) correlated charge noise. While most cases shows only a single, and slow exponential decay, the special case of $m = 2\pi k$ (with k an integer) shows a fast initial Gaussian followed by a slow exponential decay. Regardless of the chosen value of m, the decay converges to $\langle\widetilde{\uparrow}|\mathscr{U}_{n\to\infty}|\widetilde{\uparrow}\rangle = \frac{1}{2}$. We find that for most m, the initial rapid decay is absent due to decoupling over potentially many shuttle rounds. Thus, the (partial) noise-decoupling effect occurs for most choices of the waiting times in the initial quantum dot. We find that the fast decay of the basis states can only be observed for $\langle\phi_{\mathrm{QD2}}\rangle = m \pm \delta$ with m being multiples of 2π and $\delta \leq 0.02\pi$. Since our experimental results do not show a fast Gaussian decay of the basis states, we believe that our timing is chosen such that the fast initial Gaussian dephasing is echoed out [45]. Consequently, we can fit the decay for the shuttling of spin basis states to an exponential decaying function $\exp(-n/n^*)$. We note that the final slow decay can either originate from spin randomization or from dephasing.

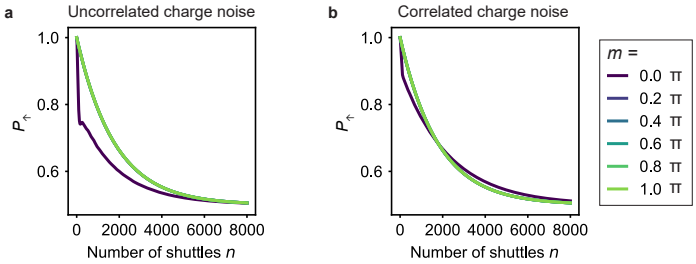

Figure 6.12: **Simulation of the basis state decay.** Evolution of the spin-up probability $P_\uparrow$ as a function of the number of shuttling events simulated using Eq. (6.1) for **a**, uncorrelated and **b**, correlated quasistatic fluctuations for various $\langle\phi_{\mathrm{QD2}}\rangle = m$. For both correlated and uncorrelated noise, the fast initial decay vanishes, except when m is close to (a multiple of) 2π. In the simulation the following parameters were chosen: quantization axis difference $\theta_{23} = 52°$, high-frequency dephasing rate $\gamma^{\varphi}_{\mathrm{r,QD2}} = \gamma^{\varphi}_{\mathrm{r,QD3}} = 0.00125$, relaxation rate $\gamma^{\mathrm{r}}_{\mathrm{r,QD2}} = \gamma^{\mathrm{r}}_{\mathrm{r,QD3}} = 0.000125$, standard deviation of the quasistatic fluctuations $\sigma_{\phi_{\mathrm{QD2}}} = \sigma_{\phi_{\mathrm{QD3}}} = 0.004$. For uncorrelated fluctuations $\sigma_{\phi_{\mathrm{QD2}}} \to \sqrt{2}\sigma_{\phi_{\mathrm{QD2}}}$ to get identical free induction decays. These parameters lead to a pure dephasing after $n^* = 63$ shuttles in absence of decoupling.

RAMSEY, HAHN-ECHO, AND CPMG DYNAMICAL DECOUPLING

The decay of the superposition states can be computed from the same superoperator via the amplitude

$$A = \frac{1}{2}\max_{\varphi}\left[\langle\widetilde{\varphi}_+|\mathcal{U}_{2n\ \mathrm{shuttle}}|\widetilde{\phi}_+\rangle - \langle\widetilde{\varphi}_-|\mathcal{U}_{2n\ \mathrm{shuttle}}|\widetilde{\phi}_+\rangle\right], \tag{6.14}$$

where $|\widetilde{\xi}_\pm\rangle$ is the vectorized density matrix of the state $|\xi_\pm\rangle = \frac{1}{2}(|\uparrow\rangle \pm e^{i\xi}|\downarrow\rangle)$ with $\xi = \varphi, \phi$. The initial phase of the superposition state is in general unknown due to the unsynchronized clock between the AWG and the vector source (see section below) and may vary for each single shot measurement of the experiment. However, the phase difference between initial and final state is fixed for each shot. We have numerically confirmed that the dynamics is only slightly affected by an additional averaging over the initial phase of the initial superposition state for $\langle\phi_{\mathrm{QD2}}\rangle = m$ with m being close to multiples of 2π (same regime in which the fast initial decay can be observed for the basis state). For other choices, the initial phase has a negligible impact and is averaged out after a few shuttling rounds.

The quantum process of a dynamical decoupled $2n$ shuttles, shuttling between QD_2 and QD_3 back-and-forth n times, is given by the sequential application of the individual processes:

$$\mathcal{U}^{\mathrm{Echo}}_{2n\ \mathrm{shuttles}} = \langle\prod_{j=0}^{n/2}\mathcal{U}^{(j)}_{\mathrm{QD2}}\mathcal{U}^{(j)}_{\mathrm{r,QD2}}\mathcal{U}^{(j)}_{\mathrm{QD3}}\mathcal{U}^{(j)}_{\mathrm{r,QD3}}\,\mathcal{U}_{\mathrm{x},\pi/2}\prod_{j=n/2}^{n}\mathcal{U}^{(j)}_{\mathrm{QD2}}\mathcal{U}^{(j)}_{\mathrm{r,QD2}}\mathcal{U}^{(j)}_{\mathrm{QD3}}\mathcal{U}^{(j)}_{\mathrm{r,QD3}}\rangle, \tag{6.15}$$

$$\mathcal{U}^{\text{CPMG}}_{2n\text{ shuttles}} = \langle \prod_{j=0}^{n/4} \mathcal{U}^{(j)}_{\text{QD2}} \mathcal{U}^{(j)}_{\text{r,QD2}} \mathcal{U}^{(j)}_{\text{QD3}} \mathcal{U}^{(j)}_{\text{r,QD3}} \mathcal{U}_{\text{y},\pi/2} \prod_{j=n/4}^{3n/4} \mathcal{U}^{(j)}_{\text{QD2}} \mathcal{U}^{(j)}_{\text{r,QD2}} \mathcal{U}^{(j)}_{\text{QD3}} \mathcal{U}^{(j)}_{\text{r,QD3}} \mathcal{U}_{\text{y},\pi/2} \prod_{j=3n/4}^{n} \mathcal{U}^{(j)}_{\text{QD2}} \mathcal{U}^{(j)}_{\text{r,QD2}} \mathcal{U}^{(j)}_{\text{QD3}} \mathcal{U}^{(j)}_{\text{r,QD3}} \rangle, \quad (6.16)$$

where $\mathcal{U}_{\text{x,y},\pi/2}$ are superoperator representation of the spin-flips around the x and y axis. For corner shuttling, shuttling between QD_2 to QD_3 to QD_4 and back n times, one needs to make the substitution:

$$\mathcal{U}^{(j)}_{\text{r,QD2}} \mathcal{U}^{(j)}_{\text{QD3}} \mathcal{U}^{(j)}_{\text{r,QD3}} \rightarrow \mathcal{U}^{(j)}_{\text{r,QD2}} \mathcal{U}^{(j)}_{\text{QD3}} \mathcal{U}^{(j)}_{\text{r,QD3}} \mathcal{U}^{(j)}_{\text{QD4}} \mathcal{U}^{(j)}_{\text{r,QD4}} \mathcal{U}^{(j)}_{\text{QD3}} \mathcal{U}^{(j)}_{\text{r,QD3}}, \quad (6.17)$$

where $\mathcal{U}^{(j)}_{\text{QD4}}$ is the j-th superoperator describing the dynamics in dot QD_4, $\mathcal{U}^{(j)}_{\text{r,QD4}}$ is the j-th superoperator describing the dynamics of ramping to quantum dot QD_4. The dynamics within the qubit subspace without decoherence is analogously given by:

$$\begin{aligned} U_{\text{r,QD2}} U_{\text{QD3}} U_{\text{r,QD3}} U_{\text{QD4}} U_{\text{r,QD4}} U_{\text{QD3}} U_{\text{r,QD3}} &= \exp\left(-i\frac{\phi_{\text{QD3}}}{2}(\cos(\theta_{23})\sigma_z + \sin(\theta_{23})\sigma_x)\right) \\ &\times \exp\left(-i\frac{\phi_{\text{QD4}}}{2}(\cos(\theta_{34}+\theta_{23})\sigma_z + \sin(\theta_{34}+\theta_{23})\sigma_x)\right) \\ &\times \exp\left(-i\frac{\phi_{\text{QD3}}}{2}(\cos(\theta_{23})\sigma_z + \sin(\theta_{23})\sigma_x)\right), \end{aligned}$$

where θ_{34} is the effective tilt angle between the quantization axes of QD_3 and QD_4 that also takes the ramping time into consideration, $\phi_{\text{QD3,a(b)}}$ is the effective phases accumulated in QD_3 before (after) shuttling to QD_4, and ϕ_{QD4} is the effective phases accumulated in QD_4.

Note that in general the quantization axes of QD_2, QD_3 and QD_4 do not need to lay in the same plane. To account for the misalignment we use the Euler-angle decomposition, i.e. by adding a rotation around the quantization axis of QD_3 before the shuttling to QD_4 and adding the inverse rotation after the shuttling back to QD_3. The additional phase commutes (by design) with the idling dynamics in QD_3. Consequently, the additional rotation can be added/subtracted from the rotation accumulated during idling in QD_3 (care has to be taken with the relaxation decay dynamics). Since we do not know the phase of the rotation in our experiment, we assume in our simulations that all three quantization axes are in the xz-plane. We have numerically confirmed that the dynamics is only mildly affected by this choice and only close to $\langle\phi_{\text{QD2}}\rangle = m$ with m being a multiple of 2π.

In Fig. 6.13, we have simulated for the corner shuttling the evolution of the coherence, i.e. the amplitude (see Eq. (6.14)) of the superposition state, for a (a) Ramsey, (b) Hahn-echo, and (c) CPMG dynamical decoupling sequence for various m using uncorrelated quasistatic charge noise. When m is a multiple of 2π, the dynamical decoupling for the CPMG sequence shows a significant improvement compared to the Hahn-echo. In contrast, when m is a multiple of π, a Hahn-echo sequence achieves a similar decoupling effect as the CPMG sequence because of the interplay between the phase and spin flips in QD_2. This could possibly explain the reduced effect of CPMG measured in corner shuttling. We note that simulations considering time-correlated phase fluctuations,

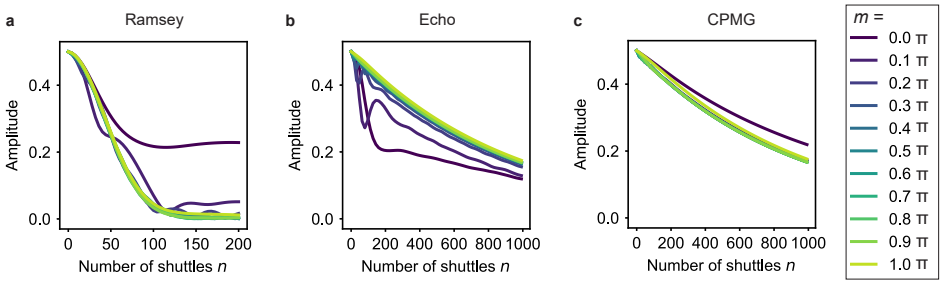

Figure 6.13: **Simulation of the dynamics for the Ramsey, Hahn-echo and CPMG sequences for corner shuttling.** Evolution of the superposition state for corner shuttling as a function of the number of shuttling events using eq. (6.14) for uncorrelated quasistatic fluctuations for varying phases $\langle\phi_{\mathrm{QD2}}\rangle = m$ and assuming perfect single-qubit gates $\mathcal{U}_{x,y,\pi/2}$. The gain of implementing a CPMG dynamical decoupling sequence compared to an echo is negligible. In the simulation the following parameters were chosen: quantization axis differences $\theta_{23} = 52°$ and $\theta_{34} = 40°$, high-frequency dephasing rate $\gamma^{\varphi}_{\mathrm{QD2}} = \gamma^{\varphi}_{r,\mathrm{QD3}} = \gamma^{\varphi}_{r,\mathrm{QD4}} = 0.00125$, relaxation rate $\gamma^{\mathrm{r}}_{r,\mathrm{QD2}} = \gamma^{\mathrm{r}}_{r,\mathrm{QD3}} = \gamma^{\mathrm{r}}_{r,\mathrm{QD4}} = 0.000125$, standard deviation of the quasistatic fluctuations $\sigma_{\phi_{\mathrm{QD2}}} = \sigma_{\phi_{\mathrm{QD3}}} = \sigma_{\phi_{\mathrm{QD4}}} = 0.009$. These parameters lead to a pure dephasing after $n^* = 63$ shuttles in absence of decoupling. We note that the decay in these simulations are underestimated as they include only quasistatic noise.

instead of quasistatic phase fluctuations, show qualitatively similar results for the improvement of decoupling using CPMG sequences compared to Hahn-echo sequences.

6.7. ALTERNATIVE SHUTTLING PROTOCOLS TO MITIGATE UNINTENDED ROTATIONS

6.7.1. ADIABATIC SHUTTLING

For completeness, we also investigate the performance of the shuttling processes when the shuttling pulses are adiabatic, i.e. when there is no spin rotation induced by the difference between the quantization axes of the quantum dots. Fig. 6.14 shows the results of such investigations for the shuttling of basis states and for the shuttling of superposition states. In both cases, we obtain significantly lower performance compared to those achieved with diabatic pulses (see Fig. 6.5). According to our findings, dephasing can largely explain this difference in performance for the coherent shuttling experiments. As the time required for each shuttling event is increased in the adiabatic experiments, the qubit experiences more dephasing during each shuttling step and the phase coherence is lost after a smaller number of shuttling steps n. The use of echoing pulses allows us to get an improvement of the coherent shuttling performance by a factor 6 to 8, larger than those obtained for diabatic shuttling.

For shuttling basis states, the lower performance suggests that the probability of having a spin-flip during a shuttle increases if the latter is performed adiabatically. This could originate from the longer time spent in the vicinity of the charge transition, where spin randomization induced by charge noise is enhanced [44]. Overall, the data in Fig. 6.14 clearly show that an approach based on diabatic spin shuttling is preferable for hole spin

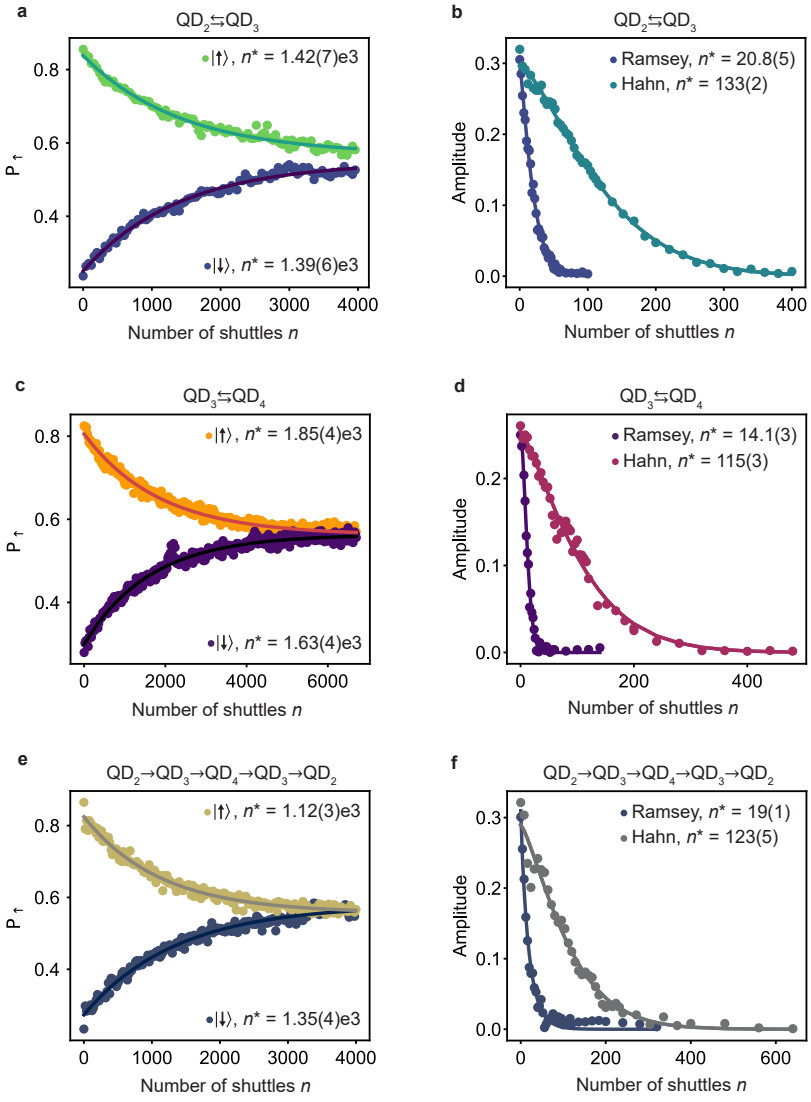

Figure 6.14: **Performance of adiabatic shuttling.** **a**, **b**, **c**, Spin polarization as a function of the number of shuttling steps n for a qubit initialized in the basis states. **d**, **e**, **f**, Amplitude as a function of the number of shuttling steps n for qubits initialized in a superposition state, without (Ramsey) and with echo pulse (Hahn).

qubits in germanium.

6.7.2. RABI CONTROL AFTER SHUTTLING

Since the rotations induced by diabatic shuttling are coherent, it should be possible to compensate these rotations by applying a microwave pulse. This requires the synchro-

nisation of the internal clocks of the arbitrary waveform generators (AWGs) and the microwave source. Fig. 6.15.a shows the pulse sequence used to investigate this strategy. A spin prepared in the $|\downarrow\rangle$ state is shuttled back-and-forth once between QD_2 and QD_3. The idle time in QD_3 is purposely chosen such that the spin does not experience a $2\pi m$ rotation around the tilted quantization axis. As a result, after the shuttling, the spin is not in the $|\downarrow\rangle$ state anymore. Back in QD_2, an EDSR pulse is applied of which the phase ϕ and duration t_{MW} are varied. Finally, the spin is readout.

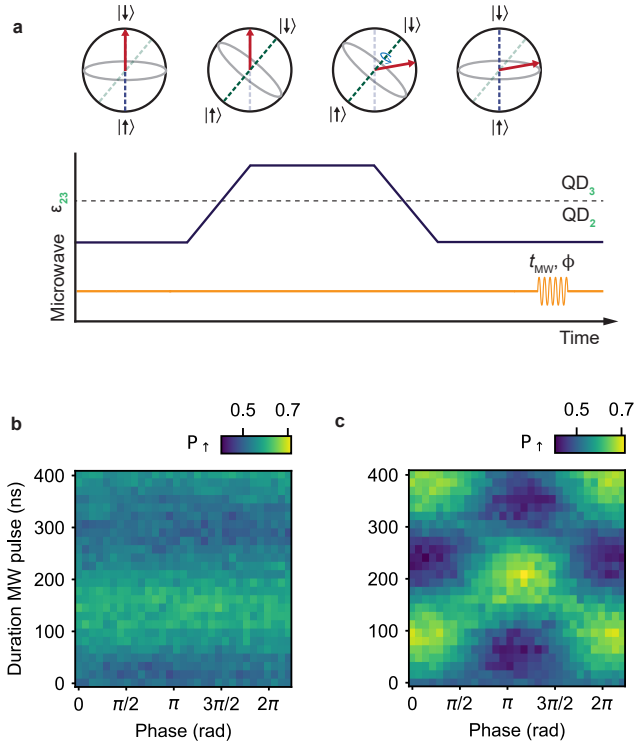

Figure 6.15: **Compensating shuttling-induced oscillations with a final EDSR pulse. a**, Schematic of the pulse sequence used for testing the effect of an EDSR pulse after shuttling a spin qubit. A spin qubit is initialized in the $|\downarrow\rangle$ state and shuttled back-and-forth between QD_2 an QD_3. Finally, a microwave pulse of duration t_{MW} and phase ϕ is applied. **b**, Results of the measurement sequence depicted in (a), in the case where the clock of the AWGs and the microwave source are not synchronized. **c**, Results in the case where the clocks of the AWGs and the microwave source are synchronized. The reduced visibility of the oscillations in the spin-up probability, compared to the data presented in the main text, is due to a different tuning of the device.

Fig. 6.15.b and c show the result of this experiment, without and with synchronisation of internal clocks of the AWG and microwave source. From Fig. 6.15.b it is clear that, if the internal clocks are not synchronized, the measured spin-up probability does not depend on the phase of the microwave pulse. Due to the lack of synchronization, the phase of the EDSR pulse (with phase ϕ and duration t_{MW}) varies between the single shot

measurements of a single experiment, viewed in the lab frame. Therefore, the information about the phase of the spin after shuttling is lost and it is not possible to coherently drive the spin. In Fig. 6.15.c, we recover an oscillation in spin-up probability as a function of the phase of the microwave source, which indicates that the state of the spin is well-defined after the shuttling. It is therefore possible to coherently drive the spin after shuttling. The results in Fig. 6.15.b and c illustrate the importance of the synchronization of AWGs and microwave source clocks in the prospect of using a final EDSR pulse to compensate rotations induced by shuttling. The experiments presented in the main text of the manuscript were performed without synchronisation between the microwave source and the AWGs.

6.8. EXTENDED DATA

6.8.1. SPIN RANDOMIZATION NEARBY THE INTERDOT CHARGE TRANSITION

In Fig. 6.2.b and c, we show the evolution of the qubit resonance frequency f_L along the detuning axis of the QD_2-QD_3 quantum dot pair and of the QD_3-QD_4 quantum dot pair. f_L is measured by shuttling the spin and applying a 4 µs long EDSR pulse on one plunger gate. While f_L can be clearly determined when the hole is well-localized in one quantum dot, it cannot be measured nearby the charge transition as the spin-up probability has a high value over the whole range of frequency spanned. We think that this is the result of a combination of different effects.

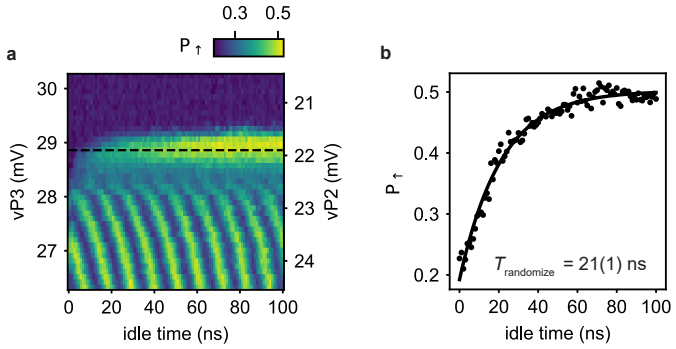

Figure 6.16: **Randomization of spin states around the QD_2 - QD_3 charge transition. a**, Shown is the result of the shuttling of a spin in the $|\downarrow\rangle$ state while changing the detuning and the idle time. Note that in contrast to the measurement shown in Fig. 6.3b of the main text, the time resolution on the x-axis is not large enough to distinguish the oscillations with gigahertz frequency, instead what is visible here is an aliasing pattern. **b**, The data plotted and fitted here correspond to a linecut of (a), taken at the dashed line. The typical time it takes for the spin to randomize (while starting in the $|\downarrow\rangle$ state) is 21 ± 1 ns and is extracted by fitting an exponential function. The error bar corresponds to one standard deviation from the best fit.

Since the two quantum dots have different quantization axes, the system effectively behaves as a flopping-mode qubit nearby the charge transition [41, 50–52] and the EDSR driving is thus expected to be more efficient. This appears, in Fig. 6.2.b, when the qubit is in QD_2: along the resonance line, we observe an alternation of high and low spin-up

probabilities that witness rapid variations of the Rabi frequency. As a consequence, the power broadening increases significantly in the vicinity of the charge transition which prevents us from resolving the qubit resonance frequency. We have not observed such effects in the other quantum dots and speculate it is due to the driving efficiency and the depahsing. In this studied device, the four qubits can usually be efficiently driven with one particular plunger gate. This drivability is likely the origin why the effect disappears once the qubit is in in QD_3 in Fig. 6.2b.

The gradient of shear strains induced by the thermal contraction of the gate electrodes can lead to large increases of the Rabi frequency [53]. It is likely that this effect is enhanced in the vicinity of the charge transition, as the hole is delocalized between the two quantum dots and its wavefunction extends below the edges of several gates. Finally, nearby the charge transition, excitations to higher energy states induced by charge noise are more likely to occur [44], especially on the relatively long timescale of 4 µs. These transitions to higher energy states lead to a randomization of the spin states, which explains the large spin-up probabilities observed over the full frequency range.

This last argument is supported by the data shown in Fig. 6.16. This figure shows the result of shuttling a qubit in a $|\downarrow\rangle$ state while changing the detuning and varying the idle time (similar to Fig. 6.3a of the main text). It becomes clear that once the spin approaches the charge anticrossing between QD_2 and QD_3 (indicated by the striped black line in Fig. 6.16a), the time it takes for the spin state to be randomized decreases very rapidly to about $T_{\text{randomize}} = 21 \pm 1$ ns (fit to an exponential decay shown in Fig. 6.16.b). The randomization of the spin close to the charge anticrossing could also be an explanation for the fact that the spin-up probability measured for shuttling basis states decays to the value of 0.5 instead of 0.

6.8.2. QUANTIFYING THE QUANTIZATION AXIS TILT ANGLE

ESTIMATION BASED ON THE VISIBILITY OF THE OSCILLATIONS INDUCED BY THE CHANGE IN QUANTIZATION AXIS

The tilt angle θ between the quantization axis of two different quantum dots can be estimated based on the amplitude of the oscillations induced by diabatically shuttling a qubit in the $|\downarrow\rangle$ state. This approximation relies on a simple geometric construction in the Bloch sphere.

Fig. 6.17.a shows the Bloch sphere projected on the plane defined by the quantization axes of the two quantum dots (dark blue and dark green). At the beginning of the experiment, the qubit is initialized in the $|\downarrow\rangle$ state (red arrow). After shuttling to the neighboring quantum dot, the qubit state changes due to the difference between the quantization axes. In the Bloch sphere, this can be represented by rotations of the state vector around the second quantization axis. After half a period (orange arrow), the state projection on the quantization axis of the quantum dot where the experiment started differs maximally from that of the initial state. This sets the visibility M of the oscillations induced by the change of quantization axis.

In practise, this visibility is reduced due to imperfect initialization and readout. This can be taken into account by assuming that the state vectors have a norm $V < 1$ with V being the visibility of Rabi oscillations measured in the quantum dot where the shuttling experiment starts. We neglect relaxation which is irrelevant at the time scale of few

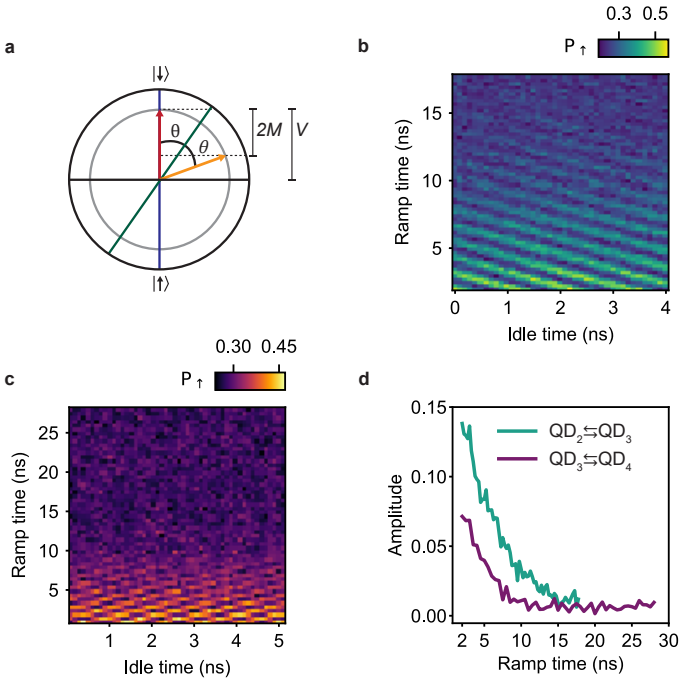

Figure 6.17: **Estimation of the tilt angle based on the amplitude of the oscillations induced by the difference in quantization axis. a,** Geometric construction in the Bloch sphere allowing to determine the tilt angle θ between the quantization axes of adjacent quantum dots (blue and green). θ is determined from the visibility M of the oscillations induced by the change in quantization axes and the visibility of the Rabi oscillations V. **b**, **c**, Oscillations induced while shuttling a qubit in a $|\downarrow\rangle$ state between QD_2 and QD_3 (b) and between QD_3 and QD_4 (c) for increasing ramp times. **d**, Amplitude of the oscillations as function of the ramp times.

nanoseconds [54] and thus assume that the norm of the vector state stays constant during the rotations. We find that:

$$\theta = \frac{1}{2}\arccos(1-2M/V) \text{ with } 0 \leq \theta \leq \pi. \tag{6.18}$$

We use this expression to evaluate θ_{23} (θ_{34}), the tilt angle between the quantization axes of QD_2 and QD_3 (QD_3 and QD_4). Fig. 6.17.b and c show the oscillations induced by the change in quantization axis as function of the pulse ramp time t_{ramp}. The amplitude $M/2$ of these oscillations is fitted and plotted in 6.17.d. As discussed in the main text, the amplitude of the oscillations drop rapidly to zero as t_{ramp} increases, because the shuttling becomes more adiabatic with respect to the difference in quantization axis. For the evaluation of θ we use the amplitude $M/2 = 0.14$ (0.07) of the oscillations at the shortest $t_{\text{ramp}} = 2$ ns. We remark that there is no clear saturation of M at the smallest ramp times, which suggests that the shuttling process is still not fully diabatic and that higher visibilities could be achieved by shuttling faster. Rabi oscillations for the driving of the qubit in QD_2 (QD_3) have a visibility of $V = 0.61$ (0.48) giving us $\theta_{23} \geq 42°$ ($\theta_{34} \geq 33°$).

These large values for θ illustrate the strong influence of the local electric field on the direction of the quantization axis in germanium hole spin qubits operated with an in-plane external magnetic field.

ESTIMATIONS BASED ON FITS WITH A FOUR-LEVEL MODEL

To get an additional independent evaluation of the tilt angles, we can fit the evolution of the qubit resonance with a four-level model. To derive such a model, we consider a single hole in a germanium double quantum dot placed in an external magnetic field B. We assume that there is a finite tunnel coupling t_c between the two quantum dots QD_A and QD_B and their quantization axes are tilted with respect to each other by an angle θ. This last assumption is sufficient to take into account all effects of the spin-orbit interaction, providing a suitable basis transformation and a renormalization of the tunneling terms.

The system can be described in the basis $\{|A,\uparrow_A\rangle, |A,\downarrow_A\rangle, |B,\uparrow_A\rangle, |B,\downarrow_A\rangle\}$, where 'A' or 'B' indicates the position of the hole (in quantum dot QD_A or QD_B) and $\uparrow_A$ or $\downarrow_A$ specifies its spin states in the frame of quantum dot A. Its Hamiltonian is then given by:

$$H_{\text{model}} = H_{\text{charge}} + H_{\text{Zeeman}} =$$

$$\begin{pmatrix} \epsilon & 0 & t_c & 0 \\ 0 & \epsilon & 0 & t_c \\ t_c & 0 & -\epsilon & 0 \\ 0 & t_c & 0 & -\epsilon \end{pmatrix} + \frac{1}{2} B \mu_B \begin{pmatrix} g_A(\epsilon) & 0 & 0 & 0 \\ 0 & -g_A(\epsilon) & 0 & 0 \\ 0 & 0 & g_B(\epsilon)\cos(\theta) & g_B(\epsilon)\sin(\theta)e^{i\varphi} \\ 0 & 0 & g_B(\epsilon)\sin(\theta)e^{-i\varphi} & -g_B(\epsilon)\cos(\theta) \end{pmatrix}, \tag{6.19}$$

where ϵ is the detuning energy of the double quantum dot system (taken as zero at the charge transition), μ_B is the Bohr magneton and g_i are the g-factors in the different quantum dots, φ is the azimuthal angle between the two quantization axes. Note that, with this convention, ϵ corresponds to half of the difference between the electrochemical potentials of the two quantum dots and a tunnel gap of $2t_c$ at the anticrossing. We remark that this model is similar to that of a flopping-mode qubit [50]. Diagonalizing the Hamiltonian, we obtain the qubit resonance frequency f_L given by:

$$f_L = \frac{\mu_B B}{h} \frac{\sqrt{(2\epsilon^2 + t_c^2)(g_A(\epsilon)^2 + g_B(\epsilon)^2) + 2\epsilon(g_B(\epsilon)^2 - g_A(\epsilon)^2)\sqrt{\epsilon^2 + t_c^2} + 2g_A(\epsilon)g_B(\epsilon)t_c^2\cos(\theta)}}{2\sqrt{\epsilon^2 + t_c^2}}, \tag{6.20}$$

The evolution of f_L along the detuning axes can then be fitted to extract the tilt angles and the tunnel couplings between neighbouring quantum dots. For this purpose, we first express the detuning energies in terms of gate voltages as $\epsilon_{23} = -\frac{\eta_{23}}{2}(vP_3 - vP_3^0)$ and $\epsilon_{34} = -\frac{\eta_{34}}{2}(vP_4 - vP_4^0)$ where $\eta_{23} = 0.166$ meV/mV and $\eta_{34} = 0.150$ meV/mV are the effective lever arms along the detuning axis. They are defined as $\eta_{23} = \beta_3 + \beta_2\gamma_{23}$ and $\eta_{34} = \beta_4^* + \beta_3^*\gamma_{34}$ where $\beta_2 = 0.084$ meV/mV, $\beta_3 = 0.080$ meV/mV ($\beta_3^{(*)} = 0.084$ meV/mV, $\beta_4^{(*)} =$

0.075 meV/mV) are the virtual gate lever arms measured nearby the QD_2-QD_3 (QD_3-QD_4) charge transition via photon-assisted tunnelling experiments [55] and where $\gamma_{23} = |\Delta vP_2/\Delta vP_3|$=1.026 ($\gamma_{34} = |\Delta vP_3/\Delta vP_4| = 0.889$) are the slopes of the detuning axis. We extract the evolution of f_L as function of vP_3 (vP_4) from the data displayed in Fig. 6.18.a-b (Fig. 6.19.a-c) and fit it with eq.(Fig. 6.20).

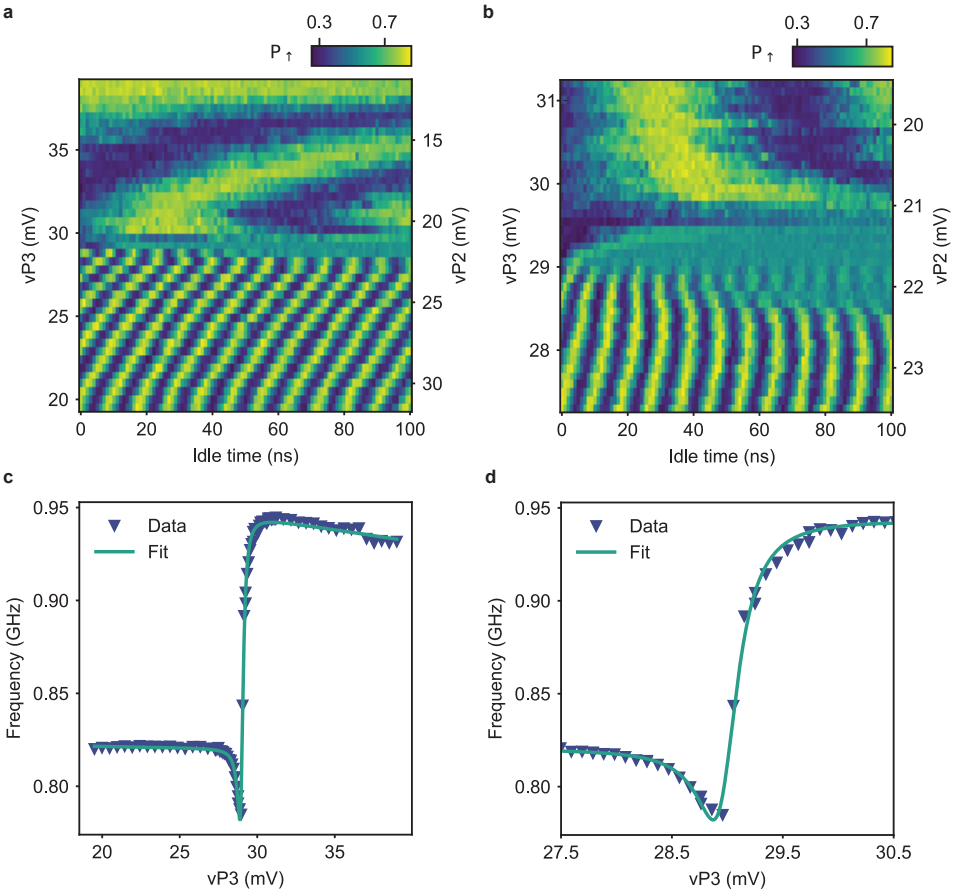

Figure 6.18: **Evaluation of the tilt angle between QD_2 and QD_3 quantization axes using a four-level model. a**, Free evolution experiments for shuttling a qubit in superposition state between QD_2 and QD_3 back-and-forth. The superposition state is prepared in QD_2. **b**, Zoom-in on the vicinity of the charge transition. The two data sets are identical to those displayed in Fig. 1.h. **c**, **d**, Resonance frequency extracted from the oscillations along the detuning axis in (a) and (b) and fit with the model of eq. (6.20).

Fig. 6.18.c-d display the evolution of f_L along the ϵ_{23} detuning axis which is fitted to the above model assuming a linear dependence of g with vP_3. We observe that the model reproduces well the measured evolution. This allows to estimate an interdot tunnel coupling t_c of 4.4±0.2 GHz and a tilt angle θ_{23} of 51.8±0.7°. The error bars correspond to one standard deviation from the best fit. This evaluation is consistent with the lower

bound found using the previous method.

Fig. 6.19.d-e display the evolution of f_L along the ϵ_{34} detuning axis. In this case, fitting the data does not allow to extract the tilt angle, even if we assume a quadratic dependence of the g-factor with the gate voltage. Indeed, for $0° \leq \theta \lesssim 40°$, the shape of f_L curve is nearly solely determined by the tunnel coupling and the variation of the g-factor with vP_4. Consequently, the data can be equally well fitted by models where θ_{34} is fixed at 0°, 10°, 20°, 30° or 40°. This leads to such a large uncertainty on the value of θ_{34} that it prevents us from extracting it. Nevertheless, the tunnel coupling between QD_3 and QD_4 can still be estimated from these fits and, for θ_{34} fixed to 40° (30°), we find $t_c = 8 \pm 1$ ($t_c = 6.2 \pm 0.8$) GHz.

What does become clear, however, is that we cannot obtain proper fits of the data with model where θ_{34} is fixed to values larger than 40°. The underlying reason appears when plotting the expected evolution of f_L in such model: for $\theta_{34} \gtrsim 50°$, f_L should display a minimum that we do not observe experimentally. This suggests that θ_{34} is lower than 50°.

This analysis also allows us to estimate the degree of adiabaticity of the charge transfers between the neighbouring quantum dots i and j. For that, we use the Landau-Zener formula $P_{LZ}^{ij} = \exp(\frac{-2\pi t_c^2 t_{ramp}}{2\hbar\Delta\epsilon_{ij}})$ that gives us the probability of having a transition to the excited charge state while changing the detuning linearly by $\Delta\epsilon_{ij} = \frac{\eta_{ij}}{2}\Delta vP_{ij}$ in a time t_{ramp}. We emphasize that the factor 2 in front of $\Delta\epsilon_{ij}$ comes from our definition of ϵ_{ij}. Taking $\Delta vP_3 = 19.5$ mV for shuttling between QD_2 and QD_3, $\Delta vP_4 = 18$ mV for shuttling between QD_3 and QD_4 and $t_{ramp} = 4$ ns, we find $P_{LZ}^{23} \simeq 2 \times 10^{-2}$ and $P_{LZ}^{34} \simeq 2 \times 10^{-7}(9 \times 10^{-5})$. The values obtained for the shuttling between QD_3 and QD_4 suggest that the charge transfer between these two quantum dots is adiabatic. In contrast, there is non-negligible probability of exciting higher charge states while shuttling between QD_2 and QD_3 with these settings.

To improve the fidelity of the shuttling process between QD_2 and QD_3, we increased the tunnel coupling by lowering the barrier gate voltage vB_{23} from −40 mV to −75 mV. Fig. 6.20 shows the results of similar analysis performed after lowering the barrier gate voltage. Fitting the evolution of the resonance frequency along the detuning axis, we find that $t_c = 16.1 \pm 0.6$ GHz and $\theta_{23} = 54.2 \pm 0.6°$. For these experiments, $\eta_{23} = 0.164$ and $\Delta vP_3 = 24$ mV, thus we find $P_{LZ}^{23} \simeq 2 \times 10^{-19}$. In this gate voltage configuration, the shuttling process is fully adiabatic with respect to the charge degree of freedom. Consequently, we used these barrier gate voltage settings to have better shuttling performance and, in particular, for the experiments presented in Fig. 6.5 and Fig. 6.7.

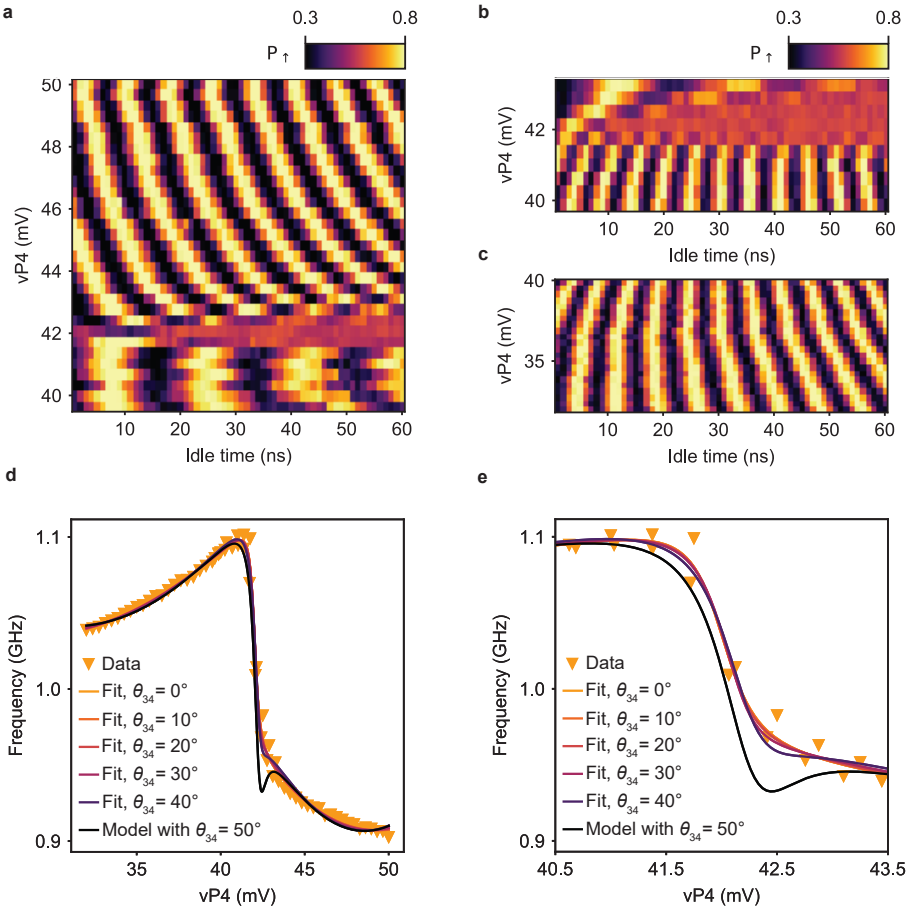

Figure 6.19: **Evaluation of the tilt angle between QD_3 and QD_4 quantization axes using a four-level model. a**, **b**, **c**, Free evolution experiments for the adiabatic shuttling of a qubit in a superposition state between QD_3 and QD_4 back-and-forth. In (a) the qubit is prepared in superposition in QD_4, while in (b) and (c) the superposition state is prepared in QD_3. **d**, **e**, Evolution of the resonance frequency along the detuning axis, extracted from the oscillations in (a), (b) and (c), and fits with models of eq. (6.20) where the tilt angle is fixed. The expected evolution for $\theta_{34} = 50°$ is computed using the parameters extracted from the fit with $\theta_{34} = 40°$.

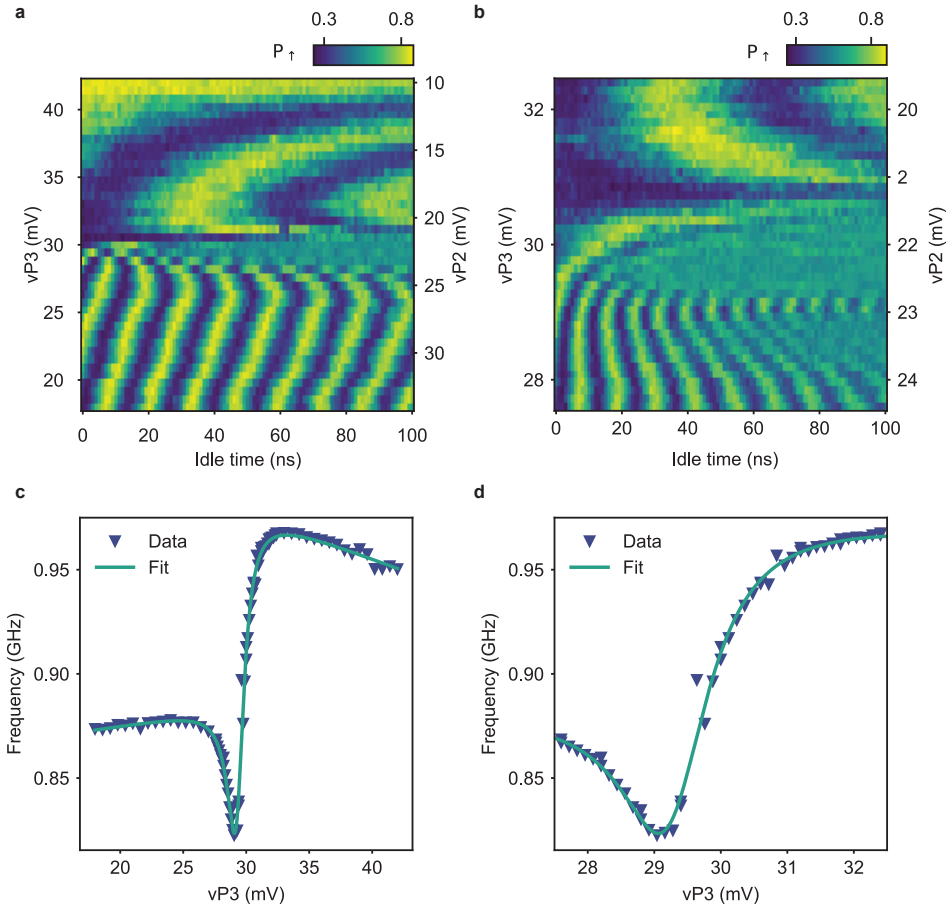

Figure 6.20: **Evaluation of the tilt angle between QD_2 and QD_3 quantization axes using a four-level model at a lower barrier gate voltage. a**, Free evolution experiments for shuttling a qubit in a superposition state between QD_2 and QD_3 back-and-forth. The superposition state is prepared in QD_2. **b**, Zoom-in on the vicinity of the charge transition. **c**, **d**, Resonance frequency extracted from the oscillations along the detuning axis extracted from (a) and (b) and fit with the model of eq. (6.20). Compared to Fig. 6.18, here the barrier gate voltage vB_{23} is lower (−75 mV instead of −40 mV) leading to a higher tunnel coupling. These settings correspond to the settings used to acquire the data displayed in Fig. 6.5 and Fig. 6.7.

	$QD_2 \rightleftarrows QD_3$	$QD_3 \rightleftarrows QD_4$	Corner	Triangular
T_2^* in QD_2 (ns)	$(2.8\pm0.1)\times10^2$	N. A	$(2.8\pm0.1)\times10^2$	$(2.8\pm0.1)\times10^2$
α in QD_2	1.8±0.2	N. A	1.8±0.2	1.8±0.2
T_2^* QD_3 (ns)	$(4.1\pm0.3)\times10^2$	$(5.0\pm0.3)\times10^2$	$(4.1\pm0.3)\times10^2$	$(4.1\pm0.3)\times10^2$
α QD_3	1.6±0.2	1.8±0.3	1.6±0.2	1.6±0.2
T_2^* (ns) in QD_4	N. A.	$(3.1\pm0.2)\times10^2$	$(3.1\pm0.3)\times10^2$	$(3.1\pm0.3)\times10^2$
α in QD_4	N. A.	1.8±0.2	1.4±0.3	1.4±0.3
t^* (ns) shuttling	339±5	408±9	$(3.5\pm0.1)\times10^2$	$(3.4\pm0.2)\times10^2$
α shuttling	1.41±0.05	1.30±0.07	1.13±0.07	1.11±0.08

Table 6.2: **Dephasing times and decay coefficients for static and shuttled qubits.** The dephasing times T_2^* for static qubits are measured with standard Ramsey experiments (data shown Fig. 6.21), performed at the starting and the end points of the shuttling pulses. The dephasing time t^* for shuttled qubits are extracted by fitting the amplitude as a function of the total time, as shown in Fig. 6.21. The error bars indicate one standard deviation from the best fits. The voltages applied on the barrier gates vary between experiments, which can lead to different T_2^* and α values for a static qubit in a given quantum dot.

6.8.3. $T_2^\star$ OF STATIC QUBIT AND SHUTTLING PERFORMANCE AS A FUNCTION OF SHUTTLE TIME

To get some insight on how the shuttling performance compare to the typical coherence times in the system, we plot in Fig. 6.21 the qubit dephasing times T_2^* along side the results of the shuttling experiments as function of time. We evaluate the T_2^* of a static qubit at the locations in the charge stability diagrams corresponding to the starting and the end points of the shuttling pulses. The T_2^* values are measured using a standard Ramsey protocol. The resulting oscillations are fitted by $A\cos(2\pi t f+\varphi_0)\exp(-(t/T_2^*)^\alpha)+A_0$ allowing to extract both T_2^* and the decay coefficients α. The corresponding data and fits are shown in Fig. 6.21.a-b.

Moreover, for all the shuttling processes, we calculate for each number of shuttling events n the total time between the two $\pi/2$ pulses of the Ramsey shuttling experiments. Fig. 6.21.c-f show the results of shuttling experiments used to quantify the performances. These data are identical to those shown in Fig. 6.5 and Fig. 6.7, but the amplitude decay is shown as a function of the time duration of the shuttling experiments.

An overview of the fit parameters is shown in Table 6.2. Since the total measurement time for the shuttling experiments (several thousands of seconds) is very different from that for the Ramsey experiments (several hundreds of seconds), and therefore the type and amount of noise integrated are different, some caution is required when comparing the decay parameters. However, it is clear that the dephasing times of static and moving qubits are of the same order of magnitude.

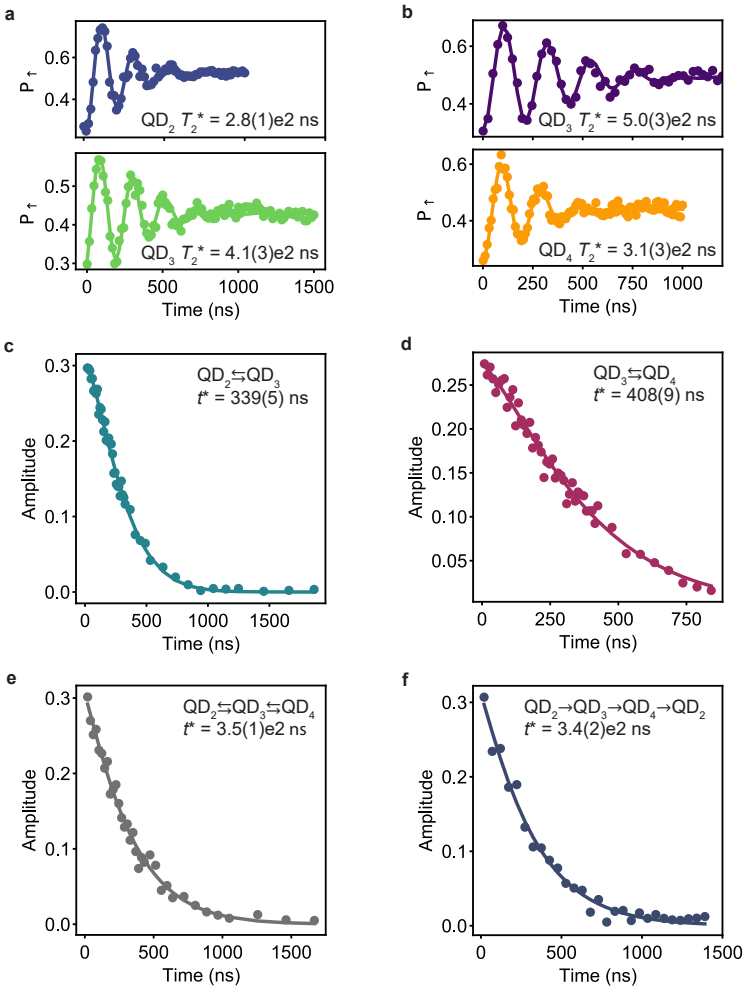

Figure 6.21: **Comparison of the dephasing times for static and shuttled qubits. a**, **b**, Results of Ramsey experiments for a spin in QD_2 and QD_3 (a) (QD_3 and QD_4 in (b)) at the same plunger and barrier gate voltages settings as the shuttling experiments between QD_2 and QD_3 (a) (QD_3 and QD_4 in (b)). **c**, **d**, The result of the shuttling experiment, to assess the shuttling performance with a superposition state (without echo pulse), between QD_2 and QD_3 (c) (QD_3 and QD_4 in (d)), same as in Fig. 3g (3h) of the main text. However, here the amplitude is plotted as a function of the total time between the two $\pi/2$-pulses. **e**, **f**, Similar to (a) and (b), but for the corner shuttling and the triangular shuttling. The gate voltage settings for these experiments are the same as for the Ramsey experiments shown in (a) for QD_2 and QD_3 and for QD_4 shown in (b). The error bars indicate one standard deviation from the best fits.

6.8.4. CHARGE STABILITY DIAGRAM OF PAIR QD_2-QD_4 AND TRIANGULAR SHUTTLING

The charge stability diagram of the quantum dot pair QD_2-QD_4, measured in a configuration identical to that of the triangular shuttling, is displayed in Fig. 6.22. No clear interdot charge anticrossing is visible, which suggests that the tunnel coupling between the two quantum dots is very low. This is expected, considering the device geometry, and it forces us to split the final pulse for the triangular shuttling in two parts. As depicted in Fig. 6.22, the voltages are first changed to bring the system close to the (1100)-(1001) degeneracy point before applying a second pulse that brings the system in the (1100) charge state. This reduces the probability that we excite the (1101) charge state, while transferring the qubit.

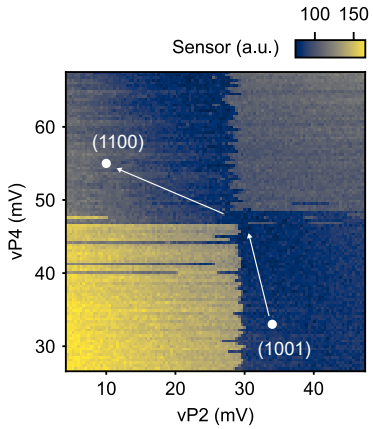

Figure 6.22: **Charge stability diagram of quantum dot pair QD_2-QD_4.** No clear interdot transition can be distinguished. The shuttling of a spin qubit from QD_2 to QD_4 is performed using two voltage pulses (white arrows). The labels $(N_1 N_2 N_3 N_4)$ represent the charge occupation in the quantum dots.

BIBLIOGRAPHY

[1] L. M. K. Vandersypen et al. “Interfacing spin qubits in quantum dots and donors—hot, dense, and coherent”. In: npj Quantum Information 3.1 (Sept. 2017), p. 34. ISSN: 2056-6387.

[2] N. W. Hendrickx et al. “A four-qubit germanium quantum processor”. In: Nature 591 (2021), pp. 580–585.

[3] Stephan G. J. Philips et al. “Universal control of a six-qubit quantum processor in silicon”. In: Nature 609.7929 (Sept. 2022), pp. 919–924. ISSN: 1476-4687.

[4] W. I. L. Lawrie et al. “Simultaneous single-qubit driving of semiconductor spin qubits at the fault-tolerant threshold”. In: Nature Communications 14.3617 (2023).

[5] A. R. Mills et al. “Two-qubit silicon quantum processor with operation fidelity exceeding 99%”. In: Science Advances 8 (2022), eabn5130.

[6] A. Noiri et al. “Fast universal quantum gate above the fault-tolerance threshold in silicon”. In: Nature 601 (2022), pp. 338–342.

[7] Xiao Xue et al. “Quantum logic with spin qubits crossing the surface code threshold”. In: Nature 601.7893 (Jan. 2022), pp. 343–347. ISSN: 1476-4687.

[8] L. Petit et al. “Universal quantum logic in hot silicon qubits”. In: Nature 580 (2020), pp. 355–359.

[9] C. H. Yang et al. “Silicon qubit fidelities approaching incoherent noise limits via pulse engineering”. In: Nature Electronics 2.4 (2019), pp. 151–158.

[10] L. C. Camenzind et al. “A hole spin qubit in a fin field-effect transistor above 4 kelvin”. In: Nature Electronics 5 (2022), pp. 178–183.

[11] Francesco Borsoi et al. “Shared control of a 16 semiconductor quantum dot crossbar array”. In: Nature Nanotechnology (Aug. 2023). ISSN: 1748-3395.

[12] R. Van Meter and D. Horsman. “A blueprint for building a quantum computer”. In: Communications of the ACM 56 (2013), pp. 84–93.

[13] D. P. Franke et al. “Rent’s rule and extensibility in quantum computing”. In: Microprocessors and Microsystems 67 (2019), pp. 1–7.

[14] Ruoyu Li et al. “A crossbar network for silicon quantum dot qubits”. In: Science Advances 4.7 (2018), eaar3960.

[15] A. Noiri et al. “A shuttling-based two-qubit logic gate for linking distant silicon quantum processors”. In: Nature Communications 13 (2022), p. 5740.

[16] J. M. Taylor et al. “Fault-tolerant architecture for quantum computation using electrically controlled semiconductor spins”. In: Nature Physics 1 (2005), pp. 177–183.

[17] J. M. Boter et al. “The spider-web array–a sparse spin qubit array”. In: Phys. Rev. Applied 18 (2022), p. 024053.

[18] M. Künne et al. “The SpinBus Architecture: Scaling Spin Qubits with Electron Shuttling”. In: arXiv (2023). eprint: 2306.16348.

[19] A. R. Mills et al. “Shuttling a single charge across a one-dimensional array of silicon quantum dots”. In: Nature Communications 10 (2019), p. 1063.

[20] I. Seidler et al. “Conveyor-mode single-electron shuttling in Si/SiGe for a scalable quantum computing architecture”. In: npj Quantum information 8 (2022), p. 100.

[21] R. Xue et al. “Si/SiGe QuBus for single electron information-processing devices with memory and micron-scale connectivity function”. In: Nature Communications 15 (2024), p. 2296.

[22] H. Flentje et al. “Coherent long-distance displacement of individual electron spins”. In: Nature Communications 8 (2017), p. 501.

[23] T. Fujita et al. “Coherent shuttle of electron-spin states”. In: npj Quantum Information 3 (2017), p. 22.

[24] P.-A. Mortemousque et al. “Coherent control of individual electron spins in a two-dimensional quantum dot array”. In: Nature Nanotechnology 16 (2021), pp. 296–301.

[25] P.-A. Mortemousque et al. “Enhanced Spin Coherence while Displacing Electron in a Two-Dimensional Array of Quantum Dots”. In: PRX Quantum 2 (2021), p. 030331.

[26] B. Jadot et al. “Distant spin entanglement via fast and coherent electron shuttling”. In: Nature Nanotechnology 16 (2021), pp. 570–575.

[27] J. Yoneda et al. “Coherent spin qubit transport in silicon”. In: Nature Communications 12 (2021), p. 4114.

[28] A. M. J. Zwerver et al. “Shuttling an Electron Spin through a Silicon Quantum Dot Array”. In: PRX Quantum 4 (2023), p. 030303.

[29] T. Struck et al. “Spin-EPR-pair separation by conveyor-mode single electron shuttling in Si/SiGe”. In: Nature Communications 15 (2024), p. 1325.

[30] A. Sammak et al. “Shallow and Undoped Germanium Quantum Wells: A Playground for Spin and Hybrid Quantum Technology”. In: Adv. Funct. Mater. 29.14 (2019), p. 1807613.

[31] G. Scappucci et al. “The germanium quantum information route”. In: Nature Reviews Materials 6 (2021), pp. 926–943.

[32] N. W. Hendrickx et al. “Fast two-qubit logic with holes in germanium”. In: Nature 577 (2020), pp. 487–491.

[33] N. W. Hendrickx et al. “A single-hole spin qubit”. In: Nat. Commun. 11 (2020), p. 3478.

[34] D. Jirovec et al. “A singlet-triplet hole spin qubit in planar Ge”. In: Nature Materials 20 (2021), pp. 1106–1112.

[35] D. Jirovec et al. “Dynamics of hole Singlet-Triplet qubits with large g-factor differences”. In: Phys. Rev. Lett. 128 (2022), p. 126803.

[36] C.-A. Wang et al. “Probing resonating valence bonds on a programmable germanium quantum simulator”. In: npj Quantum Information 9.58 (2023).

[37] N. W. Hendrickx et al. “Sweet-spot operation of a germanium hole spin qubit with highly anisotropic noise sensitivity”. In: Nature Materials (May 2024). ISSN: 1476-4660.

[38] S. A. Studenikin et al. “Enhanced charge detection of spin qubit readout via an intermediate state”. In: Appl. Phys. Lett. 101.23 (2012), p. 233101.

[39] P. Harvey-Collard et al. “High-Fidelity Single-Shot Readout for a Spin Qubit via an Enhanced Latching Mechanism”. In: Phys. Rev. X 8 (2 2018), p. 021046.

[40] W. I. L. Lawrie. “Spin Qubits in Silicon and Germanium”. In: PhD Thesis (2022).

[41] P. M. Mutter and G. Burkard. “All-electrical control of hole singlet-triplet spin qubits at low-leakage points”. In: Phys. Rev. B 104 (19 2021), p. 195421.

[42] S. Bosco et al. “Squeezed hole spin qubits in Ge quantum dots with ultrafast gates at low power”. In: Phys. Rev. B 104 (11 2021), p. 115425.

[43] Chien-An Wang et al. “Modelling of planar germanium hole qubits in electric and magnetic fields”. In: arXiv (2022). eprint: 2208.04795.

[44] Jan A. Krzywda and Ł Cywi ński. “Interplay of charge noise and coupling to phonons in adiabatic electron transfer between quantum dots”. In: Phys. Rev. B 104 (2021), p. 075439.

[45] Stefano Bosco, Ji Zou, and Daniel Loss. “High-fidelity spin qubit shuttling via large spin-orbit interaction”. In: arXiv (2023). eprint: 2311.15970.

[46] P. Huang and X. Hu. “Spin qubit relaxation in a moving quantum dot”. In: Phys. Rev. B 88 (2013), p. 075301.

[47] V. Langrock et al. “Blueprint of a Scalable Spin Qubit Shuttle Device for Coherent Mid-Range Qubit Transfer in Disordered Si/SiGe/SiO_2”. In: PRX Quantum 4 (2 2023), p. 020305.

[48] M. Lodari et al. “Light effective hole mass in undoped Ge/SiGe quantum wells”. In: Phys. Rev. B 100 (2019), p. 041304.

[49] R. Blume-Kohout et al. “A Taxonomy of Small Markovian Errors”. In: PRX Quantum 3 (2 May 2022), p. 020335.

[50] M. Benito et al. “Electric-field control and noise protection of the flopping-mode spin qubit”. In: Phys. Rev. B 100 (2019), p. 125430.

[51] X. Croot et al. “Flopping-mode electric dipole spin resonance”. In: Phys. Rev. Res. 2 (1 2020), p. 012006.

[52] R.-Z. Hu et al. “Flopping-mode spin qubit in a Si-MOS quantum dot”. In: Applied Physics Letters 122 (2023), p. 134002.

[53] José Carlos Abadillo-Uriel et al. “Hole-Spin Driving by Strain-Induced Spin-Orbit Interactions”. In: Phys. Rev. Lett. 131 (9 Sept. 2023), p. 097002.

[54] W. I. L. Lawrie et al. “Spin Relaxation Benchmarks and Individual Qubit Addressability for Holes in Quantum Dots”. In: Nano Lett. 20.10 (2020). PMID: 32833455, pp. 7237–7242.

[55] T. Oosterkamp et al. “Microwave spectroscopy of a quantum-dot molecule”. In: Nature 395 (1998), pp. 873–876.

7

OPERATING SEMICONDUCTOR QUANTUM PROCESSORS WITH HOPPING SPINS

Qubits that can be efficiently controlled are essential for the development of scalable quantum hardware. Although resonant control is used to execute high-fidelity quantum gates, the scalability is challenged by the integration of high-frequency oscillating signals, qubit crosstalk and heating. Here, we show that by engineering the hopping of spins between quantum dots with a site-dependent spin quantization axis, quantum control can be established with discrete signals. We demonstrate hopping-based quantum logic and obtain single-qubit gate fidelities of 99.97%, coherent shuttling fidelities of 99.992% per hop, and a two-qubit gate fidelity of 99.3%, corresponding to error rates that have been predicted to allow for quantum error correction. We also show that hopping spins constitute a tuning method by statistically mapping the coherence of a 10-quantum dot system. Our results show that dense quantum dot arrays with sparse occupation could be developed for efficient and high-connectivity qubit registers.

Parts of this chapter have been published in C.-A. Wang, V. John, H. Tidjani, C.X. Yu, A.S. Ivlev, C. Déprez, F. van Riggelen-Doelman, B.D. Woods, N.W. Hendrickx, W.I.L. Lawrie, L.E.A. Stehouwer, S.D. Oosterhout, A. Sammak, M. Friesen, G. Scappucci, S.L. de Snoo, M. Rimbach-Russ, F. Borsoi, M. Veldhorst, Operating semiconductor quantum processors with hopping spins, *Science* **385**, 447-452 (2024).

7.1. INTRODUCTION

Loss and DiVincenzo proposed hopping of electrons between two quantum dots as an efficient method for coherent spin control [1]. By applying discrete pulses to the quantum dot gates, a single spin can be transferred between qubit sites with differently oriented spin quantization axes, thereby enabling two-axis control of the qubit. Universal quantum logic is then achieved through a tunable exchange interaction between spins residing in different quantum dots. That work initiated the field of semiconductor spin qubits and inspired more than two decades of extensive research, but a successful implementation of Loss and DiVincenzo's initial proposal has remained elusive because of experimental challenges [2].

Alternative methods for coherent single-spin control have emerged, including electron spin resonance [3, 4] and electric dipole spin resonance using either micromagnets [5, 6] or spin-orbit interaction [7–10] to enable a coupling between the electric field and the spin degree of freedom. However, all of these methods rely on resonant Rabi driving and require high-power, high-frequency analog control signals that already limit qubit performance in small quantum processors [11–13]. The development of local, efficient, low-power control mechanisms of semiconductor spins is now a key driver [14–16]. To this end, qubits encoded in multiple spins and in multiple quantum dots, such as singlet-triplet, hybrid, and exchange-only qubits, have been investigated as possible platforms [2]. Although these qubit encodings have enabled digital single-qubit control, they also come with new challenges in coherence, control, and creation of quantum links. For example, the exchange-only qubits are susceptible to leakage outside of their computational subspace and require four exchange pulses to execute an arbitrary single-qubit gate and ≥ 12 exchange pulses for a single two-qubit gate [17–19].

Here, we demonstrate that single-spin qubits can be operated using baseband control signals, as envisaged in the original proposal for quantum computation with quantum dots [1]. We used hole spins in germanium quantum dots, in which the strong spin-orbit interaction gives rise to an anisotropic g-tensor that is strongly dependent on the electrostatic and strain environment [20]. We harnessed the resulting differences in the spin quantization axis between quantum dots [21, 22] to achieve high-fidelity single-qubit control using discrete pulses by shuttling the spin between quantum dot sites. A key advantage in such a hopping-based operation is that the spin rotation frequency is given by the Larmor precession. The latter remains sizeable even at small magnetic fields where quantum coherence is substantially improved [23, 24]. This enabled us to perform universal quantum control with error rates exceeding the thresholds predicted for practical quantum error correction[25] while also operating with low-frequency baseband signals. We then exploited the differences in quantization axes to map the spin dephasing times and g-factor distributions of an extended 10-quantum dot array, thereby efficiently gathering statistics on relevant metrics in large spin qubit systems.

7.2. RESULT

7.2.1. HIGH-FIDELITY SINGLE-QUBIT OPERATIONS AND LONG QUBIT COHERENCE TIMES AT LOW MAGNETIC FIELD

A large difference in the orientation of the spin quantization axes between quantum dots is essential for hopping-based qubit operations. Holes in planar germanium heterostructures manifest a pronounced anisotropic g-tensor, with an out-of-plane g-factor $g_\perp$ that can be two orders of magnitude larger than the in-plane component, $g_\parallel$ [20, 24, 26, 27]. Consequently, a small tilt of the applied magnetic field from the in-plane g-tensor will lead to a strong reorientation of the spin quantization axis in the out-of-plane direction. Subsequently, when an in-plane magnetic field is applied, the orientation of the spin quantization axis is highly sensitive to the local g-tensor, and thus to confinement, strain, and electric fields, thus becoming a site-dependent property [21, 24, 28, 29]. Here, we exploited this aspect to establish hopping-based quantum operations in two different devices: a four-quantum dot array [30] arranged in a 2×2 configuration and a 10-quantum dot system arranged in a 3-4-3 configuration.

We populated the four-quantum dot array with quantum dots Dm with $m \in [[1, 4]]$ with two hole spins Q_A and Q_B which can be shuttled between quantum dots by electrical pulses on the gate electrodes (Fig. 7.1A). A magnetic field up to 40 mT was applied to split the spin states and positioned in-plane up to sample-alignment accuracy (see Section 7.4). The relatively small magnetic fields ensured that the maximum qubit frequency (140 MHz) and its corresponding precession period (7 ns) were within the bandwidth of the arbitrary waveform generators used. In combination with engineered voltage pulses with sub-nanosecond resolution [21] (Section 7.9.1), we were able to shuttle a spin qubit to an empty quantum dot and thereby accurately change the qubit precession direction several times within one precession period. Altogether, this enables efficient single-qubit control through discrete voltage pulses (Fig. 7.1B).

The net effect of a multiple-shuttle protocol is a rotation $R(\hat{n},\theta)$ of the spin state around an axis $\hat{n}$ and with an angle θ. To implement a specific rotation such as the quantum gate $X_{\pi/2}$, the number of required shuttling steps depends on the angle between the two quantization axes. Because of the large angle between the axes of D1 and D4, $\theta_{14} > 90°/4 = 22.5°$, a pulse consisting of four shuttling steps is sufficient to realize a precise quantum gate $X_{\pi/2,A}$ (Section 7.7.1 and the supplementary materials [31], Section 3). As outlined on the top right panel of Fig. 7.1C, such a four-shuttle pulse moves the spin between D1 and D4 four times with waiting periods t_1 and t_4, respectively. By measuring the spin-flip probability of Q_A, $P_{A\uparrow}$, after two consecutive rotations $R(\hat{n},\theta)^2$, we could determine the values of t_1 and t_4 where $P_{A\uparrow}$ is maximal, which occurs when $R(\hat{n},\theta) = X_{\pi/2,A}$.

Although this method allows calibration of the pulse timing to compose an $X_{\pi/2,A}$ gate, it is not necessarily the optimal trajectory. Different choices of (t_1, t_4) are possible (Fig. 7.1C), including a composition of four-shuttle pulses with different waiting times in D4. The latter implementation allows for the construction of gates with a rotation angle θ less sensitive to Larmor frequency fluctuations in D4. We constructed such a gate by fitting the data in Fig. 7.1C to an effective model and determined the quantization axes angle θ_{14} between the quantum dots D1 and D4, the individual Larmor frequencies, and

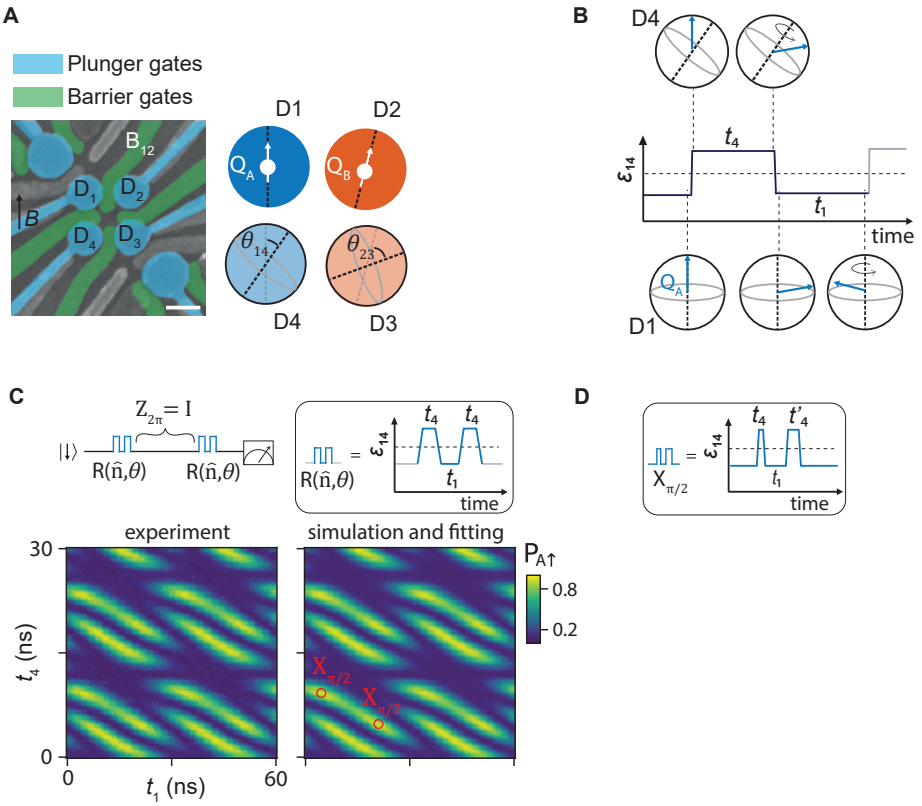

Figure 7.1: **Hopping-based single-qubit operations - schematics and tune-up.** **(A)** Left: scanning electron microscopy image of the 2×2 quantum dot array device [30], including gate-defined charge sensors at two corners. Scale bar, 100 nm. Right: schematic of the two spin qubits, Q_A and Q_B. The black dashed lines mark the relative quantization axis direction in the quantum dot pair D1-D4 (D2-D3), with the angle θ_{14} (θ_{23}). **(B)** Example of a baseband pulse $\epsilon_{14}(t)$ used to manipulate qubit Q_A, by shuttling the spin back and forth between quantum dots D1 and D4 and allowing the spin to precess in the individual quantum dots for the time t_4 and t_1. **(C)** Tune-up procedure of a four-shuttle pulse for the $X_{\pi/2}$ gate of Q_A at 20 mT. Top: pulse sequence of the experiment. Bottom left: measured spin-up probability $P_{A\uparrow}(t_1, t_4)$. Bottom right: simulation results. The red markers identify the timings for implementing an $X_{\pi/2,A}$ gate and corresponds to the maximal spin-up probability. The markers are periodic in t_1 and t_4, but for clarity we only plot a few of them. **(D)** Calibrated pulse for $X_{\pi/2,A}$ gate with unequal wait time t_4 and t_4'.

the effective precession time during the ramp. Through simulation of the qubit dynamics, we designed a more noise-resilient $X_{\pi/2,A}$ gate based on four shuttling steps with unequal wait times t_4 and t_4' in D4 (Fig. 7.1D). Following the same approach, we design an $X_{\pi/2,B}$ gate for Q_B that only requires a two-shuttle protocol because the angle of the difference in quantization axes of D2 and D3, θ_{23}, is very close to 45° (supplementary materials [31], Section 3).

We further calibrated the pulse timing using repetition sequences, as shown in Fig. 7.2C, and in AllXY sequences [32] (see the supplementary materials [31], Section 3). The $Y_{\pi/2}$ gate in the AllXY sequences was realized by $Y_{\pi/2} = Z_{\pi/2}X_{\pi/2}Z_{3\pi/2}$ and the $Z_{\pi/2}$ gate was

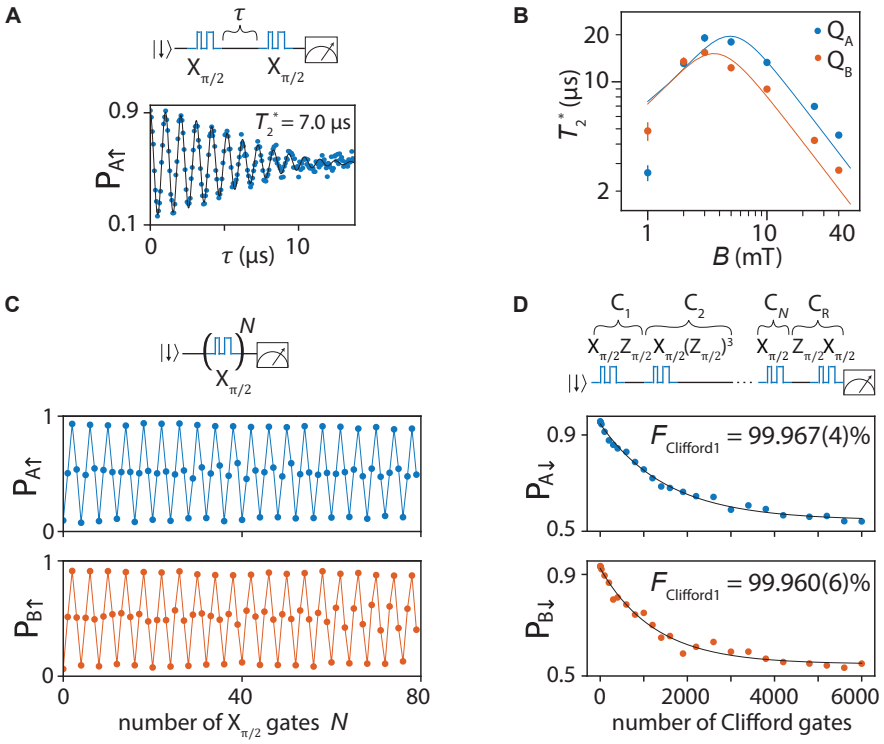

Figure 7.2: **Hopping-based single-qubit operations - gate fidelity and coherence times at low magnetic field.** **(A)** Free induction decay obtained from Ramsey experiments at 25 mT. **(B)** T_2^* as a function of magnetic field. The data points are fitted with an effective model including electric noise and nuclear noise (Section 7.9.2). **(C)** Spin-up probability after applying a varying number of $X_{\pi/2}$ gates on each qubit. **(D)** Example of a pulse sequence in Q_A single-qubit randomized benchmarking and the measurement results of both qubits. The uncertainties are obtained from bootstrapping with 95% confidence intervals.

implemented by idling the qubit for the time defined by its precession in the lab frame. The calibrated $X_{\pi/2}$ gates had a total gate time of 98 (35) ns for $Q_A(Q_B)$, corresponding to effective qubit rotation frequencies of 2.6 (7.1) MHz, considerable compared with the Larmor frequencies $f_{A(B)}$ = 42.6 (89.5) MHz at the in-plane magnetic field of 25 mT.

The high ratio between qubit rotation and Larmor frequency results in low power dissipation, which is a critical aspect for scaling up quantum processors [33]. To compare the power consumption of the hopping-based single-qubit control with the electric dipole spin resonance technique, we defined the required number of voltage oscillations to flip a qubit, N_{cycles}, and the derived energy efficiency, $\eta = 1/N_{\text{cycles}}$, which we found largely determines the power dissipation under the assumption that dielectric losses are dominant over other dissipation mechanisms (Section 7.5). For our system, we estimate an efficiency of η = 25(50)% for $Q_A(Q_B)$. By comparison, previous demonstrations of high-fidelity universal qubit logic in silicon exhibited η in the range of 0.04 to 0.07% [11, 12, 15]. Moreover, despite applying sizeable amplitudes to move the spins between localized orbitals of adjacent quantum dots, we still obtained a factor of 20 re-

duction in power dissipation with respect to the electric dipole spin resonance technique (Section 7.5). Engineering lower required pulse amplitudes and increasing the orthogonality of the spin quantization axes will enable a further reduction of the dissipated power. Furthermore, the hopping-based approach can simplify the signal delivery and required control electronics and thus alleviate the detrimental heating effects.

Having established universal single-qubit control, we used the set of gates $\{X_{\pi/2}, Y_{\pi/2}\}$ to investigate the qubit coherence times at low magnetic fields. By using a Ramsey sequence (Fig. 7.2A), we obtained a dephasing time T_2^* of 7.0 (4.5) μs at 25 mT for Q_A(Q_B), an order of magnitude larger than that measured at 1 T in the same sample [23, 30]. We were able to further extend the coherence times using Hahn and Carr-Purcell-Meiboom-Gill (CMPG) techniques, obtaining $T_2^{\mathrm{H}} = 32(24)\,\mu$s and $T_2^{\mathrm{CPMG-512}} = 1.9(1.7)$ ms, respectively. The dependence of the dephasing times as a function of magnetic field (Fig. 7.2B) indicates that charge noise remains the main cause for decoherence for magnetic fields as low as 5 mT (Section 7.9.2).

We characterize the single-qubit gate fidelity using randomized benchmarking (RB) and gate set tomography (GST) [34–36] (Section 7.6.1 and Section 7.6.2). The results of RB with average Clifford fidelity (Fig. 7.2D) set the lower bounds of the $X_{\pi/2}$ average gate fidelity at $F_{X_{\pi/2},A} \geq 99.967(4)\%$ and $F_{X_{\pi/2},B} \geq 99.960(6)\%$, consistent with the error modeling (Section 7.8.1). Using GST we benchmarked the $X_{\pi/2}$ and $Y_{\pi/2}$ gates, obtaining an average gate fidelity $\gtrsim 99.9\%$. From the GST analysis, we infer that dephasing is the dominant contribution to the average gate infidelity. Taking into account the multiple shuttling steps to execute a single gate, we estimate a coherent shuttling fidelity per hop as high as $F_{\mathrm{shuttle}} = 99.992\%$ (Section 7.6.3).

7

7.2.2. HIGH-FIDELITY TWO-QUBIT EXCHANGE GATE

We now focus on assessing the single-qubit and two-qubit gate performance in the two-qubit space. We implemented a two-qubit state preparation and measurement (SPAM) protocol (Figs. 7.3A,B). For the state preparation, we adiabatically converted the two-spin singlet in D2 to the triplet $|Q_AQ_B\rangle = |\downarrow\downarrow\rangle$. For the state measurement, we performed sequential Pauli spin blockade (PSB) readouts on Q_A and Q_B by loading ancillary spins from the reservoir and adiabatic conversion to the state $|\downarrow\downarrow\rangle$ in quantum dots D3 and D4. The difference in the effective g-factor between the quantum dots D1 and D2 allows for the construction of a controlled-Z (CZ) gate even at low magnetic fields. We did so by pulsing the virtual barrier gate voltage vB_{12}, which controls the exchange coupling J between Q_A and Q_B from 10 kHz to 40 MHz (Fig. 7.4C) (Section 7.9.3 and Section 7.7.2). Because the maximum exchange coupling strength is non-negligible compared with the Zeeman energy difference ΔE_Z and the qubit frequency f_A, pulse shaping is essential to mitigate coherent errors [12, 37]. We implemented exchange pulses with a Hamming window and performed the CZ gate calibration (Fig. 7.4D) (Section 7.9.4).

We now advance to benchmarking a two-qubit gate in germanium, by executing two-qubit randomized benchmarking (Section 7.6.1 for further details, and Section 7.6.2 for two-qubit GST). Individual Clifford gates were implemented by sequentially applying one or more of the gates CZ, $X_{\pi/2}^{A(B)}$, $Z_{\pi/2}^{A(B)}$, and I. From the fit of the decay constants of the reference and interleaved sequence in Fig. 7.4E, we determined the average Clifford gate fidelity as $F_{\mathrm{Clifford2}} = 98.60(6)\%$ and the average CZ gate fidelity as $F_{\mathrm{CZ}} = 99.33(10)\%$,

consistent with the result of error modeling (Section 7.8.2). For the single-qubit gate performance in the two-qubit space, we estimate the lower bound of fidelity, averaged between both qubits, as $\frac{1}{2}(F_{X_{\pi/2},A} + F_{X_{\pi/2},B}) \geq 99.90(5)\%$. We believe that these high fidelities to result from the high driving efficiency and relatively long $T_2^\star$ at low magnetic field.

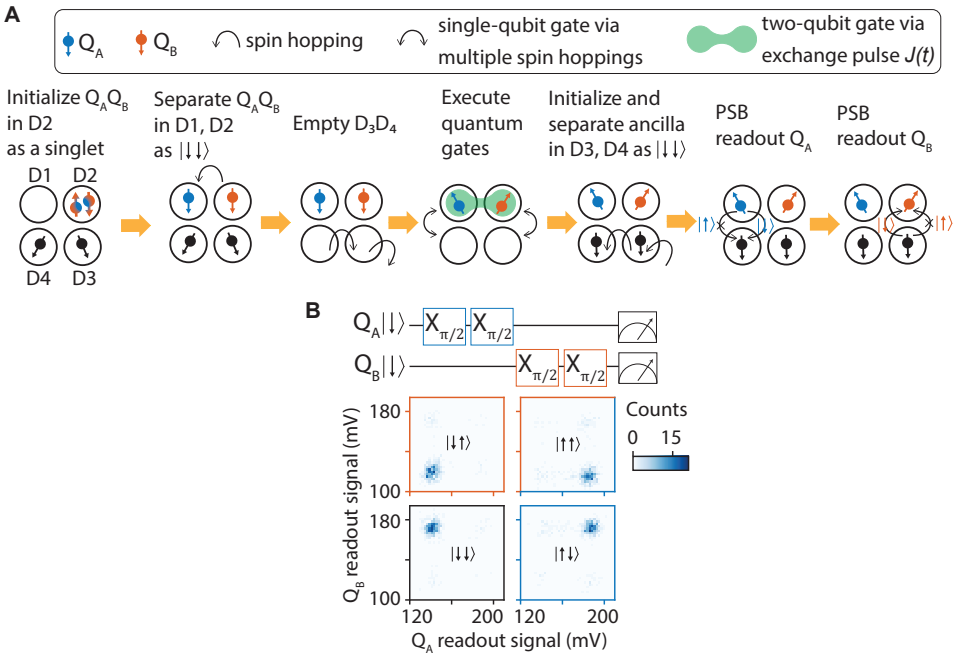

Figure 7.3: **High-fidelity two-qubit gate in germanium - schematics.** **(A)** Schematics of two-qubit initialization, manipulation and individual readout. $|Q_AQ_B\rangle$ was initialized by relaxing to the singlet ground state in D2 and then adiabatically moving one spin to D1. Quantum circuits consisting of single-qubit gates (spin hoppings) and two-qubit gates (exchange pulse $J(t)$) were performed. The final quantum state was read out by preparing ancillary spins and then performing two PSB readouts. In each readout, the chemical potentials of the quantum dots were pulsed such that the spin can either move to the neighboring dot (indicated by arrows) or stay in the original dot (indicated by arrows with × markers) with probabilities depending on the spin state $|Q_{A(B)}\rangle$. **(B)** Two dimensional histograms of the sensor signals formed by 500 single-shot measurements for four different two-qubit states, which are prepared by applying $X_{\pi/2,A(B)}$ gates.

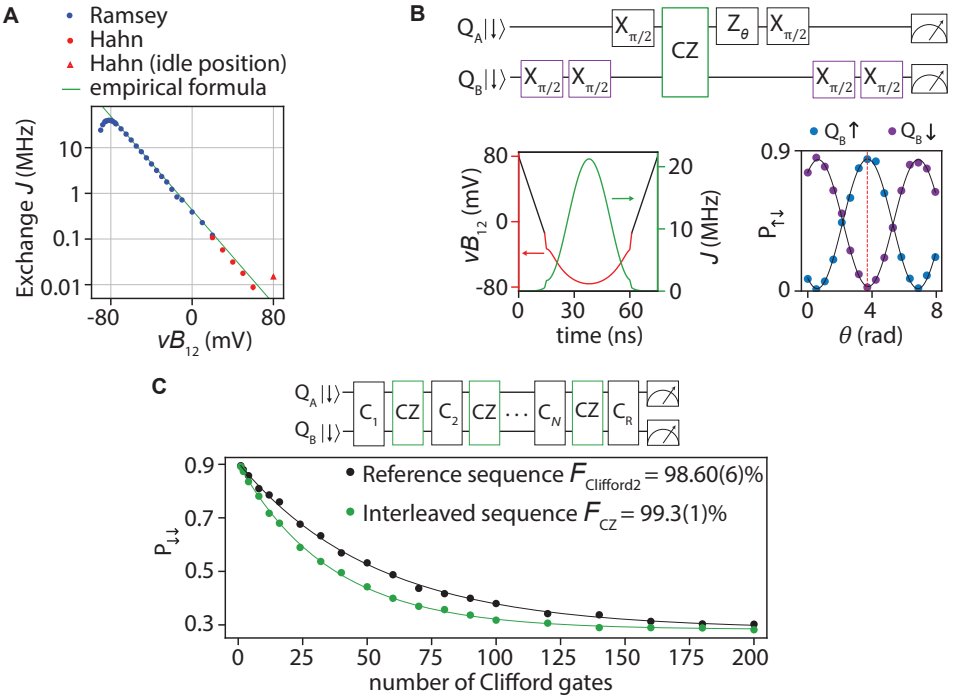

Figure 7.4: **High-fidelity two-qubit gate in germanium - measurement results.** **(A)** Exchange coupling as a function of virtual barrier gate vB_{12}, measured by Ramsey (Hahn echo) experiments in the large (small) coupling regime. The idle position corresponds to the barrier voltage where single qubit gates were performed, but at slightly different plunger gate voltage. The empirical formula for mapping vB_{12} and J is detailed in Section 7.9.4. The bending on the left side of the plot results from the energy level anti-crossing when $J \sim f_A$. **(B)** The voltage pulse of the CZ gate was shaped to have exchange $J(t)$ in the form of a Hamming window, as illustrated on the bottom left. The CZ gate calibration circuit for single-qubit phases is on the top, with the measurement outcome plotted on the bottom right. The target qubit (Q_A) phase depends on the control qubit Q_B being in the state $|\downarrow\rangle$ in blue ($|\uparrow\rangle$ in purple). The red dashed line marks the required single-qubit phase of Q_A for the CZ gate. **(C)** Gate sequence and measurement result of two-qubit interleaved RB.

7.2.3. HOPPING SPINS TO BENCHMARK LARGE AND HIGH-CONNECTIVITY QUANTUM DOT ARCHITECTURES

The presented sparse occupation of a quantum dot array allows the construction of high-fidelity hopping-based quantum logic, but it may also facilitate the implementation of quantum circuits with high-connectivity. Although two-dimensional quantum circuits with nearest neighbor connectivity can already tolerate high error rates [25, 38, 39], an increased connectivity may substantially lower the physical qubit overhead and lower the logical qubit error rate [40]. We therefore envision a qubit architecture with sparse occupation (Fig. 7.5A) to be a potential platform. Here, qubits may be shuttled to remote sites for distant two-qubit logic, and single-qubit logic can be executed during this

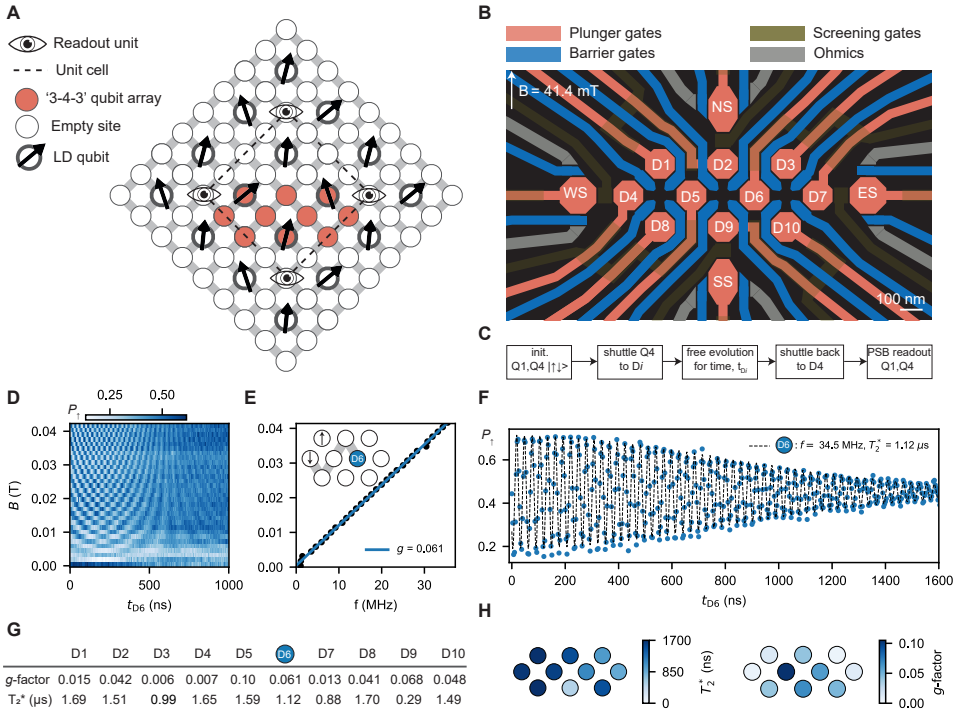

Figure 7.5: **Hopping spins to benchmark large and high-connectivity quantum dot architectures.** **(A)** Our vision of a semiconductor quantum computing architecture comprising hopping Loss-DiVincenzo (LD) spin qubits (black arrows), readout units (eyes), and empty quantum dot sites for shuttling operations. **(B)** Layout of the 10 quantum dot array, with gate-defined charge sensors labelled in analogy to the four cardinal points (NS, ES, WS, and SS). **(C)** Control sequence used to characterize the array. A spin originally in D4 was shuttled across the whole array, allowed to evolve at a certain quantum dot, and read out. **(D)** Qubit rotations induced by the difference in quantization axes as a function of idling time in quantum dot D6 and magnetic field. **(E)** D6 Larmor frequency, extracted from the Fourier analysis of (D) versus magnetic field. Linear fit yields an estimated g-factor of 0.062. Inset shows the shuttling trajectory of the spin qubit from D4 to D6. **(F)** Extended time evolution in D6 at B = 41.4 mT, yielding a qubit frequency of 34.51 MHz and a dephasing time of T_2^* =1.12 μs. The experimental trace was fitted (dashed lines) as described in Section 7.9.6. **(G and H)** Table and visualization of the extracted parameters: g-factors and T_2^*, respectively.

trajectory.

As a first step toward such architectures, we developed and characterized an extended system comprising 10 quantum dots. The system (Fig. 7.5B) consists of a multilayer gate architecture with quantum dots, Dn with $n \in [[1,10]]$, and peripheral charge sensors, which may be integrated within the array through development of vertical interconnects such as in [41]. By exploiting dedicated (virtual) barrier and plunger gate voltages, we prepared the quantum dots D1 and D4 in the single-hole regime, leaving the others empty (see Section 14 of the supplementary material [31], and Section 7.9.5).

The hopping-based qubit gates were used to rapidly characterize the different quantum dot g-factors and coherence times. After initializing the associated qubit pair Q1,Q4 into its $|\uparrow\downarrow\rangle$ eigenstate, we diabatically shuttled the Q4 spin to another quantum dot site, Dn. We let it precess for a time $t_{\mathrm{D}n}$, after which the spin was shuttled back and read out. The misalignment between the spin quantization axes gives rise to spin rotations with the Larmor frequency $f_{\mathrm{D}n}$ [21]. The resulting oscillations are shown as a function of waiting time in D6, t_{D6}, and magnetic field (Fig. 7.5D). From the linear scaling of the D6 Larmor frequency with the magnetic field, we extracted an effective g-factor of 0.062 (Fig. 7.5E) and from the decay of the oscillations a dephasing time of $T_2^* = 1.12\,\mu$s (Fig. 7.5F). Repeating this protocol to reach all the quantum dots, we extracted the Larmor frequency and dephasing time at each site, as displayed in Figs. 7.5G, H. For the case of Q1 (Q4), we shuttled the spin to D5 (D8) back and forth twice, interleaved by a varying precession time in D1, t_{Q1} (in D4, t_{Q4}), which we explain in detail in Section 16 of the supplementary material [31]. Our experiments showed an average T_2^* of $1.3 \pm 0.4\,\mu$s at a magnetic field of 41.4 mT (Section 7.9.6), and we attribute the fast dephasing of D9 ($T_2^* =$ 290 ns) to charge noise originating from a fluctuator nearby. Furthermore, we obtained an average g-factor of 0.04 ± 0.03. The observed variability in this distribution is likely a result of multiple factors: the heterogeneity inherent in the shapes of the quantum dots (dot-to-dot variability), the presence of strain gradients in the quantum well arising from the gates above or the SiGe strained relaxed buffer below, and the impact of interface charges. The average g-factor that we obtained was considerably lower than what has been observed in the literature [10, 24, 26, 30]. We suggest that this reduction is primarily due to two phenomena: a precise in-plane magnetic field configuration and an appreciable renormalization of the gyromagnetic ratio from the pure heavy-hole value of ~ 0.18 [27, 28, 42]. Such renormalization is driven by substantial inter-band mixing between the heavy-hole and the light-hole band, which we attribute to asymmetries in the strain, as simulated in Section 18 of the supplementary material [31]. Furthermore, these simulations indicate that such a low average effective g-factor only occurs when the misalignment of the magnetic field is smaller than 0.1° with respect to the plane of the g-tensors, emphasizing the importance of accurately controlling the magnetic field orientation when operating with germanium qubits.

7.3. CONCLUSION

We have shown that hopping spin qubits between quantum dots with site-dependent g-tensors allows for coherent shuttling with fidelities up to 99.992%, single-qubit gate fidelities up to 99.97%, and two-qubit gate fidelities up to 99.3%. This method allows for efficient control with baseband pulses only and fast execution of quantum gates even

at low magnetic fields where the coherence is high. Using this approach for the control of dense quantum dot arrays with sparse qubit occupation can alleviate challenges in crosstalk and heating, while providing high connectivity. Recent theoretical developments predict that increased connectivity can substantially improve logical qubit performance and reduce the required overhead on physical qubits [40]. Sparse spin qubit arrays could be particularly suited for error correction schemes requiring either a larger number of nearest neighbors or coupling beyond nearest neighbors. A substantial challenge remains in addressing the qubit-to-qubit variation. This was already highlighted in the original work by Loss and DiVincenzo [1]. We envision that the characterization of larger qubit arrays and statistical analysis will become pivotal, with the presented 10-quantum dot array already providing a first indication that design considerations can determine relevant qubit parameters. Site-dependent quantization axes can be realized by g-tensor engineering such as in elongated quantum dots [43], by using nanomagnets, or by applying currents through nanowires above the qubit plane [44]. The developed control methods for high timing accuracy can also advance exchange-only qubits that are operated using baseband pulses [19] and affect platforms such as superconducting qubits [45]. We envision establishing high-fidelity quantum operation through low-power control in uniform and large-scale systems to be a critical step in realizing fault-tolerant quantum computing.

7.4. MATERIAL AND METHODS

The two devices are fabricated on a Ge/SiGe heterostructure with a 16 nm germanium quantum well buried 55 nm below the semiconductor/oxide interface [46, 47]. The devices gate stack is realised using a multilayer of Pd gates and Al_2O_3 gate oxide, grown by atomic layer deposition. Ohmic contacts are made by a thermally-diffused Al and Pt contact layer for the 2×2 and 10 quantum dot devices, respectively. Details on the fabrication of the first device can be found in ref. [30]. The second device is based on a similar approach, but has an additional layer of gates and gate oxide. The experiments are performed in two Bluefors dilution refrigerators with an electron temperature lower than 140 mK [48]. We estimate a possible misalignment angle between the device plane and the magnetic field axis of $\pm 2^\circ$. We also note that due to an offset in the height position of the 10 quantum dots chip on the cold finger of the cryostat with respect to the center of the field, the effective magnetic field is 69% of the applied field. We have determined this factor using the Ge-73 gyromagnetic ratio, measured via CPMG sequences on a different device mounted in the same position in a different cool-down. This factor also agrees well to what estimated using simulations of the coil field. In each of the two setups, we utilize an in-house built battery-powered SPI rack https://qtwork.tudelft.nl/~mtiggelman/spi-rack/chassis.html to set direct-current (DC) voltages, while we use a Keysight M3202A arbitrary waveform generator (AWG) to apply alternating-current (AC) pulses via coaxial lines. The DC and AC voltage signals are combined on the printed circuit board (PCB) with bias-tees and applied to the gates. In the individual bias-tee, the DC signal undergoes a resistor of 1 MΩ, and the high-frequency signal undergoes a capacitor of 100 nF. Each charge sensor is galvanically connected to a NbTiN inductor with an inductance of a few μH forming a resonant tank circuit with resonance frequencies of ~ 100 MHz. The reflectometry circuit also con-

sists of a directional coupler (ZEDC-15-2B) mounted on the mixing chamber stage. The readout signals are amplified by a cryogenic SiGe amplifier mounted on the 4 K stage (a CITLF3 with gain of 33 dB), by a room-temperature amplifier (a M2j module of the SPI Rack with a gain of 70 dB) and demodulated with a Keysight M3102A digitizer module with a sampling rate of 500 MSa/s.

7.5. POWER DISSIPATION AND SCALING ADVANTAGES OF SHUTTLING-BASED CONTROL

To execute the shuttling operations, trapezoidal voltage pulses are applied on the gates. To achieve high-fidelity single qubit control a handful of such shuttling pulses are required, each with ramp times of a few nanoseconds between two discrete voltage levels. This stands in stark contrast with state-of-the-art electron dipole spin resonance (EDSR) control where typically high frequency, sinusoidal pulses are applied, and many oscillations of the driving signal are needed to achieve the desired gate fidelity [11, 12]. This gives an advantage to a shuttling-based architecture considering energy dissipation, crosstalk and complexity of the required control electronics.

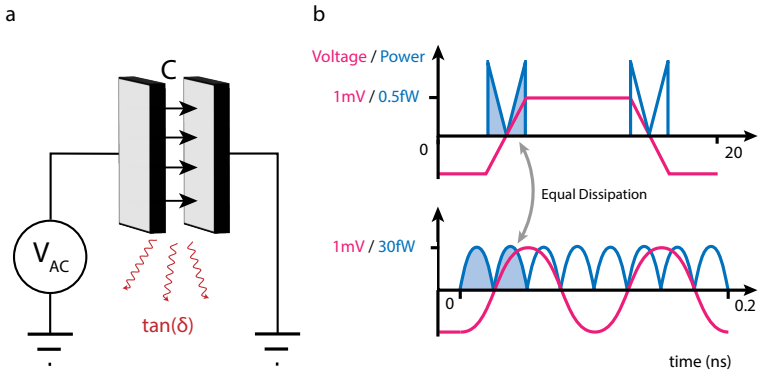

Figure 7.6: **Heat dissipation. a,** Schematic of the model of the heat dissipation, due to some capacitor C with loss tangent $\tan(\delta)$. **b,** For equal pulse amplitude and DC-offset, the heat dissipated per cycle is the same independent of the pulse shape. $C \cdot \tan(\delta) = 10^{-18}$F was assumed in this example.

Already at the current system sizes, EDSR-based devices experience a drift in qubit frequency that is linked to heat dissipation of the signal [16]. When resistive losses are limited, this heat-dissipation is believed to result from a dielectric loss of energy is stored in the electric field around the signal-line. Effectively the system is a capacitor with some loss tangent $\tan(\delta)$, defined as $\tan(\delta) = \epsilon''/\epsilon'$ in a non-conductive system, with ϵ'' and ϵ' the imaginary and real part of the electric permittivity [49]. During each charging cycle, a fraction proportional to $\tan(\delta)$ of the stored electric energy is lost as depicted in Fig. 7.6. With a DC bias around zero the total capacitive energy stored and discharged by the signal line is proportional to CV_{AC}^2, where C is the capacitance and V_{AC} the EDSR amplitude, with which the capacitor is charged. The total energy lost is proportional to $E_{\mathrm{Loss}} = N_{\mathrm{cycles}} \tan(\delta) C V_{\mathrm{AC}}^2$, where N_{cycles} gives the number of oscillations required to per-

form a qubit operation. In a simplified model, we can take the electric permittivity and with it the loss tangent of silicon and germanium to be largely independent of frequency in the relevant frequency range [50, 51]. In this model, for an identical geometry and driving amplitude, the energy dissipation is assumed to solely depends on the number of cycles of the operation and not on the pulse-shape, as indicated in Fig. 7.6. Hence $1/N_{\text{cycles}}$ is a measure of the efficiency of the operation.

For an EDSR-based X_π-gate the number of cycles is given by $N_{\text{cycles,EDSR}} = \frac{f_{\text{Larmor}}}{2f_{\text{Rabi}}}$, which is exactly the inverse of the efficiency η as defined in the main text. The driving efficiency is inherently limited by the relatively small Rabi frequency $f_{\text{Rabi}} \ll f_{\text{Larmor}}$ when operating in the weak-driving (adiabatic) regime, in which the rotating-wave approximation holds. We note that while faster driving is possible, it requires complex amplitude and phase modulation for high-fidelity implementations [37, 52] which also dissipate additional heat. An experimental demonstration of high-fidelity qubit logic is given by Xue et al. operated with Rabi (Larmor) frequencies of $f_{\text{Rabi}} = 2\,\text{MHz}$ ($f_{\text{Larmor}} = 12\,\text{GHz}$) [12, 15]. This corresponds to an efficiency of $\eta = 2f_{\text{Rabi}}/f_{\text{Larmor}} \approx 1/3000$. Similarly Noiri et al. demonstrated $\eta \approx 1/1500$ [11]. For the prior device, an EDSR amplitude of $V_{\text{AC}} \approx 5\,\text{mV}$ is reported at the bond pads of the chip [15]. This corresponds to an energy dissipation of $E_{\text{Loss}} \approx 0.075\tan(\delta)C\,\text{V}^2$ per X_π-gate for high-fidelity EDSR control.

Shuttling based gates do not face a similar inherit efficiency limitation, instead being limited by the relative tilt in quantization axis. In the main part of the paper we demonstrate that to perform an X_π-gate using shuttling, the hole is shuttled two to four times back and forth depending on the angle between the quantization axes of the quantum dot pairs. With periodic pulse timings and negligible ramp times this corresponds to $N_{\text{cycles}} = 1/\eta$. This is done with a typical amplitude $V_{\text{AC}} = 20\,\text{mV}$. Using the $N_{\text{cycles}} = 4$ figure, this corresponds to a heat-dissipation corresponding to $E_{\text{Loss}} = 2{\cdot}0.0016\tan(\delta)C\,\text{V}^2 = 0.0032\tan(\delta)C\,\text{V}^2$, where the additional factor of two accounts for the two plunger gates on which the voltage is applied.

Crosstalk, like heat dissipation, is a problem observed in the current spin-qubit devices and is expected to become more significant as the number and density of qubits increase [13]. This crosstalk can originate from close spacing of signal lines, both on and off the qubit chip. As the density of the quantum dots increases, the capacitance between the gates is expected to grow accordingly, increasing the crosstalk further. Since the admittance between signal lines is directly proportional to the signal frequency, the capacitive crosstalk will be less for low-frequency shuttling-based pulses, compared to high-frequency EDSR experiments which face challenges similar to conventional high-frequency integrated circuits [53]. In integrated circuits design, a rule of thumb is to keep the distance between traces to three times the trace width [53]. This might pose a significant limitation for qubit routing, especially for larger 2D arrays. An architecture based on the demonstrated high-fidelity shuttling gates is thus expected to be less sensitive to crosstalk, which will be advantageous in scaling to large qubit counts.

In large spin systems consisting of many hundreds or thousands of qubits, the scalability of control electronics is a major consideration. The electronic hardware required to generate the IQ modulated sinusoidal EDSR pulses need high analog voltage resolution, which is significantly more involved than the shuttling pulses consisting of two voltage levels. The lower required voltage accuracy and precision of the shuttling based

control allows scaling the qubit count while limiting the electronic overhead, cost and energy consumption. The required timing resolution of shuttling based control should be below 90 ps for a 40 MHz Larmor frequency (Section 7.9.1), higher than the sampling resolution of the IQ modulated EDSR driving. However, EDSR signals need to control the qubit phase with a similar precision as the shuttling pulses, thus requiring a similarly high resolution.

7.6. FIDELITY BENCHMARKING

7.6.1. RANDOMIZED BENCHMARKING

Experiment implementation In the single-qubit randomized benchmarking (RB), the sequence lengths are varied from { 1, 3, 10, 30, ..., 6000 }, in total 25 different lengths. We execute sequences of different lengths once in a random order. After going over all the 25 sequences, we repeat a random execution again with different random order. In total we repeat this execution 32 times. For every sequence we perform 400 single-shot readout. The final spin-down probability $P_{\mathrm{A(B)},\downarrow}$ of the RB sequences on qubit A(B) with the idled qubit B(A) is obtained by averaging over 400 single-shot readout and tracing out the qubit B(A) from the two-qubit state probability $\mathrm{P}_{\sigma\sigma'}$. An experiment takes 4.5 hours to complete, with no re-calibration within the individual experiment.

In the two-qubit interleaved randomized benchmarking (IRB), the sequence lengths are { 1, 2, 4, 8, ..., 200 }, in total 20 different lengths. The order of sequence execution is similar to the single-qubit RB. We execute a reference sequence and right afterward an interleaved sequence with the same length, and then continue on the sequences with different lengths in a random order. After going over all the 20 sequences, we repeat a random execution again with different random order. In total we repeat 128 times. For every sequence we perform 200 single-shot readout. An experiment takes 7.5 hours to complete, with no re-calibration during the individual experiment.

In both single- and two-qubit RB, we observe the 2D histograms of the charge sensor signal are well-separate even at the maximal sequence lengths, while they have an overall shift which gradually increases for the longer sequence. We speculate that the intensive pulsing locally heats up the two-level fluctuators and the high-kinetic inductors, shifting chemical potential of the single-hole charge sensor and the impedance of the LC circuits, respectively [16]. For the single-qubit RB and the first two-qubit RB (IRB_1), we apply adaptive thresholding on the histograms to obtain the two-qubit state probability $\mathrm{P}_{\sigma\sigma'}$. For the other two-qubit RB experiments ($\mathrm{IRB}_{2,3}$), we add an extra wait time of 300 μs before reloading the ancilla qubits for readout. This amount of wait time is sufficient to reduce the sensor signal shift and we are able to use pre-defined constant thresholds to obtain the two-qubit state probability $\mathrm{P}_{\sigma\sigma'}$.

Fidelity extraction In single-qubit RB, the single-qubit Cliffords consist of the gates $\mathrm{X}_{\pi/2}$, $\mathrm{Z}_{\pi/2}$, and the idle gate I. We measure the final state probability of the sequences containing m Clifford gates and a recovery Clifford gate which is the inverse of the corresponding m-Clifford sequence. The spin-down probability averaged over 32 random sequences is fitted to $P_{\downarrow}(m) = Ap^m + B$, where p is the decay rate of the sequence, m is the number of Cliffords, A and B are the parameters absorbing SPAM errors. The average

Fitting formula	Results	IRB_1	IRB_2	IRB_3
Fit with super-exponent model $P(m) = Ap^{(m^\alpha)} + B$	α_{ref}	0.862 ± 0.046	1.050 ± 0.058	0.988 ± 0.057
	α_{int}	0.867 ± 0.041	0.946 ± 0.047	0.954 ± 0.047
	r_{ref} (%)	2.55 ± 0.40	1.17 ± 0.25	1.55 ± 0.31
	r_{CZ} (%)	1.20 ± 0.68	1.36 ± 0.49	1.21 ± 0.56
Fit with single-exponent model $P(m) = Ap^m + B$	r_{ref} (%)	1.56 ± 0.07	1.40 ± 0.06	1.48 ± 0.06
	r_{CZ} (%)	0.79 ± 0.11	0.67 ± 0.10	0.86 ± 0.11

Table 7.1: **Two-qubit interleaved randomized benchmarking results for three individual runs.** The parameter settings are identical to two-qubit GST experiments, where magnetic field $B = 25$ mT and the CZ gate has maximum exchange coupling $J \approx 21$ MHz. The infidelity of the two-qubit Clifford r_{ref} is related to the decay rate of the reference RB sequence by $r_{ref} = 1 - F_{ref} = \frac{3}{4}(1 - p_{ref})$. The infidelity of the interleaved CZ gate r_{CZ} is related to the decay rates of the reference sequence and interleaved sequence by $r_{CZ} = 1 - F_{CZ} = \frac{3}{4}(1 - p_{int}/p_{ref})$. The uncertainty represents the 95% confidence interval.

Clifford fidelity is related to the decay rate by $F_{\text{Clifford1}} = 1 - \frac{1}{2}(1-p)$. The measurements in Fig. 7.2D shows the average Clifford fidelity $F_{\text{Clifford1,A}} = 99.967(4)\%$ and $F_{\text{Clifford1,B}} = 99.960(6)\%$. The uncertainties are obtained from bootstrapping re-sampling with 95% confidence intervals. The average number of gates for single-qubit Clifford is 1.0 $X_{\pi/2}$, 2.42 $Z_{\pi/2}$ and 0.04 I. Defining the infidelity of gate i as $r_i = 1 - F_i$ and assuming the Clifford gate infidelity equals to the sum of the primitive gate infidelity weighted by the average composition, $r_{\text{Clifford}} = r_{X_{\pi/2}} + 2.42 r_{Z_{\pi/2}} + 0.04 r_I$, the average Clifford fidelity sets the lower bounds of the $X_{\pi/2}$ average gate fidelity $F_{X_{\pi/2},A} \geq F_{\text{Clifford1,A}}$ and $F_{X_{\pi/2},B} \geq F_{\text{Clifford1,B}}$.

In two-qubit RB, the two-qubit Cliffords consist of the gates CZ, $X_{\pi/2}^{A(B)}$, $Z_{\pi/2}^{A(B)}$, and I. Similar to the single-qubit RB, we measure the final state probability of the sequences containing m Clifford gates and a recovery Clifford gate. The return probability of the reference sequence (interleaved sequence) is fitted to $P_{\downarrow\downarrow,\text{ref(int)}}(m) = Ap_{\text{ref(int)}}^m + B$, where $p_{\text{ref(int)}}$ is the decay rate of the sequence, m is the number of Cliffords, while A and B are the parameters absorbing the SPAM errors. From the reference sequence decay curve in Fig. 7.4E, we determine the average Clifford gate fidelity $F_{\text{Clifford2}} \equiv F_{\text{ref}} = 1 - \frac{3}{4}(1 - p_{\text{ref}}) = 98.60(6)\%$. The uncertainties are obtained from bootstrapping re-sampling with 95% confidence intervals. The average number of gates for two-qubit Clifford is 1.63 CZ, 1.60 $X_{\pi/2}^{A(B)}$, 2.68 $Z_{\pi/2}^{A(B)}$, and 0.00009 I. This implies the relation between gate errors, $r_{\text{Clifford2}} \equiv r_{\text{ref}} = 1.63 r_{CZ} + \Sigma_{i=A,B} 1.60 r_{X_{\pi/2},i} + 2.68 r_{Z_{\pi/2},i}$. From this relation we find the average Clifford gate fidelity sets the lower bound of CZ gate fidelity $F_{CZ} = 1 - r_{CZ} \geq 1 - \frac{r_{\text{ref}}}{1.63} = 99.14(4)\%$, which is consistent with the IRB result $F_{CZ} = 1 - \frac{3}{4}(1 - p_{\text{int}}/p_{\text{ref}}) = 99.33(10)\%$. We estimate the lower bound of single qubit gate fidelity in the two-qubit subspace, average between both qubits, as $\frac{1}{2}(F_{X_{\pi/2},A} + F_{X_{\pi/2},B}) = 1 - \frac{1}{2}(r_{X_{\pi/2},A} + r_{X_{\pi/2},B}) \geq 1 - \frac{1}{2}\frac{r_{\text{ref}} - 1.63 r_{CZ}}{1.60} = 99.90(5)\%$.

We perform additional check for the potential echoing effect in two-qubit RB/IRB experiments, by fitting the data with super-exponential formula. As shown in Table 7.1, the exponents are in the range of 0.86 - 1.05, showing small deviations from a pure exponential decay.

7.6.2. GATE SET TOMOGRAPHY AND COMPARISON WITH TWO-QUBIT RANDOMIZED BENCHMARKING

Gate set tomography implementation We carried out gate set tomography (GST) experiments using the python package pyGSTi [34]. For single-qubit GST, we use the default gateset {I, X, Y}, where I is the idle gate of $\frac{5}{f_A} \approx 118$ ns ($\frac{9}{f_B} \approx 102$ ns), X(Y) stands for of $X(Y)_{\pi/2}$. The six fiducials for state preparation and measurements are { null, X, Y, XX, XXX, YYY }, where null is the gate with zero idle time. The five germs are {I, X, Y, XY, XXY }. The circuit length are power of two from 1 up to 128, resulting in total 1120 sequences, which takes 17 minutes to complete in the experiment. In every sequence, the spin-up probability $P_{A(B),\uparrow}$ of qubit A(B) with the idled qubit B(A) are obtained by averaging over 500 single-shot readout and tracing out the qubit B(A) state from the two-qubit state probability $P_{\sigma\sigma'}$.

For two-qubit GST, we use the default gateset {I, X_A, X_B, Y_A, Y_B, CZ}. Here the idle gate takes 100 ns. The 11 measurement fiducials are {null, X_B, Y_B, X_BX_B, X_A, Y_A, X_AX_A, X_AX_B, X_AY_B, Y_AX_B, Y_AY_B }. The 16 preparation fiducials are measurement fiducials plus the gates {$X_AX_BX_B$, $Y_AX_BX_B$, $X_AX_AX_B$, $X_AX_AY_B$, $X_AX_AX_BX_B$ }. The 16 germs are { I, X_A, Y_A, X_B, Y_B, CZ, X_AY_A, X_BY_B, $X_AX_AY_A$, $X_BX_BY_B$, X_BY_BCZ, $CZX_AX_AX_A$, $X_AX_BY_BX_AY_BY_A$, $X_AY_BX_BY_AX_BX_A$, $CZX_BY_ACZY_BX_A$, $Y_AX_AY_BX_AX_BX_AY_AY_B$ }. The circuit length are {1,2,4,8}, resulting in total 1702 sequences, which takes 18 minutes to complete in the experiment. In every sequence the two-qubit state probability $P_{\sigma\sigma'}$ is obtained by averaging over 500 single-shot readout.

The measurement outcome of the gate sequence is analyzed in the python package pyGSTi with CPTP model, which considers the gates, the state preparation and measurement as completely positive trace-preserving processes. The corresponding process matrices are estimated and multiple derived quantities can be computed. In the case of single-qubit GST, the estimated process of the single qubit gates can be projected and decomposed into rotation operators as listed in Table 7.2. For both single-qubit and two-qubit GST, we report gate errors metrics (Table 7.3, 7.4) and SPAM error (Table 7.5, 7.6). The tables include the averaged gate infidelity $1 - \frac{\mathrm{tr}(G_{\mathrm{exp}}^{-1} G_{\mathrm{ideal}}) + d}{d(d+1)}$, non-unitary averaged gate infidelity $\frac{d-1}{d}(1 - \sqrt{u(G_{\mathrm{exp}}^{-1} G_{\mathrm{ideal}})}$, 1/2 trace distance $\frac{1}{2}\|J_a(G_{\mathrm{ideal}}) - J_a(G_{\mathrm{exp}})\|$, and 1/2 diamond-distance $\frac{1}{2}\max_\rho \|(G_{\mathrm{ideal}} \otimes I)\rho - (G_{\mathrm{exp}} \otimes I)\rho\|$. Here $d = 2^{\mathrm{N_{qubits}}}$ is the dimension of the Hilbert space, G_{exp} is the process of the gate in the GST experiment in the form of Pauli transfer matrix (PTM), G_{ideal} is the PTM of the ideal gate, $u(M) = \mathrm{tr}(J_a(M)^2)$ is the unitarity of the matrix M, $J_a(M)$ is the Jamiolkowski isomorphism map between the matrix M and the corresponding Choi Matrix, $\|.\|$ denotes the trace norm, and ρ is a density matrix of dimension n^2 [34, 54].

Discrepancy between RB and GST in two-qubit gate benchmarking The different benchmarking results obtained by GST and interleaved RB may stem from the presence of low-frequency noise. In GST, the CZ gate is repeated to amplify and extract the single-gate dephasing error r_s. Similar to the Ramsey dephasing, repeating the CZ gate N-times results in an error $r(N) = r_s^{(N^\alpha)}$ where $\alpha = 1$ if the error is Markovian, or $\alpha \approx 2$ if the dephasing error is dominated by the energy level fluctuations with $1/f$ noise spectrum [55, 56]. In the latter case, the errors of the CZ gates in different position within a repeated CZ

gate sequence (e.g. the first CZ gate and the second CZ gate) are correlated. This type of error with temporal correlation is non-Markovian. Analyzing the decay $r(N) = r_s^{(N^2)}$ using a Markovian error model can result in deviations of estimated single-gate errors from the actual error. The outcome of our GST experiments always shows model violations, which is in line with this hypothesis. On the other hand, in RB the CZ gates are placed between Cliffords that reduce the correlation of the CZ gate errors at different position of a sequence. According to the numerical study [56], under the $1/f$ noise the RB provides better than a factor-of-2 estimate of the gate error. We believe this worse-case deviation of the error estimate (a factor of 2) is smaller than the one from GST, in view of the $1/f$ noise and gate implementation in our system. Therefore, we consider the results of the interleaved RB to be more representative for the average gate fidelity, while GST is used to access the full tomographic reconstruction of the quantum processes.

Gate	Rotation axis $\hat{n} = (n_x, n_y, n_z)$	Rotation angle $\theta_{\text{rot}}(\pi)$
I_A	$(0.038, 0.027, 0.999)$	0.0038
X_A	$(1, 1\times10^{-3}, -1.7\times10^{-6})$	0.5018
Y_A	$(1\times10^{-3}, 1, 2\times10^{-7})$	0.5019
I_B	$(-0.0057, 0.014, 1)$	0.0051
X_B	$(1, -1\times10^{-4}, -2\times10^{-7})$	0.5015
Y_B	$(-1\times10^{-4}, 1, -4\times10^{-7})$	0.5016

Table 7.2: **Single qubit gate parameters determined from GST.**

Gate	Avg. gate infidelity (%)	Non-unitary avg. gate infidelity (%)	1/2 trace distance (%)	1/2 diamond-distance (%)	Eigenvalues 1/2 diamond-distance (%)
I_A	0.38 ± 0.02	0.38 ± 0.02	0.82±0.03	0.83±0.05	1.22±0.05
X_A	0.061 ± 0.008	0.061 ± 0.008	0.33±0.02	0.34±0.07	0.44±0.03
Y_A	0.058 ± 0.008	0.057 ± 0.008	0.35±0.02	0.35±0.05	0.45±0.02
I_B	0.71 ± 0.03	0.70 ± 0.03	1.32±0.06	1.33±0.09	1.97±0.09
X_B	0.019 ± 0.007	0.019 ± 0.007	0.24±0.02	0.25±0.03	0.36±0.03
Y_B	0.023 ± 0.007	0.022 ± 0.007	0.25±0.02	0.26±0.04	0.37±0.02

Table 7.3: **Single-qubit GST gate fidelity.** The single-qubit GST is performed under the same setting as single-qubit RB and two-qubit IRB and GST, where residual exchange coupling $J \approx 10-15$ kHz. The uncertainty represents the 95% confidence interval.

Gate	Avg. gate infidelity (%)	Non-unitary avg. gate infidelity (%)	1/2 trace distance (%)	1/2 diamond-distance (%)	Eigenvalues 1/2 diamond-distance (%)
$I_A \otimes I_B$	0.36 ± 0.27	0.36 ± 0.26	0.9±1.5	1.0±2.4	1.4±0.6
$X_A \otimes I_B$	0.46 ± 0.28	0.43 ± 0.28	2.0±0.9	2.7±2.4	3.6±1.6
$Y_A \otimes I_B$	0.82 ± 0.35	0.78 ± 0.35	2.7±1.2	3.5±4.5	4.4±2.4
$I_A \otimes X_B$	0.33 ± 0.27	0.32 ± 0.27	0.8±0.9	1.2±1.7	0.7±1.2
$I_A \otimes Y_B$	0.51 ± 0.39	0.49 ± 0.38	1.7±0.9	2.4±2.5	2.4±1.6
CZ	1.87 ± 0.52	1.78 ± 0.50	4.4±0.7	6.2±3.8	8.1±0.9

Table 7.4: **Two-qubit GST gate fidelity.** The parameter settings are identical to two-qubit IRB experiments, where magnetic field B = 25 mT and the CZ gate has maximum exchange coupling $J \approx 21$ MHz. The uncertainty represents the 95% confidence interval.

Qubit	Readout probability	Single-qubit GST experiment		Two-qubit GST experiment	
		Prepare $\|\downarrow\rangle$	Prepare $\|\uparrow\rangle$	Prepare $\|\downarrow\rangle$	Prepare $\|\uparrow\rangle$
Q_A	$P_\downarrow$ (%)	**96.9**	8.6	**97.3**	10.0
	$P_\uparrow$ (%)	3.1	**91.4**	2.7	**90.0**
Q_B	$P_\downarrow$ (%)	**95.0**	8.0	**95.1**	7.2
	$P_\uparrow$ (%)	5.0	**92.0**	4.9	**92.8**

Table 7.5: **Estimation of SPAM fidelity in single-qubit space based on single-qubit GST and two-qubit GST experiments.**

Readout probability	Prepare $\|\downarrow\downarrow\rangle$	Prepare $\|\downarrow\uparrow\rangle$	Prepare $\|\uparrow\downarrow\rangle$	Prepare $\|\uparrow\uparrow\rangle$
$P_{\downarrow\downarrow}$ (%)	**94.0**	6.2	8.6	1.5
$P_{\downarrow\uparrow}$ (%)	3.7	**90.7**	1.3	8.5
$P_{\uparrow\downarrow}$ (%)	2.1	0.7	**85.4**	6.0
$P_{\uparrow\uparrow}$ (%)	0.2	2.4	4.7	**84.0**

Table 7.6: **Estimation of SPAM fidelity based on two-qubit GST results.** We use the SPAM operations estimated by GST, including the initial state (a density matrix) and the positive operator-valued measure (POVM), to compute the expected readout probability when preparing specific computational states. The computational states are prepared using the imperfect initialization of $|\downarrow\downarrow\rangle$ and the perfect single-qubit gates.

7.6.3. EVALUATION OF THE SHUTTLING FIDELITY

In this section we show the connection between shuttling fidelity F_{shuttle} and the gate fidelity extracted from single-qubit randomized benchmarking. The $X_{\pi/2,A}$ gate is composed of four shuttling ramps of 2 ns and some idle periods. Because the spin state rotates during the 2 ns-ramp in a predictable way, we consider the 2 ns-ramp as a quantum gate. The average gate fidelity of this single-shuttle gate is taken as shuttling fidelity F_{shuttle}. In principle, the deterministic part of the gate can be compensated by applying a calibrated rotation after the ramp. The stochastic part of the gate (incoherent error) that cannot be compensated contributes to the shuttling infidelity.

In Table 7.7 we list the error sources and find that the wave function uncertainty due to pulse timing is the major error source. The non-integer waiting time between each shuttling step, as well as the differences in execution times of the Clifford gates, result in randomization of this error. We therefore consider the errors as uncorrelated, consistent with the assumptions of randomized benchmarking, and use the relation $r_{X_{\pi/2,A}} = 4r_{\text{shuttle}} + r_{\text{idle}}$, where $r_{X_{\pi/2,A}}$ is the infidelity of $X_{\pi/2,A}$, $r_{\text{shuttle}} = 1 - F_{\text{shuttle}}$ is the shuttling infidelity and r_{idle} is the infidelity that accounts for all the idling operations. This relation gives the lower bound of the shuttling fidelity, $F_{\text{shuttle}} = 1 - r_{\text{shuttle}} \geq 1 - \frac{1}{4} r_{X_{\pi/2,A}}$. Based on the single-qubit RB fidelity $F_{X_{\pi/2,A}} \geq 99.967(4)\%$, we calculate the shuttling fidelity $F_{\text{shuttle}} \geq 99.992(1)\%$. From the gate $X_{\pi/2,B}$ we estimate the shuttling fidelity $F_{\text{shuttle}} \geq 99.980(3)\%$. However, we remark that the quantization axis of qubit B is very close to 45°, which may result in decoupling, and therefore an underestimation of r_{idle} and possibly r_{shuttle}.

7.7. MEASUREMENT AND FIT OF DOUBLE QUANTUM DOT ENERGY SPECTRUM

7.7.1. SINGLE-QUBIT ENERGIES

Using the Ramsey sequence, we measure the free precession frequency as a function of detuning in the double quantum dot system D1-D4 as well as D2-D3, in order to characterize the tunnel couplings, the position of the anti-crossings, and the relative angle of the quantization axes under the voltage settings used for implementing the hopping-based quantum gates. The corresponding charge stability diagrams are shown in Figs. 7.7b, c. Following the modelling approach in the work [21], the system is described in the basis $\{|\text{L},\uparrow_\text{L}\rangle, |\text{L},\downarrow_\text{L}\rangle, |\text{R},\uparrow_\text{L}\rangle, |\text{R},\downarrow_\text{L}\rangle\}$, where 'L' or 'R' indicates the position of the hole in quantum dot QD_L or QD_R and $\uparrow_\text{L}$ or $\downarrow_\text{L}$ specifies its spin states in the frame of quantum dot L. Its Hamiltonian is written as:

$$H_{4\times4} = \begin{pmatrix} \epsilon & 0 & t_\text{c} & 0 \\ 0 & \epsilon & 0 & t_\text{c} \\ t_\text{c} & 0 & -\epsilon & 0 \\ 0 & t_\text{c} & 0 & -\epsilon \end{pmatrix} + \frac{1}{2}\mu_\text{B} B \begin{pmatrix} g_\text{L}(\epsilon) & 0 & 0 & 0 \\ 0 & -g_\text{L}(\epsilon) & 0 & 0 \\ 0 & 0 & g_\text{R}(\epsilon)\cos(\theta) & g_\text{R}(\epsilon)\sin(\theta)\text{e}^{-\text{i}\phi} \\ 0 & 0 & g_\text{R}(\epsilon)\sin(\theta)\text{e}^{\text{i}\phi} & -g_\text{R}(\epsilon)\cos(\theta) \end{pmatrix}, \tag{7.1}$$

where ϵ is the detuning energy of the double quantum dot system (taken as zero at the charge transition), μ_B is the Bohr magneton and the g_i are the g-factors of the quantum dot i, θ (ϕ) is the polar (azimuthal) angle between the two quantization axes. An example of the energy levels is shown in Fig. 7.8. We note that this model is similar to that of a flopping-mode qubit [57]. Diagonalizing the Hamiltonian, we obtain the qubit resonance frequency f_res (at the limit of small Zeeman energy $\mu_\text{B} B \ll t_\text{c}$):

$$f_\text{res} = \frac{\mu_\text{B} B}{h} \frac{\sqrt{(2\epsilon^2 + t_\text{c}^2)(g_\text{L}(\epsilon)^2 + g_\text{R}(\epsilon)^2) + 2\epsilon\sqrt{\epsilon^2 + t_\text{c}^2}(g_\text{R}(\epsilon)^2 - g_\text{L}(\epsilon)^2) + 2g_\text{L}(\epsilon)g_\text{R}(\epsilon)t_\text{c}^2\cos(\theta)}}{2\sqrt{\epsilon^2 + t_\text{c}^2}}, \tag{7.2}$$

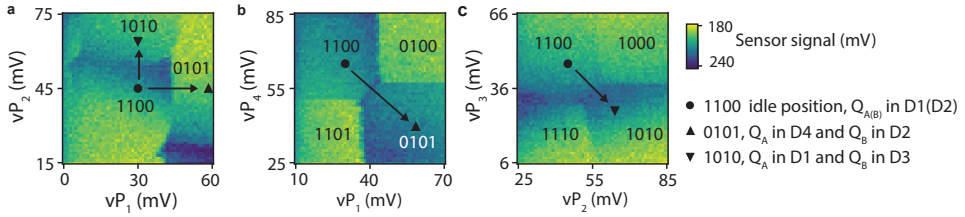

Figure 7.7: **Charge stability diagrams of the shuttling gates.** The diagrams in **a-c** show the voltages of the working points projected on the corresponding virtual plunger gates vP_i. The hole occupancies are labelled as $n_1n_2n_3n_4$. The idle position is marked as the circle, in which both qubits Q_A and Q_B are in quantum dots D1 and D2. The $X_{\pi/2}$ on $Q_{A(B)}$ is realized by shuttling between the idle position and the working point marked as the triangle in 0101 (1010) charge occupation.

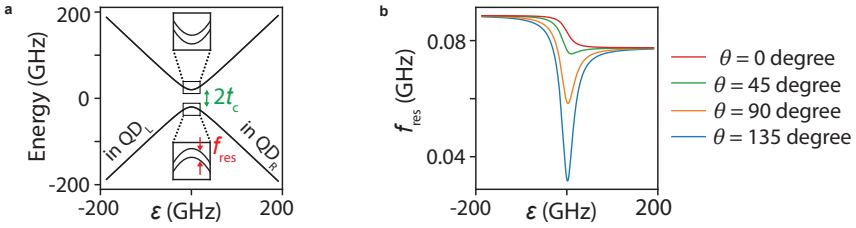

Figure 7.8: **Energy levels of a single spin. a,** An example of energy levels of the single spin in double quantum dot given by Eq. (7.1). **b,** The transition frequency between the lowest two states, f_{res}, as function of detuning energy ϵ for the quantization axes angle θ. Parameters used here: $\mu_B B g_{L(R)} = 0.078(0.089)$ GHz, $t_c = 20$ GHz.

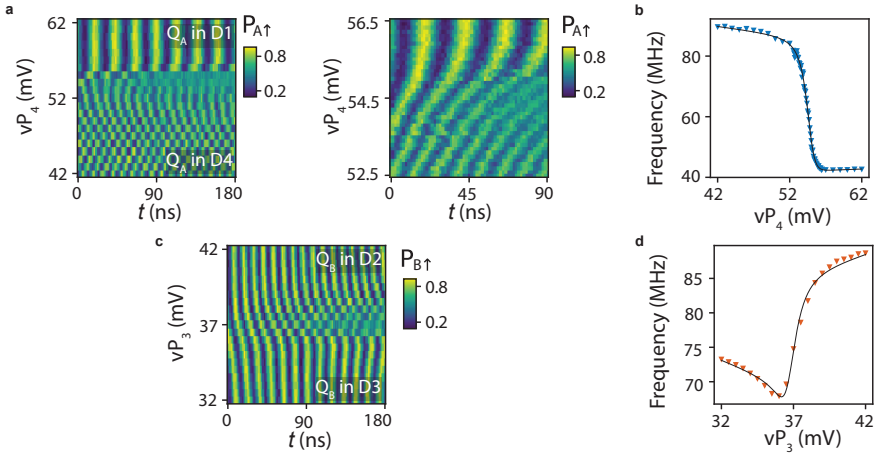

Figure 7.9: **Fitting of tunnel coupling at the shuttling gate settings via spin free precession measurement at the magnetic field of 25 mT. a,** The free evolution of Q_A at different detuning across D1-D4 anti-crossing. The panel on the right is the fine scan around the charge anti-crossing where the frequencies changes rapidly. The oscillation frequencies are extracted and plotted in **b**. **c,** The free evolution of Q_B at different detuning across D2-D3 charge anti-crossing. The oscillation frequencies are extracted and plotted in **d**. The black lines are the fits using Eq. (7.2), with the lever arm $\frac{\Delta\epsilon_{14(23)}}{\Delta vP_{4(3)}} = 0.086(0.082)$eV/V.

Assuming a linear dependence of g-factors $g_{\mathrm{L(R)}}(\epsilon)$ on the detuning ϵ, we fit the above formula to the data and extract the tunnel coupling $t_{\mathrm{c},14} = 27 \pm 1$ GHz and the angle between quantization axes $\theta_{14} = 65 \pm 2°$ for the quantum dot pair D1-D4. In the quantum dot pair D2-D3 we extract the tunnel coupling $t_{\mathrm{c},23} = 20 \pm 1$ GHz and the angle $\theta_{23} = 51 \pm 2°$. The results are shown in Fig. 7.9. We notice that the extracted quantization axis angles are higher than the values extracted from the fitting in Fig. 7.1C and Fig. 6c of the supplementary material [31], where $\theta_{14} = 41.5°$ and $\theta_{23} = 44.7°$ (see Section 3 of the supplementary material [31]). This discrepancy might be attributed to the adiabaticity of the shuttling process, and the non-linear g-factor variation as a function of voltages around the charge anti-crossing.

7.7.2. TWO-QUBIT ENERGIES AND COHERENCE TIME

We measure the qubit energies and the coherence times of the two-qubit system as shown in Fig. 7.10. We observe several features, such as the non-monotonic dependence of qubit energies as function of barrier gate voltages. To explain this result, we model the two-qubit system using an extended minimal-size Fermi-Hubbard model with the six basis states $\{S(2,0), S(0,2), T^{+}(1,1), S(1,1), T^{0}(1,1), T^{-}(1,1)\}$. The Hamiltonian is written as [58–60]

$$H_{2Q} = \begin{pmatrix} U+\epsilon_{2Q} & 0 & -t_y + i t_x & \sqrt{2}t_c & -i\sqrt{2}t_z & -t_y - i t_x \\ 0 & U-\epsilon_{2Q} & -t_y + i t_x & \sqrt{2}t_c & -i\sqrt{2}t_z & -t_y - i t_x \\ -t_y - i t_x & -t_y - i t_x & hf_+ & 0 & 0 & 0 \\ \sqrt{2}t_c & \sqrt{2}t_c & 0 & 0 & hf_- & 0 \\ i\sqrt{2}t_z & i\sqrt{2}t_z & 0 & hf_- & 0 & 0 \\ -t_y + i t_x & -t_y + i t_x & 0 & 0 & 0 & -hf_+ \end{pmatrix}. \tag{7.3}$$

The charging energy takes the value $U = 2.56$ meV [61]. The detuning energy of the two-spin system is ϵ_{2Q} (which is different than the single-spin system discussed in Section 3 of the supplementary material [31]). The Zeeman interactions are included in $hf_{\pm} = \frac{1}{2}(g_A \pm g_B)\mu_B B$. The hopping between the quantum dots is modelled through a spin-probability conserving tunnel coupling $t_c + i t_z$ and a spin-probability non-conserving tunnel coupling $t_x + i t_y$. The impact of a magnetic field is described by the Zeeman interaction Hamiltonian, where we use a local spin basis such that the two spins are aligned. Consequently, this redefines the spin-conserving and spin-non-conserving tunnel couplings.

In the experiments, we change the voltage vB_{12} at constant detuning to tune the tunnel couplings (t_c, t_x, t_y, t_z) and the resulting exchange coupling. We assume that all the tunnel couplings change exponentially as a function of the barrier gate [59] $\exp(-\frac{1}{2}\kappa \mathrm{vB}_{12})$ with identical $\kappa = 0.059$ mV^{-1} and estimate the prefactors by fitting the parameters to our measurements. This assumption also implies that the ratios $t_{x,y,z}/t_c$ remain constant. Since the eigenenergies of Hamiltonian (7.3) only depend on the absolute value of $t_c + i t_z$ and $t_x + i t_y$ and not on their complex argument (can be easily verified by computing the characteristic polynomial), the phases cannot be estimated by analyzing the eigenenergies. For the Zeeman interactions, we assume the g-factors depend linearly on the gate voltage, $g_{\mathrm{A(B)}}(vB_{12}) = g^{(0)}_{\mathrm{A(B)}} + g^{(1)}_{\mathrm{A(B)}} vB_{12}$. Finally, we set the detuning ϵ_{2Q} to a fixed value of zero, because we operate at fixed plunger gate voltages (vP1, vP2) close to

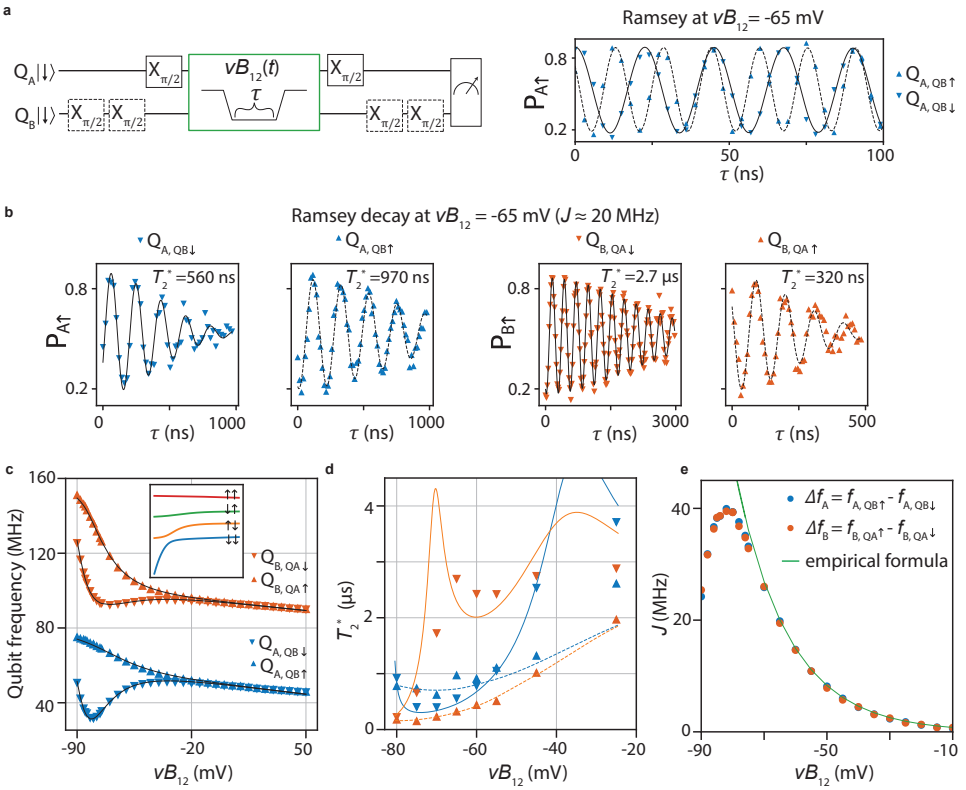

Figure 7.10: **Qubit frequencies and coherence time as a function of virtual barrier voltage at magnetic field of 25 mT. a,** The Ramsey experiments for measuring qubit frequencies as well as the free evolution decay time $T_2^\star$ at various virtual barrier gate voltage vB_{12}. The circuits here is an example of qubit A frequency measurement conditioned on qubit B state. The pulse on vB_{12} is trapezoidal with linear ramp times of 80 ns to avoid diabatic state transitions. **b,** Free induction decay of individual qubit conditioned on the other qubit at $vB_{12} = -65$ mV. The data are fitted to $P(\tau) = A\exp(-(\tau/T_2^\star)^2) + B$ to extract $T_2^\star$. **c,** The state-dependent qubit frequencies. The fitting results are plotted in black lines, with the energy diagram in the inset. **d,** The $T_2^\star$ measurement and the fitting curves. The sampling time and numbers of sample points are chosen to adapt for the qubit frequencies and decay rates that depends on vB_{12}, resulting in the $T_2^\star$ experiment time of 18-58 seconds for Q_A and 38-133 seconds for Q_B. **e,** The exchange couplings $J = \Delta f_{A(B)}$. The exchange couplings predicted by empirical formula $J = J_0\exp(-\kappa\ (vB_{12} - \Delta vB_{12}))$ is plotted, where $J_0 = 0.24$ MHz and $\kappa = 0.059$ mV^{-1}, and $\Delta vB_{12} = 10$ mV. One set of the data Δf_A is also plotted in Fig. 7.4C. We note that the data displayed in this figure and in Fig. 7.4C are taken after a charge jump that shifts vB_{12} by about $\Delta vB_{12} = 10$ mV. As an example, the measurement taken at $vB_{12} = -65$ mV in this figure should be considered as the measurement taken at $vB_{12} \approx -75$ mV in other parts of the paper.

the symmetry point for all the two-qubit experiments.

We fit the qubit frequencies in Fig. 7.10c to the eigenenergies of Eq. (7.3). Our fit shows a good agreement between the model and the experiments. We find the relative strength between spin-dependent tunnel couplings to be $\frac{t_x^2+t_y^2}{t_c^2+t_z^2} = 0.11$. The corresponding energy levels are plotted in the inset of Fig. 7.10c, where we identify the anticrossing between $|\uparrow\downarrow\rangle$ and $|\downarrow\downarrow\rangle$ as the cause of the bending of exchange coupling around

$vB_{12} = -85$ mV.

Based on this model, we estimate the dephasing of the two-spin system by considering qubit frequency fluctuations due to three noise sources: the effective electric noise on vB_{12} and fluctuations of the g-factors $g^{(0)}_{\mathrm{A(B)}}$ [12]. Assuming $1/f$ noise dominates qubit dephasing, the coherence time reads $T_2^\star = \sqrt{2/(S_{1/f}\ln\frac{0.401}{t_\mathrm{e}/t_\mathrm{m}})}$ [55, 62], where we define the evolution time t_e as the high-frequency cutoff and the total measurement time t_m as the low-frequency cutoff, $S_{1/f}$ is the strength of the single-sided spectral density of the qubit angular frequency. The strength is related to the noise spectrum of a particular noise source $x \in \{vB_{12}, g_\mathrm{A}, g_\mathrm{B}\}$ by $S_{1/f} = (\frac{\partial\omega}{\partial x})^2 S^x_{1/f}$, where $\frac{\partial\omega}{\partial x}$ is the sensitivity of the qubit angular frequency and the strength of the $1/f$ noise $S^x_{1/f}$ is defined by $S^x(\omega) = \int_0^\infty S^x(t)e^{i\omega t}dt = 2\pi S^x_{1/f}/\omega$ with the autocorrelation function $S^x(t) = \langle x(t)x(0)\rangle$. Here we choose $t_\mathrm{e} = T_2^\star$ which is the evolution time relevant for a $T_2^\star$ measurement. We assume that the three noise sources are independent and their fluctuations uncorrelated, giving rise to a total dephasing time $T^\star_{2,\mathrm{total}} = 1/\sqrt{{T^\star_{2,vB_{12}}}^{-2} + {\mathrm{T}^\star_{2,g^{(0)}_\mathrm{A}}}^{-2} + {\mathrm{T}^\star_{2,g^{(0)}_\mathrm{B}}}^{-2}}$. For the transition between two energy levels i and j, we use the derivatives of the transition angular frequency ω_{ij} with respect to the voltage fluctuations to compute theoretical predictions of the coherence time. We pay close attention to the different bandwidths (t_m, t_e) in the respective measurements. For example, the gate voltage noise $S^{vB_{12}}_{1/f}$ yields ${T^\star_{2,vB_{12}}}^{-2} = \frac{1}{2}\ln\frac{0.401}{t_\mathrm{e}/t_\mathrm{m}}(\frac{\partial\omega_{ij}}{\partial vB_{12}})^2 S^{vB_{12}}_{1/f}$. We now use the the fitting parameters obtained in Fig. 7.10c to fit the noise strength $S^{vB_{12},g_\mathrm{A},g_\mathrm{B}}_{1/f}$ to the coherence time for all the transitions. We estimate the noise strengths by minimizing the square sum of the dephasing rate differences $\Delta\frac{1}{T_2^\star}$ between theoretical and measurement values. Fig. 7.10d shows the fitting results, having qualitative agreement between the model and the experiment. The model reproduce the trend and several features of $T_2^\star(vB_{12})$, and also predicts the relative dephasing time of different qubit transitions. We find the noise strength $S^{vB_{12}}_{1/f} = 0.031\,\mathrm{mV}^2$, which is equivalent to $\sigma_{vB_{12}} = 0.78$ mV if integrating from $1\,\mu$s to 1000 seconds, a typical time scale for Ramsey measurement, and on the same order as the results reported in Ref. [12]. The noise strength of $S^{g_\mathrm{A}(g_\mathrm{B})}_{1/f}$ at this magnetic field is equivalent to the qubit frequency noise $S^{f_\mathrm{QA}(f_\mathrm{QB})}_{1/f} = (\mu_B B)^2 S^{g_\mathrm{A}(g_\mathrm{B})}_{1/f} = 130(200)\,\mathrm{kHz}^2$, which translates to $\sigma_{f_\mathrm{QA(QB)}} = 50(63)$ kHz and $T_2^\star = 4.5(3.5)\,\mu$s if integrating the noise from $1\,\mu$s to 1000 seconds.

7.8. ERROR MODELING

7.8.1. ERROR MODELING OF THE HOPPING-BASED SINGLE-QUBIT GATE

Noise estimation We model incoherent error originating from (1) fluctuations in Larmor frequencies of the individual quantum dot, (2) fluctuations in detuning energies, (3) waveform uncertainty, and (4) thermalization processes near the charge anti-crossing. First we estimate the noise strength of individual error sources. From the $T_2^\star = 7.0(4.5)\mu s$ of the static qubit A(B) at 25 mT, we estimate Larmor frequency fluctuation $\sigma_f = \frac{1}{\sqrt{2}\pi T_2^\star} =$ 32 kHz for Q_A and $\sigma_f = 50$ kHz for Q_B. For Larmor frequency fluctuations in D3 and D4, we assume that they are uncorrelated and have equal magnitude as Q_B. From the fitting of the coherence times in Fig. 7.11, we obtain the effective electric noise $\delta vP_4(\delta vP_3) =$ 0.19(0.14) mV, which is equivalent to the fluctuations in the position of the charge anti-crossing $\Delta\epsilon_{14(23),AC} = 17(12)\,\mu$eV and creates the timing fluctuation of 14(23) ps for shuttling operations of Q_A (Q_B). For the errors from waveform uncertainty (Fig. 7.12d), we compute the expected waveforms of the gates $X_{\pi/2,A(B)}$ for the time shifts t_{shift} ranging from 0 to 0.99 ns. Each waveform results in slightly different timing of shuttling, and therefore contributes to incoherent error.

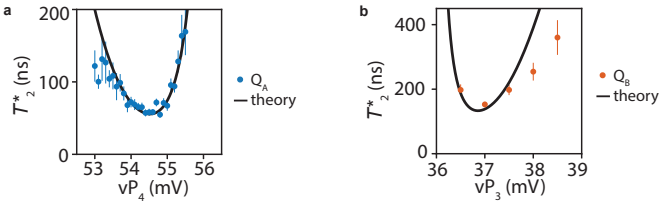

Figure 7.11: **Qubit coherence times near the charge anticrossings.** The coherence time for qubit A **(a)** and qubit B **(b)** extracted from Fig. 7.9 by fitting to the formula $P_\uparrow(\tau) = A\exp(-(\tau/T_2^\star)^2) + B$. The black curves are the expected coherence time assuming quasi-static electric noise on the gates vP4(vP3), $T_2^\star = \frac{1}{\sqrt{2}\pi\sigma_f}$ and the voltage-dependent qubit frequency fluctuation is $\sigma_f \approx \frac{\partial f}{\partial vP_i}\delta vP_i + \frac{1}{2}\frac{\partial^2 f}{\partial vP_i^2}\delta vP_i^2$ [57, 63]. We estimate the effective electric noise $\delta vP_4(\delta vP_3) = 0.19(0.14)$ mV, which minimize the square sum of dephasing rate difference $\Delta\frac{1}{T^\star}$ between the measured values and the theoretical values.

Error model We use the discrete model (Eq. (4) of the supplementary material [31]) to compute the unitary matrices of the target gates and noisy gates, and estimate the incoherent error. The method is described as follow. The unitary of a gate U is a series of free precession for various duration around the corresponding quantization axes of the quantum dots with different frequencies as depicted in Fig. 6b of the supplementary material [31]. A noise source can either change the duration or change the precession frequencies, resulting in a slightly different gate unitary. Averaging over the distribution of the noise parameter gives average gate infidelity, similar to the method used in Section 7.8.2. For the calculation of errors caused by waveform uncertainty, instead of using a single target unitary, we use a set of target unitaries generated by the waveforms with uniformly distributed time shift t_{shift}. This treatment results in a range of infidelity rather than a single value. We also estimated infidelity caused by T_1-like processes, where the qubits are thermalized to 50-50 population around the charge anti-

Error source	$X_{\pi/2,A}$ infidelity ($\times 10^{-5}$)	$X_{\pi/2,B}$ infidelity ($\times 10^{-5}$)
Larmor frequency fluctuations	3.1	0.8
detuning noise	7.2	0.13
waveform uncertainty	4.0 - 14.6	5.1 - 17.2
thermalization	0.04	0.05
total infidelity	14.3 - 25.0	6.0 - 18.1

Table 7.7: **Incoherent error estimation.** Here we present the error metric in terms of average gate infidelity in single-qubit space.

crossing with the time scale $1/\Gamma(\epsilon)$. This time scale depends on the detuning ϵ and has a minimum value around 300μs. The corresponding infidelity per gate is therefore estimated by integrating the transition rates over the ramp time and multiplying the number of shuttles, $\frac{N_{\text{shuttle}}}{3}\int_0^{t_{\text{ramp}}}\Gamma(\epsilon(t))dt$.

As summarized in Table 7.7, the results show that a large portion of errors arises from the waveform uncertainty. The relative impact of the detuning noise and Larmor frequency fluctuations depends on the details of the pulses and quantization axes angle. The thermalization process has little contribution, because of the extended thermalization time at low field and the short ramp time we use. The estimated infidelity of both qubits are on the same order as the measured infidelity, $r_{X,A(B)} \approx 0.03$ (0.04)% given by randomized benchmarking (RB) and $r_{X,A(B)} \approx 0.06$ (0.02)% given by gate set tomography (GST). The deviations can arise from unaccounted error sources as well as the robustness of the benchmarking protocols under realistic experimental conditions.

7.8.2. ERROR MODELING OF THE TWO-QUBIT GATE

In this section we estimate the average gate infidelity of the CZ gate due to the coherent error and incoherent error. In a d-dimensional Hilbert space, for a unitary operation implemented in the experiment, U_{exp}, the corresponding average fidelity is [64]

$$F = \frac{|\text{tr}(U_{\text{ideal}}^{-1}U_{\text{exp}})|^2 + d}{d(d+1)}. \tag{7.4}$$

Coherent error To evaluate coherent errors, we compute the time evolution of the two-qubit state under the influence of the gate voltage pulse $\nu B_{12}(t)$ with a pulse shape matching a Hamming window [37] as depicted in Fig. 7.4D by solving the time-dependent Schrödinger equation numerically [65]. If the system evolves adiabatically, the final state only acquires one conditional two-qubit phase and two single-qubit phases. These phases can be calibrated in the experiment by fine-tuning the time and amplitude of the pulse [37]. On the other hand, non-adiabatic state transitions, as shown in Fig. 7.17cd, result in errors that cannot be simply calibrated. In our simulation, we fine-tune the voltage pulses $\nu B_{12}(t)$ to achieve a conditional phase of π, compute the unitary time evolution operator of the quantum process without noise, and compensate for the single qubit Z rotations. We find the resulting unitary evolution has an average gate infidelity 0.089%. Additionally, we decompose the error in the Pauli basis and express the simulated unitary by the dominant terms, $U_{\text{exp}} = e^{-i(-0.010\text{YI}-0.021\text{XY}+0.021\text{YX})}U_{\text{ideal}}$. This

result is in good agreement with the fact that the implemented pulse shape is designed to suppress the transition $|\uparrow\downarrow\rangle \rightarrow |\downarrow\uparrow\rangle$ while the transitions induced by spin-non-conserving tunneling are not fully suppressed. We believe that a further reduction of non-adiabatic transitions can be achieved by incorporating Eq. (7.3) directly into the optimization process for finding the pulse.

Incoherent error Incoherent errors are dominantly caused by the 1/f-type low-frequency fluctuations in νB_{12} and g-factors $g_{A,B}$, which result in the random deviations of the unitary operation U_{exp} from the ideal operation U_{ideal}. We can now write the unitary operation $U_{exp}(x)$ that is dependent on a stochastic parameter x of the noise source. While this can be straightforward generalized to multiple sources, we consider for simplicity only fluctuations of the accumulated phases and neglect fluctuations of the transition matrix elements caused by the non-adiabatic time evolution discussed in the previous paragraph. This allows us to further approximate the 1/f spectral noise with quasistatic fluctuations by integrating over the corresponding frequencies $\sigma^2 = 2\int_{t_m^{-1}}^{t_e^{-1}} \frac{S_x}{f} df$. Assuming x to be a stochastic variable drawn from a Gaussian distribution with zero mean and standard deviation of σ, we can replace the quantity $|\mathrm{tr}(U_{ideal}^{-1}U_{exp})|$ in Eq. (7.4) with the expectation value [66, 67],

$$\langle|\mathrm{tr}(U_{ideal}^{-1}U_{exp})|^2\rangle = \int_{-\infty}^{\infty} |\mathrm{tr}(U_{ideal}^{-1}U_{exp}(x))|^2 \frac{1}{\sqrt{2\pi}\sigma} e^{-\frac{x^2}{2\sigma^2}} dx. \tag{7.5}$$

We estimate the accumulated phases by integrating the qubit frequencies $f_{Qi,Qj}(t,x)$ over time under the influence of the voltage pulse $\nu B_{12}(t)$ and the noise amplitude x. The corresponding (stochastic) unitary matrix in the basis $|\downarrow\downarrow\rangle, |\uparrow\downarrow\rangle, |\downarrow\uparrow\rangle, |\uparrow\uparrow\rangle$ is then given by

$$U_{exp}(x) = \begin{pmatrix} 1 & 0 & 0 & 0 \\ 0 & e^{-2\pi i \int f_{QB,QA\downarrow}(t,x)dt} & 0 & 0 \\ 0 & 0 & e^{-2\pi i \int f_{QA,QB\downarrow}(t,x)dt} & 0 \\ 0 & 0 & 0 & e^{-2\pi i \int f_{QA,QB\downarrow}(t,x)+f_{QB,QA\uparrow}(t,x)dt} \end{pmatrix}. \tag{7.6}$$

The standard deviation of the noise σ is estimated in a way similar to the $T_2^\star$ fitting in Fig. 7.10d and depends on the low(high)-frequency cutoff $t_m^{-1}(t_e^{-1})$ as $\sigma \propto \frac{1}{T_2^\star} \propto \sqrt{\ln \frac{0.401}{t_e/t_m}}$ [55, 62]. In the case of two-qubit IRB experiments, the total experimental time is $t_m = 2680$ s and t_e is chosen as the total gate time of 108 ns (including padding time). Based on these experimental conditions and the results of the $T_2^\star$ fitting in Section 7.7.2, we estimate the effective standard deviations $\sigma_{\nu B_{12}} = 0.88$ mV, $\sigma_{f_{QA}} = 57$ kHz and $\sigma_{f_{QB}} = 72$ kHz during the IRB experiments. Taking the above considerations, we obtain an average gate infidelity 0.23%, where the main contribution from the noise is caused by fluctuations of νB_{12} accounting for an error of 0.19%.

In summary, we find that incoherent error caused by dephasing are dominant over coherent errors for the average gate fidelity. The total average gate infidelity from the models is equal to 0.32%, which is on the same scale as the estimated value of 0.67 ± 0.09% extracted from the IRB experiment, while it significantly differs from the estimated value of 1.87 ± 0.52% extracted from the GST experiment (Table 7.1 and Table 7.4). The

deviations can arise from unaccounted error sources as well as the robustness of the benchmarking protocols under realistic experimental conditions.

7.9. EXTENDED DATA

7.9.1. TIMING PRECISION OF SHUTTLING PULSES

High fidelity hopping-based gates require a precise timing of shuttling pulses. A qubit fidelity above 99.99% can be achieved when the rotation has an incoherent error of less than 1.3 degrees. In a simplified example where two quantum dots having quantization axes which are perpendicular, the timing error of ramps for an $X_{\pi/2}$ shuttling gate on a qubit with a Larmor frequency of 40 MHz should be less than 90 ps. This timing precision is far below the sample rate of 1 GSa/s of the used AWG. Ramps can be timed with precision higher than the sample rate, because the voltage resolution of the AWG can be used to shift the ramp in time as shown in Fig. 7.12a. The time resolution Δt_{res} of a ramp with a duration long enough to be not affected by the transients at the start and end of the ramp can be approximated by $\Delta t_{\text{res}} = t_{\text{ramp}} \Delta V / A$, where t_{ramp} the duration of the ramp, ΔV the voltage resolution of the AWG and A the amplitude of the ramp. This approximation assumes that the low-pass filter has a cut-off frequency just below the Nyquist frequency. Surprisingly, the sample rate has no direct effect on the time resolution of the ramp. A higher sample rate combined with a higher cut-off frequency allows the generation of shorter ramps and shorter ramps have a higher time resolution. The voltage resolution and thus the time resolution effectively decrease when oversampling is used, i.e. when the cut-off frequency is significantly lower than the Nyquist frequency.

We have used AWGs with a voltage resolution of 0.37 mV and pulses with an amplitude on the order of 200 mV at the AWG outputs (this translates to 25.2 mV on the device due to the attenuation on the line) and a ramp time of 2 ns. This setting gives a time resolution of 3.7 ps, which meets the requirement for high-fidelity gates. However, the ramps

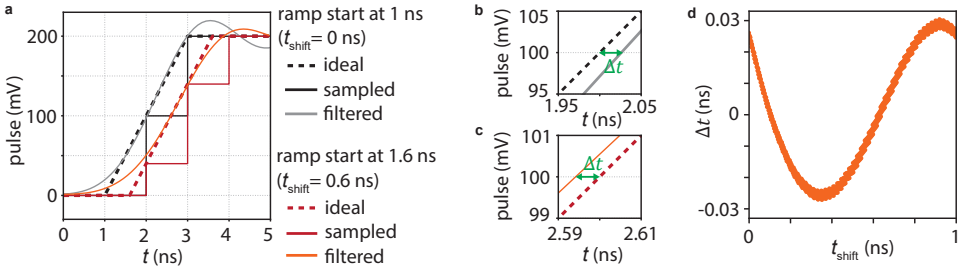

Figure 7.12: **Pulse timing. a,** Digital inputs and analogue outputs of the AWG for two pulses with time shifts $t_{\text{shift}} = 0$ and 0.6 ns. The dotted lines are the ideal linear ramps with 0.6 ns time shift that we are aiming for. The solid lines are the digital inputs, represented by the discrete sampling with 1 ns resolution. To produce a time shift of 0.6 ns, a 60 mV decrement of the digital input is made on the rising ramp. The low-pass filtering of the AWG results in the smoothened output voltages represented by the solid curves, as well as the oscillations (ringing) after the ramp. **b, c,** Zoom-in of the pulses around the middle of the ideal ramps. The deviation in time between the ideal ramps and the analogue outputs at half of the voltage amplitude is denoted as Δt. **d,** The deviation Δt as a function of time shift t_{shift}. The data set is generated with equally distributed time shifts from 0 to 0.999 ns. The mean of the distribution corresponds to $\Delta t = 0$. The analogue outputs in all the plots are calculated using the measured step response of the AWG.

for the shuttling pulses are short with respect to the transient response of the low-pass filter. The filter of the AWG adds small wiggles to the short ramps making the timing less precise. This effect is shown in Fig. 7.12d, where the time deviation for the ramps with different time shift t_{shift} are plotted. From these calculated ramps we have derived a maximum deviation of 30.4 ps from the average and a standard deviation of 19.4 ps, satisfying the basic requirements for 99.99% fidelity. We modeled our gate implementation in Section 3 of the supplementary material [31] and estimate the incoherent error due to such timing deviation, as summarized in Table 7.7.

7.9.2. COHERENCE TIMES OF THE INDIVIDUAL QUBITS

Because the g-tensor and hyperfine interaction for heavy hole qubits are expected to be highly anisotropic, a small magnetic field offset pointing towards an out-of-plane direction can change the dephasing time significantly. For our device, we find that the measured qubit frequencies are not completely linear in magnetic field for field strength of 1 mT. Therefore, we can estimate the magnetic field offset for in-plane and out-of-plane direction by fitting the measured qubit frequency to $hf(B_{\text{ext}}) = \sqrt{(g_{\parallel}\mu_B(B_{\text{ext}}+B_0^{\parallel}))^2+(g_{\perp}\mu_B B_0^{\perp})^2}$ (Fig. 7.13b and inset). Our best fits show perpendicular magnetic field offsets $g_{\perp}\mu_B B_0^{\perp} =$ 1.4(1) MHz for Q_A, 1.8(2) MHz for Q_B and parallel offsets $B_0^{\parallel} = 0.08(3)$ mT for Q_A, 0.13(2) mT for Q_B. The perpendicular offsets are 10 and 13 μT assuming an out-of-plane g-factor $g_{\perp} = 10$. The offsets might originate from magnetic materials on the sample board, trapped flux in superconducting magnet, polarized nuclear spins, Meisner effect of the metallic top gates, or the Earth magnetic field.

To estimate the magnetic field dependence of the dephasing time, we consider a simplified model assuming Gaussian quasi-static fluctuations of the qubit frequency originating from nuclear spin noise and quasi-static fluctuations of the g-factor caused by charge noise. The qubit frequency for an external applied magnetic field B_{ext} is given by

$$f(B_{\text{ext}},\delta g,\delta f_{\text{n}}) = \frac{1}{h}\sqrt{((g_{\parallel}+\delta g)\mu_B(B_{\text{ext}}+B_0^{\parallel}))^2+(\delta f_{\text{n}}+g_{\perp}\mu_B B_0^{\perp})^2}. \tag{7.7}$$

In linear order, the in-plane g-factor fluctuation δg gives rise to qubit frequency fluctuation $\delta f_{\delta g} = f(B_{\text{ext}},\delta g,0) - f(B_{\text{ext}},0,0)$ with standard deviation $\sigma_{f,\delta g}$ and the out-of-plane hyperfine field fluctuations δf_{n} give rise to qubit frequency fluctuation $\delta f_{\text{n}} = f(B_{\text{ext}},0,\delta f_{\text{n}}) - f(B_{\text{ext}},0,0)$ with standard deviation $\sigma_{f,\delta f_{\text{n}}}$. Assuming both noise sources to be independent and uncorrelated, the standard deviation of the total qubit frequency fluctuation at B_{ext} is $\sigma_f = \sqrt{\sigma_{f,\delta g}^2+\sigma_{f,\delta f_{\text{n}}}^2}$ giving rise to a coherence time $T_2^{\star} = \frac{1}{\sqrt{2}\pi\sigma_f}$. From our fit in Fig. 7.2B (replotted in Fig. 7.13c), we extract an effective hyperfine noise $\delta f_{\text{n}} =$ 52(7) kHz for Q_A and 78(8) kHz for Q_B, corresponding to the coherent time $T_2^{\star} = 4.3(6)$ and 2.9(3) μs. This result is larger than $\delta f_{\text{n}} = 34.4$ kHz reported in Ref. [68] in D3 of the same device and significantly smaller than $\delta f_{\text{n}} = 250$ kHz reported in Ref. [24]. The difference could arise from microscopic details in the device, the simplicity of the model, as well as the complexity of the nuclear spin noise at low magnetic fields, where the ^{73}Ge nuclear spins have a quadrupolar splitting caused by strain which has a similar magnitude as the precession frequency.

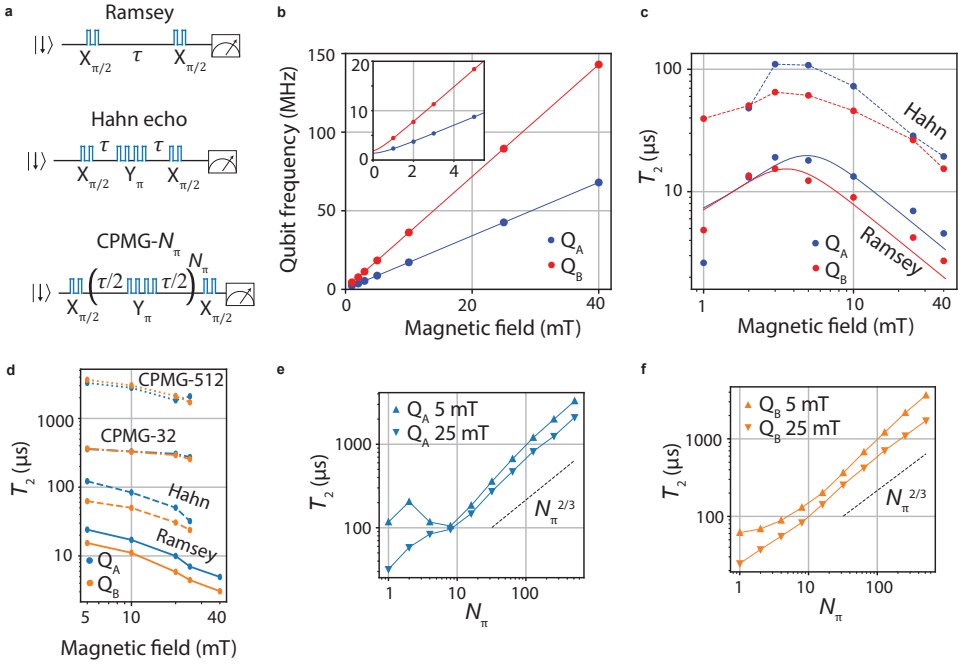

Figure 7.13: **Coherence time and dependence on magnetic field strength at the idle position of the qubits. a,** The pulse sequences consisting of hopping-based gates $X_{\pi/2}(Y_{\pi/2})$ for measuring qubit frequency and $T_2^\star$ (Ramsey), for T_2^{H}(Hahn echo), and T_2^{CPMG}(CPMG-N_π). **b,** The frequencies of qubits Q_A and Q_B as a function of external magnetic field. The inset is the zoom-in at low field regime, where a non-linear behavior is observed. The fitting method is described in the text. Here the superconducting magnet is in the driven mode. In this mode, the power supply is galvanically connected to its power supply. It introduces extra noise in the system compared to the normal operation mode. Note that field below 5 mT can only be reached with the magnet in driven mode. **c,** The $T_2^\star$ and T_2^{H} as a function of external magnetic field when the magnet is at the driven mode. The $T_2^\star$ is extracted from the Ramsey measurement with an average of 10 traces and the experimental time 12-19 minutes. Here we replot the data in Fig. 7.2B for easier comparison. **d,** The coherence time as a function of magnetic field above 5 mT when magnet is in the normal operation mode. The longest coherence time is obtained at 5 mT, with $T_2^\star = 24.1\,\mu$s, $T_2^{\mathrm{H}} = 122\,\mu$s and $T_2^{\mathrm{CPMG-512}} > 3$ ms. The $T_2^\star$ is extracted from the Ramsey measurement with an average of 10 traces and the experimental time 12-19 minutes. When fitting $T_2^{\mathrm{CPMG-512}}$ of Q_A, we disregard data points corresponding to total evolution time $\tau N_\pi > 4$ ms that are influenced by the reservoir-induced decay. Exemplary CPMG datasets are shown in Fig.7.14. **e,f,** The T_2^{CPMG} as function of number of π-pulses for both qubits at two different magnetic fields.

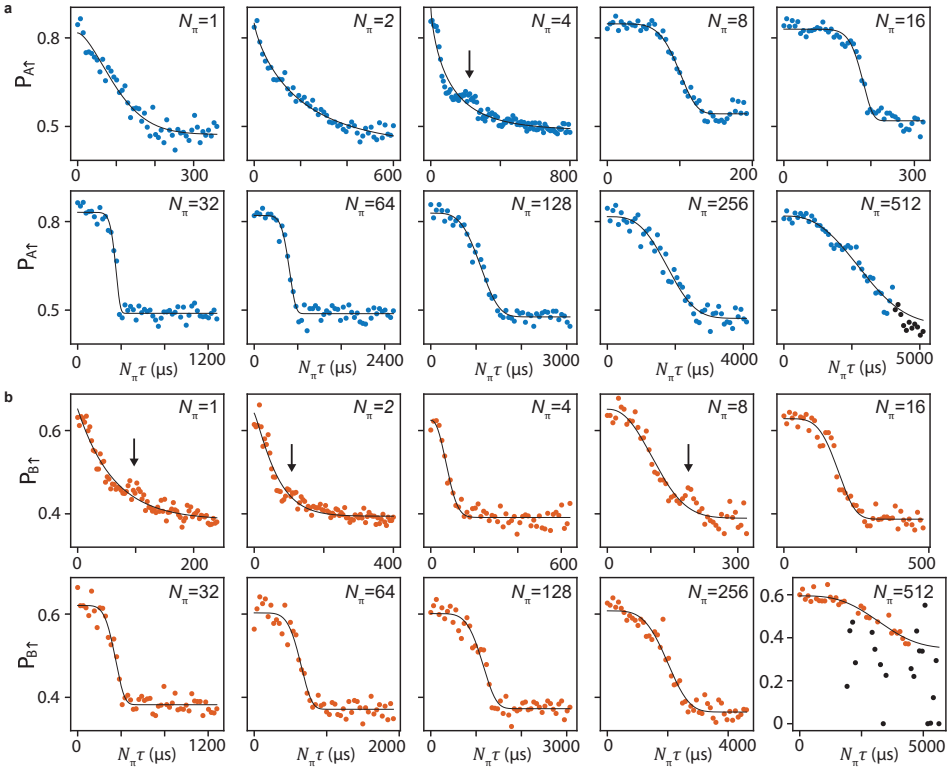

Figure 7.14: **Coherence time with dynamical decoupling pulses at magnetic field of 5 mT. a,** The coherence of qubit A and **b,** the coherence of qubit B as a function of total evolution time $N_\pi\tau$ with CPMG dynamical decoupling sequence (schematics depict in Fig. 7.13a). The collapse and revival of coherence (peaks marked by black arrows in the plots $N_\pi \leq 8$) should be attributed to hyperfine noise of ^{73}Ge nuclear spin. We notice that at such low magnetic field the expected linewidth of hyperfine noise becomes comparable to the nuclear spin precession frequency, which might explain the observed smoother features compared to the work [24]. Despite the collapse-and-revival features, we still fit the data to the formula $P(t) = A\exp(-(t/T_2)^\alpha) + B$ to extract coherence time T_2. We also notice the coherence at $N_\pi\tau = 0$ almost stay the same for the plots from $N_\pi = 1$ to $N_\pi = 512$, which implies the spin states do not have noticeable decay with numbers of shuttles up to 4096(2048) times for qubit $Q_{A(B)}$. We remark that the black data points in the plots $N_\pi = 512$ are removed from the coherence time fitting, due to the decay induced by tunnel coupling to the reservoir in (a), and due to the charge jumps of the sensor in (b). In both cases, the fitted T_2 should still be valid because the fitting curves agree with the data, and the fitted T_2 fall on the trend of T_2-N_π data in Fig. 7.13e,f.

7.9.3. MEASUREMENT PROTOCOL FOR RESIDUAL EXCHANGE COUPLINGS

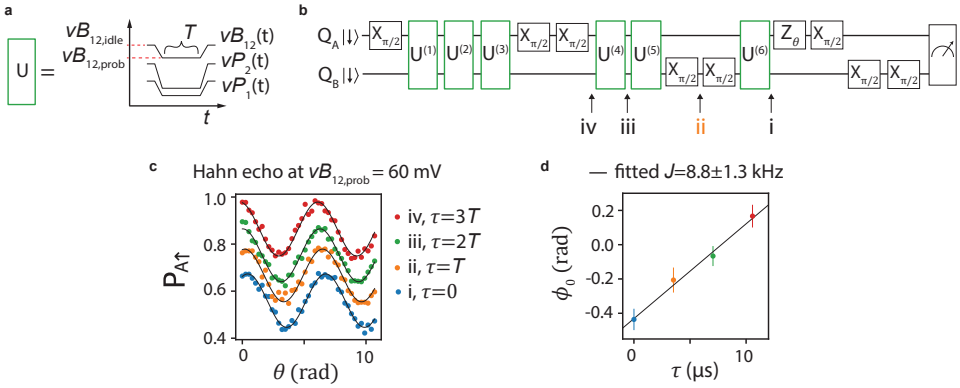

Figure 7.15: **Measurement of exchange coupling using a Hahn echo sequence at magnetic field of 25 mT. a,** Illustration of a pulse used to probe the exchange coupling at $vB_{12,\mathrm{probe}}$ starting from the idle point $vB_{12,\mathrm{idle}}$ where the single-qubit gates are performed. The virtual gate voltages $vP_{1,2}$ are ramped to the values used for the Ramsey experiments (Fig. 7.10) as well as the GST and RB experiments. **b,** The circuits for Hahn echo measurement, probing the difference of accumulated phases on qubit A induced by the flipped state of qubit B. Echo fringes of qubit A are measured in **c** by inserting $X^2_{\pi/2,\mathrm{B}}$ at various positions of the circuits {i,ii,iii,iv}, which lets Q_A interact with flipped Q_B for various amount of time $\tau = nT$, $n = \{0,1,2,3\}$. (b) shows the gates $X^2_{\pi/2,\mathrm{B}}$ inserting at the position ii. **c,** The fringes of the Hahn echo measurement. The data sets are shifted vertically for clearer display. The fringes are fitted to $A\cos(\theta+\phi_0)+B$ as black lines and the extracted phase offsets ϕ_0 are plotted in **d**. The linear fit of the phase offsets ϕ_0 as a function of evolution time τ gives the Q_B-state-dependent frequency variation of Q_A. The phase accumulation during the ramp and the idle time before and after the pulses $X^2_{\pi/2,\mathrm{B}}$ are corrected by the residual exchange at the idle position, which is 15(1) kHz measured via the same method. We note that the measurement displayed in this figure are taken after a charge jump of vB_{12}, similar to the situation described in the caption of Fig. 7.10.

7.9.4. CALIBRATION OF THE PULSE-SHAPED CZ GATES

We implement exchange pulses with a Hamming window $J(t) = J_{\text{on}}(0.54-0.46\cos(\pi t/\tau_{\text{ramp}}))$, using an empirical relation between the exchange coupling and the gate voltage vB_{12} , $J(vB_{12}) = J_0 \exp(-\kappa\ vB_{12})$ where $J_0 = 0.24$ MHz and $\kappa = 0.059$ mV^{-1}. The CZ gate calibration is performed in the following order:

1. Conditional phase calibration: for a given pulse amplitude $vB_{12,\text{on}}$, we measure the accumulated state-dependent phases as function of the ramp time τ_{ramp}, as described in Fig. 7.16bc. We find the ramp time $\tau_{\text{ramp}} = \tau^{\pi}_{\text{ramp}}$ that allows the state-dependent phase difference of π (Fig. 7.16d). The pulse amplitudes and ramp times allowing conditional phase of π are measured and plotted in Fig. 7.16e.

2. Single-qubit phase correction: as described in Fig. 7.4D, after applying an exchange pulse with a given pulse amplitude and the ramp time, the target qubit Q_A picks up a phase that should be calibrated to zero if the control qubit $|Q_B\rangle = |\downarrow\rangle$, and to π if the control qubit $|Q_B\rangle = |\uparrow\rangle$. The same correction needs to apply to both qubits.

3. GST calibration: we fine-tune the ramp time τ_{ramp} and the single-qubit phase correction with the error reports from gate set tomography (GST) [12, 54].

We measure the non-adiabatic transitions of the implemented exchange pulses in Fig. 7.16. We observed the gate is sufficiently adiabatic when maximum exchange is below 20 MHz, motivating the choice of CZ gate parameter $vB_{12,\text{on}} = -76$mV for two-qubit RB and GST experiments.

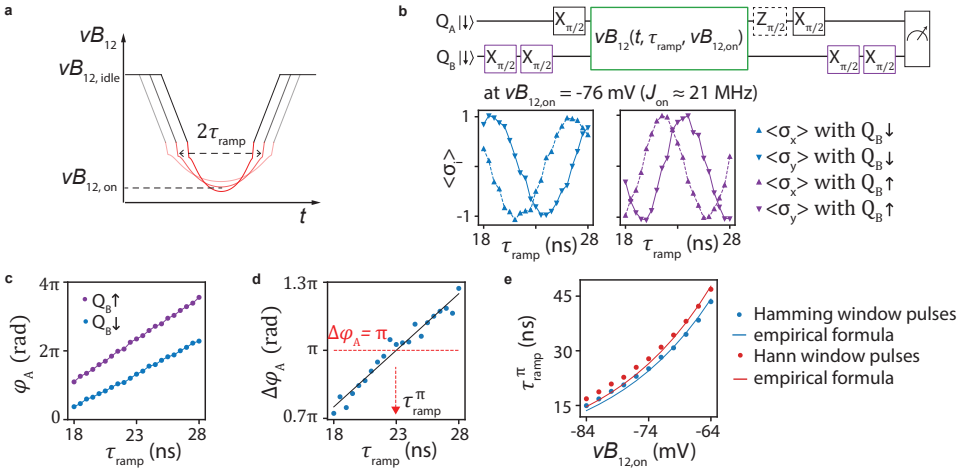

Figure 7.16: **Calibration of the conditional phase for the pulse-shaped CZ gates. a,** The illustration of virtual barrier gate voltage $vB_{12}(t)$ with two pulse parameters $vB_{12,\mathrm{on}}$ and τ_{ramp} . The pulse $vB_{12}(t)$ generates Hamming window waveform $J(t) = J_{\mathrm{on}}(0.54 - 0.46\cos(\pi t/\tau_{\mathrm{ramp}})$. The maximum exchange coupling J_{on} is predicted by empirical formula $J_{\mathrm{on}} = J_0 \exp(-\kappa\ vB_{12,\mathrm{on}})$, where $J_0 = 0.24$ MHz and $\kappa = 0.059$ mV^{-1}. **b,** The normalized $\langle\sigma_{\mathrm{x(y)}}\rangle$ of qubit A depending on the state of qubit B, as a function of τ_{ramp} at a certain gate voltage $vB_{12,\mathrm{on}}$. The values $\langle\sigma_{\mathrm{x(y)}}\rangle$ are measured by the $X_{\pi/2}$ without (with) $Z_{\pi/2}$ before the readout, normalized with the Ramsey amplitudes of a reference experiments without the exchange pulse. Here is an example of $vB_{12,\mathrm{on}} = -76$ mV. **c,** The state-dependent phases of the qubit A as a function of the ramp time τ_{ramp}. **d,** The ramp time for the state-dependent π phase shift, $\tau_{\mathrm{ramp}} = \tau^{\pi}_{\mathrm{ramp}}$, is determined by linear interpolation and finding the point where the state-dependent phase shift $\Delta\varphi_{\mathrm{A}} = \varphi_{\mathrm{A,B}\uparrow} - \varphi_{\mathrm{A,B}\downarrow} = \pi$. **e,** The ramp time $\tau^{\pi}_{\mathrm{ramp}}$ that results in CZ gate at various gate voltages $vB_{12,\mathrm{on}}$. We also tune up the CZ gates with Hann window pulses using the same method. The predictions are based on the analytical formula $t_{\mathrm{ramp}} = 0.25/(a_0 J_0 \exp(-\kappa\, vB_{12,\mathrm{on}}))$, where $a_0 = 0.54(0.5)$ for Hamming (Hann) window.

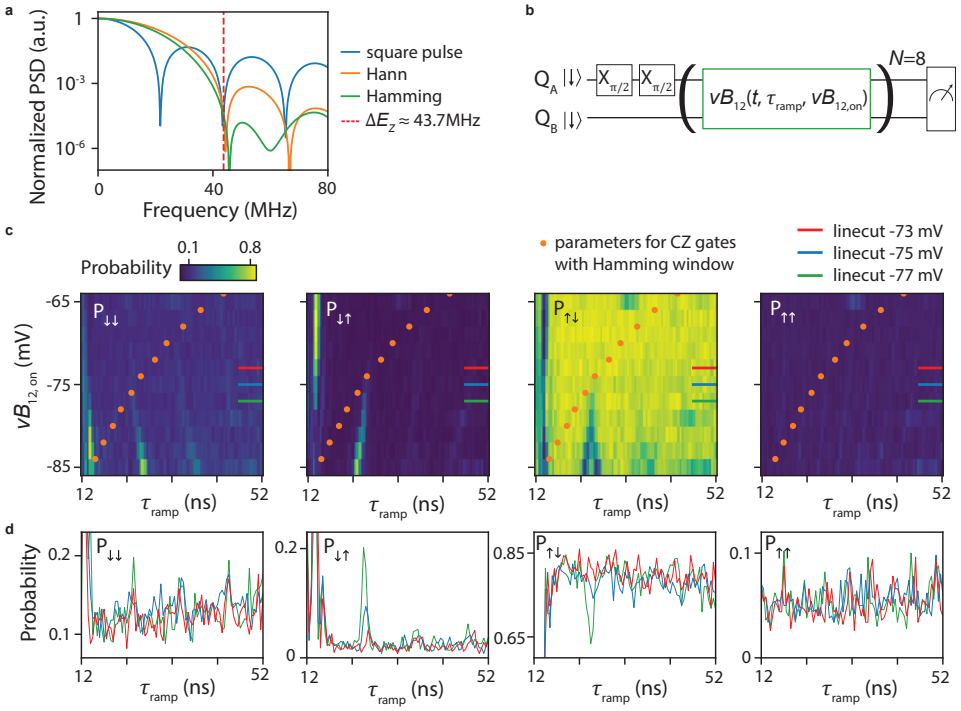

Figure 7.17: **Exchange pulse shapes and the resulting non-adiabatic state transitions.** **a,** The power spectrum density (PSD) of the exchange pulse shapes, indicating the energy emission that can drive non-adiabatic state transitions. Hamming (Hann) window functions are $J(t) = J_{\rm on}(a_0 - (1-a_0)\cos(\pi t/\tau_{\rm ramp}))$, where $a_0 = 0.54(0.5)$. All the shapes have the same pulse time of 46 ns, close to the value used in the RB and GST experiments. **b,** The circuit for measuring state transitions induced by the exchange pulses. We use eight exchange pulses to amplify the transition probability. The pulses with the Hamming window shape parameters $(\tau_{\rm ramp}, vB_{12,\rm on})$ are applied on the state $|\uparrow\downarrow\rangle$, and the full two-qubit state is readout at the end. **c,** The probability $P_{\sigma\sigma'}$ that indicates non-adiabatic state transitions are measured at 25 mT ($\Delta E_Z \approx 43.7$ MHz). The parameters $(\tau_{\rm ramp}, vB_{12,\rm on})$ for CZ gates, taken from Fig. 7.16e, are marked in orange circles. The linecuts at $vB_{12,\rm on} = -73, -75, -77$ mV (corresponding $J_{\rm on} \approx 18, 20, 23$ MHz) are displayed in **d**. An onset of SWAP transition, $|\uparrow\downarrow\rangle \rightarrow |\downarrow\uparrow\rangle$, is observed as the emerging dip (peak) around $\tau = 25$ ns in the plot of $P_{\uparrow\downarrow(\downarrow\uparrow)}$ when $vB_{12,\rm on}$ becomes more negative. In the nearby parameter space we observe another transition dip (peak) $|\uparrow\downarrow\rangle \rightarrow |\downarrow\downarrow\rangle$. Combining with other measurement data (not showing here), we interpret this transition as Q_B-state-dependent Q_A transition.

7.9.5. SHUTTLING ACROSS MULTIPLE QUANTUM DOTS: DETUNING AND BARRIER VOLTAGE DEPENDENCE

We probe the oscillations induced by differences in quantization axes as a function of detuning and barrier voltages. In practice, to shuttle from D4 to D8, we follow this protocol:

1. initialize the D1, D4 double quantum dot system in the $|\uparrow\downarrow\rangle$;
2. ramp the gate voltages from the set point defined as (1,0) to the (0,1), passing through the (1,0)-(0,1) charge anticrossing (AC). Here, the first number defines the filling of D4, and the second of D8. Ramp times in between these points are of $\sim$ 10 ns;
3. wait in the (0,1) point for a varying free-precession time;
4. pulse back to the AC, and to the (1,0) setpoint;
5. readout the spin via Pauli spin blockade.

To probe the dependence of the D8 Larmor frequency, we sweep the detuning of the (0,1) set point. The results of this measurement are shown in Fig. 7.18a. Oscillations starts to arise when the gate voltage overcomes the charge anticrossing, that is found at $\epsilon_{4,8} = 10$ mV. For lower detuning voltages, the spin remains in D4, and therefore oscillations are not present. The Fast Fourier Transform of the data shows well the dependence of the Larmor frequency in the detuning voltage window. Similar measurements are shown for the case of a spin transfer from D8 to D5 (Fig. 7.18b), from D6 to D10 (Fig. 7.18c) and from D3 to D7 (Fig. 7.18d). We observe that, except for the region around the charge anticrossing, the qubit frequencies are not strongly affected by the detuning voltages. Rather, barrier gates do have a much stronger effect on the qubit frequencies, which mostly shift linearly, as illustrated in Fig. 7.19. Interestingly, the D7 Larmor frequency crosses zero as a function of J6, suggesting a change of sign in the g-factor of the qubit.

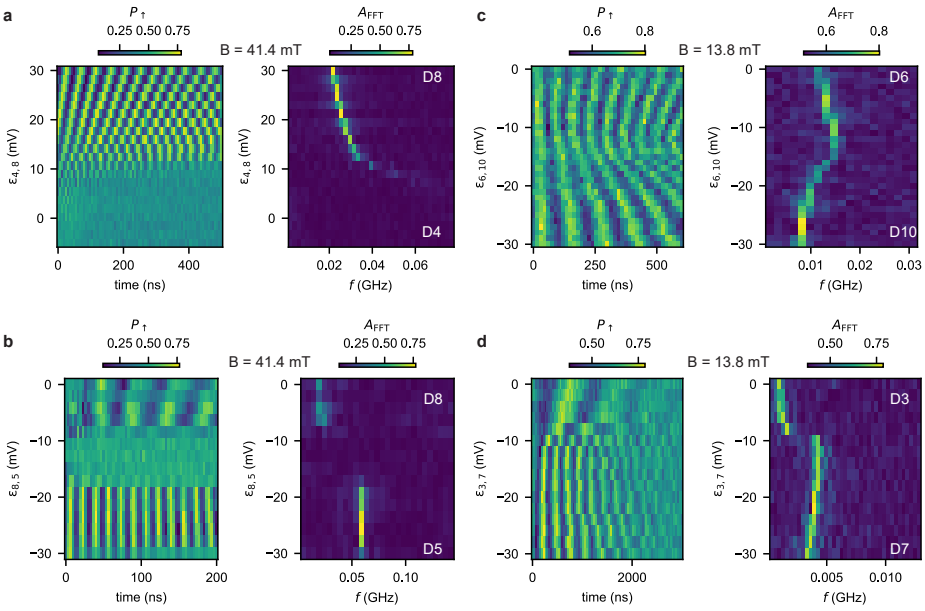

Figure 7.18: **Detuning dependence of the hopping-induced spin oscillations. a,** We vary the detuning gate voltage of the (0, 1) set point, corresponding to the shuttling sequence that moves the single spin from D4 to D8, i.e., from the (1,0) to the (0,1) charge state, across the charge interdot. Similarly to ref. [21], oscillations arise when the spin is transferred from one dot to the other. We observe that the onset of the oscillations corresponds to the charge interdot point. The panel on the right shown the FFT of the data. In **b, c, d,**, we illustrate similar measurements taken for spin shuttling from D8 to D5, from D6 to D10, from D3 to D7, respectively.

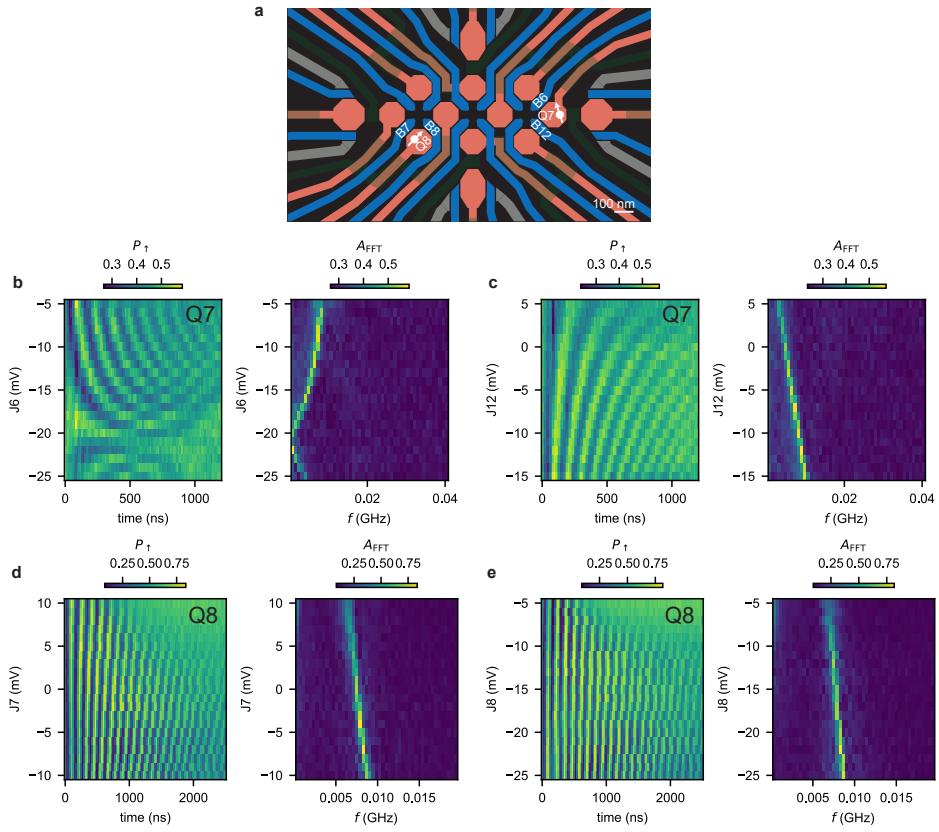

Figure 7.19: **Barrier gate dependence of the hopping-induced spin oscillations. a,** Device layout indicating the two quantum dots D8 and D7, together with the surrounding barrier gates. **b, c** D7 Larmor frequency evolution while sweeping the J6 and J12 voltages, respectively. **d, e** D8 Larmor frequency evolution as a function of J7 and J8. Small changes in the barrier voltages induce a linear shift of the D8 frequency.

7.9.6. DEPHASING TIMES AND LARMOR FREQUENCIES IN THE 10 QUANTUM DOT ARRAY

We study the dephasing times (T_2^*) of the 10 quantum dots by shuttling a spin diabatically from the double quantum dot system D1, D4 to each of the quantum dots, and let it evolve for a varying idle time. We measure the decay of the oscillations as a function of the time spent in each site by fitting the data shown in Fig. 7.20 and Fig. 7.5F using the equation: $A \cdot \sin(2\pi f t + \phi) \exp\left(-(t/T_2^*)^2\right) + C$. Here, $2 \cdot A$ is the visibility, f the Larmor frequency, t the free precession time, ϕ the starting phase, and C the oscillations offset. The Larmor frequency of an isolated Loss-diVincenzo spin qubit satisfies the relation: $f = \frac{g\mu_B B}{h}$, with g the g-factor, μ_B the Bohr magneton, B the applied magnetic field and h the Planck constant. From the measurements of the oscillations as a function of magnetic field, we extract the g-factor for all the 10 quantum dots (Fig. 7.21). We find that except for the tunnel coupled Q1, Q4 qubits, f shows a linear dependence to the magnetic field. The deviation from the linear trend can be explained from the coexistence of finite exchange coupling and non-parallel quantization axes.

In general, the lower-than-unity and varying visibilities of the hopping-induced oscillations (Figs. S21, S22, S24, S25) are caused by both SPAM errors and by the non-orthogonality of the quantization axes of adjacent quantum dots. As the estimated SPAM fidelities are typically in the range of 80-95% (details for qubits A, B in Tables 7.5 and 7.6), we speculate that the origin of oscillation amplitudes below ~ 0.8 and their variability are mainly due to unfavourable spin alignment. In the current approach, we adopted a simple and sequential tuning approach, which can result in reduced rotations in the Bloch sphere. However, we could envision more involved tuning protocols that would lead to a higher contrast if desired, such as further optimization of the time spent in each dot and possibly additional shuttling steps to ensure that a phase rotation in a dot leads to a full amplitude rotation.

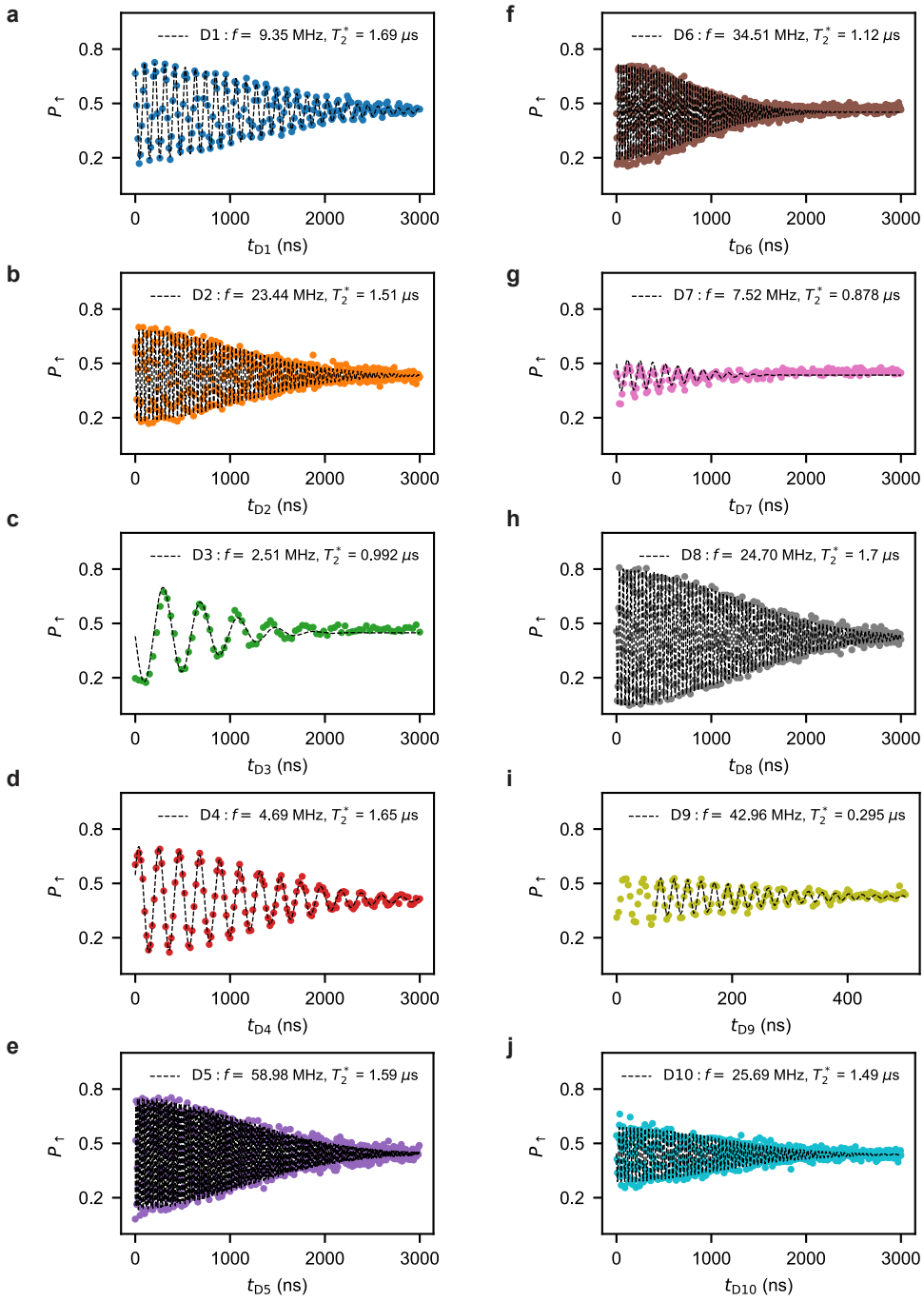

Figure 7.20: T_2^* **of the 10 quantum dot array at 41.4 mT. a-j,** Each panel is measured using the same method as presented in Fig. 7.5. We fit the dataset of D9 from 68 ns onward as we observe a frequency shift in the first ~ 100 ns possibly due to a delay in the electrical response.

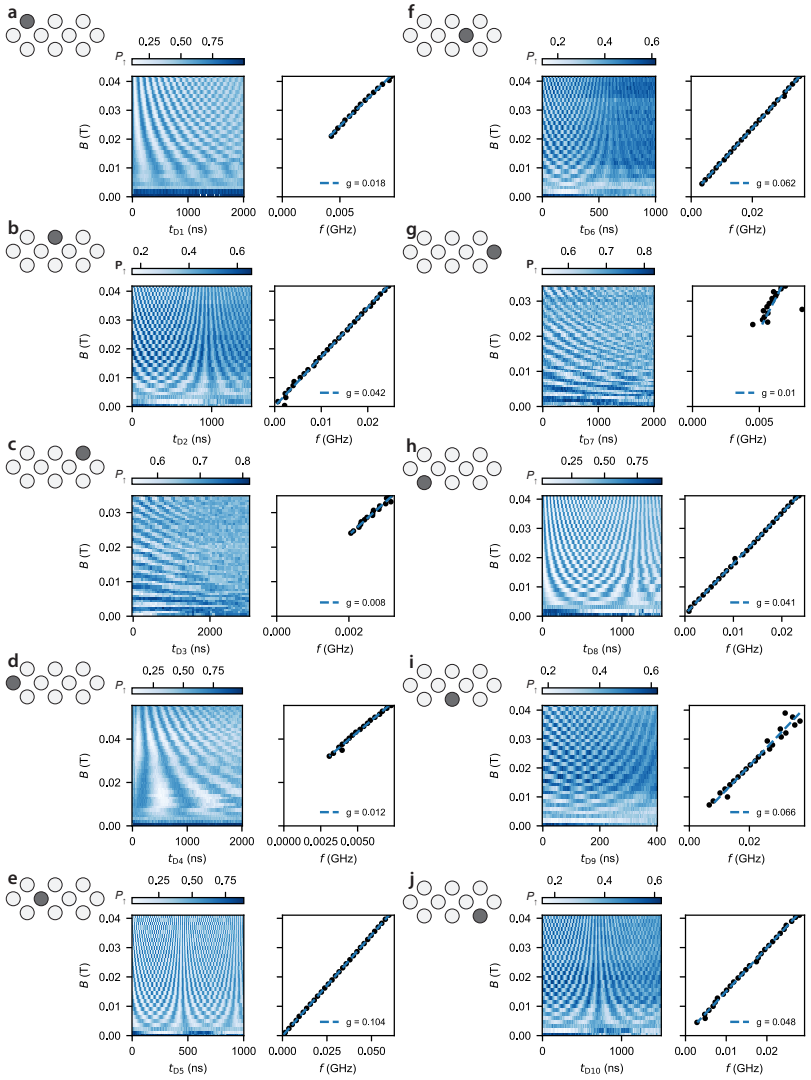

Figure 7.21: **Single-qubit rotations as a function of in-plane magnetic field for the 10 quantum dots. a-j,** We repeat the experiments shown in Fig. 7.5 and Fig. 7.20 as a function of magnetic field to obtain a more accurate estimate of the g-factors. We linearly fit the oscillation frequencies as a function of the magnetic field. We observe that all qubits but Q1 and Q4 display a Larmor frequency that intersects zero at zero magnetic field.

BIBLIOGRAPHY

[1] Daniel Loss and David P. DiVincenzo. "Quantum computation with quantum dots". In: Physical Review A 57.1 (Jan. 1998), pp. 120–126. ISSN: 1050-2947.

[2] Guido Burkard et al. "Semiconductor spin qubits". In: Rev. Mod. Phys. 95 (2 June 2023), p. 025003.

[3] F. H. L. Koppens et al. "Driven coherent oscillations of a single electron spin in a quantum dot". In: Nature 442.7104 (Aug. 2006), pp. 766–771. ISSN: 1476-4687.

[4] M. Veldhorst et al. "An addressable quantum dot qubit with fault-tolerant control-fidelity". In: Nature Nanotechnology 9 (2014), pp. 941–985.

[5] M. Pioro-Ladrière et al. "Micromagnets for coherent control of spin-charge qubit in lateral quantum dots". In: Applied Physics Letters 90.2 (2007), p. 024105.

[6] Jun Yoneda et al. "A quantum-dot spin qubit with coherence limited by charge noise and fidelity higher than 99.9%". In: Nature Nanotechnology 13.2 (Feb. 2018), pp. 102–106. ISSN: 1748-3395.

[7] Denis V. Bulaev and Daniel Loss. "Electric Dipole Spin Resonance for Heavy Holes in Quantum Dots". In: Phys. Rev. Lett. 98 (9 Feb. 2007), p. 097202.

[8] S. Nadj-Perge et al. "Spin–orbit qubit in a semiconductor nanowire". In: Nature 468.7327 (Dec. 2010), pp. 1084–1087. ISSN: 1476-4687.

[9] Ke Wang et al. "Ultrafast coherent control of a hole spin qubit in a germanium quantum dot". In: Nature Communications 13.1 (Jan. 2022), p. 206. ISSN: 2041-1723.

[10] N. W. Hendrickx et al. "Fast two-qubit logic with holes in germanium". In: Nature 577.7791 (Jan. 2020), pp. 487–491. ISSN: 0028-0836.

[11] A. Noiri et al. "A shuttling-based two-qubit logic gate for linking distant silicon quantum processors". In: Nature Communications 13 (2022), p. 5740.

[12] Xiao Xue et al. "Quantum logic with spin qubits crossing the surface code threshold". In: Nature 601.7893 (Jan. 2022), pp. 343–347. ISSN: 1476-4687.

[13] Stephan G. J. Philips et al. "Universal control of a six-qubit quantum processor in silicon". In: Nature 609.7929 (Sept. 2022), pp. 919–924. ISSN: 1476-4687.

[14] K. Takeda et al. "Optimized electrical control of a Si/SiGe spin qubit in the presence of an induced frequency shift". In: npj Quantum Information 4.1 (Oct. 2018), p. 54. ISSN: 2056-6387.

[15] Brennan Undseth et al. "Nonlinear Response and Crosstalk of Electrically Driven Silicon Spin Qubits". In: Phys. Rev. Appl. 19 (4 Apr. 2023), p. 044078.

[16] Brennan Undseth et al. “Hotter is Easier: Unexpected Temperature Dependence of Spin Qubit Frequencies”. In: Phys. Rev. X 13 (4 Oct. 2023), p. 041015.

[17] Maximilian Russ and Guido Burkard. “Three-Electron Spin Qubits”. In: J. Phys. Condens. Matter 29.39 (2017), p. 393001.

[18] Reed W. Andrews et al. “Quantifying error and leakage in an encoded Si/SiGe triple-dot qubit”. In: Nature Nanotechnology 14.8 (Aug. 2019), pp. 747–750. ISSN: 1748-3395.

[19] Aaron J. Weinstein et al. “Universal logic with encoded spin qubits in silicon”. In: Nature 615.7954 (Mar. 2023), pp. 817–822. ISSN: 1476-4687.

[20] G. Scappucci et al. “Crystalline materials for quantum computing: Semiconductor heterostructures and topological insulators exemplars”. In: MRS Bulletin 46.7 (2021), pp. 596–606.

[21] Floor van Riggelen-Doelman et al. “Coherent spin qubit shuttling through germanium quantum dots”. In: arXiv (2023). eprint: 2308.02406.

[22] B. Jadot et al. “Distant spin entanglement via fast and coherent electron shuttling”. In: Nature Nanotechnology 16 (2021), pp. 570–575.

[23] W. I. L. Lawrie et al. “Simultaneous single-qubit driving of semiconductor spin qubits at the fault-tolerant threshold”. In: Nature Communications 14.3617 (2023).

[24] N. W. Hendrickx et al. “Sweet-spot operation of a germanium hole spin qubit with highly anisotropic noise sensitivity”. In: Nature Materials (May 2024). ISSN: 1476-4660.

[25] Austin G. Fowler et al. “Surface codes: Towards practical large-scale quantum computation”. In: Phys. Rev. A 86.3 (Sept. 2012), p. 032324. ISSN: 1050-2947.

[26] D. Jirovec et al. “Dynamics of hole Singlet-Triplet qubits with large g-factor differences”. In: Phys. Rev. Lett. 128 (2022), p. 126803.

[27] Chien-An Wang et al. “Modelling of planar germanium hole qubits in electric and magnetic fields”. In: arXiv (2022). eprint: 2208.04795.

[28] José Carlos Abadillo-Uriel et al. “Hole-Spin Driving by Strain-Induced Spin-Orbit Interactions”. In: Phys. Rev. Lett. 131 (9 Sept. 2023), p. 097002.

[29] Cedric Corley-Wiciak et al. “Nanoscale Mapping of the 3D Strain Tensor in a Germanium Quantum Well Hosting a Functional Spin Qubit Device”. In: ACS Applied Materials & Interfaces 15.2 (Jan. 2023), pp. 3119–3130. ISSN: 1944-8244.

[30] N. W. Hendrickx et al. “A four-qubit germanium quantum processor”. In: Nature 591 (2021), pp. 580–585.

[31] Chein-An Wang et al. “Universal Control of Four Singlet-Triplet Qubits”. In: Science (2024).

[32] Matthew Reed. “Entanglement and quantum error correction with superconducting qubits”. In: Dissertation (Yale University) (2013).

[33] L. M. K. Vandersypen et al. “Interfacing spin qubits in quantum dots and donors—hot, dense, and coherent”. In: npj Quantum Information 3.1 (Sept. 2017), p. 34. ISSN: 2056-6387.

[34] Erik Nielsen et al. “Probing Quantum Processor Performance with pyGSTi”. In: Quantum Science and Technology 5.4 (2020), p. 044002. ISSN: 2058-9565.

[35] R. Blume-Kohout et al. “Demonstration of qubit operations below a rigorous fault tolerance threshold with gate set tomography”. In: Nature Communications 8.1 (Feb. 2017), p. 14485. ISSN: 2041-1723.

[36] J. P. Dehollain et al. “Optimization of a solid-state electron spin qubit using gate set tomography”. In: New J. Phys. 18.10 (Oct. 2016), p. 103018.

[37] Maximilian Rimbach-Russ et al. “Simple Framework for Systematic High-Fidelity Gate Operations”. In: Quantum Science and Technology 8.4 (2023), p. 045025. ISSN: 2058-9565.

[38] David S. Wang, Austin G. Fowler, and Lloyd C. L. Hollenberg. “Surface code quantum computing with error rates over 1%”. In: Phys. Rev. A 83 (2 Feb. 2011), p. 020302.

[39] Bence Hetényi and James R. Wootton. “Tailoring quantum error correction to spin qubits”. In: arXiv (2023). eprint: 2306.17786.

[40] Sergey Bravyi et al. “High-threshold and low-overhead fault-tolerant quantum memory”. In: Nature 627 (2024), pp. 778–782.

[41] Wonill Ha et al. “A Flexible Design Platform for Si/SiGe Exchange-Only Qubits with Low Disorder”. In: Nano Letters 22.3 (Feb. 2022), pp. 1443–1448. ISSN: 1530-6984.

[42] Biel Martinez et al. “Hole spin manipulation in inhomogeneous and nonseparable electric fields”. In: Phys. Rev. B 106 (23 Dec. 2022), p. 235426.

[43] S. Bosco et al. “Squeezed hole spin qubits in Ge quantum dots with ultrafast gates at low power”. In: Phys. Rev. B 104 (11 2021), p. 115425.

[44] Ruoyu Li et al. “A crossbar network for silicon quantum dot qubits”. In: Science Advances 4.7 (2018), eaar3960.

[45] Daniel L. Campbell et al. “Universal Nonadiabatic Control of Small-Gap Superconducting Qubits”. In: Phys. Rev. X 10 (4 Dec. 2020), p. 041051.

[46] Amir Sammak et al. “Shallow and Undoped Germanium Quantum Wells: A Playground for Spin and Hybrid Quantum Technology”. In: Advanced Functional Materials 29.14 (Apr. 2019), p. 1807613. ISSN: 1616-3028.

[47] M. Lodari et al. “Low percolation density and charge noise with holes in germanium”. In: Mater. Quantum. Technol. 1 (2021), p. 011002.

[48] Francesco Borsoi et al. “Shared control of a 16 semiconductor quantum dot crossbar array”. In: Nature Nanotechnology (Aug. 2023). ISSN: 1748-3395.

[49] David M. Pozar. Microwave engineering. 4th ed. Wiley, 1998.

[50] A C Baynham, A F Gibson, and J W Granville. “On the Dielectric Constant of Germanium at Microwave Frequencies”. In: Proceedings of the Physical Society 75.2 (Feb. 1960), p. 306.

[51] Jerzy Krupka et al. “Dielectric properties of semi-insulating silicon at microwave frequencies”. In: Applied Physics Letters 107.8 (Aug. 2015), p. 082105. ISSN: 0003-6951.

[52] L. S. Theis et al. “Counteracting Systems of Diabaticities Using DRAG Controls: The Status after 10 Years (a)”. In: EPL (Europhysics Letters) 123.6 (2018), p. 60001. ISSN: 0295-5075.

[53] Felix D. Mbairi, W. Peter Siebert, and Hjalmar Hesselbom. “High-Frequency Transmission Lines Crosstalk Reduction Using Spacing Rules”. In: IEEE Transactions on Components and Packaging Technologies 31.3 (2008), pp. 601–610.

[54] R. Blume-Kohout et al. “A Taxonomy of Small Markovian Errors”. In: PRX Quantum 3 (2 May 2022), p. 020335.

[55] John M. Martinis et al. “Decoherence of a superconducting qubit due to bias noise”. In: Phys. Rev. B 67 (9 Mar. 2003), p. 094510.

[56] Jeffrey M. Epstein et al. “Investigating the limits of randomized benchmarking protocols”. In: Phys. Rev. A 89 (6 June 2014), p. 062321.

[57] M. Benito et al. “Electric-field control and noise protection of the flopping-mode spin qubit”. In: Phys. Rev. B 100 (2019), p. 125430.

[58] P. M. Mutter and G. Burkard. “All-electrical control of hole singlet-triplet spin qubits at low-leakage points”. In: Phys. Rev. B 104 (19 2021), p. 195421.

[59] Simon Geyer et al. “Two-Qubit Logic with Anisotropic Exchange in a Fin Field-Effect Transistor”. In: Nature Physics (2022).

[60] Xin Zhang et al. “Universal Control of Four Singlet-Triplet Qubits”. In: arXiv (2023). eprint: 2312.16101.

[61] Valentin John et al. “Bichromatic Rabi Control of Semiconductor Qubits”. In: Phys. Rev. Lett. 132 (6 Feb. 2024), p. 067001.

[62] Łukasz Cywi ński et al. “How to enhance dephasing time in superconducting qubits”. In: Phys. Rev. B 77 (17 May 2008), p. 174509.

[63] Maximilian Russ and Guido Burkard. “Asymmetric Resonant Exchange Qubit under the Influence of Electrical Noise”. In: Phys. Rev. B 91.23 (2015), p. 235411.

[64] L. H. Pedersen, N. M. Møller, and K. Mølmer. “Fidelity of quantum operations”. In: Physics Letters A 367.1 (2007), pp. 47–51. ISSN: 0375-9601.

[65] J. R. Johansson, P. D. Nation, and Franco Nori. “QuTiP 2: A Python Framework for the Dynamics of Open Quantum Systems”. In: Computer Physics Communications 184.4 (2013), pp. 1234–1240. ISSN: 0010-4655.

[66] Todd Green, Hermann Uys, and Michael J. Biercuk. “High-Order Noise Filtering in Nontrivial Quantum Logic Gates”. In: Phys. Rev. Lett. 109 (2 July 2012), p. 020501.

[67] J.P.G. van Dijk et al. “Impact of Classical Control Electronics on Qubit Fidelity”. In: Phys. Rev. Appl. 12 (4 Oct. 2019), p. 044054.

[68] W. I. L. Lawrie. “Spin Qubits in Silicon and Germanium”. In: PhD Thesis (2022).

8

CONCLUSION

8.1. CONCLUSIONS

This thesis presents the development of spin-qubit control protocols in the germanium quantum dot array. The main findings are summarized below:

- We benchmark the two-qubit controlled-Z gate of hole spin qubits in germanium, with fidelity above 99% (**chapter 7**) and highly tunable two-qubit exchange interaction, from residual value $J_{\text{off}} = 10 - 15$ kHz to the maximal value $J_{\text{on}} \approx 21$ MHz.

- At low magnetic field (< 40 mT), we control low frequency spin qubits, encoded in two-spin ST^- states (**chapter 3**) and in a single spin (**chapter 7**), using baseband pulses. We measure the coherence time T_2 that is an order of magnitude longer than the one measured at higher magnetic field (1 T) in the same sample.

- We shuttle a spin between quantum dots, observe the spin state evolution around non-parallel quantization axes, and control such evolution to make an identity gate for quantum information transfer application (**chapter 6**) and an $X_{\pi/2}$ gate for fast single-qubit operations (**chapter 7**).

- We model the g-factor, the electric susceptibility, and the resulting spin dephasing of a germanium quantum dot (**chapter 4**).

- We show the protocol for simultaneously turning on the exchange interactions in a four-spin system (**chapter 3**).

- We demonstrate coherent Rabi driving via multi-photon processes in a two-spin system (**chapter 5**).

8.2. OUTLOOK

In the current status of germanium spin qubit, it is essential to advance both qubit numbers and operation fidelity in order to reach the next milestones, such as error correction code with higher distance or demonstration of quantum supremacy. Here the operation includes single-qubit gates, two-qubit gates, initialization, readout, shuttling and idling. In the following subsections we discuss several possible changes can be made, or what can still be learned, in order to improve qubit operation fidelity in a scalable way. We'll mostly focus on Loss-Divincenzo single-spin qubit, discussing the potential benefits, challenges and trade-off.

8.2.1. MICROSCOPIC ORIGIN AND CONTROLLABILITY OF QUANTIZATION AXES AND EFFECTIVE G-FACTORS

The spin quantization axes within and between the quantum dots, and their electrical susceptibility, are highly relevant for spin qubit operations. For operations of single-qubit gates, the efficient driving is enabled by intrinsic spin-orbit coupling. The driving can be faster by making quantization axes more sensitive to control signals (analogue to the hopping-based operations in **chapter 7**). In contrast, for other qubit operations including the idle gate (drive one qubit and idle the other, as shown in Fig. 8.1 and Fig. 8.2),

two-qubit gates (except CROT), shuttling, and readout, it is desirable to have quantization axes insensitive to signals and parallel to each other (or anti-parallel for two-qubit gates [1]) . Therefore, it would be helpful to understand the origin of the quantization axes variations (e.g. how much it is from intrinsic spin-orbit coupling and from g-tensor variations) and if it is controllable at the level of device design and fabrication.

Controllability of g-factors is also relevant for qubit operations. Typically, the adiabatic CZ gate is the most straightforward implementation of two-qubit gates, due to the spin-orbit coupling and anisotropic exchange in germanium double dot. The g-factor difference determines the Zeeman energy gradient ΔE_Z, and therefore the EDSR crosstalk and the shortest possible gate time of adiabatic CZ. To have short gate time, it is desired to have sizable g-factor difference between two quantum dots where two-qubit gates are carried out. On the other hands, the large g-factor difference introduces side effects, such as higher dephasing error rate during shuttling, and faster relaxation of $T_0(1,1)$ at PSB point (likely to enable parity readout [2]). Therefore, it will be also helpful to understand how to control the g-factor variations.

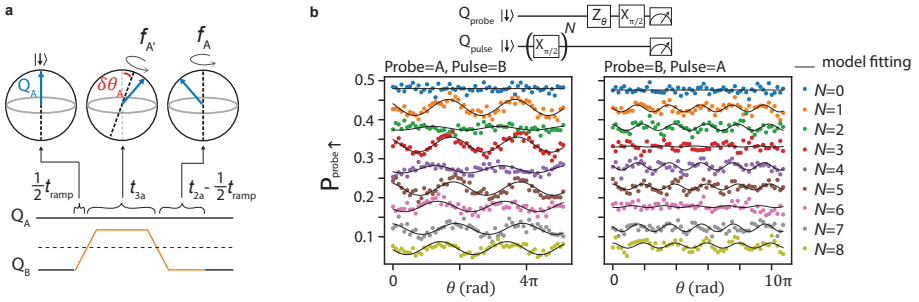

Figure 8.1: **Rotation crosstalk of single qubit gates. a,** The illustration of a simplified model (Eq. (4) of the supplementary material [3]) used for simulating the rotation crosstalk by the gate $X_{\pi/2,B}$ on qubit A. The voltage pulse on qubit B changes the quantization axis of Q_A by $\delta\theta_A$ and the precession frequency to $f_{A'}$. $f_{A'}$ is estimated in the phase crosstalk experiments in Fig. 8.2. The precession of qubit A around the perturbed quantization axis gives rise to the unintended rotation. **b,** The measurement of rotation crosstalk. For clarity the data sets are shifted vertically by −0.05. The circuit for the measurement is on the top, where $X_{\pi/2,\text{pulse}}$ is applied N times, wait for a varying wait time represented by the phase θ, and then $X_{\pi/2,\text{probe}}$ to make the readout signal sensitive to the small rotation angle. Fitting the data simultaneously, we extract the amount of perturbation on quantization axes $\delta\theta_A = 1.90 \pm 0.14°$ and $\delta\theta_B = 0.70 \pm 0.07°$. The device setting is the same as in **chapter 7**, with magnetic field of 25 mT.

8

8.2.2. POSSIBLE IMPROVEMENT ON TWO-QUBIT GATES

According to the result of gate set tomography (GST) and the modeling in **chapter 7**, the decoherence is the dominant error for two-qubit gate. In particular, the fluctuation of the exchange coupling (qubit-qubit interaction) has the largest contribution. We list several possible directions to improve the gate fidelity, especially for incoherent errors:

(1) Diabatic CZ or other type of diabatic gate might have shorter gate time and thus may result in smaller dephasing error. The challenge is the complex two-qubit interaction in germanium. In a simpler system that tunneling processes preserve spin, the isotropic exchange $\propto \vec{\sigma}\cdot\vec{\sigma}$ couples $|\uparrow\downarrow\rangle$ and $|\downarrow\uparrow\rangle$, and leaves $|\downarrow\downarrow\rangle$ and $|\uparrow\uparrow\rangle$ unaffected. In

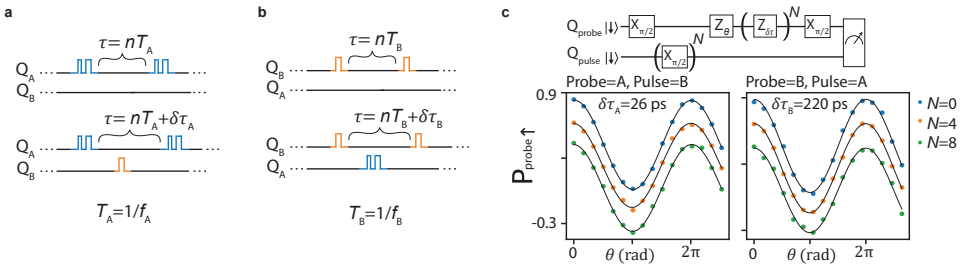

Figure 8.2: **Phase crosstalk of single qubit gates and phase correction. a,** The illustration of phase crosstalk induced by the gate $X_{\pi/2,B}$ on qubit A. In the absence of $X_{\pi/2,B}$, performing two successive $X_{\pi/2,A}$ requires zero or integer numbers of free precession period $\tau = nT_A$ in between. In the presence of $X_{\pi/2,B}$, an additional wait time $\delta\tau_A$ between $X_{\pi/2,B}$ and the next $X_{\pi/2,A}$ is required for correcting the phase induced by $X_{\pi/2,B}$. **b,** The illustration of phase crosstalk induced by the gate $X_{\pi/2,A}$ on qubit B. **c,** The measurement of phase correction. For clarity the data sets are shifted vertically by −0.2. By adding N phase gates $Z_{\delta\tau_{A(B)}}$, we align the phases of the Ramsey oscillations, indicating that the phase shift due to the crosstalk scales linearly with the number of gates N. The device setting is the same as in **chapter 7**, with magnetic field of 25 mT.

contrast, the spin-dependent tunnelings in germanium couples all the four spin states. To make a specific gate (e.g. CNOT, CZ, SWAP), the pulse needs to achieve the target rotation and at the same time cancel out unwanted four-spin evolution. It requires further development for such pulses and the corresponding tune-up method for specific device parameters (spin-dependent tunnelings and Zeeman energies) [1, 4]. The approximation of diabatic CZ (SWAP) can be made in the limit $J_{on} \ll \Delta E_Z$ ($J_{on} \gg \Delta E_Z$), with coherent error scales as $\frac{J_{on}}{\Delta E_Z}(\frac{\Delta E_Z}{J_{on}})$. Notice that coherent errors are typically harder to model, can have higher worst-case impact, and can be less tolerant in error correction codes [5], compared to incoherent errors. Therefore, it is desired to reach the limits ($J_{on} \ll \Delta E_Z$ or $J_{on} \gg \Delta E_Z$).

(2) From the device design perspective, shorter potential barrier between two spins in theory should lower the tunability of the exchange with respect to the gate voltage, as well as the sensitivity to charge noise. To have the same J_{on}/J_{off} ratio, the less tunable device requires larger voltage amplitude on the barrier gate. This brings an advantage of larger signal-to-noise ratio (SNR): the signal (applied barrier gate voltage) is enhanced compared to the noise (the equivalent barrier voltage fluctuation due to charge noise). The trade-off is the larger power dissipation on the device, and the possible g-tensor modulation that rotates the spins. To reduce the voltage amplitude, one may think of another operation scheme that make use of shuttling instead of large barrier pulses. In this scheme, two spins are shuttled to a double dot that has smaller interdot distance in order to make a two-qubit gate with less incoherent error. However, this scheme may cause other problems, such as the diabatic evolution around the non-parallel quantization axes between the dots.

(3) Lowering the field to reduce the Zeeman energy fluctuation of the individual qubit may still have marginal improvement (which is already implemented in **chapter 7**). The trade-off (for adiabatic CZ gate) is the longer gate time due to the smaller Zeeman energy difference ΔE_Z.

(4) From the material perspective, it will be beneficial to have advanced heterostruc-

tures and device fabrications that allow lower charge noise and electrical susceptibility of g-factor.

8.2.3. STATE PREPARATION AND MEASUREMENT: FIDELITY AND TIME

One of the important ingredients of quantum error correction is mid-circuit measurement: repeatedly reading out some of the qubits (ancilla qubits) during the circuit execution of the other qubits (data qubits). As a theoretical example of operating surface code as quantum memory [6], the thresholds of readout error r_{read} were estimated to be on the order of 10 % if gates have no error ($r_{\text{gate}} = 0$) and if the data qubits have no idling error ($r_{\text{idle}} = 0$) during the readout of ancilla qubits. The threshold of r_{gate} increases to the values on the order of 0.4 % (exact number depend on the code variant and error biases) if the readout is fast ($r_{\text{idle}} = 0$) and with high fidelity ($r_{\text{read}} = 0$). Therefore, it is beneficial to have high fidelity state preparation and measurement (SPAM) within spin decoherence time and also induce minimal coherent errors on data qubits.

Taking the parameters in the experiments of **chapter 7**, the initialization and readout time of a single spin using a two-spin system are $5-10\ \mu s$ separately, and the overall SPAM fidelity is ≈ 93 %. In the same setting, the measured coherence times are $T_2^\star \approx 5\mu s$, $T_2^H \approx 20\mu s$, and $T_2^{\text{CPMG-512}} \approx 1700\mu s$. This SPAM fidelity puts the system at the theoretical thresholds that require perfect single- and two-qubit gates, as well as perfect execution of dynamical decoupling sequences.

We list several possible directions to improve the readout and initialization:

(1) Bringing the two-spin system through noise-sensitive anti-crossings can give rise to errors. In the qubit experiments we typically pulse the voltage of the device (equivalent to detuning energy and tunnel coupling) from the initialization point to qubit operation point, and then from the qubit operation point to readout point. During the pulsing, the two-spin state goes through ST^- anti-crossing and 11-02 charge anti-crossing. The associated errors can come from the coherent (Landau Zener transition) and incoherent evolutions (relaxation and absorption). These errors may be improved by studying the energy levels, the coherent (incoherent) evolution around the anti-crossings, and how they depends on the control parameters, such as detuning energy, tunnel coupling, magnetic field, phonon and photon temperatures. Taking an theoretical example in Fig. 2.4d, the ST^- anti-crossing hybridizes the charge states and the spin states ($T^-(1,1)$ and $S(2,0)$) when $E_{Z+} \gtrsim \sqrt{2}t_c$ [7], allowing fast thermalization with photons that are present as noise on the detuning voltage. This spin-photon coupling should be suppressed if S and T^- have similar charge configuration, such as the situation $E_{Z+} \ll \sqrt{2}t_c$ in Fig. 2.4e.

(2) The charge lifetime at the readout point of Pauli spin blockade is typically limited by the relaxation $T^{\pm,0}(1,1)$ to $S(2,0)$. The error occurs if the relaxation time is not much longer than the integration time of the charge sensor. The relaxation time can be effectively extended using charge latching with the help of the nearby reservoir [8] or quantum dots. Further improvement relies on in-depth study on the relaxation process and how it depends on the control parameters (e.g. tunnel coupling, detuning energy, temperature). On the contrary, for initialization with high fidelity in a short time, it requires fast relaxation from $T^{\pm,0}(2,0)$ to $S(2,0)$. The relaxation might be speed up by coupling more to the reservoir [9] or populating the environment with more phonons (possibly

by sending a strong readout pulse to the charge sensor).

(3) Radio-frequency (RF) reflectometry, in the form of SET or dispersive gate sensing, could be further engineered to have faster response time and higher signal-to-noise ratio (SNR). Here we briefly discuss the SET implementation. A complete discussion for both reflectometry methods can be found in [10]. To begin with, it would be informative to investigate if the LC circuit we used can be well-approximated as the standard matching circuit when the device is turn-on, or if there are additional effective circuit elements induced possibly by the loss of the substrate or by accumulating 2D hole gas, which can complicate the impedance matching conditions [11]. If the matching circuit behaves similar to the standard one, the SNR of the reflected signal depends on both reflection coefficient variation and power [10] as

$$\mathrm{SNR} = |\Delta\Gamma|^2 \frac{P_{\mathrm{in}}}{P_{\mathrm{noise}}} \approx \left| \frac{Z_{\mathrm{load}} Z_0}{(Z_{\mathrm{load}} + Z_0)^2} \right| \left(\frac{\Delta R_{\mathrm{s}}}{R_{\mathrm{s}}} \right)^2 \frac{V_{\mathrm{device}}^2}{2R_{\mathrm{s}}} \frac{1}{P_{\mathrm{noise}}} \tag{8.1}$$

at the circuit resonance $\omega = \frac{1}{\sqrt{LC}}$ and in the small signal regime $\frac{\Delta R_{\mathrm{s}}}{R_{\mathrm{s}}} \ll 1$, where $P_{\mathrm{in}} = \frac{1}{1-|\Gamma|^2} \frac{V_{\mathrm{device}}^2}{2R_{\mathrm{s}}}$ is the signal power sent toward the circuit, $\Gamma = \frac{Z_{\mathrm{load}} - Z_0}{Z_{\mathrm{load}} + Z_0}$ is the reflection coefficient, $\Delta\Gamma \approx \frac{2Z_{\mathrm{load}} Z_0}{(Z_{\mathrm{load}} + Z_0)^2} \frac{\Delta R_{\mathrm{s}}}{R_{\mathrm{s}}}$ is the reflection coefficient variation (at resonance) due to the SET resistance variation ΔR_{s}, R_{s} is the SET resistance, $Z_{\mathrm{load}}(\omega)$ is the impedance of the circuit and approximately equals to $\frac{L}{R_{\mathrm{s}} C}$ at resonance, Z_0 is the transmission line characteristic impedance (typically 50 Ω), V_{device} is the sinusoidal voltage amplitude across the SET, and P_{noise} is the noise power. The SNR typically becomes optimal at matching condition $Z_{\mathrm{load}} = Z_0$. The bandwidth at the resonance is $\mathrm{BW} \approx \left(\frac{L}{R_{\mathrm{s}} C} + Z_0 \right) \frac{1}{2\pi L}$ and becomes $\frac{Z_0}{\pi L}$ at matching. Notice that the response time may not be entirely limited by BW, as the technique used in superconducting qubit systems where readout resonators can be ring up fast with a pulse having higher amplitude at beginning [12, 13]. The improvement of SNR and BW should happen by decreasing P_{noise}, R_{s}, C, increasing $\frac{\Delta R_{\mathrm{s}}}{R_{\mathrm{s}}}$ and the upper limit of V_{device}, while at the same time maintain the matching condition $R_{\mathrm{s}} Z_0 = \frac{L}{C}$. In the literature there are improvements made for individual parameters: Better P_{noise} can be achieved in SQUID or Josephson parametric amplifiers [14, 15]; R_{s} should be lowered (in theory) by more symmetric couplings to the reservoirs and small tunnel junction resistance (if the Coulomb island is classical such as a metallic SET [16]); C could be reduced by using accumulation gates as coupling capacitors [11]; the increased V_{device} was shown in metallic SET with small island which enhances charging energy [16]; the matching condition can be reached by tuning the circuit *in-situ* [17, 18].

(4) Instead of using RF reflectometry, fast charge readout ($\lesssim 10\mu s$) is possible by measuring the dc current of the SET via the amplifier close to the device [9, 19–23]. The dc-SET method has shown 940 ns integration time for PSB readout that gives SNR = 6.5 of two charge states and overall SPAM visibility higher than 99 % [9]. Compared to RF reflectometry, the advantage of this method is that it doesn't require LC resonators nearby the qubit device. On the other hands, it requires space and cooling power for cryogenic amplifiers.

(5) To make readout much faster than decoherence time while still being able to scale up the readout apparatus together with qubit numbers, it might be more straightfor-

ward to extend the coherence time such that we only need dc-SETs with amplifiers at high temperature stages (or even at room temperature). This will relax the requirements of high-bandwidth charge detection scheme which needs inductors or amplifiers close enough to the charge sensors to minimize the capacitance. The coherence time can be extended by dynamical decoupling, as implemented in other qubit platforms [24, 25]. The time scales should be further extended by operating at lower magnetic field with isotopically-purified germanium. For example, based on field dependent $T_2^\star$ in **chapter 7** and the relation $\sigma_{\text{hf}} \propto \sqrt{g_{^{73}\text{Ge}}}$ between effective hyperfine noise σ_{hf} and the concentration $g_{^{73}\text{Ge}}$ [26, 27], the 700 ppm ^{73}Ge (about 100 times diluted compared to natural abundance 7.76%) is estimated to have hyperfine noise weaker than electric noise at the field above 0.3-0.5 mT. At 0.5 mT, we make an optimistic prediction $T_2^\star = 100 - 200\mu s$ by assuming hyperfine noise from silicon and other impurity atoms in the spacer and the quantum well is not dominant (requires further experimental verification). Such a coherence time is much longer than RF reflectometry readout and is comparable to dc-SETs readout with room temperature amplifiers. Going to lower field has additional benefits, including the longer T_1 at the PSB point, and lower requirements on time resolution and bandwidth. The expected challenges are the longer measurement time, the sparse operations (to suppress residual exchange), and if the single- and two-qubit gates can still have high fidelity.

BIBLIOGRAPHY

[1] Simon Geyer et al. “Two-Qubit Logic with Anisotropic Exchange in a Fin Field-Effect Transistor”. In: Nature Physics (2022).

[2] Amanda E. Seedhouse et al. “Pauli Blockade in Silicon Quantum Dots with Spin-Orbit Control”. In: PRX Quantum 2 (1 Jan. 2021), p. 010303.

[3] Chein-An Wang et al. “Universal Control of Four Singlet-Triplet Qubits”. In: Science (2024).

[4] J Qi, Z.-H Liu, and H. Xu. “Spin–orbit interaction enabled high-fidelity two-qubit gates”. In: New J. Phys. 26.10 (Jan. 2024), p. 013012.

[5] Joel J. Wallman and Joseph Emerson. “Noise tailoring for scalable quantum computation via randomized compiling”. In: Phys. Rev. A 94 (5 Nov. 2016), p. 052325.

[6] Bence Hetényi and James R. Wootton. “Tailoring quantum error correction to spin qubits”. In: arXiv (2023). eprint: 2306.17786.

[7] J. H. Ungerer et al. “Strong coupling between a microwave photon and a singlet-triplet qubit”. In: Nature Communications 15.1 (2024), p. 1068. ISSN: 2041-1723.

[8] P. Harvey-Collard et al. “High-Fidelity Single-Shot Readout for a Spin Qubit via an Enhanced Latching Mechanism”. In: Phys. Rev. X 8 (2 2018), p. 021046.

[9] Jacob Z. Blumoff et al. “Fast and High-Fidelity State Preparation and Measurement in Triple-Quantum-Dot Spin Qubits”. In: PRX Quantum 3 (1 Mar. 2022), p. 010352.

[10] Florian Vigneau et al. “Probing quantum devices with radio-frequency reflectometry”. In: Applied Physics Reviews 10.2 (Feb. 2023), p. 021305. ISSN: 1931-9401.

[11] Y.-Y. Liu et al. “Radio-Frequency Reflectometry in Silicon-Based Quantum Dots”. In: Phys. Rev. Appl. 16 (1 July 2021), p. 014057.

[12] Evan Jeffrey et al. “Fast Accurate State Measurement with Superconducting Qubits”. In: Phys. Rev. Lett. 112 (19 May 2014), p. 190504.

[13] Y. Liu et al. “High fidelity readout of a transmon qubit using a superconducting low-inductance undulatory galvanometer microwave amplifier”. In: New J. Phys. 16.10 (Nov. 2014), p. 113008.

[14] F. J. Schupp et al. “Sensitive radiofrequency readout of quantum dots using an ultra-low-noise SQUID amplifier”. In: Journal of Applied Physics 127.24 (June 2020), p. 244503. ISSN: 0021-8979.

[15] S. Schaal et al. “Fast Gate-Based Readout of Silicon Quantum Dots Using Josephson Parametric Amplification”. In: Phys. Rev. Lett. 124 (6 Feb. 2020), p. 067701.

[16] Henrik Brenning et al. “An ultrasensitive radio-frequency single-electron transistor working up to 4.2 K”. In: Journal of Applied Physics 100.11 (Dec. 2006), p. 114321. ISSN: 0021-8979.

[17] N. Ares et al. “Sensitive Radio-Frequency Measurements of a Quantum Dot by Tuning to Perfect Impedance Matching”. In: Phys. Rev. Appl. 5 (3 Mar. 2016), p. 034011.

[18] Rafael S. Eggli et al. “Cryogenic hyperabrupt strontium titanate varactors for sensitive reflectometry of quantum dots”. In: Phys. Rev. Appl. 20 (5 Nov. 2023), p. 054056.

[19] E. H. Visscher et al. “Broadband single-electron tunneling transistor”. In: Applied Physics Letters 68.14 (Apr. 1996), pp. 2014–2016. ISSN: 0003-6951.

[20] J. Pettersson et al. “Extending the high-frequency limit of a single-electron transistor by on-chip impedance transformation”. In: Phys. Rev. B 53 (20 May 1996), R13272–R13274.

[21] I. T. Vink et al. “Cryogenic amplifier for fast real-time detection of single-electron tunneling”. In: Applied Physics Letters 91.12 (Sept. 2007), p. 123512. ISSN: 0003-6951.

[22] L. A. Tracy et al. “Single shot spin readout using a cryogenic high-electron-mobility transistor amplifier at sub-Kelvin temperatures”. In: Applied Physics Letters 108.6 (Feb. 2016), p. 063101. ISSN: 0003-6951.

[23] M. J. Curry et al. “Single-Shot Readout Performance of Two Heterojunction-Bipolar-Transistor Amplification Circuits at Millikelvin Temperatures”. In: Scientific Reports 9 (2019), p. 16976.

[24] Google Quantum AI. “Suppressing quantum errors by scaling a surface code logical qubit”. In: Nature 614.7949 (Feb. 2023), pp. 676–681. ISSN: 1476-4687.

[25] D. Bluvstein et al. “Logical quantum processor based on reconfigurable atom arrays”. In: Nature 626.7997 (Feb. 2024), pp. 58–65. ISSN: 1476-4687.

[26] Pericles Philippopoulos, Stefano Chesi, and W. A. Coish. “First-principles hyperfine tensors for electrons and holes in GaAs and silicon”. In: Phys. Rev. B 101 (11 Mar. 2020), p. 115302.

[27] N. W. Hendrickx et al. “Sweet-spot operation of a germanium hole spin qubit with highly anisotropic noise sensitivity”. In: Nature Materials (May 2024). ISSN: 1476-4660.

SUMMARY

Spins in gate-defined semiconductor quantum dots are considered as a compelling platform for quantum computation. As introduced in Chapter 1 and Chapter 2, hole spins in germanium quantum dots have several advantages. They allowed a rapid development of planar germanium spin qubits from single quantum dots to qubit arrays, with prototypical demonstrations of quantum algorithms, quantum error correction and high-fidelity single qubit control. Based on this development, in this thesis we further explore the physics and control protocols enabled by hopping spins in the quantum dot array.

Exchange interaction between two spins originates from spin hoppings to the virtual orbital states of the neighbouring quantum dots. It is essential to have controllable spin-spin interactions for applications in quantum information processing, quantum information transfer and quantum simulations. In Chapter 3 we experiment with control protocols of exchange couplings in a 2×2 germanium quantum dot array. We show the coherent control of the four-spin singlet states and triplet states when all the nearest neighbour tunnel couplings in the array were turned on. The results of the four-spin dynamics agree with a simple isotropic exchange model when the energy levels are not degenerate, which allows us to measure and equalize all the exchange couplings even though the device has capacitive crosstalk between the gates and the potential barriers. When the exchange couplings are tuned such that the states are nearly degenerate, we observe non-negligible state leakage and we attribute to the spin-orbit couplings and Zeeman energy gradient.

The sizeable spin-orbit interaction in germanium allows spin qubits to be efficiently driven but also couples the qubit to charge noise. In Chapter 4, we investigate the optimal condition of the electric field and magnetic field applied to a germanium quantum dot, aiming to maximize the spin dephasing time in the presence of charge noise. Through numerical simulations, sweet spots with respect to multiple fluctuating charge traps can be found under certain conditions for different magnetic field alignments. This investigation forms a basis for understanding and improving coherence time of hole spin qubits, and for future studies involving spatially inhomogeneous strain and potential profile.

The spin-orbit interaction can rotate the spin in the process of spin hoppings to virtual orbital states. This model can explain the experimental finding in Chapter 5, where the multi-photon spin resonance is excited by bichromatic driving signals. In such a scheme, the spin is rotated coherently by applying two frequencies on two gate electrodes of the quantum dot device. The strength of the spin resonance depends on the detuning energy of the double quantum dot, indicating the underlying mechanism of the spin-dependent interdot tunnel couplings.

Spin shuttling has been proposed for quantum information transfer between distant spin qubits. It has been studied in quantum dot array of GaAs and Si. In Chapter 6 we realized the first experiment of coherent spin shuttling in germanium. There, we

move a spin from one quantum dot to the other and back, observing coherent evolution where the spin state is rotated between $|\downarrow\rangle$ and $\alpha|\downarrow\rangle + \beta|\uparrow\rangle$ with a frequency corresponding to the Larmor frequency of the other dot. We identify this effect as the spin precession around the spin quantization axis of the other dot that is not parallel to the original dot, which is likely caused by the strong spin-orbit interaction in germanium. Although this rotation is non-trivial, it is stable in time and therefore it allows coherent spin control. We can fine-tune the timing of the shuttling pulses to make the state evolution an identity gate for every shuttling event between two quantum dots. With the fine-tuned pulses, we quantify the performance of the shuttling and obtain effective lengths above 300 μm for polarized states, 49 μm (9 μm) for superposition states with (without) dynamical decoupling.

Based on the finding in Chapter 6, in Chapter 7 we tune the shuttling pulses to make the state evolution an $X_{\pi/2}$ gate with precision allowing average gate fidelity > 99.9%. The sizable angles of $40° - 45°$ between quantization axes of the quantum dots allow efficient qubit driving via baseband signal, in contrast to the commonly used sinusoidal signals (EDSR). We use such hopping-based quantum gate to measure coherence time at magnetic field ranging from 40 mT to 1 mT, and observe trends indicating dephasing dominated by electric noise at high fields and by nuclear noise at low fields. By applying the shuttling operations to a 10-quantum dot array, we acquire statistics of coherence time and g-factor for individual quantum dot.

High-fidelity two-qubit control is one of the crucial elements for quantum computation. It has been demonstrated for electron spin-qubits in silicon but is still missing for hole spin-qubits. In Chapter 7, we use hopping-based single-qubit gates to tune up the two-qubit gate. The two-qubit adiabatic CZ gate is characterized by both interleaved randomized benchmarking (IRB) and gate set tomography (GST), obtaining the average gate fidelity F_{CZ} = 99.3% based on IRB and F_{CZ} = 98.1% based on GST. The high-fidelity gates are compatible with highly-tunable two-qubit interaction (exchange coupling), which has a residual value $J_{off} = 10 - 15$ kHz and a maximal value $J_{on} \approx 21$ MHz accessible via baseband voltage pulsing. $T_2^\star$ measurements and numerical simulations in the exchange-on situation show that fluctuation in the exchange coupling is the dominant error source, which will need to be improved in the future.

SAMENVATTING

Spins in halfgeleider kwantumstippen, gevormd met metalen contacten, worden beschouwd als een aantrekkelijk platform voor kwantum berekeningen. Zoals geïntroduceerd in Hoofdstuk 1 en Hoofdstuk 2 hebben gaten-spins in germanium kwantumstippen verschillende voordelen. Ze maakten een snelle ontwikkeling mogelijk van planaire germanium-spinqubits, van enkele kwantumstippen tot qubit-arrays, met prototypische demonstraties van kwantumalgoritmen, kwantumfoutcorrectie en controle van enkele qubits met een hoge kwaliteit. Op basis van deze ontwikkelingen onderzoeken we in dit proefschrift verder de fysica en controleprotocollen die mogelijk worden gemaakt door hoppende spins in de kwantumstipt-array.

Uitwisselingsinteractie tussen twee spins vindt zijn oorsprong in spin-hoppings naar de virtuele orbitale toestanden van de aangrenzende kwantumstippen. Het is essentieel om controleerbare spin-spin-interacties te hebben voor toepassingen in kwantuminformatieverwerking, kwantuminformatieoverdracht en kwantumsimulaties. In Hoofdstuk 3 experimenteren we met protocollen om de uitwisselingskoppeling in een 2×2 germanium kwantumstip-array te controleren. We laten de coherente controle zien van de vier-spin singlettoestanden en triplettoestanden wanneer alle naburige tunnelkoppelingen in de array waren ingeschakeld. De resultaten van de vier-spindynamica komen overeen met een eenvoudig isotroop uitwisselingsmodel wanneer de energieniveaus niet ontaard zijn, waardoor we alle uitwisselingskoppelingen kunnen meten en egaliseren, ook al heeft het apparaat capacitieve overspraak tussen de contacten en de potentiaal barrières. Wanneer de uitwisselingskoppelingen zo zijn afgestemd dat de toestanden bijna ontaard zijn, nemen we een niet te verwaarlozen toestandslekkage waar en schrijven we deze toe aan de spin-baankoppelingen en de Zeeman-energiegradiënt.

De omvangrijke spin-baan-interactie in germanium maakt het mogelijk dat spin-qubits efficiënt worden aangedreven, maar koppelt de qubit ook aan ladingsruis. In Hoofdstuk 4 onderzoeken we de optimale toestand van het elektrische veld en het magnetische veld dat wordt toegepast op een germaniumkwantumstip, waardoor de spin-defaseringstijd in de aanwezigheid van ladingsruis wordt gemaximaliseerd. Door middel van numerieke simulatie kunnen onder bepaalde omstandigheden 'sweet spots' worden gevonden met betrekking tot meerdere fluctuerende ladingsvallen voor verschillende magnetische velduitlijningen. Dit onderzoek vormt een basis voor het begrijpen en verbeteren van de coherentietijd van gat spin qubits, en voor toekomstige studies met ruimtelijk inhomogene rek en potentiaalprofiel.

De spin-baan-interactie kan de spin roteren tijdens het spin-hoppen naar virtuele orbitale toestanden. Dit model kan de experimentele bevinding uit Hoofdstuk 5 verklaren, waarbij de multi-foton-spinresonantie wordt opgewekt door bichromatische aandrijfsignalen. In een dergelijk schema wordt de spin coherent geroteerd door twee frequenties aan te brengen op twee contact-electroden van het kwantum stip-apparaat.

De sterkte van de spinresonantie hangt af van de ontstemmingsenergie van de dubbele kwantumstip, wat het onderliggende mechanisme van de spin-afhankelijke tussendotse tunnelkoppeling aangeeft.

Een spin-pendel is voorgesteld voor de overdracht van kwantuminformatie tussen verre spinqubits. Het is onderzocht in een kwantumstip-array van GaAs en Si. In Hoofdstuk 6 hebben we het eerste experiment van coherente spin-pendel in germanium gerealiseerd. Daar verplaatsen we een spin van de ene kwantumstip naar de andere en terug, en observeren we een coherente evolutie waarbij de spintoestand wordt geroteerd tussen $|\downarrow\rangle$ en $\alpha|\downarrow\rangle + \beta|\uparrow\rangle$ met een frequentie die overeenkomt met de Larmorfrequentie van het andere stip. We identificeren dit effect als de spin-precessie rond de spin-kwantisatie-as van de andere stip die niet parallel is aan de oorspronkelijke stip, wat waarschijnlijk wordt veroorzaakt door de sterke spin-baan-interactie in germanium. Hoewel deze rotatie niet triviaal is, is deze stabiel in de tijd en maakt daarom een coherente spincontrole mogelijk. We kunnen de timing van de pendelpulsen nauwkeurig afstemmen om van de toestandsevolutie een identiteitspoort te maken voor elke pendelgebeurtenis tussen twee kwantumstippen. Met de nauwkeurig afgestemde pulsen kwantificeren we de prestatie van het pendelen en verkrijgen we effectieve lengtes boven 300 μm voor gepolariseerde toestanden, 49 μm (9 μm) voor superpositietoestanden met (zonder) dynamische ontkoppeling.

Gebaseerd op de bevindingen in Hoofdstuk 6, stemmen we in Hoofdstuk 7 de pendelpulsen af om van de toestandsevolutie een $X_{\pi/2}$ poort te maken met een precisie die een gemiddelde poortbetrouwbaarheid > 99.9% mogelijk maakt. De aanzienlijke hoeken van $40° - 45°$ tussen de kwantisatie-assen van de kwantumstippen maken een efficiënte qubit-aansturing via het basisbandsignaal mogelijk, in tegenstelling tot de algemeen gebruikte sinusoïdale signalen (EDSR). We gebruiken een dergelijke op hoppen gebaseerde kwantumpoort om de coherentietijd te meten bij een magnetisch veld variërend van 40 mT tot 1 mT, en observeren de trends die duiden op door elektrische ruis gedomineerde defasering bij hoge velden en nucleaire ruis gedemoniseerde defasering bij lage velden. Door de pendel-operaties toe te passen op een array van 10-kwantumstippen, verkrijgen we statistieken van de coherentietijd en de g-factor voor individuele kwantumstippen.

Hoog-betrouwbare twee-qubit-controle is een van de cruciale elementen voor kwantumberekeningen. Het is aangetoond voor elektronenspinqubits in silicium, terwijl het nog steeds ontbreekt voor gatspinqubits. In Hoofdstuk 7 gebruiken we de op hoppen gebaseerde single-qubit-poorten om de twee-qubit-poort af te stemmen. De adiabatische CZ-poort met twee qubits wordt gekarakteriseerd door zowel verwoven gerandomiseerde prestatiemeting (IRB) als poortverzameling tomografie (GST), waarbij de gemiddelde poortbetrouwbaarheid $F_{CZ} = 99.3\%$ wordt verkregen op basis van IRB en $F_{CZ} = 98.1\%$ gebaseerd op GST. De hoog-betrouwbare zijn compatibel met zeer afstembare twee-qubit-interactie (uitwisselingskoppeling), met de restwaarde $J_{off} = 10 - 15$ kHz en de maximale waarde $J_{on} \approx 21$ MHz haalbaar met uitwisselingsregime. De $T_2^\star$ meting en numerieke simulatie bij de uitwisselingssituatie laten zien dat fluctuatie in de uitwisselingskoppeling de dominante foutbron is, die in de toekomst moet worden verbeterd.

DATA AVAILABILITY

The data, analysis and simulation codes used in chapters 2 to 8 are available on Zenodo or 4TU.ResearchData repositories with DOI listed in Table 8.1.

Chapter	Repository
2 and 8	doi.org/10.4121/1be5c21a-d0b0-4b7c-b73e-eb7103162660.v1
3	doi.org/10.5281/zenodo.7998145
4	doi.org/10.5281/zenodo.13385169
5	doi.org/10.4121/bb43fe1d-f503-49e8-9f17-ce7d734f015d.v1
6	doi.org/10.5281/zenodo.11203148
7	doi.org/10.4121/158ba07a-4375-4c17-bf7b-289726f5452a.v2

Table 8.1: The data repositories of individual chapters.

ACKNOWLEDGEMENTS

The work presented in this thesis is not an individual effort, but the outcome of interactions with the people around me. It has been a privilege to work in this environment. Here I would like to thank all the people who have provided guidance, inspiration, and support during my time at TU Delft.

I want to thank my promotor, **Menno**, for giving me the opportunity to join your group. Your guidance and support throughout my PhD have been invaluable. I have appreciated the ways you conduct research: you always mention the big picture that I often miss; you look at the future and consider ways to improve; you give creative and practical advice, as well as tips that boost efficiency; you think more about cooperation and contribution rather than competition; you often find the bright side of challenges. Apart from research, you show care for our personal well-being. I am glad to be part of your group.

Giordano, thank you for being my co-promotor, and strong support on providing materials for every experiment. I appreciate your advices on several projects including the hybrid germanium experiment, although I did not have the experiment fully work out. I am sure there will be many exciting discoveries along that direction. **Lieven**, thank you for being my promotor in my first year, allowing me to be in collaboration with your group, and having insightful feedback on our manuscripts presented in this thesis. I appreciate your leadership, fostering collaborative and harmonious atmosphere within spin-qubit groups and Qutech. **Max**, thank you for supervision and theoretical supports on several projects. Without your efforts, many important parts of the analysis in the papers will be missing. I enjoy learning from you the various concepts in quantum physics and the latest developments. I wish you the very best in your new role as group leader.

Luca, **Gertjan**, **Nico**, **Will**, thank you for sharing their knowledge and providing support in many ways during the early stages of my PhD, despite the challenging times of corona. **Marcel**, at beginning of our PhD we spent quite some time in the cleanroom and around the measurement setup. It was fun to be in the lab, observing, discussing and learning together. I appreciate your willingness of sharing many practical details, from cleanroom techniques to doctoral regulations. May your have smooth transition into the new group. **Floor**, I like how you involved right people to push forward the shuttling experiments. Also, thank you for reminding me the importance of relaxing atmosphere, by stopping me talking about physics during lunch break. I do recognize this perspective and will try to put it into practice. **Hanifa**, I like the atmosphere you bring, sometimes serious, scientific and critical, sometimes cheerful and spontaneous. I respect your courage to pursue new directions in experiment and career. Wish your journey in the US be exciting and fulfilling. **Coréntin**, I always appreciate the enthusiasm you bring to research. It is remarkable how you manage entire projects while still paying close attention to the smallest experimental details. I have learnt a lot when working with you. Thank you as well for organizing fun activities (uitje in France) that brought

us together. A special thank-you to **Cécile** and **Valentin** for being my paranymphs at the defense. **Cécile**, I'm glad to have you as my colleague that I can have time speaking Chinese. Also thank you for letting me take care of Yuzu. I had a lot of fun. **Valentin**, I appreciate your humor, which always comes at just the right moment. You have nice ideas on making workflows more systematic and scalable. One of them is Quantum Dot Designer, which helped me obtain my final credits in the programming course. I am happy we were able to accomplish it in the end. **Francesco**, I admire your determination and persistence in driving the experiments forward. Wish you a great start in Copenhagen. **Sasha**, I've found our scientific discussion enjoyable. You have great ambition. I am exciting to see your ideas coming to life. **Dingshan**, thanks for your passion and hard work. Being a mentor for your master project was a unique experience. **Michael**, your presence always brings a relaxing vibe. I've enjoyed our chats from time to time. **Job**, I like the stories you shared, whether funny or informative, during lunch time. Wish you all the best in finishing PhD. **Marion**, **Barnaby**, **Damien**, **Dario**, **Zarije**, **Setareh**, I believe you will continue expanding our knowledge of germanium spin qubits. I look forward to the new discoveries in the future.

I would like to thank everyone in spin qubit groups for being part of a collaborative, diverse and inclusive environment. Sincere thanks to **Sander** for answering my questions and coming up solutions that are key to the experiments, from hardware specs to software implementation. **Sergey**, cleanroom are full of unpleasant surprises, and you are not hesitate to offer suggestions. I really appreciate your help. **Amir**, thanks for introducing me the cleanroom database, and providing prefabs that are readily to be used. **Alberto**, thank you for sharing the recipe and experience on device fabrication. **Stephan**, I had luck sitting on the other side of screen in qclab2, and learning your tricks for searching my first PSB signal. **Tzu-Kan**, thank you for sharing your measurement techniques from quantum simulation projects. **Yuta**, **Xin**, thanks for sharing your findings from time to time. I always learnt new things from our discussions. **Brennan**, **Irene**, **Eline**, **Xiao**, thank you for practical suggestions regarding gate tuning and GST experiments.

I have to thank the support from **Jason**, **Olaf**, **Matt**, **Jelle**, **Roy**, **Siebe**, **Raymond**, **Raymond**, **Roy**, **Nico**, for maintaining lab equipment, creating cool solutions under all sorts of constraints, and taking time explaining how things work.

I would like to express my gratitude to my committee members - **Sefano**, **Leo**, **Leo**, **Ferdinand**, **Yann-Michel** - for dedicating their time to reviewing my thesis.

Lastly, outside of the lab I would like to thank my friends and family for their company and support.

CURRICULUM VITÆ

Chien-An Wang

23-02-1994 Born in Chiayi, Taiwan.

EDUCATION

2008–2012 High School
Chiayi Senior High School, Chiayi, Taiwan

2012–2016 Bachelor in Electrical Engineering
National Taiwan University, Taipei, Taiwan

2017–2019 Master of Science in Applied Physics
Technical University of Delft, Delft, Netherlands
Thesis: Al-InSb devices based on VLS nanowires
Supervisors: Prof. dr. ir. L. P. Kouwenhoven

2020–2025 PhD. candidate
Technical University of Delft, Delft, Netherlands
Thesis: Interacting and Hopping Spin Qubits in Germanium
Promotor: Dr. ir. M. Veldhorst
Co-Promotor: Dr. G. Scappucci

LIST OF PUBLICATIONS

9. **C.-A. Wang**, V. John, H. Tidjani, C.X. Yu, A.S. Ivlev, C. Déprez, F. van Riggelen-Doelman, B.D. Woods, N.W. Hendrickx, W.I.L. Lawrie, L.E.A. Stehouwer, S.D. Oosterhout, A. Sammak, M. Friesen, G. Scappucci, S.L. de Snoo, M. Rimbach-Russ, F. Borsoi, M. Veldhorst, *Operating semiconductor quantum processors with hopping spins*, Science **385**, 447-452 (2024)..

8. X. Zhang, E. Morozova, M. Rimbach-Russ, D. Jirovec, T.-K. Hsiao, P. Cova Fariña, **C.-A. Wang**, S.D. Oosterhout, A. Sammak, G. Scappucci, M. Veldhorst, L.M.K. Vandersypen, *Universal control of four singlet-triplet qubits*, Nature Nanotechnology (2024).

7. F. van Riggelen-Doelman, **C.-A. Wang**, S.L. de Snoo, W.I.L. Lawrie, N.W. Hendrickx, M. Rimbach-Russ, A. Sammak, G. Scappucci, C. Déprez, and M. Veldhorst, *Coherent spin qubit shuttling through germanium quantum dots*, Nature Communication **15**, 5716 (2024).

6. V. John, F. Borsoi, Z. György, **C.-A. Wang**, G. Széchenyi, F. van Riggelen, W.I.L Lawrie, N.W. Hendrickx, A. Sammak, G. Scappucci, A. Pályi, and M. Veldhorst, *Bichromatic Rabi control of semiconductor qubits*, Physical Review Letters **132**, 067001 (2024).

5. T.-K. Hsiao, P. Cova Fariña, S.D. Oosterhout, D. Jirovec, X. Zhang, C.J. van Diepen, W.I.L. Lawrie, **C.-A. Wang**, A. Sammak, G. Scappucci, M. Veldhorst, E. Demler, and L.M.K. Vandersypen, *Exciton Transport in a Germanium Quantum Dot Ladder*, Physical Review X **14**, 011048 (2024).

4. M. Meyer, C. Déprez, T.R. van Abswoude, D. Liu, **C.-A. Wang**, S. Karwal, S.D. Oosterhout, F. Borsoi, A. Sammak, N.W. Hendrickx, G. Scappucci, M. Veldhorst, *Electrical control of uniformity in quantum dot devices*, Nano Letters **23** (7), 2522-2529 (2023).

3. **C.-A. Wang**, H. Ekmel Ercan, Mark F. Gyure, G. Scappucci, M. Veldhorst, and M. Rimbach-Russ, *Modelling of planar germanium hole qubits in electric and magnetic fields*, npj Quantum Information **10**, 102 (2024).

2. **C.-A. Wang**, C. Déprez, H. Tidjani, W.I.L. Lawrie, N.W. Hendrickx, A. Sammak, G. Scappucci, and M. Veldhorst, *Probing resonating valence bonds on a programmable germanium quantum simulator*, npj Quantum Information **9**, 58 (2023).

1. G. Badawy, S. Gazibegovic, F. Borsoi, S. Heedt, **C.-A. Wang**, S. Koelling, M.A. Verheijen, L.P. Kouwenhoven, and E.P.A.M. Bakkers. *High Mobility Stemless InSb Nanowires*, Nano Letters **19** (6), 3575-3582 (2019).